Spectroscopic networks and variational models for hyperfine-resolved molecular line lists

Charles Bowesman

A dissertation submitted in partial fulfillment
of the requirements for the degree of
Doctor of Philosophy
of
University College London.

Department of Physics & Astronomy
University College London

January 2024

I, Charles Bowesman, confirm that the work presented in this thesis is my own. Where information has been derived from other sources, I confirm that this has been indicated in the work.

Abstract

Spectroscopic data in the form of line lists underpin the study of molecules in many astrophysical regions of interest and recent advances in observational techniques have necessitated the production of these data to a high-resolution standard. Line lists for the refractory species aluminium monoxide (AlO) and vanadium monoxide (VO) which are of interest in stellar and exoplanetary atmospheres, as well as H_3^+ which is known to exist in ionospheres of giant planets and the interstellar medium are presented. These data are computed using variational nuclear motion calculations and are further augmented through several post-processing steps to prepare them for use in high-resolution spectroscopy. Four such methods for adjusting calculated term energies and providing uncertainty estimates are detailed, outlining the impetus behind the construction of so-called hybrid line lists.

The primary source of high-resolution term energies and associated uncertainties is the MARVEL (measured active vibration-rotation energy levels) procedure which obtains empirical energy values from spectroscopic networks of measured transition data. Hyperfine-unresolved MARVEL networks for $^{27}Al^{16}O$, H_3^+, H_2D^+, D_2H^+ and $^{51}V^{16}O$ are constructed, in addition to a hyperfine-resolved $^{51}V^{16}O$ network. These empirical energies are used to replace their calculated counterparts and high-accuracy machine-learned predicted energy shifts are computed for levels not observed through experiment. The refined energies of $^{27}Al^{16}O$ are used to inform corrections to line lists for three isotopically substituted species of AlO. Existing ExoMol line lists for H_3^+ and H_2D^+ are updated and new line lists for the other deuterated isotopologues, D_2H^+ and D_3^+, are produced. Previously recorded spectra of VO intercombination bands are assigned and facilitate the construction of a new, 15 electronic state spectroscopic model for $^{51}V^{16}O$ with the novel inclusion of six different hyperfine coupling terms. This is used to produce a line list comprising fully hyperfine-resolved term energies and transition intensities for VO.

Impact Statement

The development of the high-resolution line lists presented here is essential to support future spectroscopic studies of molecules in various astrophysical mediums, particularly the interstellar medium (ISM), exoplanets and stars. The work presented here on H_3^+ and its deuterated isotopologues will support the accurate constraint of ISM processes such as the cosmic ray ionisation rate and better allow for estimations of the error on these measurements owing to the provision of uncertainties as part of this work. This will additionally allow for the more accurate analysis of ionospheric effects on Jupiter and the other gas giants in our solar system, where H_3^+ is known to exist. It is believed that H_3^+ will likely play a similar role in some giant planets outside of our solar system and will similarly be important to characterise the atmospheric chemistry in those environments.

The new VO line list presented in this work will hopefully enable the reliable detection of VO in exoplanet atmospheres, as existing data sets have so fair failed to do so. Owing to the new inclusion of hyperfine couplings, the hyperfine-resolved HyVO line lists can be used to generate spectra that differ considerably from previous line lists, both in terms of the positions of spectral features and their intensities. These changes are due to a more thorough treatment of the quantum mechanical couplings present within the spectroscopic model used to represent the molecule, as well as additional refinements against experimental measurements. Consequently, future observations aiming to detect VO in an astrophysical setting can be more confident in their results, be they detections or non-detections.

While AlO is known to exist in the atmospheres of cool stars and hot exoplanets it also has many applications outside of astrophysics. Due to its use of aluminium in propellants, the study of AlO in combustion also relies on accurate spectroscopic data. The same is true for studying the oxidation of aluminium in laser induced plasmas which have a range of industrial applications including but not limited to quantifying the purity of aluminium alloys.

The developments on the various techniques used to improve the accuracy of calculated line lists, particular the MARVELisation and predicted shifts, help to maximise the accuracy to which line lists can be provided. This is particularly true of the predicted shifts method, which uses machine learning to "fill in the gaps"; corrections to the calculated energies of levels not observed through experiment are predicted based on the observed trends in nearby known levels. This is done with high accuracy and maximises the amount of data that can be provided to a high-resolution standard. As new spectroscopic data can be slow to produce, being able to provide coverage of as many levels as possible is invaluable. This pipeline allows

for the iterative improvement of these line lists as new experimental data becomes available: the MARVEL networks are simply added to and new predicted shifts can be computed at each iteration.

Acknowledgements

My foremost thanks must go to my supervisors Jonathan Tennyson and Sergey Yurchenko, whose expert guidance made my PhD a seamless experience. Similarly, I must thank Tony Lynas-Gray, Bridgette Cooper, Alec Owens, Mikhail Semenov, Marco Pezzella, Georgi Mitev, Kyriaki Kefala, Elizabeth Guest, Ryan Brady, Wilfrid Somogyi, Andrei Sokolov, Apoorva Upadhyay, Jingxin Zhang, Thomas Mellor, Oleksiy Smola and Armando Perri for their continuous help, advice and general good company.

I would like to thank Samuel A. Meek, Tibor Furtenbacher and Atilla G. Császár for discussion on the treatment of hyperfine transitions in spectroscopic networks. I would also like to further thank Tibor Furtenbacher and Atilla G. Császár for making the latest versions of the MARVEL code available and for useful discussions. The work on H_3^+ and its isotopologues was made possible by Marco Pezzella, Nikolay F. Zobov and Irina I. Mizus' work performing the calculations for the new MiZo line lists for D_2H^+ and D_3^+ and for János Sarka and Bill Poirier's work on assigning additional levels of H_3^+. It would not have been possible to finish my work on VO during the course of my PhD without the prior efforts of Laura McKemmish and Qianwei Qu, who continued to provide helpful discussion on the unique problem of VO. I would also like to thank Scott W. Hopkins for his help with the fiddly assignment of several spectra of VO recorded by him and his colleagues, and Eileen Döring for proving her experimental results prior to publication, as they were crucial in obtaining a good fit to the ground state of VO.

This work was supported by the European Research Council (ERC) under the European Union's Horizon 2020 research and innovation programme through Advance Grant number 883830 and the UK STFC under grant ST/R000476/1. The final calculations of this work were performed using the DiRAC Data Intensive service at Leicester, operated by the University of Leicester IT Services, which forms part of the STFC DiRAC HPC Facility (https://dirac.ac.uk). The equipment was funded by BEIS capital funding via STFC capital grants ST/K000373/1 and ST/R002363/1 and STFC DiRAC Operations grant ST/R001014/1. DiRAC is part of the National e-Infrastructure.

Research Paper Declaration

1. **Bowesman, C.A.**, Shuai, M., Yurchenko, S.N., Tennyson, J., 2021. A high-resolution line list for AlO. Mon. Not. Roy. Astron. Soc. 508, 3181–3193. doi:10.1093/mnras/stab2525. Discussion of available experimental data sources and MARVEL networks adapted for Chapter 3. Hybrid line list/postprocessing methodology adapted for Chapter 2.

2. **Bowesman, C.A.**, Akbari, H., Hopkins, S., Yurchenko, S.N., Tennyson, J., 2022. Fine and hyperfine resolved empirical energy levels for VO. J. Quant. Spectrosc. Radiat. Transf. 289, 108295. doi:10.1016/j.jqsrt.2022.108295. Discussion of available experimental data sources, MARVEL networks and spectra assignments adapted for Chapter 5. Hyperfine deperturbation procedure adapted for Chapter 2.

3. **Bowesman, C.A.**, Mizus, I.I., Zobov, N.F., Polyansky, O.L., Sarka, J., Poirier, B., Pezzella, M., Yurchenko, S.N., Tennyson, J., 2023. ExoMol line lists - L: High-resolution line lists of H_3^+, H_2D^+, D_2H^+ and D_3^+. Mon. Not. Roy. Astron. Soc. 519, 6333–6348. doi:10.1093/mnras/stad050. Material adapted for Chapter 4.

4. **Bowesman, C.A.**, Yurchenko, S.N., Tennyson, J., 2023. A hyperfine-resolved spectroscopic model for vanadium monoxide ($^{51}V^{16}O$). Mol. Phys. 122, e2255299. doi:10.1080/00268976.2023.2255299. Discussion of spectroscopic model, refinement process and assignment of perturbations adapted for Chapter 5.

5. **Bowesman, C.A.**, Qu, Q., McKemmish, L.K., Yurchenko, S.N., Tennyson, J., 2024. ExoMol line lists – LV. Hyperfine-resolved molecular line list for vanadium monoxide ($^{51}V^{16}O$). Mon. Not. Roy. Astron. Soc. 529, 1321–1332. doi:10.1093/mnras/stae542. Line list calculations and discussion adapted for Chapter 5. Hybrid line list/postprocessing methodology adapted for Chapter 2.

6. McKemmish, L.K., **Bowesman, C.A.**, Kefala, K., Perri, A.N., Syme, A.M., Yurchenko, S.N., Tennyson, J., 2024. A hybrid approach to generating diatomic line lists for high resolution studies of exoplanets and other hot astronomical objects: Updates to ExoMol MgO, TiO and VO line lists. RAS Tech. Instr. (in prep.). Details of VO MARVEL network update adapted for Chapter 5.

Contents

1 Introduction **11**

2 Methodology **17**
2.1 Variational methods 18
2.1.1 Hyperfine couplings 21
2.2 The MARVEL procedure 26
2.2.1 Assessing spectroscopic network inconsistencies 31
2.3 Hyperfine deperturbation 33
2.3.1 Relative intensities 34
2.3.2 Deperturbation uncertainty scaling 35
2.3.3 Effectiveness 37
2.4 Hybrid line lists 39
2.4.1 MARVELisation 39
2.4.2 Effective Hamiltonians 40
2.4.3 Predicted shifts 40
2.4.4 Pseudo-experimental energy levels 42
2.4.5 Calculated Levels 42
2.4.6 Source Tags 42

3 Aluminium Monoxide **44**
3.1 Overview 44
3.2 Method 45
3.2.1 Experimental data sources 47
3.2.2 MARVELised data sources 47
3.2.3 Hyperfine deperturbation 50
3.2.4 Effective Hamiltonians 50
3.2.5 The MARVEL network 51
3.2.6 Predicted energy shifts 53
3.2.7 Pseudo-experimental energy levels 55
3.2.8 Calculated levels 55
3.3 New line list 56
3.3.1 States files 56
3.3.2 Partition functions 57
3.3.3 Spectra 58
3.4 Summary 59

3.A AlO MARVEL data 63

4 H_3^+ and its deuterated isotopologues **66**
4.1 Overview 66
4.2 Method 67
4.3 MARVELised data sources 68
4.3.1 H_3^+ network 70
4.3.2 H_2D^+ network 71
4.3.3 D_2H^+ network 72
4.4 Line list calculations 73
4.4.1 Updated H_3^+ and H_2D^+ 73
4.4.2 New line lists 73
4.4.3 D_2H^+ nuclear motion calculations 74
4.4.4 D_3^+ nuclear motion calculations 74
4.4.5 D_3^+ effective Hamiltonian calculations 75
4.4.6 States files 75
4.4.7 Partition functions 80
4.5 Spectra 81
4.5.1 Rotational spectra 81
4.5.2 Mid and far infrared spectra 82
4.6 Summary 83
4.A H_3^+ MARVEL data 87

5 Vanadium Monoxide **94**
5.1 Overview 94
5.2 Experimental data sources 98
5.2.1 MARVELised data sources 98
5.2.2 Connecting the doublet and quartet manifolds 101
5.2.3 New spectra assignment 101
5.2.4 Unresolved doublet spin-orbit separations 103
5.2.5 Effective Hamiltonian parameters for doublet states 104
5.3 MARVEL networks 106
5.3.1 Hyperfine-resolved network 107
5.3.2 Hyperfine-unresolved network 107
5.4 Spectroscopic Model 109
5.4.1 DUO model 110
5.4.2 Hyperfine couplings 113
5.4.3 Results 116
5.4.4 Perturbations 119
5.4.5 Transition dipole moments 120
5.5 Hybrid line list 120
5.5.1 New line list 122
5.5.2 Partition functions 125
5.6 Discussion 128
5.6.1 Spectra 129
5.6.2 Hyperfine effects 131

5.6.3 VOMYT Comparisons 133
5.7 Summary 136
5.A VO MARVEL data 138

6 Conclusion **141**
6.1 Summary 141
6.2 Future work 143

Bibliography **149**

Chapter 1

Introduction

The ExoMol project was conceived with the aim of providing comprehensive spectroscopic data for the analysis of exoplanet atmospheres (Tennyson and Yurchenko, 2012), a field of study that has grown rapidly after the first detection of an exoplanet by Mayor and Queloz (1995) and the subsequent detection of the first molecule in an exoplanet atmosphere (Tinetti et al., 2007). The majority of these studies rely on transit spectroscopy, where an exoplanet is observed as it passes through the line of sight between the observer and a host star. During this time, the spectrum of the exoplanet's atmosphere can be observed superimposed on that of its star, primarily in absorption. In a similar manner, an exoplanet emission spectrum is observed when the planet is passes towards an eclipse. See the comprehensive reviews by Tinetti et al. (2013) and Madhusudhan (2019) for further details. Analysis of these spectra, and the determination of the atmospheric constituents, presupposes the knowledge of spectra of various molecules in the relevant conditions. In particular, this relies on having models for molecules applicable for a range of temperatures, often up to several thousand Kelvin. While spectra recorded experimentally can provide a snapshot of a molecule under certain conditions, creating a dataset that can be applied over a range of conditions requires the computation of energy levels and the probabilities for transitions between them. With these two pieces of information, it is possible to simulate spectra under a given set of conditions, such as at a specific temperature or resolution, and together are commonly referred to as a "line list". Hence, a database of line lists covering an array of molecules was critical for enabling the study of exoplanet atmospheres and the thorough classification of their constituents.

While an assortment of other projects that provided spectroscopic data existed at the ExoMol project's inception, they were limited in the wavelengths, species and, crucially, the temperatures they were able to provide data for. Much of the available data was generally geared towards molecules observed in the far infra-red in cold regions like the interstellar medium (ISM), in stark contrast to the atmospheres of so called "hot Jupiters", one of the most frequently observed class of exoplanets with temperatures often approaching 3 000 K. While this project was primarily focused on exoplanets, hence the "Exo" in the name, the molecular data it aimed to produce was also applicable to the atmospheres of cool stars, such as the very abundant M dwarfs, or substellar objects, such as brown dwarfs. Though other projects working to provide comprehensive line list data such as HITRAN (Gordon et al., 2022) and GEISA (Delahaye et al., 2021) have existed from the 1970s and 1980s respectively, they

primarily focus on molecules relevant to the Earth's atmosphere and atmospheres of planets in our solar system respectively. Though the HITEMP project exists as a "sister" project to HITRAN (Rothman et al., 2010) it still focuses on the same terrestrial species, albeit at higher temperatures. Similarly, the spectroscopic data of TheoReTS (Rey et al., 2016), NASA AMES (Huang et al., 2017) and MoLLIST (Bernath, 2020) are limited in the molecules they consider, though the data they do provide is often high-accuracy; data provided by the CDMS (Endres et al., 2016) is generally intended for low temperature, pure-rotational microwave spectroscopy and NIST (Kramida et al., 2020) only provides atomic data. Consequently, their data are not designed for use in the study of such hot environments, where vastly different chemistries occur. Such atmospheres often involve atomic species that are not relevant to the study of the Earth's atmosphere, particularly metal oxides like those discussed in Chapter 3 and Chapter 5. Hence, a methodology was adopted to calculate the energy levels and transitions for various molecules of interest, relying on a combination of variational nuclear motion calculations and *ab initio* electronic structure calculations (Tennyson, 2012). Multiple programs have been built or updated to aid in this goal, resulting in several in-house program suites for the computation of energy levels and transitions intensities for diatomics (Yurchenko et al., 2016b), triatomics (Tennyson et al., 2004) and polyatomics (Yurchenko et al., 2007). These programs rely on the variation principle and are discussed in Section 2.1.

With the deployment of new space telescopes such as the James Webb Space Telescope, which now frequent new analyses of exoplanet atmospheres, and the upcoming Atmospheric Remote-sensing Infrared Exoplanet Large-survey (ARIEL) mission (Tinetti et al., 2018) opportunities for exoplanet observations are continuing to grow. However, these missions rely on equipment with relatively low resolving power, with $R \gtrsim 3\,000$ (Labiano, A. et al., 2021) and $R \leq 100$ respectively, especially compared to the abilities of spectrographs on ground-based telescopes which are able to achieve resolving powers close to or even greater than $R = 100\,000$ (Fisher et al., 2020). While new ground-based telescopes with similar high-resolutions capabilities are forthcoming, such as the Extremely Large Telescope (ELT) (Brandl et al., 2010), the observational capabilities of such instruments are limited by telluric contaminants. These high-resolution instruments are increasingly used in conjunction with cross-correlation/Doppler shift spectroscopy, which tracks the variation in the Doppler shift in an exoplanet's spectrum over the duration of its transit (Snellen, 2014). This technique allows for the contributions of telluric species in the spectra to be isolated and discarded as they do not vary with the target exoplanet's radial velocity, being effectively stationary in the Earth's atmosphere and primarily only fluctuating in line depth (Birkby, 2018). Though the effective execution of this technique is very powerful, it relies heavily on the existence of high-resolution spectroscopic data to accurately target the desired features for cross-correlation.

The ExoMol project initially focused mainly on providing line lists with "complete" descriptions of molecular spectra, which is to say, providing line positions and intensities for all possible lines in a given molecule's spectra at any temperature. A truly complete line list would contain an infinite number of transitions, owing to an infinite number of continuum states, which is obviously infeasible. Instead, line

lists consider a finite number of states either up to a given rotational, vibrational or energy cutoff and are commonly referred to as complete *up to* the temperature at which more highly excited states would become important. This focus on completeness was due to work such as that on the spectra of CH_4 by Yurchenko et al. (2014) demonstrating how the change in total opacity owing to the larger number of spectral features in a complete line list compared to other, incomplete line lists resulted in factor of 20 increase in the retrieved abundance.

Though completeness is evidently essential then for the accurate determination of the physical properties of exoplanet atmospheres, techniques were simultaneously being developed to also provide as much of the data to a high-resolution standard (Tennyson and Yurchenko, 2018, 2019). This began the second phase of the ExoMol project, so called "ExoMol HD", which saw the extensive use of the MARVEL methodology (Furtenbacher et al., 2007) to provide high-accuracy empirical energy levels for supplementing or replacing calculated energy levels. The XABC line list for NO (Qu et al., 2021) was the first such ExoMol line list made from scratch in the new format. As it has now become the standard in the ExoMol group to incorporate these MARVEL energy levels into newly produced line lists, where sufficient experimental data exists to determine them, much work has also gone into updating existing line lists to this new, high-resolution standard (Tennyson et al., 2020). The work to update all existing ExoMol line lists to this same standard is ongoing. Line lists incorporating energies and explicit uncertainties determined by MARVEL are now available for C_2 (Yurchenko et al., 2018a; McKemmish et al., 2020), NH_3 (Coles et al., 2019; Furtenbacher et al., 2020a), C_2H_2 (Chubb et al., 2018, 2020b), $H_2{}^{16}O$ (Polyansky et al., 2018; Furtenbacher et al., 2020b), $H_2{}^{17}O$ and $H_2{}^{18}O$ (Polyansky et al., 2017; Furtenbacher et al., 2020c), TiO (McKemmish et al., 2017, 2019), H_2CO (Al-Refaie et al., 2015; Al-Derzi et al., 2021), AlH (Yurchenko et al., 2018b, 2024c), NO (Qu et al., 2021), SiO (Yurchenko et al., 2022), CaH (Owens et al., 2022a), MgH (Owens et al., 2022a), SiN (Semenov et al., 2022), CaOH (Owens et al., 2022b), H_2CS (Mellor et al., 2022), AlCl (Yurchenko et al., 2023), YO (Yurchenko et al., 2024a), SO (Brady et al., 2024) and CH_4 (Yurchenko et al., 2024b).

The work presented in this thesis aimed to produce high-resolution line lists for aluminium monoxide (AlO), H_3^+ and vanadium monoxide (VO). For the first two of these molecules, the work also included line lists for several isotopologues. High-resolution line lists were produced for all of the isotopologues of AlO included in the ATP line list (Patrascu et al., 2014) and for the MiZATeP (H_3^+) (Mizus et al., 2017) and ST (H_2D^+) Sochi and Tennyson (2010) line lists, using techniques described in Section 2.4. New line lists were computed for D_2H^+ and D_3^+ and post-processed using the same techniques to a similar high-resolution standard, to complete the set of deuterated isotopologues. For VO, the initial intention was to also update the existing VOMYT line list of McKemmish et al. (2016b) though it became apparent after the initial MARVEL study that an entirely new line list and underlying spectroscopic model would need to be computed. This was due to the distinctive hyperfine structure of $^{51}V^{16}O$, arising from the large nuclear spin of the ^{51}V atom. Consequently, the new line list for this species does not consider other isotopologues.

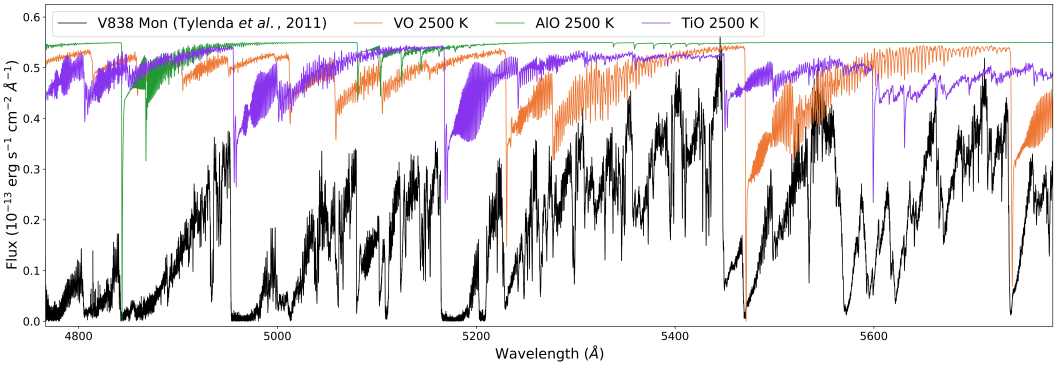


Fig. 1.1: The absorption spectrum of V838 Mon recorded by Kamiński et al. (2009) at a resolving power of $R \approx 34\,000$ using the Keck HIRES instrument (Vogt et al., 1994). The spectra of VO, AlO and TiO at 2 500 K, computed with ExoCross (Yurchenko et al., 2018), are overlaid to show the important features arising from each molecule.

Aluminium monoxide (AlO) and vanadium monoxide (VO), among many other metal-bearing species, are refractory species that are known to exist in the atmospheres of ultra-hot Jupiter exoplanets and some of the coolest classifications of stars. These molecules have high equilibrium condensation temperatures, meaning in high-temperature exoplanet environments they can remain in the gas phase high up in the atmosphere, instead of depleting out down to lower altitudes (Wakeford et al., 2016). At high altitudes, these species absorb large amounts of incident stellar radiation, driving heating and hence atmospheric temperature inversions, where the temperature increases with altitude (Gandhi and Madhusudhan, 2019). Such molecules effectively play the same roles in their host atmospheres as telluric absorbers like O_3 do in the Earth's stratosphere, though the specific mechanism by which this occurs is still debated for some molecules (Spiegel et al., 2009; Parmentier, Vivien et al., 2018). In these environments, refractory species can also aid in the formation of condensate species in clouds, which can have a profound effect on exoplanet transmission spectra (Parmentier et al., 2016). Given VO is often seen in the same stellar spectra as TiO and given the relation between stellar and planetary composition (Hinkel and Unterborn, 2018) both are considered to be of importance in ultra-hot Jupiters (Fortney et al., 2008, 2021) and the peaks of their strong electronic bands in the visible often fall in-between each other. The spectrum of the nova V838 Mon recorded by Kamiński et al. (2009) and shown in Fig. 1.1 conveniently show how these prominent features, as well as those of AlO, are arranged.

The other molecule considered in this work, H_3^+, plays a different role in exoplanet atmospheres. In planets it is primarily observed through emission from the ionosphere, at much higher altitudes than the metal oxides mentioned previously, which are generally observed via absorption features. This emission is believed to be important in balancing external heating and may be crucial for atmospheric stability (Koskinen et al., 2007). Where it is present, especially in the ISM, it is also believed to be a key precursor in hydrocarbon chemistry, by donating a hydrogen atom to molecules when almost all collisions occur (Larsson, 2008).

In order to produce these new line lists and provide high-accuracy term energies, it was necessary to perform a series of MARVEL studies on each of the molecules considered here. These studies are performed by compiling all available and relevant experimental data into spectroscopic networks, from which energy values with accompanying uncertainties are obtained - see Section 2.2 for details. The aim of this is to allow as many transitions as possible to be provided with high-resolution accuracy and, by explicit provision of uncertainties in the individual energies, to allow those transitions which are accurately known to be identified. The selective use of only the high-accuracy transitions derived from MARVEL energies allows for the extremely reliable study of select regions in spectra. To provide these uncertainties, the original ExoMol data model of Tennyson et al. (2016b) was updated to incorporate an uncertainty column (Tennyson et al., 2020). These MARVEL energies are used in the preprocessing and postprocessing refinement stages: the spectroscopic models used to compute line lists are refined against the empirical values; the energies of experimentally known levels are used instead of their calculated counterparts. In the case of VO, the MARVEL study also necessitated the assignment of spectra recorded in previous experiment, the results of which were ultimately critical in obtaining a well-determined description of the energy levels.

Over the course of these projects, hyperfine deperturbation techniques have been developed and refined to handle the inclusion of hyperfine-resolved data in hyperfine-unresolved datasets. This serves to maximise the total number of transitions that can be included in MARVEL inputs, as hyperfine-unresolved transitions usually make up the majority of the experimental data available. The networks of H_3^+ and its deuterated isotopologues contain no hyperfine-resolved transitions and the AlO network was constructed using a small number of deperturbed hyperfine transitions. Conversely, the available spectroscopic data for VO was almost evenly split between hyperfine-resolved and unresolved, and warranted the construction of spectroscopic networks for both cases. The techniques that have been developed place a particular focus on uncertainty estimation: deperturbed uncertainties are important to get right as overestimating them can lose the high accuracy of the original hyperfine resolved data, while underestimating them can result in a significant number of MARVEL network transition inconsistencies.

This thesis is presented as follows. Chapter 2 outlines the methodologies used in the production of the three high-resolution line lists produced during my PhD, discussing the use of variational methods, the theory underpinning the MARVEL algorithm, hyperfine transition deperturbation and the motivations behind hybrid line lists. Chapter 3 presents a MARVEL study of AlO, the production of a hybrid line list and the suitability of spectra generated from it for experiment. Chapter 4 details MARVEL studies of H_3^+, H_2D^+ and D_2H^+, updates to the existing line lists of the first two of these species and production of new line lists for D_2H^+ and D_3^+. Chapter 5 describes the creation of two MARVEL networks, incorporating newly assigned spectra, and their use in refining a new, hyperfine-resolved spectroscopic model for VO. Containing both energies and intensities adjusted based on experimental data, the model is then used to assign previously unassigned perturbations and ultimately produce a new line list. Chapter 6 gives the conclusions of this work and outlines

potential future work.

Chapter 2

Methodology

The creation of molecular line lists primarily relies on quantum mechanical calculations to compute the term energies and transition moments for a molecular system. This work considers calculations performed using the diatomic variational nuclear motion code Duo (Yurchenko et al., 2016b) and the triatomic Discreet Variable Representation (DVR) code DVR3D (Tennyson et al., 2004), although a suite of other codes exist that are often used for similar systems or for those comprising a larger number of atoms (Kozin et al., 2004; Yurchenko et al., 2007; Mitrushchenkov, 2012). The theory behind the implementation of these codes is given in Section 2.1. Spectroscopic models, which these codes rely on, describe the potential energy curves/surfaces, couplings and transitions dipole moments (or indeed higher order moments) contained within the molecular system, generally using *ab initio* forms obtained from a range of quantum chemistry programs as their starting point. These models have frequently relied on empirical values derived from spectroscopic experiments for refinement, iteratively tweaking the components of the model to best reproduce these empirical energy levels and/or intensities. While this process has proved to be very effective at accurately recreating experimental measurements, recent works have looked for further improvement with the aim of ensuring the suitability of line list for use in high-resolution studies.

To this end, it became clear that if empirical energies are known to a high accuracy from experiment and are used in the refinement process, then they may as well be used in the final product. While some line lists have been produced using exclusively empirical energies and intensities, they often lack the completeness that calculations provide, which predict positions and intensities for transitions not seen in experiments. Though individual experiments can provide a set of empirical energy levels that well describe the transitions in a given region, the amalgamation of empirical and calculated data aimed to provide both completeness and high accuracy. Accordingly, the Marvel procedure (Furtenbacher et al., 2007) was developed to allow for the combination of multiple sets of transition data into a single, empirical data set. The details of this process are discussed in Section 2.2 and Section 2.3 details hyperfine deperturbation techniques developed to supplement the transitions data used in the Marvel procedure. The idea of combining calculated and empirical energies in the same line list was the first step in the advent of so called "hybrid" line lists. This and other techniques utilised in the construction of these hybrid line lists are given in Section 2.4.

2.1 Variational methods

Increasingly, people have been developing spectroscopic models for open shell diatomic molecules based on the use of potential energy curves (PECs) and appropriate couplings. Recent examples include *ab initio* studies of the hyperfine-resolved spectrum of H_2 (Jozwiak et al., 2021), the work of Augustovicova and Spirko (2021b,a), Havalyova et al. (2021) and the MOLLIST project (Bernath, 2020), which employed a hybrid approach, in addition to the multitude of line lists produced as part of the ExoMol project (Tennyson et al., 2020). The use of such spectroscopic models has proved an effective tool for well describing known spectroscopic bands, for predicting the position of previously unseen features and for reassigning existing spectra. For example, the study of the 5 lowest electronic states of CaO using a variational model (Yurchenko et al., 2016a) led to the reassignment of the vibronic states for a large portion of the experimentally derived energies, extending these assignments to much higher J values and proposing a new description of a number of the observed resonances. Variational methods were shown to be an extremely effective tool for the calculation of molecular spectra after a series of calculations for the molecule H_3^+ and its deuterated isotopologues (Tennyson and Sutcliffe, 1984, 1985, 1986; Miller and Tennyson, 1987, 1988b,c,a; Miller et al., 1989) ultimately led to the detection of H_3^+ in the atmosphere of Jupiter (Drossart et al., 1989). While H_3^+ has the least complicated electronic structure of the triatomic molecules of astrophysical interest, owing to it being a two-electron problem, this was soon followed by a wealth of high-accuracy variational calculations of the spectra of the much more complex H_2O (Polyansky et al., 1994; Lynas-Gray et al., 1995; Schryber et al., 1995; Polyansky et al., 1996; Viti et al., 1997; Partridge and Schwenke, 1997).

The variational principle is well known to accurately characterise the ground states of quantum mechanical systems, obtaining energy eigenvalues through the optimisation of approximate wavefunctions. For most of the diatomic molecules and some polyatomic molecules of interest however, consideration of electronically excited states is also essential. This can be achieved by expanding the variational method to optimise a set of appropriate rovibronic basis functions for all states from the ground state up to some target excited state (Tennyson, 2012). These results are used to solve the nuclear motion Hamiltonian and is done under the Born-Oppenheimer approximation that the nuclear and electronic wavefunctions are separate. It is generally after this point that the effects of other terms, such as spin-orbit couplings, are incorporated (Tennyson and Yurchenko, 2017). The variational nuclear motion code Duo of Yurchenko et al. (2016b) solves the nuclear motion problem assuming an existing partial solution to the electronic Hamiltonian, provided in the form of potential energy curves describing the electronic states of the molecule for which energies are to be computed. While larger molecular systems require more complex descriptions of the electronic potential, i.e.: higher dimension potential energy surfaces, the diatomic problem is one dimensional, depending only on the internuclear distance. Duo begins to solve the Hamiltonian by obtaining vibrational eigenvalues for each electronic state by solving the rotationless Schrödinger equation, which are in turn used to construct a full set of rovibronic

basis functions, defined as

$$|state, v, \Lambda, S, \Sigma, J, \Omega\rangle = |state, \Lambda, S, \Sigma\rangle |state, v\rangle |J, \Omega, M_J\rangle, \tag{2.1}$$

where *state* is a label for each electronic state, v the vibrational quantum number, Λ is the projection of the electron orbital angular momentum, S the total electron spin, Σ is the projection of the electron spin, J the total electron angular momentum, Ω is the projection of the total angular momentum $\Omega = \Lambda + \Sigma$ and M_J is the projection of the total angular momentum along the z-axis. Here the z-axis is space fixed, whereas the projections Λ, Σ and Ω are along the molecular axis. The construction described uses Hund's case a coupling and though this does not generally well describe the couplings present in singlet or Σ electronic states, the calculation of energies is independent of the quantum number labelling due to a complete angular basis, hence it is not impacted by the chosen coupling scheme. With the updates to Duo that enable to computation of hyperfine-resolved energy levels (Qu et al., 2022a), the basis functions are transformed to include an additional term that couples J to a single nuclear spin, I, such that

$$|state, v, \Lambda, S, \Sigma, J, \Omega, I, F\rangle = |state, \Lambda, S, \Sigma\rangle |state, v\rangle |J, \Omega, M_J\rangle |J, I, F, M_F\rangle, \tag{2.2}$$

where F is the total angular momentum and M_F its projection along the z-axis. The terms M_J and M_F are omitted from the left-hand sides of Eq. (2.1) and Eq. (2.2) as Duo computes field-free energies; with no field to couple to these can be neglected. The basis functions in Eq. (2.2) describe the Hund's case a_β coupling scheme (Frosch and Foley, 1952).

Spin-orbit coupling is an extremely important effect to consider when characterising electronic states with a projected electron orbital angular momentum $\Lambda > 0$. Under Hund's case a coupling, the projection of the total angular momentum Ω takes values in integer steps between $\Lambda - \Sigma$ and $\Lambda + \Sigma$, hence splitting a given electronic state into $2S + 1$ spin-orbit components or sometimes fine structure components. Using spherical tensor notation, this can be expressed as

$$\mathcal{H}_{SO} = A\left(R\right) \mathrm{T}^1\left(\mathbf{L}\right) \cdot \mathrm{T}^1\left(\mathbf{S}\right) = A\left(R\right) \sum_q \left(-1\right)^q \mathrm{T}^1_q\left(\mathbf{L}\right) \cdot \mathrm{T}^1_{-q}\left(\mathbf{S}\right), \tag{2.3}$$

where $A\left(R\right)$ is the spin-orbit coupling radial function, the matrix elements of which are readily found in the literature (Brown and Carrington, 2010). In systems with multiple open shell electrons, Eq. (2.3) can be expressed as the sum of each of their interactions. The diagonal $q = 0$ terms give rise to the different Ω components of a given state, while those with $q = 1$ facilitate coupling between different electronic states. This off-diagonal coupling allows for mixing between spin-orbit components of different states with the same $|\Omega|$ values to mix and is both important for facilitating intensity stealing between electronic states and for characterising perturbations between nearby states (Tennyson et al., 2016a). Spin-spin and spin-rotation interactions are also important interactions, the latter especially so in Σ electronic states where it is responsible for the fine structure splitting in absence of

spin-orbit interactions, though the magnitude of these effects is generally smaller in comparison.

DVR calculations, such as those performed herein with the code DVR3D, are not truly variational. This is owing to how DVR methods calculate matrix elements at the discreet grid points, assuming that the potential energy Hamiltonian is diagonal over the chosen grid (Corey and Tromp, 1995). As this approach utilises Gaussian quadrature or similar methods to compute these integrals the result is exact when considering a sufficient number of grid points, for a given order of polynomial. In regions of the grid that are too sparse however, the integrals are inexact. This can also occur when considering non-polynomial integrals or expressions with behaviours like $\frac{1}{r^2}$. Accordingly the matrix elements calculated in this way are not strictly upper bounds on the energy eigenvalues, whereas they necessarily are in the case of the variational method (Lombardi et al., 2004). A number of augmented DVR methods exist to address this result (Corey and Tromp, 1995; Barletta et al., 2004).

Duo calculations are performed over a finite grid, such that all potential energy curves and coupling terms are defined as functions of the internuclear distance r and evaluated at a series of evenly spaced points between an upper and lower limit. As the calculations require evaluation at each point of the grid, a complete description of the potentials and couplings extending to infinity is impossible, but appropriate implementation of relevant coupling terms can ensure that the desired behaviour is obtained towards dissociation. While an infinite grid is not feasible, it is still possible to well describe the important features of potential energy curves within a finite grid ranging over a few angstroms - see Fig. 5.10 for an example. This comes with a caveat however, in that while bound states can be well described in this way, unbound and quasibound states are strongly dependent on the grid size, owing to how the calculation effectively treats the edges of the grid as infinite potential barriers - see Hazi and Taylor (1970); Mandelshtam et al. (1993); Dulieu et al. (1997) for discussion in context of the stabilisation method. With the use of potential energy curves in this way, Duo is able to calculate energies for a complete set of levels up to dissociation, or indeed some other lower energy threshold when needing to reduce the size of the calculation. Given transitions dipole moments are also incorporated into the spectroscopic model as functions of r, Duo is able to calculate a complete set of transition probabilities for all possible transitions between the calculated energies. Updates to the Duo code are underway to enable the calculation of transition probabilities arising from magnetic dipole and electric quadrupole moments (Somogyi et al., 2021).

While the potential energy and coupling terms in a spectroscopic model often take initial forms from *ab initio* calculations, they are frequently refined against empirical energies derived from experiments. Such empirical energies are often limited in scope as the realities of experimental techniques make it functionally impossible to observe every single transition and hence obtain energies for every level. The subset of energies known from experiment does however enable the accurate determination of the shape of certain regions of a given electronic potential energy curve, i.e.: the regions from which the known energies arise. In most cases, the experimental characterisation of electronic states comes from their low-lying

vibrational bands and hence the bottoms of the potential wells are usually the most accurate. Beyond the regions that correspond to experimental data, the potential energy curves extrapolate to higher energies and provide predictions for levels arising from higher vibrational or rotational excitations. The refinement of potential energy curves against empirical data is often weighted to minimise deviation from their initial *ab initio* forms, though in cases where the initial form describes the empirical data very poorly, they may be disregarded. This is done to try and ensure that the extrapolation of the potentials produces reasonable energies for higher levels. Where *ab initio* representations are discarded, attempts are still made to retain a reasonable shape for the potential, though without the aid of a weighted fit. When defining potential energy curves and coupling terms in a spectroscopic model, analytical representations are frequently used - see Section 5.4.1 for examples of some of the common expressions.

While variational methods provide complete descriptions of the energy levels within a molecular system, perturbation theory-based models alternatively provide high-accuracy descriptions of a subset of levels. Perturbative models aim to describe molecules using effective Hamiltonian representations, a series of polynomial functions describing each vibronic band, characterised by a set of molecular constants. In most cases, each vibronic band is treated as a distinct system so that the constants need not be defined, for example, as a function of the vibrational excitation within a given electronic state. This enables a set of molecular constants to be fit with very high accuracy to the experimental data of a vibronic band without needing to consider how that expression would extrapolate to higher bands. This is in contrast to the variational approach, where the parameters most commonly used in the analytical representations of potential energy curves have an effect across the whole potential and accordingly all levels resulting from it. The MoLLIST project (Bernath, 2020) is an example of the effective application of perturbation theory in the construction of high-resolution line lists. MoLLIST and other similar projects use programs such as PGopher (Western, 2017) to both fit experimental data and to solve effective Hamiltonians to obtain term energies. In conjunction with programs like LEVEL (Le Roy, 2017) and RKR1 (Le Roy, 2017), dipole moments can be computed to obtain accompanying transition intensities for these high-accuracy energies.

Studies such as the work of Syme and McKemmish (2021) on the CN molecule demonstrate how the perturbative approach taken by MoLLIST is generally more accurate than variational calculations, here performed with Duo, when it comes to reproducing empirical Marvel energies. The application of variational methods to the calculation of water line lists, however, demonstrated its significant power to accurately predict energy levels in rotationally excited states well beyond what was possible with perturbation theory (Polyansky et al., 1994). By introducing the Marvelisation process to the outputs of variational calculations however, it is possible to obtain both the completeness of variational calculations and the high accuracy of experimental data.

2.1.1 Hyperfine couplings

The Duo code (Yurchenko et al., 2016b) was updated by Qu et al. (2022a) to include a suite of hyperfine modules for the computation of hyperfine-resolved energy levels

and intensities. This update implemented seven different hyperfine coupling curves that describe the effects of five different kinds of hyperfine coupling and contribute to the overall nuclear hyperfine coupling Hamiltonian, $\mathcal{H}_{\text{hfs}}$. This section will give an overview of these different couplings and how the radial functions implemented in Duo relate to them.

The first of the hyperfine couplings implemented in Duo describes the magnetic interaction between a nucleus and unpaired electrons and is often referred to as the Fermi contact interaction. In the general case this interaction can be expressed in terms of vectors of electron spin S and nuclear spin I such that

$$\mathcal{H}_{\text{FC}} = \sum_i \sum_n \frac{2}{3} g_S g_n \mu_B \mu_N \mu_0 \delta\left(\mathbf{r}_{in}\right) \mathrm{T}^1\left(\mathbf{S}_i\right) \cdot \mathrm{T}^1\left(\mathbf{I}_n\right), \tag{2.4}$$

where g_S is the free electron g-factor, g_n is the nuclear spin g-factor of the n-th nucleus, μ_B is the electron Bohr magneton, μ_N is the nuclear magneton, μ_0 is the vacuum permeability, $\delta\left(\mathbf{r}_{in}\right)$ is the Dirac delta function acting on the relative position of the i-th electron from the n-th nucleus, and T^k denotes a rank-k spherical tensor operator (Kato, 1993; Man, 2013). $\mathbf{S}$ and $\mathbf{I}$ refer to the electron spin and nuclear spin operators in the space-fixed frame. The effect of the Dirac delta in this expression is to impose the condition that the expectation value of the electron wavefunction at the site of the nucleus must be non-zero, i.e.: the electron spin density at the nucleus is non-zero. This is only the case when the electron occupies an s-orbital, or indeed has some s-orbital character. For states arising from configurations involving unpaired electrons with significant s-orbital character, the Fermi contact interaction is often the largest contributor to hyperfine effects.

In the recent hyperfine update to Duo of Qu et al. (2022a), couplings were only introduced to describe diatomic systems containing one nucleus of non-zero spin. Accordingly, Eq. (2.4) can be simplified and expressed as a sum over the contributions from all of the unpaired electrons in the system such that

$$\mathcal{H}_{\text{FC}} = \sum_i \frac{2}{3} g_S g_N \mu_B \mu_N \mu_0 \delta\left(\mathbf{r}_i\right) \mathrm{T}^1\left(\mathbf{I}\right) \cdot \mathrm{T}^1\left(\mathbf{S}_i\right), \tag{2.5}$$

where g_N is the nuclear spin g-factor of the one nucleus with non-zero spin, $\mathbf{r}_i$ is the position of the i-th electron relative to the nucleus with non-zero spin and $\mathbf{S}_i$ the i-th electron's spin. Eq. (2.5) can be rewritten in terms of a single-valued function of the internuclear distance R, enabling the implementation of the Fermi contact interaction in Duo as a standard radial function. This function takes the form

$$b_F\left(R\right) = \frac{2}{3} g_S g_N \mu_B \mu_N \mu_0 \left\langle state, \Lambda, S, \Sigma \middle| \sum_i \delta\left(\mathbf{r}_i\right) \frac{\mathrm{T}_0^1\left(\mathbf{s}_i\right)}{\Sigma} \middle| state, \Lambda, S, \Sigma \right\rangle, \tag{2.6}$$

where $\mathbf{s}_i$ is now the spin of the i-th electron in the body-fixed frame (Kato, 1993).

Another coupling that contributes to the hyperfine splitting of energy levels is the nuclear electric quadrupole interaction. This can be described as the scalar product of the electric field gradient outside the nucleus, $\mathrm{T}^2\left(\nabla \mathbf{E}\right)$, and the quadrupole

moment inside the nucleus, $\mathrm{T}^2(\mathbf{Q})$, such that

$$\mathcal{H}_{\mathrm{EQ}} = -e\mathrm{T}^2(\nabla\mathbf{E}) \cdot \mathrm{T}^2(\mathbf{Q}), \tag{2.7}$$

where e is the elementary charge and the electric field gradient and quadrupole moment tensors are defined in terms of spherical harmonics using electron and proton coordinates respectively. The contribution of this coupling to hyperfine effects varies significantly with the nuclear spin, I. This is because a nuclear electric quadrupole moment only occurs when a nucleus is distorted into an oblate or prolate shape, as the charge distribution of a spherical nucleus is symmetric. It should be noted that while a distorted nucleus is generally necessary for a nuclear quadrupole moment to arise, not all distorted nuclei have one (Neugart and Neyens, 2006). These distortions to the nucleus are energetically favourable for certain numbers of protons and neutrons and give rise to configurations where the angular momenta from the individual nucleons are effectively unable to cancel each other out to the same extent (Butler, 2020). The Wigner-Eckart theorem can be used to describe a general relationship between the total nuclear angular momentum, the nuclear spin, for any nuclear multipole moment described by a rank-k spherical tensor operator, such that unless $2I \geq k$ they are zero, i.e.: a nuclear octupole moment can only occur when $I \geq \frac{3}{2}$. In the cases of atoms with large nuclear spins, such as $I = \frac{7}{2}$ for ^{51}V as discussed in Chapter 5, the strength of the nuclear electric quadrupole interaction can be on the same order or indeed larger than the Fermi contact interaction. By applying the Wigner-Eckart theorem to Eq. (2.7) to evaluate the electric quadrupole reduced matrix elements (Cook and De Lucia, 1971) one can obtain the relation

$$\langle I \| -e\mathrm{T}^2(\mathbf{Q}) \| I \rangle = \frac{eQ}{2} \begin{Bmatrix} I & 2 & I \\ -I & 0 & I \end{Bmatrix}^{-1}, \tag{2.8}$$

where Q is the nuclear quadrupole moment and the final term is a Wigner 6-j symbol. It can be seen that, as the value of the 6j-symbol decreases with I, the reduced matrix elements of the electric quadrupole are larger for systems with larger nuclear spin. By considering Eq. (2.8) and equivalent expressions for higher order multipole moments, it can be seen that not only do higher order multipole moments start to occur as nuclei become more physically distorted, obtaining larger nuclear spins, but the strength of the existing moments increase as a function of I too.

The reduced matrix elements of the gradient of the electric field tensor $\mathrm{T}^2(\nabla\mathbf{E})$ in Eq. (2.7) can similarly be evaluated such that

$$\begin{aligned} &\langle state, v, \Lambda, S, \Sigma, J, \Omega \| \mathrm{T}^2(\nabla\mathbf{E}) \| state, v', \Lambda', S', \Sigma', J', \Omega' \rangle \\ &= \sum_q (-1)^{J-\Omega} \begin{Bmatrix} J & 2 & J' \\ -\Omega & q & \Omega' \end{Bmatrix} \sqrt{(2J+1)(2J'+1)}\delta_{\Sigma,\Sigma'} \\ &\quad \times \langle state, v | \langle state, \Lambda, S, \Sigma | \mathrm{T}^2_q(\nabla\mathbf{E}) | state, \Lambda', S', \Sigma' \rangle | state, v' \rangle. \end{aligned} \tag{2.9}$$

where $q = 0$ corresponds to the diagonal component of the tensor and higher values to additional off-diagonal components. In particular, the $q = \pm 2$ off-diagonal by two

component relates the $\Lambda = +1$ and $\Lambda = -1$ states, hence providing contributions to the Λ doubling in Π states (Brown and Carrington, 2010). The expectation value of $\mathrm{T}^2_q(\nabla\mathbf{E})$ in Eq. (2.9) can be evaluated as a function of the internuclear distance R,

$$q_0(R) = -2\langle state, \Lambda, S, \Sigma | \mathrm{T}^2_0(\nabla\mathbf{E}) | state, \Lambda', S', \Sigma' \rangle \tag{2.10}$$

for the diagonal component, and

$$q_2(R) = -2\sqrt{6}\langle state, \Lambda, S, \Sigma | \mathrm{T}^2_{\pm 2}(\nabla\mathbf{E}) | state, \Lambda', S', \Sigma' \rangle \tag{2.11}$$

for the off-diagonal by 2 component, where $\Lambda = \pm 1$ and $\Lambda' = \mp 1$. Given the constant eQ in Eq. (2.8), these interactions are often referred to as eQq_0 and eQq_2 respectively and are implemented in Duo as radial functions.

The interaction between the electron spin and nuclear spin magnetic dipoles is one of the more elaborate contributions to the hyperfine Hamiltonian considered here and can be expressed as

$$\mathcal{H}_{\mathrm{dip}} = \sum_i -\sqrt{10} g_S g_N \mu_B \mu_N \frac{\mu_0}{4\pi} \mathrm{T}^1(\mathbf{I}) \cdot \mathrm{T}^1\left(\mathbf{S}_i, \mathbf{C}^{(2)}\right), \tag{2.12}$$

where $\mathbf{C}^{(2)}$ is the rank-2 spherical harmonic tensor, and the final term can be expressed in the form

$$\mathrm{T}^1_q\left(\mathbf{S}_i, \mathbf{C}^{(2)}\right) = -\sqrt{3} \sum_{q_1 q_2} (-1)^q \mathrm{T}^1_{q_1}(\mathbf{S}_i) C^{(2)}_{q_2}(\theta_i, \phi_i) r_i^{-3} \begin{pmatrix} 1 & 2 & 1 \\ q_1 & q_2 & -q \end{pmatrix}, \tag{2.13}$$

where θ_i, ϕ_i and r_i are the spherical polar coordinates of the i-th electron. This interaction can be evaluated in two parts, by considering the operators that are diagonal or off-diagonal in Λ, obtaining two different functions of R (Brown and Carrington, 2010). The matrix elements of the diagonal component ($q = 0$) can be expressed in a form that depends on the radial function

$$c(R) = 3 g_S g_N \mu_B \mu_N \frac{\mu_0}{4\pi} \left\langle state, \Lambda, S, \Sigma \middle| \sum_i C^{(2)}_0(\theta_i, \phi_i) r_i^{-3} \frac{\mathrm{T}^1_0(\mathbf{s}_i)}{\Sigma} \middle| state, \Lambda, S, \Sigma \right\rangle, \tag{2.14}$$

and the off-diagonal components ($q = \pm 2$) depend on the function

$$d(R) = -\sqrt{6} g_S g_N \mu_B \mu_N \frac{\mu_0}{4\pi} \times \left\langle state, \Lambda, S, \Sigma \middle| \sum_i C^{(2)}_{\mp 2}(\theta_i, \phi_i) r_i^{-3} \frac{\mp\sqrt{2}\mathrm{T}^1_{\pm 1}(\mathbf{s}_i)}{\sqrt{S(S+1) - \Sigma(\Sigma \pm 1)}} \middle| state, \Lambda', S', \Sigma' \right\rangle. \tag{2.15}$$

Both $c(R)$ and $d(R)$ are implemented in Duo and the full derivations of the matrix elements of the electron spin nuclear spin dipole-dipole interaction can be found in the literature (Brown and Carrington, 2010; Qu et al., 2022a).

The nuclear spin-orbit interaction is the coupling between the nuclear spin and

the electron orbital angular momentum. Its is described by the Hamiltonian

$$\mathcal{H}_{IL} = \sum_i 2g_N\mu_B\mu_N \frac{\mu_0}{4\pi} r_i^{-3} \mathrm{T}^1(\mathbf{I}) \cdot \mathrm{T}^1(\mathbf{L}_i), \tag{2.16}$$

where $\mathrm{T}^1(\mathbf{L}_i)$ is the orbital angular momentum of the i-th electron. As with Eq. (2.12), the matrix elements that are diagonal in Λ can be evaluated independently, obtaining a form that can be expressed involving a function of R. For this interaction, this function is defined as

$$a(R) = 2g_N\mu_B\mu_N \frac{\mu_0}{4\pi} \left\langle state, \Lambda, S, \Sigma \middle| \sum_i r_i^{-3} \frac{\mathrm{T}^1_0(\mathbf{l}_i)}{\Lambda} \middle| state, \Lambda, S, \Sigma \right\rangle, \tag{2.17}$$

where l_i is the orbital angular momentum of the i-th electron in the body-fixed frame. While off-diagonal components can be obtained from Eq. (2.16) through evaluation of the $\mathrm{T}^1_{\pm 1}(\mathbf{L}_i)$ operator, hence coupling states with different Λ, they are not implemented in the current version of Duo (Qu et al., 2022a).

The nuclear spin additionally couples to the total electron angular momentum, giving rise to the nuclear spin-rotation interaction which can be summarised as

$$\mathcal{H}_{\mathrm{IJ}} = c_I(R)\, \mathrm{T}^1(\mathbf{I}) \cdot \mathrm{T}^1(\mathbf{J}), \tag{2.18}$$

where $c_I(R)$ is again a radial function describing the non-zero components of the nuclear spin-rotation tensor. The nuclear-spin rotation tensor operator contains both nuclear and electric contributions, but it can be shown that it reduces to a constant for a given value of R in a diatomic molecule (Flygare, 1974; Brown and Carrington, 2010). This form again only applies to the case where only one atom has non-zero nuclear spin; in cases where more than one atom has nuclear spin, $\mathcal{H}_{\mathrm{IJ}}$ can be expressed as the sum of the nuclear spin tensors of each atom, with each having their own value of c_I.

The total hyperfine Hamiltonian in Duo is hence constructed as

$$\mathcal{H}_{\mathrm{hf}} = \mathcal{H}_{\mathrm{FC}} + \mathcal{H}_{\mathrm{EQ}} + \mathcal{H}_{\mathrm{dip}} + \mathcal{H}_{\mathrm{IL}} + \mathcal{H}_{\mathrm{IJ}}. \tag{2.19}$$

The appropriate hyperfine Hamiltonian is constructed under Hund's case a_β coupling and used to transform the Hund's case a rovibronic Hamiltonian into the final diagonalised hyperfine Hamiltonian (Qu et al., 2022a). Other couplings can provide contributions to the overall hyperfine interaction, such as Zeeman and diamagnetic interactions. These effects require a magnetic field however, and the current implementation of the Duo code computes field-free energy levels. Future studies may wish to adapt the code to include direct consideration of interactions with magnetic fields. As it stands, it is possible to estimate the effects of a weak magnetic field on the energy levels and hence spectra of a molecule through the use of Landé g-factors.

2.2 The Marvel procedure

The Marvel (measured active vibration-rotation energy levels) procedure of Furtenbacher et al. (2007) allows for the inversion of heterogeneous datasets of transitions from high-resolution spectroscopic experiments to give empirical energy levels with associated uncertainties (Furtenbacher et al., 2007; Furtenbacher and Császár, 2012; Tóbiás et al., 2019). Marvel utilises ideas from graph theory to construct spectroscopic networks consisting of energy levels as nodes and transitions as edges, see Császár and Furtenbacher (2011). These networks are constructed from an input list of assigned transitions that connect an upper and lower energy level. This process allows for observations from multiple sources to be combined into a single, consistent data set, and for the determination of an uncertainty for each energy level based on the uncertainties of the input transition that define that level. Use of energy levels calculated by Marvel can greatly improve the accuracy with which a line list can predict transition frequencies, see Section 2.4.1 for discussion.

The Marvel procedure achieves this by inverting transition matrices, which yields a set of empirical energy levels with individual uncertainties (Furtenbacher and Császár, 2012). This process is built upon the idea that, with a list of N_t transition frequencies, the corresponding upper and lower energies can be obtained through the relation

$$\mathbf{aX} = \mathbf{Y}, \tag{2.20}$$

where $\mathbf{Y}$ is a column matrix containing the transition frequencies with dimensions $1 \times N_\mathrm{t}$, $\mathbf{X}$ is a $1 \times (N_\mathrm{e} - 1)$ matrix containing the energy levels to be obtained, N_e is the number of unique energy levels involved in the transitions and $\mathbf{a}$ is a $N_\mathrm{t} \times (N_\mathrm{e} - 1)$ matrix containing elements a_{ij} (Furtenbacher et al., 2007). The elements a_{ij} map the j-indexed energies of $\mathbf{X}$ to the i-indexed transitions of $\mathbf{Y}$, such that

$$a_{ij} = \begin{cases} +1, & \text{if } E_j \text{ is the upper energy level of the } i\text{-th transition,} \\ -1, & \text{if } E_j \text{ is the lower energy level of the } i\text{-th transition,} \\ 0, & \text{otherwise.} \end{cases} \tag{2.21}$$

The construction of the matrix of energies $\mathbf{X}$ with dimensions $1 \times (N_\mathrm{e} - 1)$ rather than $1 \times N_\mathrm{e}$ is possible because the lowest energy level in the network is defined as having an energy of 0 cm^{-1}. Accordingly, this zero-energy level can be omitted from $\mathbf{X}$ and transitions involving this level have only one non-zero entry in their corresponding column of $\mathbf{a}$ such that they only map to their upper state energy.

There are two key points that inform the approach taken in solving Eq. (2.20) to obtain the elements of $\mathbf{X}$. Firstly, given that it is often the case that there are multiple measurements for the same observed transition from different sources, the system of linear equations is generally overdetermined. Secondly, each observed transition frequency in $\mathbf{Y}$ has an associated uncertainty, where δ_i is the uncertainty in the i-th transition. These uncertainties are inverted to obtain a set of weightings, $w_i = \delta_i^{-2}$, such that transitions with smaller associated uncertainties have greater weight. Hence, by constructing a new $1 \times N_\mathrm{t}$ matrix $\mathbf{w}$ containing the associated

transition weights, the mapping matrix **a** can be transformed to

$$\mathbf{A} = \mathbf{a}^{\mathrm{T}}\mathbf{w}\mathbf{a}, \tag{2.22}$$

and the transition matrix **Y** to

$$\mathbf{B} = \mathbf{a}^{\mathrm{T}}\mathbf{w}\mathbf{Y}, \tag{2.23}$$

to obtain the new relation

$$\mathbf{A}\mathbf{X} = \mathbf{B}, \tag{2.24}$$

which can be solved as a simple series of linear equations. In practice, Eq. (2.24) is solved through $\mathrm{LDL}^{\mathrm{T}}$ Cholesky factorisation, benefiting from the fact that **a** and accordingly **A** are very sparse matrices, with the vast majority of elements being 0 (Furtenbacher et al., 2007; Furtenbacher and Császár, 2012; Császár et al., 2016). It can be seen from the construction of the matrices in Eq. (2.22) and Eq. (2.23) that they satisfy the requirements for $\mathrm{LDL}^{\mathrm{T}}$ decomposition in that **A** and **B** are real positive-definite matrices. Much work has gone into refining the MARVEL algorithm over the years, improving the efficiency with which the often very large matrices are calculated and inverted, and building on the methods by which final energy uncertainties are determined. In the current implementation, the uncertainty on the energy E_j is taken as its standard deviation given by

$$\epsilon_j = \sqrt{\mathbf{A}^{-1}_{jj}}, \tag{2.25}$$

where $\mathbf{A}^{-1}_{jj}$ is the j-th diagonal element of the inverse of the matrix **A** given in Eq. (2.22).

Tóbiás et al. (2019) used an adapted version of the MARVEL methodology to iteratively solve the energy levels of the spectroscopic network in blocks, where the first block comprises the transitions with the smallest experimental uncertainties and each subsequent block contains transitions with uncertainties approximately one order of magnitude larger. Tennyson et al. (2024) implemented an uncertainty bootstrapping method, which assesses how final energy values change with the random variation of the transition uncertainties. If the energy of a level does not vary with the variation of the uncertainties on the transitions that define it, it can be considered to be well determined and hence results in a smaller uncertainty for on the energy. The more an energy value varies with changes to the transition uncertainties, the less well the energy is determined within the network and hence a higher uncertainty is assigned to it. The variation of transition uncertainties is performed by multiplying them by a random value between 1 and 10. Given levels are sensitive to inconsistencies between the transitions that define them, increases to the uncertainties of inconsistent transitions reduces the separation between the level energy and the energy implied by the inconsistent transitions. Such levels will hence have a larger variation in their energy, meaning the levels affected by inconsistent transitions will likely see the largest increase in the uncertainty on their energies with bootstrapping. The bootstrapping method is therefore a useful tool for dealing with inconsistencies within networks, without the need for modifying individual

transition uncertainties to achieve a fully self-consistent network.

As the MARVEL procedure determines empirical energies for the levels connected by observed transitions, it also enables the determination of energy differences between levels that have no observed transitions between them (Tobias et al., 2020). Hence it allows for the calculation of transition frequencies for any possible transition between any levels contained within a MARVEL network, often to very high accuracy. For example, applying this technique to formaldehyde allowed for the determination of 367 779 transition frequencies from the empirical energy levels derived from 16 403 observational transitions (Al-Derzi et al., 2021). Additionally, provided the experimental uncertainties in the transition data are set appropriately, the use of MARVEL avoids having to take special measures to treat effects such as perturbations or resonances separately. Put simply, the MARVEL procedure does not require any underlying spectroscopic model for the system as MARVEL treats each level as a node within the network, rather than addressing the physics implied by the quantum numbers assigned to it. Given the large number of perturbations known to occur in the spectra of molecules like VO, this approach avoids a considerable number of additional calculations.

To construct a MARVEL network, a list of transitions frequencies and associated upper and lower state identifiers must be compiled. Traditionally, these transition frequencies would need to all be provided in the same units, but recent updates have implemented a new feature that allows for the frequency units used for each experimental source to be specified in an accompanying "segment" file. As each transition is provided with a tag, comprising the name of the experimental source and a counting number in the format "`SourceName.1`", MARVEL handles the conversion of input transition frequencies and uncertainties into consistent units. The upper and lower states of each transition are identified using a set of relevant quantum numbers, though in practice any unique identifiers could be used. The set of quantum numbers chosen to identify a given state is configurable but must be uniform throughout the whole network, with both upper and lower states labelled with the same set of quantum numbers. The quantum number schemes used for each spectroscopic network discussed in this work are described in their respective chapters, Chapters 3 to 5. As the set of quantum numbers used must be the same for all levels, the existence of hyperfine-resolved data alongside hyperfine-unresolved data, i.e.: levels also characterised by the additional quantum number F, pose an issue. To address this, the hyperfine deperturbation procedures outlined in Section 2.3 were constructed.

Earlier versions of MARVEL took inputs containing one uncertainty entry for each transition, specifically the transition's reported experimental uncertainty, but later versions added a second uncertainty entry. This second entry is initially also set to the experimental uncertainty but exists to allow for a transition's uncertainty to be updated while also retaining the initial experimental uncertainty, which was overwritten in earlier versions. If a transition is determined to be consistent with the network, which is to say that the upper and lower state energy values implied by it are in agreement with the energies implied by any other transitions to those same levels, then this second uncertainty column will not be changed. If the transition is not consistent however, MARVEL will determine an "optimal" uncertainty for

it. This optimal uncertainty is MARVEL's prediction for the uncertainty that the transitions would need to have to become consistent, i.e.: for it to produce energy values for its upper and lower state levels in agreement with the rest of the network. This value is only a prediction however, as adjusting the uncertainty of a single transitions results in the cascading re-evaluation of energies and uncertainties in the network. Accordingly, adjusting a transition's uncertainty to its optimal value may require an iterative set of adjustments for the energy levels to converge and be considered consistent. The energy level uncertainty bootstrapping procedure of Tennyson et al. (2024) effectively solves the same problem but avoids having to decide what constitutes a reasonable increase to a transition's uncertainty by doing it randomly over many iterations.

Earlier versions of MARVEL, specifically the 2.*x* releases as used for the work on AlO described in Chapter 3, identified transitions as inconsistent and flagged them for invalidation when the optimal uncertainty was greater than both the input uncertainty and 0.05 cm^{-1} (accordingly transitions with an initial uncertainty greater than this threshold were not immediately invalidated). When a transition is "invalidated", its frequency is set to negative so that it is ignored by the MARVEL procedure, with a record of it still being kept in the data set. The fixed threshold did however mean that a transition input with uncertainty on the order of 10^{-5} cm^{-1} could have an optimal uncertainty several orders of magnitude greater than its input and not be flagged as problematic. This made it less straightforward to determine whether it was worth updating the uncertainty on a given transitions or whether it should simply be invalidated. Accordingly, this was changed for the 3.*x* and later releases which instead use the ratio of optimal and input uncertainty. Adjustments to a transition's uncertainty are often made up to an optimal/input ratio of 10, though special consideration is given to outliers. As an example, a transition input with an uncertainty of 1.0×10^{-3} cm^{-1} that MARVEL determines to have an optimal uncertainty of 1.2×10^{-3} cm^{-1} is likely worth updating to the optimal uncertainty value. It is often the case that large transition data sets report a single uncertainty for all transitions, often based on the accuracy of the best measurement and in many cases using a value twice the standard deviation, but there will be transitions (approximately 5%) that lie slightly outside this and are better represented with a larger uncertainty. On the other hand, if MARVEL were to determine an optimal uncertainty for the same transition of 1×10^{-2} cm^{-1}, the ratio between the input an optimal is much larger and likely indicative of a real inconsistency, the potential causes of which are discussed in Section 2.2.1.

When MARVEL is run, it outputs a set of energy levels for the primary component of the spectroscopic network. The term "primary" component is used here to refer to the component of the network containing the largest number of unique energy levels, which in most cases also contains the largest number of transitions. It is ideally the case that the primary component is the network component containing the energy level corresponding to the zero-energy level of the molecule in question. The energies of the levels within a given network component are all defined relative to the lowest energy level within the component. Hence, energy levels within components not connected to the primary component do not have their energies defined on the

same scale and are not known relative to the zero-energy level. While it is possible to gleam some insight into the structure of energy levels from the relative separations within these disconnected components, they are not generally sufficient to make informed corrections to a spectroscopic model as they are not well defined relative to the rest of the system. Moreover, these disconnected components are generally small and often comprise a single "path", containing only a non-repeating sequence of transitions between distinct energy levels. Such components contain no "cycles", i.e.: there is only a single path between any two nodes in the component and hence there is no way to validate the energy separations implied by the transitions (Császár et al., 2016; Tóbiás et al., 2017; Arendas et al., 2020). These are referred to as acyclic in graph theory and the energies obtained from network components of this kind are much less reliable. Because of this, the disconnected network components of MARVEL networks are not generally analysed beyond attempts to connect them to the primary component.

In the same manner that disconnected acyclic components provide energies without verifiable consistency, so too do "leaves". A leaf or sometimes external node/vertex in this context is an energy level that is connected by a single transition to the rest of the network, so while it has a defined energy, its energy value is not corroborated by another consistent transition connecting it to another energy level within the network (forming a cycle). While it would be ideal to obtain a spectroscopic network where all energy levels are of degree two or higher, i.e.: all energy levels are involved in two or more transitions, this will rarely be achievable simply due to the availability of transition data.

There are numerous ways to represent the transitions and energy levels contained within a MARVEL network. Due to the high number of parameters through which a network can be defined, there are however some properties that each approach fails to clearly convey. For example, an illustration of the hyperfine-resolved MARVEL network of $^{51}V^{16}O$ is shown in Fig. 2.1, generated using the Kamada and Kawai (1989) force-directed graph drawing algorithm which aims to minimise the number of overlapping edges (transitions) and hence arranges the nodes (energy levels) by their connectivity. This method is hence agnostic to the quantum number labelling applied to the energy levels. While these kinds of plots do not provide much insight into the energy level structure of the system in question, they do provide some insight into the nature of the available transition data that may not be immediately apparent. For example, while there is a clear, well connected central part of the network, there appear to be several "strand" structures in the bottom half of the plot that only connect to one another via this central set of energy levels. Additionally, the energy levels at the ends of these strands, and the single energy levels seen stuck on to the central set of levels are the leaves discussed above. Conversely, Fig. 2.2 shows the low-F energy levels of the same network, arranged based on the term energy and F values. While this more clearly shows the physical properties of the energy levels in the network, visualisation of the network's connectivity is limited and information about the arrangement of individual hyperfine levels is hard to discern. In later chapters, graphical representation of MARVEL networks is primarily done through showing the derived energy levels and their relative positions, while

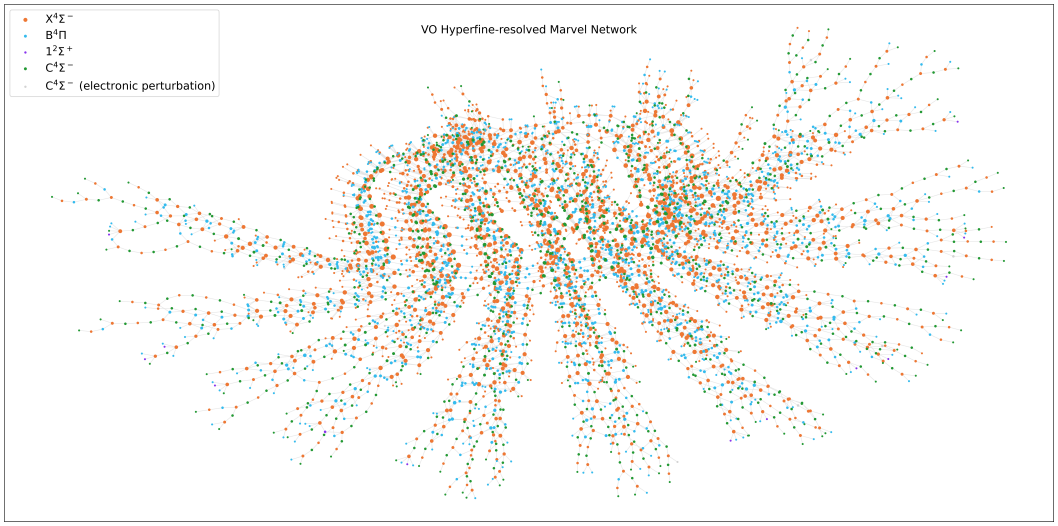


Fig. 2.1: The hyperfine-resolved MARVEL network of $^{51}V^{16}O$, constructed using the Kamada and Kawai (1989) force-directed graph drawing algorithm. Different coloured nodes represent energy levels in different electronic states and the grey line between nodes represent experimental transitions contained within the MARVEL network. The sizes of nodes are scaled here with the degree of the node, i.e.: by the number of transitions that the energy level is involved in. Nodes are arranged based on connectivity and to minimise the crossing of transitions; the node coordinates do not imply anything to do with the value of the energy level.

information on the transitions involved in these networks is provided in tables or plots showing the overall electronic bands that have been measured.

Each spectroscopic network is effectively a multigraph where edges have their own identity, as multiple transitions are allowed between the same levels as they are differentiated by their tags (Furtenbacher et al., 2014). Additionally, the networks can be treated like a rooted tree in that the positions of the nodes and hence energy values are defined relative to the zero-energy level, or at least the lowest energy level of a given component (Árendás et al., 2016). While transitions can be considered to have direction, in the sense of transitions to a lower or upper state in emission and absorption, spectroscopic networks are not considered to be directed networks (Tóbiás et al., 2017). This is because the direction of a transition to or from a given energy level is irrelevant, rather it is only the energy difference between the levels implied by the transition that matters.

MARVEL is by construction an active methodology, which means that as new high-resolution data becomes available it can straightforwardly be used to produce improved and extended sets of empirical energy levels. As part of the work being undertaken in the ExoMol project, line lists can be updated with an improved set of MARVEL energies whenever new spectroscopic data is published.

2.2.1 Assessing spectroscopic network inconsistencies

MARVEL is capable of identifying inconsistencies within a network, such that two or more transitions imply a different energy value for a given energy level. While each

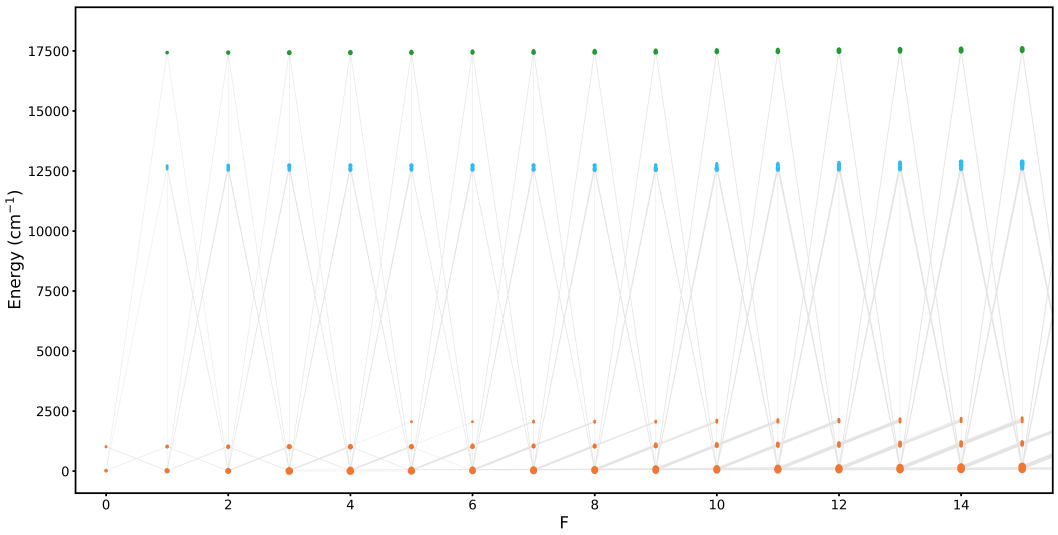


Fig. 2.2: The hyperfine-resolved MARVEL network of $^{51}V^{16}O$, up to levels with $F = 15$. Energy levels are coloured according to their electronic state and their size is set based on the number of transitions that connect to them, as in Fig. 2.1, but arranged based on their term energy and F values.

transition effectively comprises three pieces of information, the transition frequency, the upper and lower state quantum number labels, the sheer number of transitions within a network can often make identifying a small number of issues rather time consuming. Moreover, a single inconsistency can cause a cascade of issues that can make identifying the source of any problem difficult. The errors in the data often arise from the incorrect digitisation of the source material. As attempts are made to incorporate all available data sources into the MARVEL networks, data is often taken from older publications that sometimes contain tables written up by hand, are only available via low-resolution scans where individual digits in transition frequencies have blurred together, or simply contain mistakes. Sometimes these mistakes are obvious, such as a series of R-branch transitions at wavenumbers of the order 7 000 cm^{-1} having one entry reported as 9 000 cm^{-1}, but when the error is in fourth decimal place the correct value is not obvious. While it is sometimes possible to correct mistakes in the source material using common sense, when there is no obvious correction the transitions must be invalidated. It is often the case that digitisation of the source material using tools such as optical character recognition incorrectly reads a digit. The same is true of human error when manually typing up a source's data. Accordingly, all of the transition data is manually inspected at some point, which can take a considerable amount of time. Even when all data has been correctly reported and digitised however, inconsistencies can still occur. In some cases an inappropriate uncertainty will be reported, such as the very common situation of an experiment reporting a single uncertainty figure for all their transitions as mentioned previously. While the MARVEL optimal uncertainty is a good guide here, it is sometimes appropriate to increase the uncertainty for all transitions from a given source.

Perfectly recorded transition frequencies will still produce inconsistencies even if the transition's assignment is incorrect. This often occurs in regions populated by multiple hot bands in polyatomics, where vibrational assignments can be extremely tricky (see Section 4.3.1) or in regions where electronic state perturbations occur in diatomics. In the case of perturbed transitions, two measurements are usually provided for both the perturbed and perturbing electronic states and it is usually a case of trial and error to find which pair of state assignments produces a consistent network. This is discussed in Section 5.4.4 and can be used in conjunction with spectroscopic models to assign the perturbing state. Some sources report non-physical assignments, such as a P($J'' = 0.5$) assignment implying an impossible upper state $J' = -0.5$, or transitions to low values of J that do not exist in high-Ω fine structure components. These are usually the result of tabulation errors, though it is often not immediately obvious what the correct assignment should be, requiring a set of energy levels to compare against. The implied transition assignments are evaluated algorithmically to ensure all upper and lower state quantum numbers are physical and that all transitions obey selection rules, though allowances are made for special cases such as spin-forbidden transitions.

Despite these precautions, there can still be inconsistencies in the data. Rarer examples include experimental wavelength calibration errors, contamination of the spectra by isotopically substituted species, or entire P- and R-branches having their J assignment off by 1 or more. Thankfully, these were not applicable to the MARVEL networks discussed here. Section 3.2.2 (AlO), Section 4.3 (H_3^+) and Section 5.3 (VO) provide summaries of the MARVEL networks for their respective molecules and any corrections that had to be made to the transition data in their construction.

One method for seeking out the source of inconsistencies within a network is the analysis of sets of cycles, or cycle bases, as the sum of the transitions frequencies along a cycle from one node back to itself must be conserved, which is to say they must sum to a value within the combined uncertainty of all transitions involved in the cycle (Tóbiás et al., 2017). As development of the MARVEL procedure is ongoing, similar new tools that expedite the process of identifying and resolving inconsistencies in spectroscopic networks will likely continue to emerge.

2.3 Hyperfine deperturbation

While the majority of published experimental spectroscopic data is not hyperfine resolved, there often exists a small subset of data that is. Given that hyperfine splittings are generally small, this hyperfine-resolved data is often measured to very high accuracies, higher than that of the hyperfine-unresolved measurements. This is understandable, as Doppler-limited experiments that are unable to resolve hyperfine splittings cannot by definition have accuracies on that scale. In addition to the hyperfine-resolved data being more accurate, it sometimes covers regions of spectra not covered by other, hyperfine-unresolved experiments. Accordingly, the ability to utilise the benefits of hyperfine-resolved data to expand the number of energies in a hyperfine-unresolved network, as well as potentially increase the network connectivity and further constrain the accuracy to which term energies are known, would be of great benefit in the construction of accurate spectroscopic

networks. Such techniques have been implemented elsewhere for incorporating hyperfine-resolved data into hyperfine-unresolved MARVEL networks to supplement their energy level coverage Tennyson et al. (2009).

The use of effective Hamiltonian calculations to determine term energies and hence synthetic hyperfine-unresolved transition frequencies by using molecular constants from fits to hyperfine-resolved data was considered as a possible solution to this problem. Unfortunately, setting the hyperfine constants to zero in these calculations while using the other constants obtained in the fits, such as the rotational constant and its distortions, to derive hyperfine-unresolved transitions frequencies often failed to reproduce hyperfine-unresolved observations in regions where data was available for comparison. This was likely due to potentially unavoidable issues with the fitting of the effective Hamiltonian constants and is discussed below. So as to avoid having to try and refit effective Hamiltonian constants to all of the hyperfine-resolved spectra, a technique to deperturb the hyperfine-resolved transitions was developed. The end result is the same as it would have been using effective Hamiltonians but is agnostic to the quality of published fits. Over the course of my work this deperturbation procedure was developed to enable the amalgamation of hyperfine-resolved and hyperfine-unresolved data sets and is outlined in this chapter. The creation of this procedure began with the analysis of hyperfine-resolved, pure-rotation transitions in the ground state of AlO (Chapter 3) and was adapted further for use with hyperfine-resolved rovibronic transitions in VO (Chapter 5). The deperturbing procedure was especially needed for the hyperfine-resolved spectroscopic data of VO, given the unusually large number of hyperfine-resolved transition measurements available in the literature. This section is adapted from the hyperfine deperturbation discussion published in Bowesman et al. (2022) which includes discussion on how the uncertainties from the hyperfine-resolved data is propagated onto the resultant deperturbed line centres.

2.3.1 Relative intensities

In this work, deperturbation techniques that had been previously implemented elsewhere were refined. To carry out the deperturbation, a weighted mean transition frequency is determined. This is done to simulate how a set of hyperfine transitions would combine into a single spectral feature at a lower resolution and as such are weighted by their intensities. As transition intensities are often not reported however, relative values are calculated using a method previously applied by Fast and Meek (2021) to hyperfine transitions of SH and similarly in the production of the AlO and VO MARVEL networks, presented in Chapters 3 and 5. Considering the line strengths of hyperfine components between a common J' and J'' and with fixed nuclear spin I,

$$S_{F'F''} = (2F'+1)(2F''+1)\begin{Bmatrix} F' & F'' & 1 \\ J'' & J' & I \end{Bmatrix}^2 \frac{S_{J'J''}}{g_{ns}}, \tag{2.26}$$

it can be seen that the rotational line strength $S_{J'J''}$ is the same for all hyperfine components of a given transition. The inclusion of the nuclear spin degeneracy factor, g_{ns}, ensures that the sum of all of the individual hyperfine component line

strengths equals that of the deperturbed rotational line strength. Hence by dropping the terms that do not vary between each hyperfine component, the relative intensity of the hyperfine transitions is obtained as

$$I(F', F'', J'', J', I) \propto (2F'+1)(2F''+1) \begin{Bmatrix} F' & F'' & 1 \\ J'' & J' & I \end{Bmatrix}^2 . \tag{2.27}$$

This form is derived from the square of the reduced matrix element of the electric dipole moment and its derivation can be readily found in the literature (Cook and De Lucia, 1971; Zare, 1988; Bunker and Jensen, 2006; Emery, 2006; Brown and Carrington, 2010) along with a multitude of applications to atomic and molecular spectra (Harilal et al., 2020; Murzyn et al., 2022). This expression relies on there being no additional coupling between angular momenta and hence cannot be used for transitions with $|\Delta J| > 1$, such as O- or S-branch transitions, which would violate the triangle condition on the $(J'', J', 1)$ triad in the above $6j$-symbol. Such transitions are facilitated through hyperfine coupling where the selection rule transforms to $|\Delta F| \leq 1$, allowing for transitions with $|\Delta J| \leq (2I+1)$. All other terms that do not depend on F' or F'' will be equal for all hyperfine components of a given transition and as such can be disregarded when comparing their relative intensities. It should be noted that including O- and S-branch transitions during the deperturbation process of the AlO and VO data would not have led to the characterisation of any additional energy levels. This process When deperturbing hyperfine components into a single transition, hyperfine transitions are only combined with others from the same data source. This is to ensure that any systematic effects that might be present in the data of a given source do not pollute the data of other sources. It is then left to the MARVEL procedure to subsequently evaluate the validity of multiple sources of data in combination.

2.3.2 Deperturbation uncertainty scaling

Uncertainty estimates for the deperturbed transitions are provided and are the product of a base uncertainty and three scale factors. The base uncertainty is the standard error propagation of the weighted mean of the uncertainties of the deperturbed hyperfine transitions. Each transition has a normalised weight w_i defined as the respective transition's relative intensity, calculated using Eq. (2.27), as a fraction of the total intensity of all hyperfine components being deperturbed. Given a set of hyperfine transitions with individual transition wavenumber uncertainties $\Delta\tilde{\nu}_i$, the intensity weighted mean uncertainty is defined by:

$$\Delta\tilde{\nu}_{\text{iwm}} = \left(\sum_{i=1}^{n} w_i^2 \Delta\tilde{\nu}_i^2 \right)^{\frac{1}{2}} . \tag{2.28}$$

The first scale factor used here considers the completeness of the subset of hyperfine transitions present in the dataset. To assess this, one must first determine what constitutes the full set of possible hyperfine transitions that can be expected to be observed between the upper and lower states. Though F obeys the selection rule $\Delta F = \pm 1, 0$, not all of these ΔF components will be observed due to the propensity rule

which suggests that $\Delta F = \Delta J$ transitions are strongly favoured. There are of course exceptions to this rule and most hyperfine-resolved sources report a considerable number of $\Delta F \neq \Delta J$ transitions at low J values, see Cheung et al. (1982a); Suenram et al. (1991); Adam et al. (1995); Flory and Ziurys (2008) for examples in the spectra of VO. For each set of hyperfine transitions that are deperturbed, the set of ΔF values that are present, ΔF_{pres}, are assessed and are used to determine the total possible number of hyperfine transitions with the corresponding ΔF values. This is determined for each transition individually to avoid attempting to define a cut-off value for J above which $\Delta F \neq \Delta J$ transitions are no longer considered as this did not appear to be consistent between different sources, varying dependent on their ability to resolve relatively low-intensity transitions.

Considering a transition between two levels with total angular momentum quantum J_{max} and J_{min} ($J_{\text{max}} \geq J_{\text{min}}$): the number of possible hyperfine components of the transition, n_{poss}, is limited by J_{min}. The possible number of hyperfine configurations, i.e., the possible values of F are given by the relationship $\boldsymbol{F} = \boldsymbol{J} + \boldsymbol{I}$, such that the number of possible hyperfine configurations for a given level is $n_{\text{hf}}(J) = J + I - |J - I| + 1$. If $J \geq I$ this simplifies to the expected $2I + 1$. When $J < I$ however, this value is reduced by 2 for each integer decrease in J below the value of I. n_{poss} is calculated given the values of ΔF in the set ΔF_{poss} with the following relationship:

$$n_{\text{poss}} = \begin{cases} \sum\limits_{\Delta F_{\text{poss}}} n_{\text{hf}}(J_{min}), & \text{if } J_{\text{min}} < J_{\text{max}} \leq I \\ \sum\limits_{\Delta F_{\text{poss}}} \min\left(n_{\text{hf}}(J_{min}), n_{\text{hf}}(J_{max}) - |\Delta F - \Delta J|\right), & \text{if } J_{\text{min}} < I < J_{\text{max}} \\ \sum\limits_{\Delta F_{\text{poss}}} \left(n_{\text{hf}}(J_{min}) - |\Delta J - \Delta F|\right), & \text{otherwise.} \end{cases} \tag{2.29}$$

The second case in Eq. (2.29), applicable when $J_{\text{min}} < I < J_{\text{max}}$, does not occur for either AlO or VO, however. Given both I and J are half-integer in each case, J_{min} and J_{max} must differ by more than 1 to satisfy this condition. This can occur for O- and S-branch transitions, but these are excluded from the deperturbation process due to the $|\Delta J| \leq 1$ condition imposed by Eq. (2.27).

Once n_{poss} has been calculated, it is compared against the real number of hyperfine transitions present within the data set that are to be deperturbed into a single transition, n_{pres}. These are combined into the uncertainty scale factor $\Delta\tilde{\nu}_{\text{pres}}$ with a constant $a = 4$ such that there is a 5-fold increase to the base uncertainty when only one hyperfine transition is present. There is no uncertainty increase from this factor when all possible hyperfine transitions are present ($\Delta\tilde{\nu}_{\text{pres}} = 1$):

$$\Delta\tilde{\nu}_{\text{pres}} = 1 + a \times \frac{n_{\text{poss}} - n_{\text{pres}}}{n_{\text{poss}} - 1}. \tag{2.30}$$

The term $\Delta\tilde{\nu}_{\text{pres}}$ provides the smallest uncertainty increase of the scale factors considered here.

The second uncertainty scale factor employed accounts for the distribution of

the subset of hyperfine transitions present in the data, to see if the values of F are evenly distributed about J or skewed to one side. To calculate this, the set of possible hyperfine transitions that are expected to be observed between the given upper and lower energy levels are considered again, accounting for the present values of ΔF_{pres}. For each transition, the mean value of the hyperfine quantum number in the upper and lower state is taken to give a 'centre' value, F_{c}. It is important to consider that this F_{c} term is not a quantum number for either upper or lower level but rather a metric for measuring the relative positions of hyperfine transitions. The mean of this centre is then calculated over all possible hyperfine components of the transition, $\overline{F}_{\text{c,poss}}$. The same calculation is also performed for the subset of hyperfine transitions present in the data and the magnitude of the difference between these two values is taken as the measure of the distribution of the hyperfine transitions in the dataset:

$$\Delta\tilde{\nu}_{\text{dist}} = 1 + b \times |\overline{F}_{\text{c,poss}} - \overline{F}_{\text{c,pres}}|. \tag{2.31}$$

The maximum value of the difference between the two $\overline{F}_{\text{c}}$ terms is I, occurring when only one hyperfine transition is present that has either $F = J \pm I$ in both upper and lower energy levels. Given this fact, the value of b was set to 4 such that this term produces the largest scaling of uncertainty when the distribution of transitions is most uneven.

The derived scaling terms from Eq. (2.30) and Eq. (2.31) are combined with the initial propagated uncertainty and a final scale factor c to determine the final deperturbed uncertainty, $\Delta\tilde{\nu}_{\text{dpt}}$:

$$\Delta\tilde{\nu}_{\text{dpt}} = c \times \Delta\tilde{\nu}_{\text{iwm}} \times \Delta\tilde{\nu}_{\text{pres}} \times \Delta\tilde{\nu}_{\text{dist}}. \tag{2.32}$$

The scale factor c was set to 15 based on direct comparisons between the final energy of the deperturbed hyperfine transitions and equivalently assigned, hyperfine-unresolved transitions also considered in this work. This value was chosen such that at least one standard deviation of matching, equivalent transitions were consistent in their energies and is on the same order as the difference between the experimental uncertainty in the hyperfine-resolved and hyperfine-unresolved transition data. In total, 269 matching transitions were found between the deperturbed hyperfine and hyperfine-unresolved data; 173 B $^4\Pi$–X $^4\Sigma^-$ Adam et al. (1995) and 96 C $^4\Sigma^-$–X $^4\Sigma^-$ Lagerqvist and Selin (1957) transitions. This process is illustrated in Fig. 2.3.

2.3.3 Effectiveness

To benchmark the effectiveness of this method against the commonly used effective Hamiltonian approach, comparisons were made to synthetic transitions frequencies determined from effective Hamiltonian calculations using constants from fits to hyperfine-resolved data for the X $^4\Sigma^-$ (Flory and Ziurys, 2008), B $^4\Pi$ (Adam et al., 1995) and C $^4\Sigma^-$ (Cheung et al., 1982a) states. Using the program PGOPHER (Western, 2017) to carry out the effective Hamiltonian calculations, a set of transition frequencies for every possible $\Delta J = \pm 1, 0$ transition up to $J' = 99.5$ in the B $^4\Pi$–X $^4\Sigma^-$ (0,0) and C $^4\Sigma^-$–X $^4\Sigma^-$ (0,0) bands were generated. These calculated frequencies were checked against their published hyperfine-unresolved counterparts (Lagerqvist

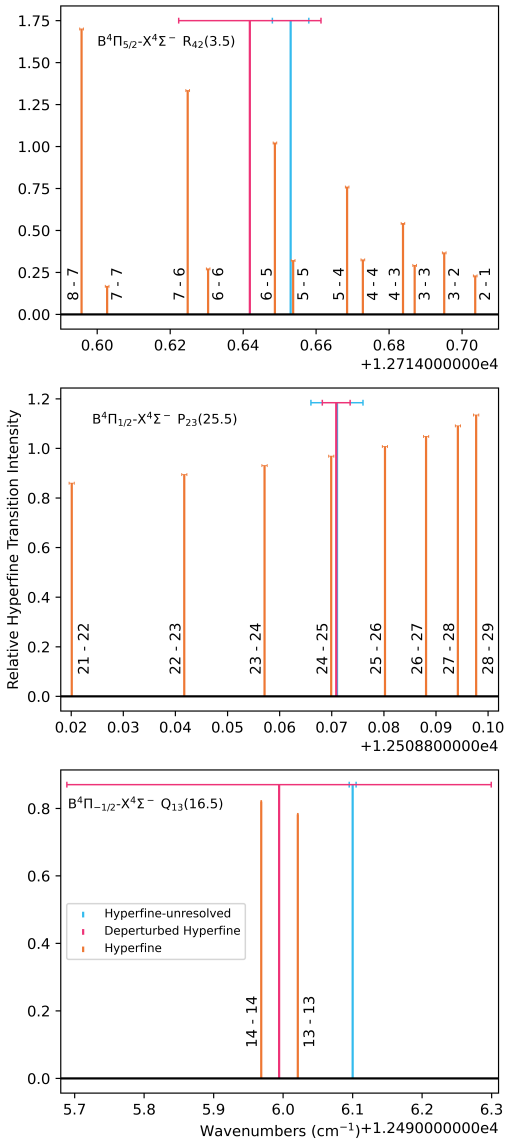


Fig. 2.3: Comparisons between the deperturbed hyperfine line centres calculated using the relative intensity weighted mean and the observed hyperfine-unresolved line centres for three B $^4\Pi$–X $^4\Sigma^-$ (0,0) transitions within the data set. The constituent hyperfine transitions that were used to calculate the deperturbed line centres are overlaid, labelled with their F' and F'' values. Top panel: example involving observed hyperfine transitions with multiple ΔF values; the transitions with $\Delta F \neq \Delta J$ are predicted to be much weaker. Middle: case where full set of $\Delta F = \Delta J$ hyperfine transitions are available, resulting in very close deperturbed and hyperfine-unresolved line centres. Bottom: case with skewed distribution of hyperfine transitions, resulting in a deperturbed line centre that is not very consistent with the observed hyperfine-unresolved equivalent. The uncertainties in the individual hyperfine transitions are all 0.005 cm^{-1} which is too small to be seen on the scale of the bottom panel.

and Selin, 1957; Adam et al., 1995) for consistency. Out of the 896 observed transitions in these bands, only 97 had their frequencies accurately recreated by the effective Hamiltonian calculations. It should be noted that the hyperfine constants are not uncorrelated with the other effective Hamiltonian constants used in the fit and therefore removing hyperfine parameters will not generally lead to same result as fitting without them. This correlation could mean that some of a given parameter's effect on the energy is instead accounted for by some of the parameters responsible for hyperfine splitting, meaning the removal of the hyperfine terms in the effective Hamiltonian unintentionally removes a necessary contribution to the hyperfine-unresolved energy calculation. Hence, this approach was deemed inadequate for high-resolution studies and an alternative method of deperturbing the hyperfine-resolved transitions was adopted.

2.4 Hybrid line lists

While the MARVELisation procedure is the main technique used here for improving the accuracy of energy levels and hence line positions, three others are employed across the production of the line lists discussed in this work: the use of effective Hamiltonian energies, the machine-learning of predicted shifts and the pseudo-experimental technique. All four of these techniques are summarised below, including a discussion on how the uncertainty on the final term energy is estimated.

2.4.1 MARVELisation

Although the parameters of a spectroscopic model are generally refined against the empirical energy levels determined in a MARVEL study, the final calculated energies do not exactly reproduce the empirical term values. Because of this, MARVELisation is the first post-processing step in the refinement of a line list; where an energy level is known empirically via MARVEL, the calculated term energy is replaced with its MARVEL value. This process has been performed during the refinement of other diatomic, triatomic and polyatomic molecular line lists to further improve the line lists ability to reproduce of experimental data; see (Al-Derzi et al., 2021; Yurchenko et al., 2022; Owens et al., 2022a; Semenov et al., 2022; Owens et al., 2022b; Mellor et al., 2022) for recent examples. This procedure is carried out simply by matching on the quantum numbers in the MARVEL data set and those output by the calculations. In the case of DUO calculations, this is simple as it provides labelling for a sufficient number of quantum numbers in order to uniquely identify any given energy level. For DVR3D this is not the case, as only J, parity and symmetry are output. In this case, matching is carried out using a closest-match approach, followed by manual inspection to ensure that the matching has identified the correct level in the J/parity/symmetry block. Given the MARVEL procedure also provides an uncertainty for its empirical term energies, this uncertainty is also taken to be the final uncertainty of the MARVELised energy level. This ensures that transitions between MARVELised energy levels reproduce the experimental measurements that were fed into the MARVEL procedure. The process of matching levels and a series of automated and manual checks can often lead to the identification of misassignments in transitions data. The particular applications of this process to the creation of the line lists described in this work are given in their respective chapters.

2.4.2 Effective Hamiltonians

While MARVEL provides a consistent description of the term energies connected by one or more transitions to the system's zero-energy level, it does not guarantee that all levels have a path to connect to this level. Some components exist in the network that are disconnected and hence do not have their energies determined relative to the same zero as other levels. In the absence of additional experimental data that would provide transitions connecting these components, transition frequencies can be estimated either based on calculated energy differences or through the use of effective Hamiltonians. In instances where a large number of transitions measurements have been recorded, effective Hamiltonian constants are often published to a high accuracy. These high-accuracy constants can then be used to calculate specific transitions frequencies to join more components of the network to the primary component. Two caveats exist here: firstly, effective Hamiltonian constants often poorly describe energy levels that are affected by resonances; secondly, an uncertainty must be carefully and conservatively estimated to ensure that the levels of the component that is being connected by these synthetic transitions are not artificially determined to a higher accuracy. In instances where a level's term energy is only determined via synthetic transitions from effective Hamiltonian calculations it is marked as an "EH" level. The program PGOPHER (Western, 2017) was used to solve the effective Hamiltonian calculations performed in this work and is discussed in Section 3.2.4.

Effective Hamiltonian calculations are often used to calculate what are sometimes referred to as "magic" numbers/transitions. These are calculated transition frequencies that are not otherwise present in the data but enable components of a spectroscopic network to be connected. Section 3.2.4 discusses one example, where these calculated frequencies were used to connect small, low-lying components of the network to supplement energy level coverage. More importantly, however, is their use in connecting the networks of different nuclear spin isomers, between which transitions are forbidden. Section 4.3 details the transition frequencies that were used for H_3^+ and its deuterated isotopologues, to combine their nuclear spin isomers into unified networks so that all their levels were defined on the same energy scale.

2.4.3 Predicted shifts

The MARVEL data for a given vibrational level within an electronic state is sometimes incomplete, with experimental transitions to some values of the principal rigorous quantum number (J or F) missing. Where this was the case, a series of fits to the known obs.-calc. values as a function of this principal quantum number can be performed, in order to predict synthetic obs.-calc. shifts. In the case of hyperfine coupling, the obs.-calc. trends vary differently for each hyperfine component, and hence such fits are also performed as a function of $F - J$. These fits can be carried out over every combination of electronic state, vibrational quantum number, fine structure component and parity for which MARVEL energies exist. Within each of these combinations, linear regression is performed in multiple segments over the missing data, such that a fit is done over the known obs.-calc. values of between 10 and 15 sequential J or F values either side of the missing data. The number of data

points either side is varied to ensure that the linear approximation to the trend in the obs.-calc. data holds, as this is only true over small number of J or F values. A Huber loss algorithm (Owen, 2007; Huber and Ronchetti, 2009; Pedregosa et al., 2011) is utilised to reduce the sensitivity of the fits to outliers, such as when the variance in obs.-calc. values can become larger for levels involved in electronic state crossings. This procedure is carried out over the full range of MARVEL data within a given band, up to the maximum known value of J or F. This interpolation avoids discontinuities between segments of the MARVELised data but does not guarantee that there is not a discontinuity between the final MARVEL data point and the subsequent calculated data in that band. Accordingly, a further correction is applied to shift all levels in a given band beyond the J_{max} or F_{max} known from MARVEL by the mean obs.-calc. shift in the final few known data points in that band. The number of data points over which this mean is taken is generally taken to be the same number as used for the regression model segments, but also excludes any data points that lie more than two standard deviations away from the mean.

Uncertainties for levels adjusted with predicted shifts are set to the sum of the mean of the uncertainty in the data included in the linear regression segment and the standard error of the regression,

$$\Delta\tilde{E}_{\text{PS}} = \sum_{i=1}^{n} \frac{\Delta\tilde{E}_i + |\delta_i - \delta_i^{\text{pred}}|}{n}, \tag{2.33}$$

where n is the number of obs.-calc. data points in the fit, $\Delta\tilde{E}_i$ is the uncertainty in a given MARVEL energy from which an obs.-calc. value is calculated, δ_i a singular obs.-calc. value and δ_i^{pred} its value predicted by the regression model. By using the error in the known obs.-calc. data points, and the error in how well the model predicts those values, it is ensured that the estimated uncertainty in the predicted shift energies is on the same order, though slightly worse, than that of the MARVEL energies.

For the levels with predicted shifts beyond the J_{max} or F_{max} for the band in question, an uncertainty is estimated using an initial base uncertainty and then scaled as a function of J or F. This initial uncertainty is taken as the standard deviation in the final known obs.-calc. data points in the band, over which the mean obs.-calc. shift was calculated. The rigorous quantum number dependent scaling is a function of how far this shift has been extrapolated beyond the J_{max} or F_{max} value in the band, using $J_{\text{ext}} = J - J_{\text{max}}$ and $F_{\text{ext}} = F - F_{\text{max}}$ such that

$$\Delta\tilde{E}_{\text{PS}} = \sigma_\delta + aJ_{\text{ext}}\left(J_{\text{ext}} + 1\right), \tag{2.34}$$

or in the case of hyperfine-resolved levels,

$$\Delta\tilde{E}_{\text{PS}} = \sigma_\delta + aF_{\text{ext}}\left(F_{\text{ext}} + 1\right), \tag{2.35}$$

where σ_δ is the standard deviation in the obs.-calc. data points that were used to determine the mean energy shift for the predict shift extrapolation and a is a constant value with units of cm^{-1}, chosen manually to scale the final uncertainty.

2.4.4 Pseudo-experimental energy levels

Polyansky et al. (2017) showed for water that the obs.-calc. difference between an empirical energy level obtained using MARVEL and its value given by a variational calculation was almost unchanged on isotopic substitution. They used this method to improve their line lists for $H_2{}^{18}O$ and $H_2{}^{17}O$; the method was more recently further refined by Furtenbacher et al. (2020c). This method was also used by McKemmish et al. (2019) to provide accurate line lists for several isotopologues of TiO which led to the identification of features due to four distinct TiO isotopologues in high-resolution spectra of M-dwarfs GJ 15A and GJ 15B by Pavlenko et al. (2020).

The pseudo-experimental correction, which is also sometimes referred to as Isotopologue Extrapolation (IE) (McKemmish et al., 2024) can be expressed as

$$E_i^{\mathrm{PE}}(X) = E_i^{\mathrm{Ca}}(X) + E_i^{\mathrm{Updated}}(Y) - E_i^{\mathrm{Ca}}(Y), \tag{2.36}$$

where X and Y denote the set of atomic mass numbers for each atom in the species for the target and primary isotopologue respectively. i is used to effectively denote a full, unique set of quantum numbers following the assignment scheme used for the species, such that the correction is being applied to the equivalently assigned level in both species.

2.4.5 Calculated Levels

For levels without a corresponding MARVEL or predicted shift energy, the initial calculated energy is retained. In this case, an estimate for the uncertainty is extrapolated from the mean obs.-calc. energy difference,

$$\Delta\tilde{E}_{\mathrm{Ca}} = \Delta\tilde{E} + aJ(J+1) + bv \tag{2.37}$$

or in the case of hyperfine-resolved energy levels,

$$\Delta\tilde{E}_{\mathrm{Ca}} = \Delta\tilde{E} + aF(F+1) + bv \tag{2.38}$$

where $\Delta\tilde{E}$ is the mean obs.-calc. energy difference of MARVEL energies in the same electronic state as the calculated level, or the global mean obs.-calc. energy difference if no MARVEL data exists for the corresponding level's electronic state. a and b are constant values with units of cm^{-1} used to scale how the estimated uncertainty increases as a function of J or F and v. In cases where calculated energies are replaced with MARVEL or predicted shift energies, the original calculated term energies are retained in the final column of the states file.

2.4.6 Source Tags

Following the adoption of the hybrid approach to line lists, it was necessary to introduce a new property that indicated which of the hybrid methods was used to produce each term energy included in the states files. The MARVELised line list of Formaldehyde produced by Al-Derzi et al. (2021) introduced the idea of differentiating entries in the states file using a two-character string on each line, either reading "Ca" if the energy was from the initial calculation or "Ma" if the energy was from MARVEL. Given the introduction of the three additional techniques

Table 2.1: Source tags used in the states files of the line lists discussed in here, to indicate the methods used to produce each term energy.

Source Tag	Meaning
Ca	Calculated with Duo or DVR3D
Ma	MARVELised energy level
EH	Effective Hamiltonian
PS	Predicted shift
PE	Pseudo-experimental correction

described in this section, the notation "EH" for effective Hamiltonian energies was adopted. Similarly, "PS" is used for levels adjusted with predicted shifts and "PE" for those adjusted with pseudo-experimental corrections.

Chapter 3

Aluminium Monoxide

3.1 Overview

Aluminium monoxide ($^{27}Al^{16}O$) is a well-known species in cool (Kaminski et al., 2013) and variable (Banerjee et al., 2003; Tylenda et al., 2005; Banerjee et al., 2012; Kaminski et al., 2016) stars through its electronic spectrum. It has been observed in Sunspots (Sriramachandran et al., 2013) as well as the winds from oxygen-rich AGB stars (Takigawa et al., 2017; De Beck et al., 2017; Danilovich et al., 2020) and stellar envelopes (Tenenbaum and Ziurys, 2009; Singh et al., 2022). The radioactive isotope ^{26}Al has a half-life of 70 000 years so observations of $^{26}Al^{16}O$ have the potential to give timing information. Thus far, observations have only been able to provide upper limits however (Banerjee et al., 2004).

Recently observations of AlO have turned away from stars and instead towards the characterisation of exoplanet atmospheres. The probable signature of AlO has been observed in the optical transmission spectra of the hot Jupiter exoplanets WASP-33b (von Essen et al., 2019) and WASP-43b (Chubb et al., 2020a), and more tentatively in hot Jupiter HAT-P-41b (Lewis et al., 2020; Sheppard et al., 2021) and sub-Saturn KELT-11b (Colon et al., 2020). AlO is also thought to be an important species for driving temperature inversion in the atmospheres of hot Jupiters (Gandhi and Madhusudhan, 2019).

The electronic spectrum of AlO is also important for various practical applications including studies of laser ablation of aluminium in air (Harilal et al., 2016; Bol'shakov et al., 2017; Ran et al., 2017; Van Woerkom et al., 2018), emission in laser-induced plasmas (Surmick and Parigger, 2014), explosions (Kimblin et al., 2017), flames (Soo et al., 2017) and emissions from solid fuel rocket exhausts (Knecht et al., 1996). Line lists were provided by Parigger and Hornkohl (2011) for such plasma studies and by Launila and Banerjee (2009) for much cooler mediums; both have the disadvantage from an astronomical perspective of only providing relative intensities. Further recent work has been done to characterise the vibrational and electronic structures of AlO (Honjou, 2010, 2014) and to calculate band strengths (Honjou, 2011, 2015), radiative lifetimes and transition probabilities (Feng and Zhu, 2019).

Patrascu et al. (2015) provided AlO line lists covering the four main isotopologues of aluminium monoxide ($^{27}Al^{16}O$, $^{26}Al^{16}O$, $^{27}Al^{17}O$, $^{27}Al^{18}O$) as part of the ExoMol project (Tennyson and Yurchenko, 2012). These line lists, hereafter referred

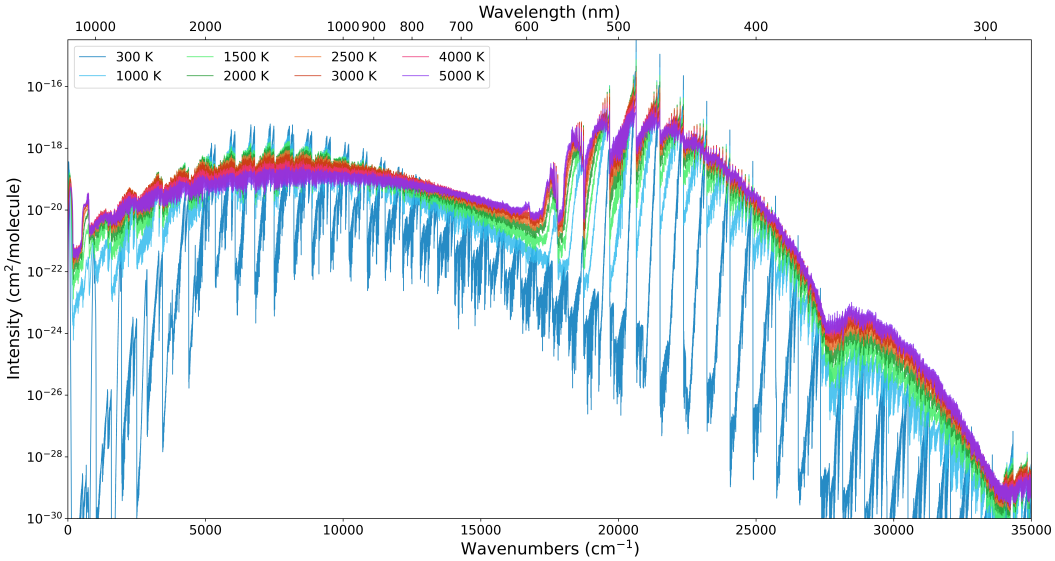


Fig. 3.1: The absorption spectra of $^{27}Al^{16}O$ computed from the MARVELised line list using the code ExoCross (Yurchenko et al., 2018). The spectra are computed at temperatures ranging from 300 K to 5 000 K using Gaussian line profiles with HWHM of 1.0 cm^{-1}.

to as the ATP line lists (from the initials of the paper's first author), were based on potential energy and dipole moment curves provided by *ab initio* electronic structure calculations (Patrascu et al., 2014) and variational nuclear motion calculations provided by the then newly developed code Duo (Yurchenko et al., 2016b). Many of the studies cited above used the ATP line lists.

High-resolution Doppler shift spectroscopy (Birkby, 2018) is the most promising method of making a secure detection of exoplanetary AlO. However, although Duo was used to improve the accuracy of the predicted line positions by fitting the potential curves to spectroscopic data, most of the ATP line lists are not of spectroscopic accuracy. In this work the ATP line lists were refactored by replacing and refining the calculated energy levels, and hence line positions, with energy values derived from empirically determined energy levels. As a result, the majority of the strong lines given by these line lists are predicted with the accuracy of high-resolution spectroscopy making them suitable for studies using high-resolution Doppler shift spectroscopy. A set of example spectra generated using the updated line list for $^{27}Al^{16}O$ over a range of temperatures is shown in Fig. 3.1 and a breakdown of the empirically determined energy levels is shown in Fig. 3.2.

3.2 Method

All four of the hybrid line list techniques described in Section 2.4 were employed to give improved energy levels and hence line positions for the line lists of AlO. The MARVELisation procedure provides the highest accuracy energy levels of the techniques considered here and relies on the set of empirical energy levels and associated uncertainties obtained from a MARVEL network. The accuracy of the empirical energy levels obtained this way relies on the accuracy of experimental

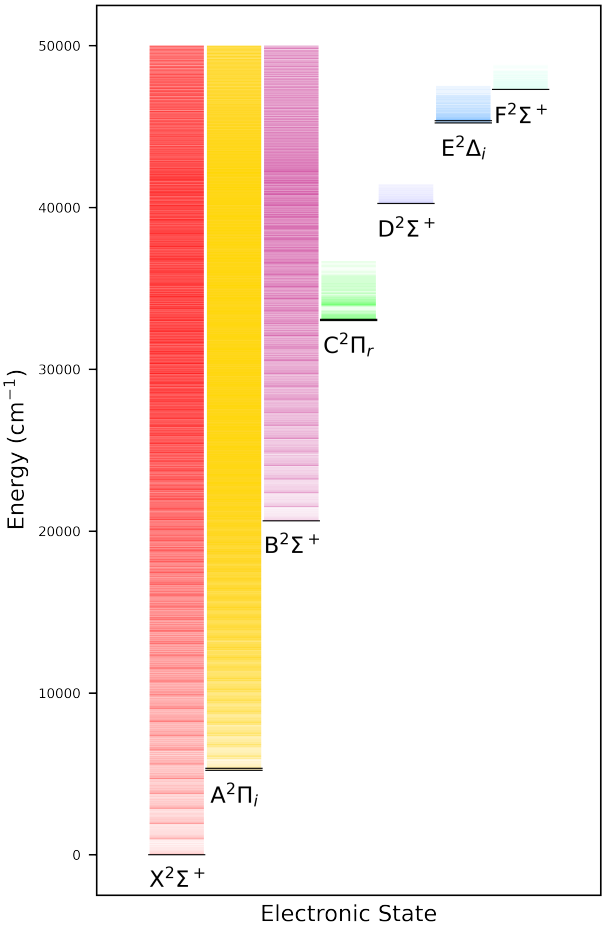


Fig. 3.2: The electronic states of $^{27}Al^{16}O$. T_0 values, taken from Launila and Berg (2011), are shown in black while each electronic state's energy levels are marked in a distinct colour. The energy levels shown here are taken from the updated states file produced for this work.

transitions data, as outlined in Section 2.2. MARVEL version 2.1 was used to construct the AlO network presented here, as it was the most recent version available at the time.

All of the measured transitions that were collected and passed through the MARVEL procedure as part of this work were from the $^{27}Al^{16}O$ species and hence the spectroscopic network constructed was for this isotopologue only. To ensure continuous coverage and to maximise the connectivity of the network, a few transitions were determined using experimental molecular constants and effective Hamiltonians. The shifts seen in the MARVEL energy levels from their original calculated term values were then used to predict the expected changes in the energies of levels in the same regime as but missing from the spectroscopic network - see Section 2.4.3. Finally, the energy levels for the three other isotopologues covered in the ATP line list are improved by determining so-called pseudo-experimental energy levels using the technique of Polyansky et al. (2017), summarised in Section 2.4.4.

In order to adapt ExoMol line lists (such as the ATP line lists) for use in high-resolution studies, the ExoMol project updated its data model to include uncertainties in the energy levels as part of the states file (Tennyson et al., 2020). These uncertainties can then be used to determine the uncertainties in the transition wavenumbers. As the published ATP line list did not contain initial uncertainty estimates it was necessary to determine these for all the energies given in the states file. How uncertainties are determined is dependent on the technique used to update their energies and are summarised in Section 2.4.

3.2.1 Experimental data sources

The following sources were considered when gathering observational data for this study: Goodlett and Innes (1959); Hébert and Tyte (1964); Tyte and Hébert (1964); Tyte (1964); Krishnamachari et al. (1966); Tawde and Korwar (1968); Mcdonald and Innes (1969); McDonald et al. (1969); Singh and Narasimham (1969); Johnson et al. (1972); Tawde and Tulasigeri (1972); Schamps (1973); Singh (1973); Yoshimine et al. (1973); Mahieu et al. (1975); Rosenwaks et al. (1975); Singh and Saksena (1981, 1982); Partridge et al. (1983); Singh and Saksena (1983); Coxon and Naxakis (1985); Singh and Saksena (1985); Singh et al. (1985); Saksena et al. (1989); Torring and Herrmann (1989); Yamada et al. (1990); Goto et al. (1994); Ito and Goto (1994); Launila and Jonsson (1994); Towle et al. (1994); Bescos et al. (1995); Sato et al. (1995); Kraus et al. (2002); Saksena et al. (2008); Londhe et al. (2010); Launila and Berg (2011); Sarvan et al. (2011); Bai and Steimle (2020); Danilovich et al. (2020); Londhe and Undre (2020). Of these 40 sources, 31 did not provide observational data so were not included in this study; these sources are detailed in Table 3.1. The majority of these 31 sources did not provide individual line measurements. Launila and Jonsson (1994) and Saksena et al. (2008) provided line measurements but their data was included in the subsequent release by Launila and Berg (2011) where some lines had been remeasured so only the later source was used in the construction of the network.

Papers such as Tawde and Tulasigeri (1972) and most of those published prior to this used different letter designations for some electronic states (excluding the ground state X) or simply did not assign any. Care was taken to ensure assignments were updated for consistency with later works, as described by Singh (1973).

3.2.2 MARVELised data sources

Transitions from all sources were updated to define their energy levels using the same set of assignments: their electronic state label, the vibrational quantum number v, the total angular momentum quantum number J, the total angular momentum excluding electronic and nuclear spin N, the fine structure (F_1/F_2) and total parity (+/-). Note that this labelling scheme is based on a Hund's case b coupling scheme while the ATP line list uses Hund's case a which replaces N and F_1/F_2 with Ω (Brown and Carrington, 2010). Some of these quantum numbers are redundant, as they are implied by the choice of others (i.e.: the combination of J and N implies the fine structure) but were included to confirm that all assignments had been updated correctly and consistently.

The following data sources are included in the new spectroscopic network

Table 3.1: A summary of all experimental sources considered but not included in this study. Bands marked with a † have been updated to the modern electronic state designation compared to the original source material.

Source	Bands/States	Comments
Goodlett and Innes (1959)	B $^2\Sigma^+$–X $^2\Sigma^+$, C $^2\Pi_r$–X $^2\Sigma^{+\dagger}$	No line measurements provided.
Hébert and Tyte (1964)	B $^2\Sigma^+$–X $^2\Sigma^{+\dagger}$	No line measurements provided.
Tyte and Hébert (1964)	B $^2\Sigma^+$–X $^2\Sigma^{+\dagger}$	No line measurements provided.
Tyte (1964)	C $^2\Pi_r$–B $^2\Sigma^{+\dagger}$	No line measurements provided.
Krishnamachari et al. (1966)	D $^2\Sigma^+$–X $^2\Sigma^{+\dagger}$	No line measurements provided, only band heads and other constants.
Tawde and Korwar (1968)	B $^2\Sigma^+$–X $^2\Sigma^{+\dagger}$	No line measurements provided.
McDonald et al. (1969)	C $^2\Pi_r$–X $^2\Sigma^+$	No line measurements provided, only combination differences.
Singh and Narasimham (1969)	D $^2\Sigma^+$–X $^2\Sigma^{+\dagger}$	No line measurements provided.
Johnson et al. (1972)	B $^2\Sigma^+$–X $^2\Sigma^+$	No line measurements provided.
Tawde and Tulasigeri (1972)	D $^2\Sigma^+$–X $^2\Sigma^{+\dagger}$	No line measurements provided.
Schamps (1973)	A $^2\Pi_i$–X $^2\Sigma^+$, B $^2\Sigma^+$–X $^2\Sigma^+$, C $^2\Pi_r$–X $^2\Sigma^+$, C $^2\Pi_r$–B $^2\Sigma^+$, D $^2\Sigma^+$–X $^2\Sigma^+$, D $^2\Sigma^+$–A $^2\Pi_i$, D $^2\Sigma^+$–B $^2\Sigma^+$, E $^2\Delta_i$–A $^2\Pi_i$	Summary of known spectral bands, no new measurements.
Yoshimine et al. (1973)	X $^2\Sigma^+$–X $^2\Sigma^+$, A $^2\Pi_i$–A $^2\Pi_i$, X $^2\Sigma^+$–A $^2\Pi_i$, B $^2\Sigma^+$–B $^2\Sigma^+$, X $^2\Sigma^+$–B $^2\Sigma^+$	No line measurements provided.
Mahieu et al. (1975)	B $^2\Sigma^+$–X $^2\Sigma^+$, D $^2\Sigma^+$–X $^2\Sigma^+$	No line measurements provided.
Rosenwaks et al. (1975)	A $^2\Pi_i$–X $^2\Sigma^+$, B $^2\Sigma^+$–X $^2\Sigma^+$, C $^2\Pi_r$–X $^2\Sigma^+$	No line measurements provided.
Partridge et al. (1983)	B $^2\Sigma^+$–X $^2\Sigma^+$	No line measurements provided.
Singh and Saksena (1983)	C $^2\Pi_r$–X $^2\Sigma^+$	No line measurements provided.
Coxon and Naxakis (1985)	B $^2\Sigma^+$–X $^2\Sigma^+$	No line measurements provided.
Singh and Saksena (1985)	C $^2\Pi_r$–A $^2\Pi_i$, D $^2\Sigma^+$–A $^2\Pi_i$	No line measurements provided, only graphical data.
Singh et al. (1985)	B $^2\Sigma^+$–X $^2\Sigma^+$	No line measurements provided, only band heads and constants.
Saksena et al. (1989)	B $^2\Sigma^+$–X $^2\Sigma^+$	No line measurements provided, only band heads and constants.
Ito (1994)	A $^2\Pi_i$–X $^2\Sigma^+$	No line measurements provided.
Launila and Jonsson (1994)	A $^2\Pi_i$–X $^2\Sigma^+$	Results included and refitted in Launila and Berg (2011).
Bescos et al. (1995)	B $^2\Sigma^+$–X $^2\Sigma^+$	No line measurements provided.
Sato et al. (1995)	B $^2\Sigma^+$–X $^2\Sigma^+$	No line measurements provided.
Kraus et al. (2002)	B $^2\Sigma^+$–X $^2\Sigma^+$	No line measurements provided.
Saksena et al. (2008)	B $^2\Sigma^+$–X $^2\Sigma^+$	Results included and extended upon in Launila and Berg (2011).
Londhe et al. (2010)	B $^2\Sigma^+$–X $^2\Sigma^+$, C $^2\Pi_r$–X $^2\Sigma^+$, C $^2\Pi_r$–A $^2\Pi_i$	No line measurements, only term values and other constants given.
Sarvan et al. (2011)	C $^2\Pi_r$–X $^2\Sigma^+$	Line measurements provided without quantum number assignments.
Bai and Steimle (2020)	B $^2\Sigma^+$–X $^2\Sigma^+$	Two upper and lower G and F assignments are provided for each measurement, unclear how to use the data.
Londhe and Undre (2020)	B $^2\Sigma^+$–X $^2\Sigma^+$	No line measurements provided; transitions recorded with alternative quantum number assignments.

described in this paper. Data source labels used in the MARVEL input file are provided in italics for each source.

69McIn (Mcdonald and Innes, 1969): Observations of transitions in the E $^2\Delta_i$–A $^2\Pi_i$ and D $^2\Sigma^+$–A $^2\Pi_i$ bands are reported. No uncertainty was provided for the line measurements in the original paper so was estimated at 0.3 cm^{-1} based on the magnitude of combination differences. The observations of the previously unrecognised, low-lying A $^2\Pi_i$ state reported here prompted a reallocation of the electronic state labels for AlO; what is now known as B $^2\Sigma^+$ was previously the lowest-lying identified band and referred to as A $^2\Sigma^+$.

73Singh (Singh, 1973): Observed transitions in the F $^2\Sigma^+$–A $^2\Pi_i$ band are reported, stating the absolute accuracy of the reported wavenumbers to be ±0.1 cm^{-1}. This paper details the electronic states of AlO and how their labelling was updated from earlier works, following the findings of Mcdonald and Innes (1969); Singh's labelling system is used in this study and in all subsequent papers discussed here.

81SiSa (Singh and Saksena, 1981): E $^2\Delta_i$–A $^2\Pi_i$ band transitions are observed. Unblended lines are reported with an accuracy of 0.05 cm^{-1}, based on their agreement with calculated lines reproduced using constants obtained from fits to their data. This value is taken as the uncertainty for these measurements. Some shoulder measurements, blended and blurred lines were also included with an estimated uncertainty 5 times this.

82SiSa (Singh and Saksena, 1982): The paper reports a series of C $^2\Pi_r$–A $^2\Pi_i$ band observations obtained through the same experimental method as their earlier work (Singh and Saksena, 1981) and as such the uncertainties were handled in the same manner.

89ToHe (Torring and Herrmann, 1989): The paper reported 12 hyperfine resolved transitions, the uncertainties of which were estimated at 0.05 cm^{-1} based on the magnitude of the obs.-calc. values the authors report.

90YaCoFuHi (Yamada et al., 1990): The paper reports 56 pure rotation, hyperfine transitions in the $v = 0$ ground state. The uncertainty was taken as the standard deviation of the fit (35 kHz ~ 1.17×10^{-6} cm^{-1}) which was reported as "only slightly larger than frequency measurement error" which was itself left out.

94GoTaYaIt (Goto et al., 1994): The paper reports a series of 50 pure rotational, hyperfine-resolved transitions in the ground state in both the $v = 1$ and 2 bands. Hyperfine transitions that they report as unresolved or not included in their fit were not considered when processing their data. Individual transitions uncertainties are not provided in the publication but it is stated that the errors are similar to the standard deviations in each vibrational band's least-squares fit; uncertainties of 29 kHz (9.67×10^{-7} cm^{-1}) and 27 kHz (9.00×10^{-7} cm^{-1}) are hence used for the $v = 1$ and 2 bands respectively.

94ToJaBoSi (Towle et al., 1994): Observations of transitions in the C $^2\Pi_r$–X $^2\Sigma^+$ band are reported with a spectral resolution of 180 MHz (0.006 cm^{-1}). This was taken as the uncertainty for this source's measurements.

11LaBe (Launila and Berg, 2011): The largest data source included in this study, reporting 21 661 observed transitions in the A $^2\Pi_i$–X $^2\Sigma^+$ and B $^2\Sigma^+$–X $^2\Sigma^+$

bands (16 342 and 5 319 respectively). Any calculated values that are included in the published results for this paper were not included in the MARVEL transition data set. The uncertainties for measurements in the A $^2\Pi_i$–X $^2\Sigma^+$ and B $^2\Sigma^+$–X $^2\Sigma^+$ bands were taken as 0.0097 cm^{-1} and 0.022 cm^{-1} respectively. A few pure-rotational X $^2\Sigma^+$–X $^2\Sigma^+$ transitions in high vibrational bands ($v = 7, 8$) were also included in this source which took the same uncertainty as the A $^2\Pi_i$–X $^2\Sigma^+$ transitions. This source provides constants that were used to calculate effective Hamiltonian transition wavenumbers for 7 low-J, pure rotational ground state transitions to join up low-lying energy levels in disconnected components of the spectroscopic network - see Section 3.2.4 for discussion.

3.2.3 Hyperfine deperturbation

While most published observational data for AlO is not reported at sufficient accuracy to resolve hyperfine splittings, Torring and Herrmann (1989); Yamada et al. (1990); Goto et al. (1994) provide measurements of hyperfine resolved, pure rotational transitions in the X $^2\Sigma^+$ ground state. Given the number of hyperfine resolved transitions was small relative to the number of hyperfine-unresolved transitions, no hyperfine-resolved network was constructed and instead the hyperfine-resolved data was deperturbed to supplement the hyperfine-unresolved network. This was done using the methodology outlined in Section 2.3.

The 12 hyperfine-resolved transitions of Torring and Herrmann (1989) were deperturbed to yield 2 hyperfine-unresolved transitions. Similarly, 56 hyperfine-resolved transitions from Yamada et al. (1990) and 50 from Goto et al. (1994) were deperturbed to yield 14 and 20 hyperfine-unresolved transitions respectively. The deperturbed Goto et al. (1994) were split evenly into 10 transitions in both the $v = 1, 2$ bands. Each deperturbed transitions was the result of between 1 and 6 hyperfine-resolved transitions, which was used to inform the deperturbed uncertainty estimates, given Eq. (2.30).

3.2.4 Effective Hamiltonians

As discussed in Section 2.4.2, the use of effective Hamiltonian calculations can be a useful and accurate tool for increasing the coverage of a MARVEL network by joining disconnected components of the network to the primary component using synthetic transitions. For AlO, these transitions were calculated using molecular parameters published by Launila and Berg (2011), determined through fits to observed A $^2\Pi_i$–X $^2\Sigma^+$ and B $^2\Sigma^+$–X $^2\Sigma^+$ transitions. Their work only provided updated parameters for the X $^2\Sigma^+$ and B $^2\Sigma^+$ states however and other published constants for the A $^2\Pi_i$ state were not sufficient to reproduce observed transitions to a comparable accuracy. Fortunately, most of the disconnected components of the network that contained low-J levels could be connected to the main component with a single synthetic R- or Q-branch rotational X $^2\Sigma^+$–X $^2\Sigma^+$ transition, though one component would have required multiple transitions to join up and as such was left out. It was identified that the lowest energy level in the network was not the lowest energy state possible: while there were transitions to the X $^2\Sigma^+$ $v = 0$, $J = 0.5$ f state, the lower energy e state was missing from the transition data. This meant that the energies in the network were defined relative to the higher energy f rotationless parity state, not

the lower energy e state. Hence, one final effective Hamiltonian transition using the constants of Launila and Berg (2011) was added to connect this lowest state, a R_1 ($J'' = 0.5$) transition with a frequency of 1.27784543 cm^{-1}, ensuring that the term energies in the network were defined relative to the correct zero energy.

In total, 7 X $^2\Sigma^+$–X $^2\Sigma^+$ effective Hamiltonian transitions were added to the MARVEL network, maximising the coverage of low-lying energy levels in the X $^2\Sigma^+$ state. Extensive coverage of the ground state is important for the construction of high-resolution line lists as the ground state energies are usually determined to very high accuracy. These effective Hamiltonian transitions were assigned an uncertainty of 0.02 cm^{-1} based on the accuracy to which the molecular constants were quoted to in their source paper (Launila and Berg, 2011). An exception to this is the single R(0.5) transition in the X $^2\Sigma^+$ (0,0) band that connected the zero-energy $J = 0.5$ e level, which was assigned an uncertainty of 0.000001 cm^{-1}. This was done to maintain the high-accuracy of the lowest energy levels in the network, as introducing a lower-accuracy transition to connect to the zero-energy level would effectively propagate a higher uncertainty up the network: while the high-accuracy levels would be well defined relative to one another, they would be limited in their overall accuracy by their less-accurate relation to the zero-energy level. It was also assumed that the blanket uncertainties of 0.0097 cm^{-1} and 0.022 cm^{-1} that were given for all the A $^2\Pi_i$–X $^2\Sigma^+$ and B $^2\Sigma^+$–X $^2\Sigma^+$ transitions of Launila and Berg (2011) were overestimations in this low-J regime and as such the predicted R(0.5) transition frequency would be much more accurate. It can be noted that the network would remain fully self-consistent if all effective Hamiltonian transitions had been provided with the same uncertainty of 0.000001 cm^{-1}, though this is the nature of connecting so-called "leaves" to a network. That is to say, as the components being connected to the main component have no other relationship to the main component's energies, there are no other transitions through which disagreements can arise. Accordingly, the other effective Hamiltonian transitions were left with their more conservative uncertainty estimates. The addition of these effective Hamiltonian transitions did not affect the MARVEL procedure's determination of uncertainties for the other energies within the network, demonstrating the benefits of using synthetic transitions to supplement energy level coverage in this manner.

Several further effective Hamiltonian transitions were produced in an attempt to extend the network to other missing, low-lying energy levels in the same quantum number regime as the spectroscopic network. After passing these through the MARVEL procedure however, the resulting term energies for these levels had uncertainties greater than those expected of the initial DUO calculations. As such, these additional transitions were not included in the final network.

3.2.5 The MARVEL network

In total, 23 972 input transitions were accessed by MARVEL when building the network and 1 499 of these were not validated after optimal uncertainties were calculated for them that were both greater than their input uncertainty and greater than the threshold uncertainty of 0.05 cm^{-1}. As these invalidate transitions connected very few new levels to the network, no attempt was made to adjust their uncertainties in order to retain them. Spot checks were manually done however, to confirm that

Table 3.2: The changes in the mean and max uncertainty of the 3 478 transitions which had their uncertainties updated to the optimal uncertainty determined by MARVEL, broken down by the source paper that the transitions were taken from.

Source	Count	Updated Uncertainty Mean/Max (cm^{-1})	Original Uncertainty Mean/Max (cm^{-1})
11LaBe	3473	0.022116/0.049903	0.012176/0.022000
94ToJaBoSi	5	0.032399/0.048087	0.006000/0.006000

the reported values had not been incorrectly digitised where the source material had been scanned. As is convention, these transitions were left in the input data file with negative wavenumber transition frequencies so that future studies can reconsider them if new data become available.

The vast majority (81.3%) of invalidated transitions came from Launila and Berg (2011), overwhelmingly in the B $^2\Sigma^+$–X $^2\Sigma^+$ band (79.4%). Transitions from this source make up a greater proportion of the total input transitions however (90.3%) and as such were validated at a higher rate than the average for all sources. Out of all the sources considered, Towle et al. (1994) had the highest proportion of invalidated transitions (17.8%) followed by Mcdonald and Innes (1969) (15.7%). None of the 36 deperturbed transitions from the three hyperfine-resolved sources (Torring and Herrmann, 1989; Yamada et al., 1990; Goto et al., 1994), nor any of the effective Hamiltonian transitions were invalidated.

For the transitions that have optimal uncertainties determined by the MARVEL procedure as greater than their input observational uncertainty but lower than the threshold uncertainty, the input uncertainty was replaced with the MARVEL optimal uncertainty. This process updated the uncertainties of 3 478 transitions and resulted in a fully self-consistent network. Of these transitions with updated uncertainties, 3 473 came from the Launila and Berg (2011) data set. This is unsurprising, given this source provides the bulk of the observational data considered here and is likely a consequence of taking a blanket uncertainty value for each electronic band in the absence of individual transition uncertainties. The change in the mean and maximum uncertainties of the transitions that had their uncertainties updated in this manner are given in Table 3.2 for all sources that were affected.

Hence, the new spectroscopic network consists of 22 473 validated transitions split into 31 components, the largest of which consists of 22 433 transitions connecting 6 485 distinct energy levels. Of these levels, one is uniquely determined by effective Hamiltonian calculations. For the other remaining components of the network, 27 consist of single transitions connecting two levels and the remaining three components consist of 2, 5 and 6 transitions. The single-transition components all contain transitions involving levels of $J = 53.5$ or above, except for one which is a single B $^2\Sigma^+$–X $^2\Sigma^+$ (6,7) P_2 (4.5) transition that could not be connected to the main component of the network with a single effective Hamiltonian transition. All of the larger disconnected components involve transitions connecting levels with $J > 112.5$. As such, these disconnected components are not considered further in this work. The self-consistency of the network means that the final derived MARVEL

energies can be used to recreate all of the input transitions wavenumbers with their uncertainties, for all transitions comprising the largest component of the network. The mean degree of the nodes in the largest component of the MARVEL network is 6.9, which translates to the average number of transitions that connect to and hence determine each energy level. The standard deviation of this however is 9.5 and is reflective of how the degree of the energy levels in the network ranges from 1 to 58. 12.2% of all energy levels are of degree 1 and are hence defined by only a single transition.

Table 3.5 breaks down the makeup of the new network by experimental data source and vibronic band. Also given are the mean and maximum uncertainties of each listed band, which are the same in most cases due to the source papers only providing blanket uncertainty measurements across all of their data. Deviations from this trend are seen in data from two sources (Singh and Saksena, 1981, 1982) due to the significant proportion of blended lines that they report. The MARVEL input and energies files are available as part of the supplementary material of Bowesman et al. (2021).

3.2.6 Predicted energy shifts

The observationally determined MARVEL levels for $^{27}Al^{16}O$ show distinct trends in energy shifts from the calculated DUO energies of the original ATP line list. These obs.-calc. differences were used to predict the expected energy shifts from the calculated term energies of levels missing from the network, as outlined in Section 2.4.3.

While the general methodology splits the data into two regions, i.e. levels within the quantum number range of the MARVEL network and those beyond it, an initial step was taken in the preparation of the AlO data to remove the fitting dependence on parity. This precaution was taken as it was believed the DUO calculated parity splitting in the levels of the ATP line list may have been sufficiently accurate already, and the effectiveness of the predicted shifts procedure had yet to be demonstrated. Subsequent work on $^{51}V^{16}O$ did not take this step; see Section 5.5 for discussion. If a level that was absent from the MARVEL network had its opposite parity, but otherwise equivalently assigned counterpart in the network, the same obs.-calc. energy correction was applied to both levels. The uncertainty for these "missing parity pair" levels was similarly taken from their opposite-parity MARVELised counterpart.

Predicted shifts were fit to the known obs.-calc. data as a function of the electronic state, v, Ω and J, where the first three variables were used to categorise the data to then produce different fits as a numerical function of J. As discussed in Section 2.4.3, this fitting is carried out over multiple segments of missing obs.-calc. data points, the size of which can be configured. In this instance, the size of these segment was fixed to 10 data points, ensuring that the approximation of the obs.-calc. function of J as linear held to a reasonable degree and provided predictions with very small mean squared errors. The DUO levels corresponding to the missing obs.-calc. data points had their calculated energies corrected by their predicted obs.-calc. energy shifts and each took the mean standard error of their segment's regression as their uncertainty. This is equivalent to Eq. (2.33) without the $\Delta\tilde{E}_i$ term, which was added to the uncertainty estimation during later work on VO. Fig. 3.3 shows the final

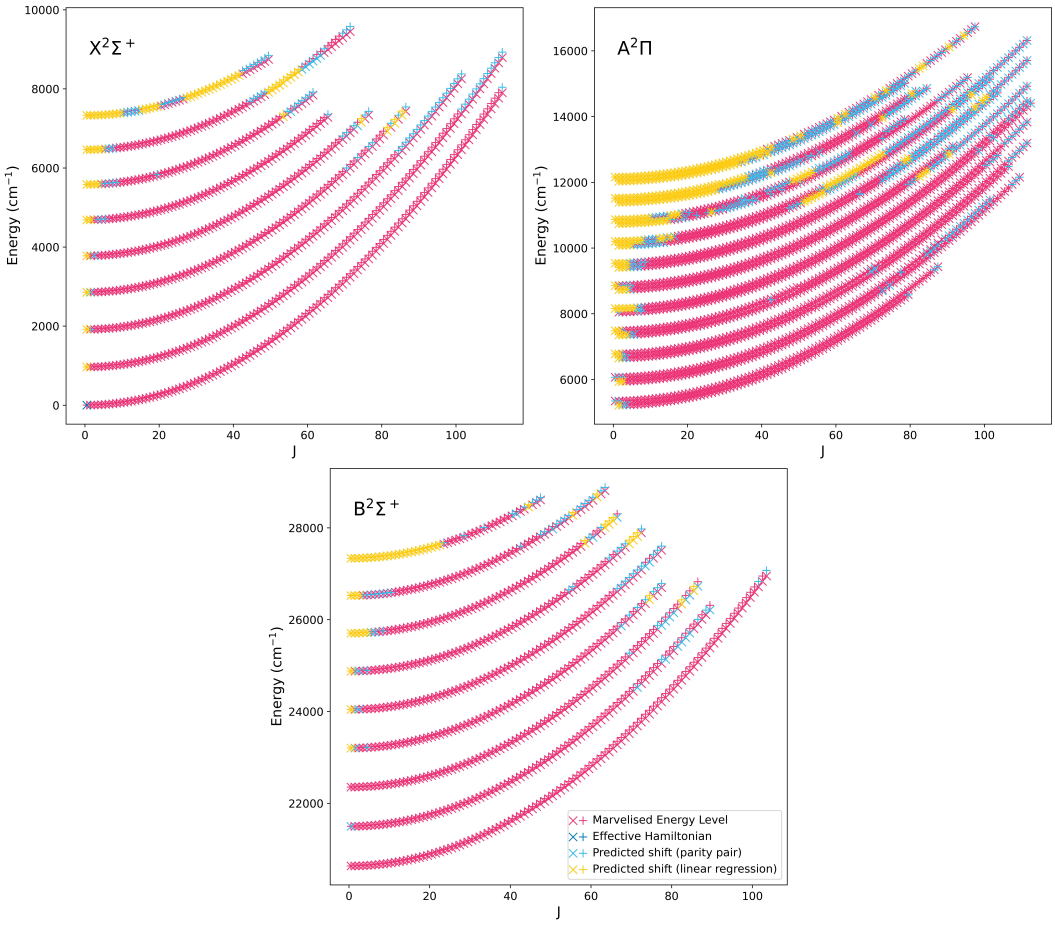


Fig. 3.3: The energy levels of the X $^2\Sigma^+$, A $^2\Pi_i$ and B $^2\Sigma^+$ states of $^{27}Al^{16}O$. Levels are coloured based on whether their final energies were determined through MARVEL (pink), effective Hamiltonian calculations (dark green), parity pair correction (blue) or energy shift regression (yellow); e and f parity states are marked with 'x' and '+' respectively.

energy term values of levels in the X $^2\Sigma^+$, A $^2\Pi_i$ and B $^2\Sigma^+$ states that were updated either with MARVEL energies, effective Hamiltonians, parity pair corrections or the regression described here.

For calculated levels in a given vibronic band above the maximum J occurring in the MARVEL data for that band, the predicted energy shift was taken to be the mean of the obs.-calc. differences in the ten highest-J levels in that band. Uncertainties were estimated for the levels shifted in this manner using Eq. (2.34), where the initial uncertainty, $\bar{\delta}$, was equal to the standard deviation of this mean obs.-calc. shift. The scale factor a was chosen as 0.0001 cm^{-1} to ensure that the uncertainties on these energies were consistently less accurate than the MARVEL energies. Given the DUO calculations extended up to $J = 300.5$ and the maximum J of levels in the MARVEL network was $J_{\max} = 119.5$, the predicted uncertainty in levels shifted this way could reach up to approximately 10 cm^{-1}. No attempt was made to extrapolate predicted shifts to higher values of v.

3.2.7 Pseudo-experimental energy levels

In the absence of experimental transition data for $^{26}Al^{16}O$, $^{27}Al^{18}O$ and $^{27}Al^{17}O$, or more importantly an insufficient amount of transitions data to construct well-connected spectroscopic networks, corrections were made to the three isotopologues based on the energy shifts determined for $^{27}Al^{16}O$. These shifts were the updated-calculated energy differences in $^{27}Al^{16}O$, i.e.: the differences between the MARVELised, effective Hamiltonian or predicted shift energies and their calculated values, rather than just the obs.-calc. shifts seen in the MARVEL levels. This saved having to redo the predicted shifts on the isotopologue energies, as the modelled obs.-calc. trends would be the same.

Following the scheme set out in Eq. (2.36), if a level in $^{27}Al^{16}O$ had been updated from its original calculated energy $E_i^{Ca}(27,16)$, either with a MARVEL energy or through predicted shift corrections to a final energy $E_i^{Updated}(27,16)$, the same final energy shift was applied to the calculated DUO energy $E_i^{Ca}(X)$ of the level with equivalent quantum number assignments in the three isotopologues $^{26}Al^{16}O$, $^{27}Al^{18}O$ and $^{27}Al^{17}O$. The term X in Eq. (2.36) is used here to denote the set of Aluminium and Oxygen mass numbers respectively, for the species $^{x_1}Al^{x_2}O$ that the correction is being applied to and i is used to denote the set of quantum numbers $(\text{state}, v, J, N, \text{finestructure}, +/-)$ used for identifying the individual energy levels of AlO in this work.

3.2.8 Calculated levels

As no attempt was made to extrapolate predicted shift corrections to higher vibrational bands, the only DUO energy values left unchanged are those that had vibrational quantum number assignments above the maximum value of v existing for their respective electronic state in the MARVEL network. Any of the original DUO energies that were not updated as part of this work instead had an estimated uncertainty value set. The uncertainty of these levels would be expected to grow with the energy, given the model would likely deviate further from experimental values as it got further from the known regions. As such, the uncertainties of calculated levels were given a quadratic dependency on J and linear dependency on v as shown in Eq. (2.37). Values for the scaling factors on the J and v terms were set to $a = 0.0001$ cm^{-1}, as used for the predicted shifts, and $b = 0.05$ cm^{-1}.

The DUO quantum number labelling of 9 pairs of X $^2\Sigma^+$ and A $^2\Pi_i$ levels, of which one or both existed in the MARVEL network, were swapped. These levels originally had obs.-calc. energy differences when matched on their quantum number assignments on the order of 60 cm^{-1} but after swapping these differences were reduced to around 0.01 cm^{-1}. This misassignment occurred due to crossings between the X $^2\Sigma^+$ $v = 6,7,8$ and A $^2\Pi_i$ $v = 1,2,3$ states, causing issues with how DUO performs its quantum number labelling. While the DUO assignments of J and parity are rigorous, the labelling of other properties such as electronic state or vibrational quantum number are not. Instead, they are based on the state providing the largest contribution to the wavefunction in the calculation and accordingly this issue arises from how the levels at these crossing are mixed and have character of both the X $^2\Sigma^+$ and A $^2\Pi_i$ states. While it is likely that other crossings exist that could

result in swapped state assignments, attempts were only made to correct the Duo assignments for levels within the scope of the spectroscopic network. Similarly, a series of equal J, Ω and parity levels with ascending v in the A $^2\Pi_i$ state had had their v assignment shifted up by one. This was obvious due to initial obs.-calc. energy differences consistently on the order of 700 cm^{-1} for these levels, roughly the expected vibrational band spacing in the A $^2\Pi_i$ state (Ito and Goto, 1994). Shifting the vibrational assignment back by one reduced the obs.-calc. to values on the expected order of 0.01 cm^{-1}. Five instances where this had occurred were identified, the first instance occurring for $J = 86.5$, $\Omega = 1.5$ e parity levels and then subsequently at higher J. It is again possible that similar v assignment shifts had occurred at even higher J, beyond the limit of the Marvel levels available to compare against; no attempt was made to correct these misassignments.

3.3 New line list

3.3.1 States files

The revised states files made available on the ExoMol website were updated to include two new properties, as part of the drive to update the ExoMol format for use with high-resolution studies. The first addition was the newly determined uncertainty, measured in wavenumbers and appearing in the fifth column of the file. The second was a source tag that indicates which method was used to determine the term energy value used in the file, differentiating those that were Marvelised, calculated or otherwise had their energies shifted. This appears in the final column of each entry. Table 2.1 lists possible values for the source tag: the tags "EH", "PS" and "PE" were introduced for the first time in the updated AlO line lists. Levels in the states files produced for this release were marked as "EH" only when they were singularly determined by synthetic effective Hamiltonian transitions; levels that were determined by both effective Hamiltonian calculations and Marvel data were marked as "Ma".

All of the updated AlO states files follow the specification outlined by Tennyson et al. (2013) to include an ID, term energy, total state degeneracy and J quantum number as the first four columns. This format is intended for use with programs such as ExoCross and Pgopher, both of which were used throughout this work. The first ten entries of the updated states file for ^{27}Al^{16}O are shown in Table 3.3.

As no entries were removed from the original ATP line list when updating them, the new line list retains the same extensive coverage of rovibronic levels in the X $^2\Sigma^+$ (28 845 levels, 30.4% of total), A $^2\Pi_i$ (54 585, 57.5%) and B $^2\Sigma^+$ (10 781, 11.4%) states. This update added energies for ^{27}Al^{16}O in higher-energy electronic states that are included in the Marvel network: C $^2\Pi_r$ (319, 0.34%), D $^2\Sigma^+$ (37, 0.04%), E $^2\Delta_i$ (224, 0.24%) and F $^2\Sigma^+$ (71, 0.07%). The full energy ranges for each electronic state in the ^{27}Al^{16}O states file are shown in Fig. 3.2. While some energies in these four additional electronic states have been included, the trans file was not updated to include transitions involving them. Indeed, the ATP model would need to be updated to include potential energy curves and transition dipole moments for these states in order to compute transitions probabilities for them. These additional electronic states were not added to the states files for the three

Table 3.3: Excerpt from the new states file for $^{27}Al^{16}O$.

i	$\tilde{E}$	g_{tot}	J	unc	τ	+/−	e/f	State	v	$\|\Lambda\|$	$\|\Sigma\|$	$\|\Omega\|$	Source Tag
1	0.000 000	12	0.5	0.000 001	inf	+	e	X2SIGMA+	0	0	0.5	0.5	EH
2	965.416 878	12	0.5	0.001 651	3.6193e+01	+	e	X2SIGMA+	1	0	0.5	0.5	PS
3	1 916.827 286	12	0.5	0.010 519	9.1761e+00	+	e	X2SIGMA+	2	0	0.5	0.5	PS
4	2 854.162 814	12	0.5	0.022 148	4.2147e+00	+	e	X2SIGMA+	3	0	0.5	0.5	PS
5	3 777.464 572	12	0.5	0.019 275	2.3874e+00	+	e	X2SIGMA+	4	0	0.5	0.5	PS
6	4 686.658 929	12	0.5	0.016 235	1.2041e+00	+	e	X2SIGMA+	5	0	0.5	0.5	PS
7	5 346.089 546	12	0.5	0.009 700	2.0501e-04	+	e	A2PI	0	1	0.5	0.5	Ma
8	5 581.908 884	12	0.5	0.014 747	4.3685e-02	+	e	X2SIGMA+	6	0	0.5	0.5	PS
9	6 067.103 586	12	0.5	0.009 700	1.2544e-04	+	e	A2PI	1	1	0.5	0.5	Ma
10	6 463.090 252	12	0.5	0.023 150	1.0436e-02	+	e	X2SIGMA+	7	0	0.5	0.5	PS

i: State counting number;
$\tilde{E}$: Term value (in cm^{-1});
g_{tot}: Total state degeneracy;
J: Total angular momentum quantum number;
unc: Estimated uncertainty of energy level (in cm^{-1});
τ: Radiative lifetime (in seconds);
+/−: Total parity;
e/f: Rotationless parity;
State: Electronic term value;
v: Vibrational quantum number;
$|\Lambda|$: Absolute value of the projection of electronic angular momentum;
$|\Sigma|$: Absolute value of the projection of the electronic spin;
$|\Omega|$: Absolute value of the projection of the total angular momentum;
Source Tag: The method used to generate the term value.

isotopologues, $^{26}Al^{16}O$, $^{27}Al^{17}O$ and $^{27}Al^{18}O$, included in the ATP lien lists, as there were no calculated term energies for them to determine pseudo-experimental corrections against.

3.3.2 Partition functions

Partition functions for the four updated states files are calculated using ExoCross (Yurchenko et al., 2018) and given in Table 3.4. Despite the variation in term energies between species being relatively small, there are significant differences in the partition functions, owing to the differing nuclear spin degeneracy factors of the constituent atoms. The total degeneracy g_{tot} of the hyperfine-unresolved levels is calculated as

$$g_{tot} = (2J+1)\,(2I_{Al}+1)\,(2I_O+1)\,, \tag{3.1}$$

where I_{Al} and I_O are the nuclear spins of the two atoms. The inclusion of nuclear spin degeneracy factors is part of both the ExoMol and HITRAN (Simeckova et al., 2006) conventions. For the species considered here, these can take the values $I_{^{26}Al} = 5$, $I_{^{27}Al} = \frac{5}{2}$, $I_{^{16}O} = 0$, $I_{^{17}O} = \frac{5}{2}$ and $I_{^{18}O} = 0$. This accounts for the roughly factor of 6 increase in the partition functions of $^{27}Al^{17}O$ compared to the other ^{27}Al-bearing species, and why they are roughly twice as large for $^{26}Al^{16}O$ compared to $^{27}Al^{16}O$. Sauval and Tatum (1984) calculated partition function values without nuclear spin degeneracy weighting for $^{27}Al^{16}O$, following the convention used by astronomers; the values are scaled appropriately and shown in Table 3.4 to be in good agreement

with the line list. This is consistent with the findings of the original ATP line list (Patrascu et al., 2015) and is not surprising given the small magnitude of the energy changes mean the MARVELised partition function values do not differ from those of the original calculated line list by more than 1%. Likewise, the $T = 300$ K partition function value of 3 926.45 from NASA JPL (Pickett et al., 1998) is in fairly good agreement, though slightly lower likely because of the lack of consideration of more highly excited states.

By considering the partition functions calculated over a states file truncated at energies less than or equal to the lowest-energy level with the highest $J = 300.5$, one can asses what temperature the line list is complete up to by seeing at what point the partition functions diverge. For the line list presented here, they only diverge from their truncated equivalents at temperatures of ~ 9500 K. Though the line lists offer a description of the X $^2\Sigma^+$, A $^2\Pi_i$ and B $^2\Sigma^+$ states that is complete to very high temperatures, the spectra generated from these states files would likely not be sufficient at such high temperatures due to the incomplete characterisation of the C $^2\Pi_r$, D $^2\Sigma^+$, E $^2\Delta_i$ and F $^2\Sigma^+$ states. As shown in the *ab initio* study of Bai et al. (2023) there are a considerable number of other states not included in the ATP model. The higher-lying states of the same spin multiplicity as the ground state that are included in the MARVEL study are more likely to be accessed by transitions, however, and hence more likely to provide larger contributions to the overall spectrum.

3.3.3 Spectra

An illustration of how the absorption spectrum of $^{27}Al^{16}O$ varies with temperature, from 300 K to 5000 K, is shown in Fig. 3.1. It should be noted that, while the states file was updated to include the empirical energy levels for the C $^2\Pi_r$, D $^2\Sigma^+$, E $^2\Delta_i$ and F $^2\Sigma^+$ states, transitions dipole moments were not calculated for them and added to the ATP spectroscopic model (Patrascu et al., 2015). Accordingly, these spectra only involve transitions between the X $^2\Sigma^+$, A $^2\Pi_i$ and B $^2\Sigma^+$ states. Fig. 3.4 shows two stick spectra near the peaks of the A $^2\Pi_i$–X $^2\Sigma^+$ and B $^2\Sigma^+$–X $^2\Sigma^+$ bands and illustrates how the line centres in the computed spectrum of $^{27}Al^{16}O$ shifted as a result of the update to the states file, from their original positions in the ATP line list. As expected from the magnitude of the energy level corrections applied to the states file, the shifts in line centres are quite small, on the order of 10^{-5} - 10^{-6} cm^{-1}. These shifts are generally smaller than the uncertainties in the MARVELised transition wavenumbers, the mean values of which are 0.0115, 0.0096 and 0.0161 cm^{-1} for the X $^2\Sigma^+$–X $^2\Sigma^+$, A $^2\Pi_i$–X $^2\Sigma^+$ and B $^2\Sigma^+$–X $^2\Sigma^+$ bands respectively. Shifts on the scale of these uncertainties would in turn require resolving powers on average of 1.1×10^6, $7.6\times10^5$and 1.4×10^6 to be observed. The relative line intensities remain essentially unchanged as the trans files have not been updated, keeping the same Einstein A coefficients as the ATP line list but differing slightly due to different partition functions. Fig. 3.5 illustrates how the X $^2\Sigma^+$–X $^2\Sigma^+$, A $^2\Pi_i$–X $^2\Sigma^+$ and B $^2\Sigma^+$–X $^2\Sigma^+$ bands contribute to the overall structure of the spectrum. Fig. 3.6 shows how the change in atomic masses upon isotopic substitution leads to slight shifts in line positions, for all four isotopologue of AlO considered here. All of these spectra were generated using the program ExoCross (Yurchenko et al., 2018).

Table 3.4: Partition functions for the four isotopologue of AlO considered here, calculated over a range of temperatures using the program ExoCross (Yurchenko et al., 2018). Values calculated by Sauval and Tatum (1984) and scaled by the nuclear spin degeneracy factor of 6 are provided for $^{27}Al^{16}O$ for comparison, valid for the range 1 000-9 000 K.

Temp. (K)	$^{27}Al^{16}O$	Sauval and Tatum (1984)	$^{27}Al^{17}O$	$^{27}Al^{18}O$	$^{26}Al^{16}O$
100	1.3113×10^{3}		8.1678×10^{3}	1.4091×10^{3}	2.3704×10^{3}
200	2.6218×10^{3}		1.6334×10^{4}	2.8183×10^{3}	4.7391×10^{3}
300	3.9672×10^{3}		2.4734×10^{4}	4.2711×10^{3}	7.1691×10^{3}
400	5.4076×10^{3}		3.3757×10^{4}	5.8361×10^{3}	9.7675×10^{3}
500	6.9883×10^{3}		4.3686×10^{4}	7.5624×10^{3}	1.2616×10^{4}
600	8.7345×10^{3}		5.4673×10^{4}	9.4761×10^{3}	1.5761×10^{4}
700	1.0660×10^{4}		6.6804×10^{4}	1.1591×10^{4}	1.9227×10^{4}
800	1.2773×10^{4}		8.0131×10^{4}	1.3917×10^{4}	2.3029×10^{4}
900	1.5082×10^{4}		9.4702×10^{4}	1.6461×10^{4}	2.7183×10^{4}
1 000	1.7595×10^{4}	1.7694×10^{4}	1.1057×10^{5}	1.9233×10^{4}	3.1702×10^{4}
1 500	3.3663×10^{4}	3.3198×10^{4}	2.1212×10^{5}	3.6991×10^{4}	6.0590×10^{4}
2 000	5.7300×10^{4}	5.7061×10^{4}	3.6163×10^{5}	6.3156×10^{4}	1.0307×10^{5}
2 500	9.1351×10^{4}	9.1139×10^{4}	5.7710×10^{5}	1.0088×10^{5}	1.6425×10^{5}
3 000	1.3866×10^{5}	1.3744×10^{5}	8.7655×10^{5}	1.5333×10^{5}	2.4922×10^{5}
3 500	2.0180×10^{5}	1.9805×10^{5}	1.2763×10^{6}	2.2336×10^{5}	3.6262×10^{5}
4 000	2.8307×10^{5}	2.7514×10^{5}	1.7911×10^{6}	3.1356×10^{5}	5.0857×10^{5}
5 000	5.0816×10^{5}	4.8771×10^{5}	3.2170×10^{6}	5.6350×10^{5}	9.1272×10^{5}
6 000	8.2839×10^{5}	7.9348×10^{5}	5.2462×10^{6}	9.1924×10^{5}	1.4877×10^{6}
7 000	1.2552×10^{6}	1.2114×10^{6}	7.9504×10^{6}	1.3933×10^{6}	2.2539×10^{6}
8 000	1.7961×10^{6}	1.7609×10^{6}	1.1377×10^{7}	1.9938×10^{6}	3.2250×10^{6}
9 000	2.4545×10^{6}	2.4616×10^{6}	1.5545×10^{7}	2.7238×10^{6}	4.4070×10^{6}
10 000	3.2293×10^{6}		2.0446×10^{7}	3.5818×10^{6}	5.7981×10^{6}

3.4 Summary

The finalised states file for $^{27}Al^{16}O$ consists of 94 862 energy levels, comprising of 1 effective Hamiltonian level, 6 484 MARVELised levels, 16 861 predicted shift levels and 71 516 calculated DUO levels. 73% of the MARVELised levels have an uncertainty lower than 10^{-2} cm^{-1}. The three isotopologues $^{26}Al^{16}O$, $^{27}Al^{17}O$, $^{27}Al^{18}O$ have had no additional levels added to their states files and hence remain the same sizes (93 350, 96 350 and 98 269 levels respectively) each now comprising over 16 000 pseudo-experimentally corrected entries.

Beyond the applications of the updated line lists to stellar and exoplanet atmospheric studies, the updated line lists can be used in conjunction with high-resolution spectroscopy as a temperature probe. Near band heads, such as that of the prominent B $^2\Sigma^+$–X $^2\Sigma^+$ (0–0) band shown in Fig. 3.7, the spacings between consecutive-J lines decrease until they appear to double back on themselves, meaning high and low J transitions of the same branch can appear in close proximity to one another. These rotational transitions can be used to probe the rotational temperature through comparison between the relative intensities of these lines, utilising the temperature sensitive Boltzmann distribution of the involved levels' populations. This technique has been applied to observed spectra of CO (Jones et al., 2005) and H_2O (Viti et al., 2008) and would be best utilised for AlO on telescopes with good coverage

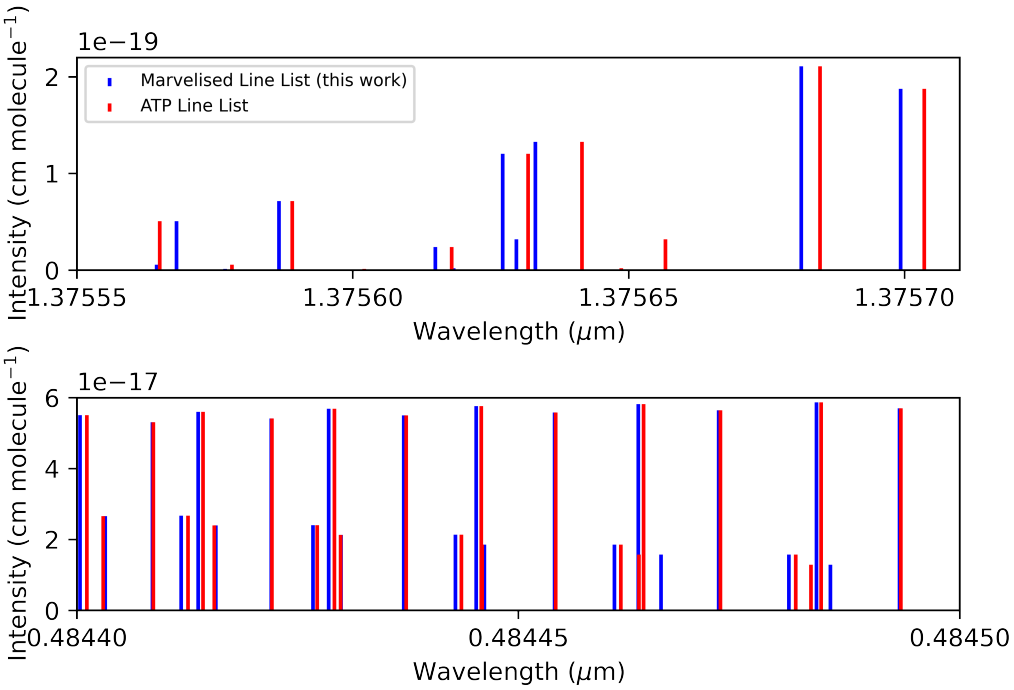


Fig. 3.4: Absorption stick spectra from the ATP (Patrascu et al., 2015) and MARVELised line lists for $^{27}Al^{16}O$, calculated at 2 000 K using the program ExoCross (Yurchenko et al., 2018). The top panel is taken from near to peak of the A $^2\Pi_i$–X $^2\Sigma^+$ band and the bottom from near the peak of the B $^2\Sigma^+$–X $^2\Sigma^+$ band.

of the visible region where the B $^2\Sigma^+$–X $^2\Sigma^+$ feature is present. Indeed, the data presented here was used for temperature calibration in shock tube experiments after its publication (Abraham et al., 2023).

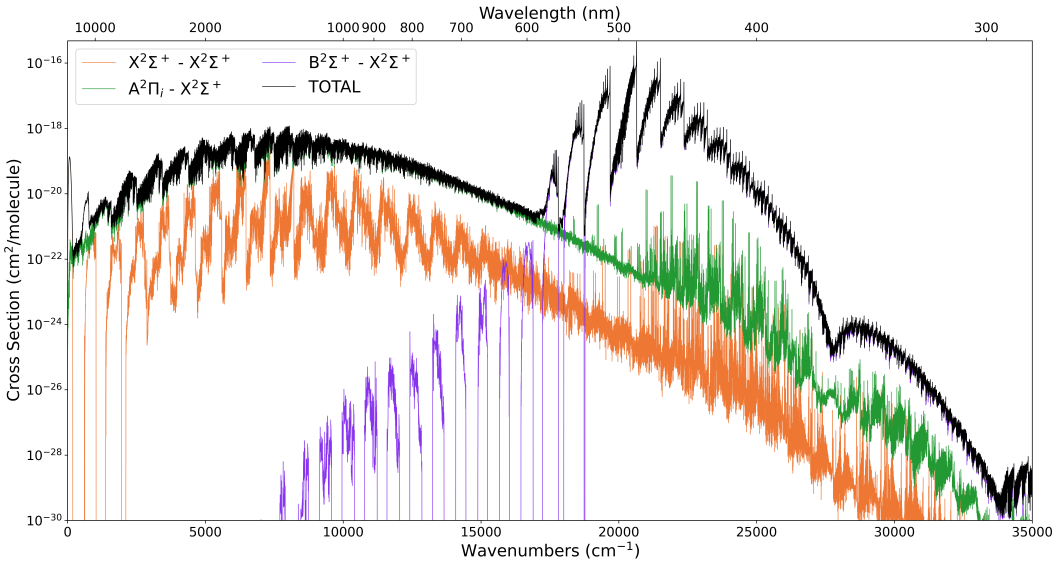


Fig. 3.5: Decomposition of the $^{27}Al^{16}O$ absorption spectra at 2 000 K, computed from the MARVELised line list using the code ExoCross (Yurchenko et al., 2018), showing the individual contributions from the $X\,^2\Sigma^+$–$X\,^2\Sigma^+$, $A\,^2\Pi_i$–$X\,^2\Sigma^+$ and $B\,^2\Sigma^+$–$X\,^2\Sigma^+$ bands. The spectra were generated using Gaussian line profiles with HWHM of 1.0 cm^{-1}.

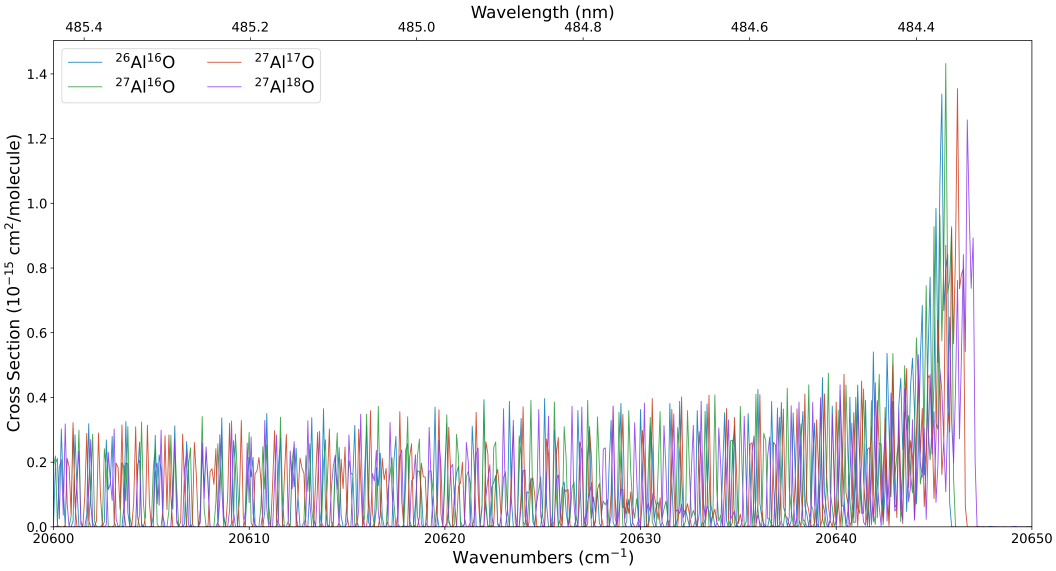


Fig. 3.6: $B\,^2\Sigma^+$–$X\,^2\Sigma^+$ (0,0) band head in the absorption spectra of the four isotopologues considered here, $^{27}Al^{16}O$, $^{26}Al^{16}O$, $^{27}Al^{17}O$ and $^{27}Al^{18}O$, all at unit abundance. The spectra were computed at 2 000 K from the updated line lists using the program ExoCross (Yurchenko et al., 2018) and have Doppler broadened line profiles, showing how the variation in atomic masses lead to subtle shifts in the individual lines and overall band positions.

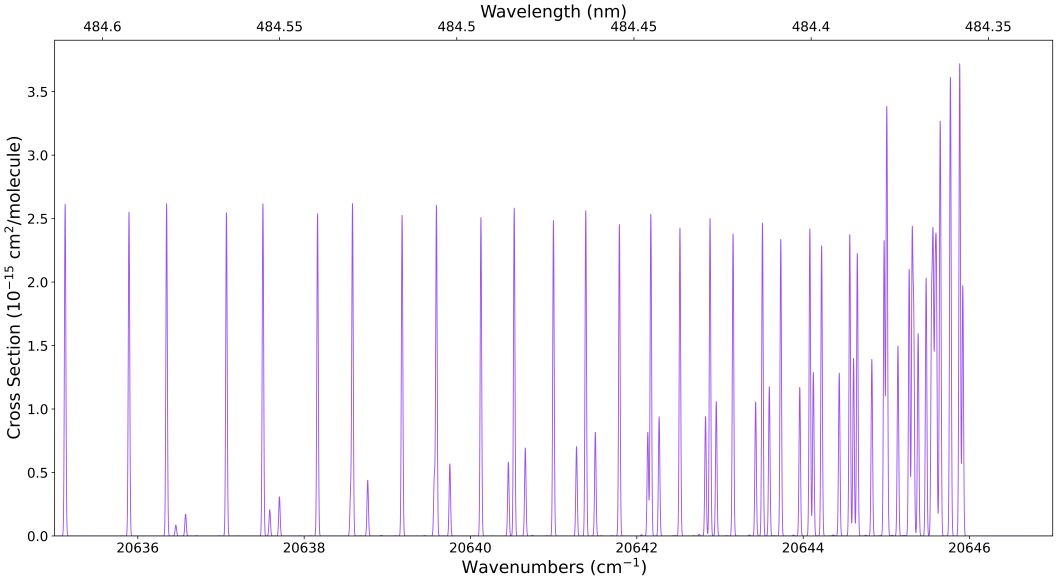


Fig. 3.7: A closeup of the B $^2\Sigma^+$–X $^2\Sigma^+$ (0-0) band head, computed at 2 000 K from the newly MARVELised line list using the code ExoCross (Yurchenko et al., 2018). The spectrum was computed using Gaussian line profiles with HWHM of 0.01 cm^{-1} to clearly distinguish the individual line profiles.

3.A AlO Marvel data

Table 3.5: Components of the AlO Marvel network. The network is broken down by the vibronic bands within each data source. For each band, the transition energy and total angular momentum J ranges are provided, along with the mean and maximum uncertainties for these transitions. The total number of transitions validated and accessed by Marvel (V/A) are also provided.

Band	Vib.	J range	V/A	Energy range (cm^{-1})	Unc. Mean/Max (cm^{-1})
69McIn (Mcdonald and Innes, 1969)					
D $^2\Sigma^+$ - A $^2\Pi_{1/2}$	0 - 0	9.5 - 46.5	64/64	34841 - 34923	0.300/0.300
D $^2\Sigma^+$ - A $^2\Pi_{3/2}$	0 - 0	9.5 - 45.5	78/78	34950 - 35033	0.300/0.300
E $^2\Delta_{3/2}$ - A $^2\Pi_{1/2}$	0 - 0	11.5 - 35.5	68/110	39909 - 39985	0.300/0.300
E $^2\Delta_{5/2}$ - A $^2\Pi_{3/2}$	0 - 0	11.5 - 36.5	107/124	39896 - 39980	0.300/0.300
73Singh (Singh, 1973)					
F $^2\Sigma^+$ - A $^2\Pi_{1/2}$	0 - 0	16.5 - 49.5	68/72	41743 - 41863	0.100/0.100
F $^2\Sigma^+$ - A $^2\Pi_{3/2}$	0 - 0	14.5 - 56.5	79/89	41850 - 41972	0.100/0.100
81SiSa (Singh and Saksena, 1981)					
E $^2\Delta_{3/2}$ - A $^2\Pi_{1/2}$	0 - 0	8.5 - 67.5	236/262	39701 - 39985	0.182/0.250
E $^2\Delta_{3/2}$ - A $^2\Pi_{1/2}$	0 - 1	17.5 - 65.5	188/214	39051 - 39265	0.191/0.250
E $^2\Delta_{5/2}$ - A $^2\Pi_{3/2}$	0 - 0	7.5 - 60.5	240/288	39754 - 39982	0.179/0.250
E $^2\Delta_{5/2}$ - A $^2\Pi_{3/2}$	0 - 1	8.5 - 60.5	249/278	39051 - 39263	0.177/0.250
82SiSa (Singh and Saksena, 1982)					
C $^2\Pi_{1/2}$ - A $^2\Pi_{1/2}$	0 - 1	3.5 - 41.5	96/123	26940 - 27091	0.108/0.250
C $^2\Pi_{1/2}$ - A $^2\Pi_{1/2}$	1 - 0	5.5 - 68.5	209/226	28514 - 28859	0.091/0.250
C $^2\Pi_{3/2}$ - A $^2\Pi_{3/2}$	0 - 1	3.5 - 29.5	62/69	27142 - 27235	0.108/0.250
C $^2\Pi_{3/2}$ - A $^2\Pi_{3/2}$	1 - 0	6.5 - 56.5	170/182	28712 - 28959	0.092/0.250
89ToHe (Torring and Herrmann, 1989)					
X $^2\Sigma^+$ - X $^2\Sigma^+$	0 - 0	0.5 - 2.5	2/2	2.5537 - 2.5539	0.050/0.050
90YaCoFuHi (Yamada et al., 1990)					
X $^2\Sigma^+$ - X $^2\Sigma^+$	0 - 0	0.5 - 10.5	14/14	2.5535 - 12.7659	1.17×10^{-5}/1.17×10^{-5}
94GoTaYaIt (Goto et al., 1994)					
X $^2\Sigma^+$ - X $^2\Sigma^+$	1 - 1	3.5 - 10.5	10/10	6.3262 - 12.6495	9.70×10^{-6}/9.70×10^{-6}
X $^2\Sigma^+$ - X $^2\Sigma^+$	2 - 2	3.5 - 10.5	10/10	6.2678 - 12.5321	9.00×10^{-6}/9.00×10^{-6}
94ToJaBoSi (Towle et al., 1994)					
C $^2\Pi_{1/2}$ - X $^2\Sigma^+$	0 - 0	0.5 - 17.5	47/59	32986 - 33030	0.007/0.031
C $^2\Pi_{3/2}$ - X $^2\Sigma^+$	0 - 0	1.5 - 11.5	27/31	33062 - 33100	0.010/0.048
11LaBe (Launila and Berg, 2011)					
X $^2\Sigma^+$ - X $^2\Sigma^+$	7 - 0	58.5 - 72.5	36/36	6125 - 6390	0.011/0.021
X $^2\Sigma^+$ - X $^2\Sigma^+$	8 - 0	9.5 - 50.5	53/53	7126 - 7343	0.011/0.029
A $^2\Pi_{1/2}$ - X $^2\Sigma^+$	0 - 0	1.5 - 88.5	522/523	4500 - 5352	0.012/0.046
A $^2\Pi_{1/2}$ - X $^2\Sigma^+$	0 - 1	0.5 - 79.5	546/546	3791 - 4388	0.011/0.041
A $^2\Pi_{1/2}$ - X $^2\Sigma^+$	0 - 2	24.5 - 52.5	44/44	3153 - 3357	0.012/0.030
A $^2\Pi_{1/2}$ - X $^2\Sigma^+$	1 - 0	0.5 - 101.5	651/656	4825 - 6074	0.012/0.047
A $^2\Pi_{1/2}$ - X $^2\Sigma^+$	1 - 1	1.5 - 93.5	612/612	4068 - 5109	0.011/0.039
A $^2\Pi_{1/2}$ - X $^2\Sigma^+$	1 - 2	18.5 - 48.5	34/34	3901 - 4104	0.012/0.036
A $^2\Pi_{1/2}$ - X $^2\Sigma^+$	2 - 0	2.5 - 112.5	725/728	5291 - 6785	0.011/0.047
A $^2\Pi_{1/2}$ - X $^2\Sigma^+$	2 - 1	6.5 - 112.5	500/500	4400 - 5819	0.011/0.035
A $^2\Pi_{1/2}$ - X $^2\Sigma^+$	2 - 2	5.5 - 47.5	33/33	4613 - 4854	0.014/0.034
A $^2\Pi_{1/2}$ - X $^2\Sigma^+$	2 - 3	12.5 - 36.5	33/33	3781 - 3900	0.012/0.038
A $^2\Pi_{1/2}$ - X $^2\Sigma^+$	3 - 0	2.5 - 114.5	709/709	5876 - 7489	0.011/0.045
A $^2\Pi_{1/2}$ - X $^2\Sigma^+$	3 - 2	8.5 - 101.5	339/342	4419 - 5562	0.012/0.043
A $^2\Pi_{1/2}$ - X $^2\Sigma^+$	3 - 3	33.5 - 45.5	9/9	4412 - 4496	0.013/0.024
A $^2\Pi_{1/2}$ - X $^2\Sigma^+$	4 - 0	6.5 - 112.5	597/597	6455 - 8161	0.011/0.046

Table 3.5 - continued

Band	Vib.	J range	V/A	Energy range (cm^{-1})	Unc. Mean/Max (cm^{-1})
11LaBe (Launila and Berg, 2011) continued					
A $^2\Pi_{1/2}$ - X $^2\Sigma^+$	4 - 1	21.5 - 68.5	127/127	6624 - 7156	0.011/0.027
A $^2\Pi_{1/2}$ - X $^2\Sigma^+$	4 - 2	12.5 - 97.5	340/340	5153 - 6235	0.013/0.047
A $^2\Pi_{1/2}$ - X $^2\Sigma^+$	5 - 0	1.5 - 91.5	454/454	7683 - 8856	0.012/0.047
A $^2\Pi_{1/2}$ - X $^2\Sigma^+$	5 - 1	6.5 - 91.5	414/414	6831 - 7887	0.011/0.040
A $^2\Pi_{1/2}$ - X $^2\Sigma^+$	5 - 2	19.5 - 38.5	9/9	6713 - 6856	0.012/0.024
A $^2\Pi_{1/2}$ - X $^2\Sigma^+$	5 - 3	17.5 - 86.5	101/101	5141 - 5956	0.012/0.046
A $^2\Pi_{1/2}$ - X $^2\Sigma^+$	6 - 0	4.5 - 111.5	327/327	7941 - 9535	0.012/0.041
A $^2\Pi_{1/2}$ - X $^2\Sigma^+$	6 - 1	10.5 - 88.5	378/378	7623 - 8559	0.011/0.044
A $^2\Pi_{1/2}$ - X $^2\Sigma^+$	6 - 3	6.5 - 75.5	124/125	5993 - 6670	0.012/0.046
A $^2\Pi_{1/2}$ - X $^2\Sigma^+$	7 - 1	8.5 - 119.5	262/262	7416 - 9233	0.011/0.037
A $^2\Pi_{1/2}$ - X $^2\Sigma^+$	7 - 3	31.5 - 53.5	15/15	6983 - 7208	0.011/0.031
A $^2\Pi_{1/2}$ - X $^2\Sigma^+$	8 - 1	10.5 - 78.5	88/88	8998 - 9889	0.010/0.010
A $^2\Pi_{1/2}$ - X $^2\Sigma^+$	9 - 2	36.5 - 83.5	131/131	8540 - 9435	0.012/0.049
A $^2\Pi_{1/2}$ - X $^2\Sigma^+$	10 - 2	41.5 - 98.5	46/46	8843 - 9968	0.010/0.010
A $^2\Pi_{3/2}$ - X $^2\Sigma^+$	0 - 0	3.5 - 80.5	450/452	4489 - 5224	0.012/0.041
A $^2\Pi_{3/2}$ - X $^2\Sigma^+$	0 - 1	1.5 - 77.5	470/470	3786 - 4259	0.010/0.050
A $^2\Pi_{3/2}$ - X $^2\Sigma^+$	0 - 2	14.5 - 35.5	37/37	3200 - 3286	0.011/0.025
A $^2\Pi_{3/2}$ - X $^2\Sigma^+$	1 - 0	2.5 - 110.5	719/723	4524 - 5944	0.012/0.047
A $^2\Pi_{3/2}$ - X $^2\Sigma^+$	1 - 1	3.5 - 93.5	565/565	4002 - 4979	0.011/0.044
A $^2\Pi_{3/2}$ - X $^2\Sigma^+$	1 - 2	41.5 - 50.5	12/12	3794 - 3864	0.014/0.035
A $^2\Pi_{3/2}$ - X $^2\Sigma^+$	2 - 0	1.5 - 107.5	721/723	5253 - 6656	0.011/0.047
A $^2\Pi_{3/2}$ - X $^2\Sigma^+$	2 - 1	5.5 - 100.5	512/512	4620 - 5690	0.011/0.049
A $^2\Pi_{3/2}$ - X $^2\Sigma^+$	2 - 2	23.5 - 33.5	11/11	4633 - 4687	0.013/0.024
A $^2\Pi_{3/2}$ - X $^2\Sigma^+$	3 - 0	3.5 - 104.5	651/653	5977 - 7358	0.011/0.047
A $^2\Pi_{3/2}$ - X $^2\Sigma^+$	3 - 2	7.5 - 84.5	326/328	4667 - 5423	0.012/0.049
A $^2\Pi_{3/2}$ - X $^2\Sigma^+$	4 - 0	1.5 - 115.5	702/702	6338 - 8052	0.011/0.048
A $^2\Pi_{3/2}$ - X $^2\Sigma^+$	4 - 1	19.5 - 74.5	115/115	6451 - 7040	0.011/0.034
A $^2\Pi_{3/2}$ - X $^2\Sigma^+$	4 - 2	2.5 - 85.5	375/377	5251 - 6126	0.012/0.046
A $^2\Pi_{3/2}$ - X $^2\Sigma^+$	5 - 0	4.5 - 111.5	478/478	7158 - 8736	0.011/0.043
A $^2\Pi_{3/2}$ - X $^2\Sigma^+$	5 - 1	5.5 - 79.5	339/339	6937 - 7764	0.011/0.034
A $^2\Pi_{3/2}$ - X $^2\Sigma^+$	5 - 3	14.5 - 72.5	72/73	5318 - 5858	0.011/0.030
A $^2\Pi_{3/2}$ - X $^2\Sigma^+$	6 - 0	3.5 - 103.5	318/318	8005 - 9413	0.012/0.046
A $^2\Pi_{3/2}$ - X $^2\Sigma^+$	6 - 1	7.5 - 99.5	327/327	7206 - 8435	0.011/0.050
A $^2\Pi_{3/2}$ - X $^2\Sigma^+$	6 - 3	10.5 - 61.5	150/150	6077 - 6544	0.011/0.048
A $^2\Pi_{3/2}$ - X $^2\Sigma^+$	7 - 0	43.5 - 83.5	30/30	9137 - 9833	0.010/0.012
A $^2\Pi_{3/2}$ - X $^2\Sigma^+$	7 - 1	4.5 - 104.5	313/313	7692 - 9109	0.011/0.037
A $^2\Pi_{3/2}$ - X $^2\Sigma^+$	8 - 1	15.5 - 95.5	176/176	8662 - 9737	0.014/0.041
A $^2\Pi_{3/2}$ - X $^2\Sigma^+$	8 - 2	32.5 - 84.5	47/47	7908 - 8685	0.016/0.038
A $^2\Pi_{3/2}$ - X $^2\Sigma^+$	9 - 1	51.5 - 77.5	40/40	9595 - 10051	0.013/0.039
A $^2\Pi_{3/2}$ - X $^2\Sigma^+$	9 - 2	27.5 - 86.5	58/58	8480 - 9372	0.012/0.033
A $^2\Pi_{3/2}$ - X $^2\Sigma^+$	10 - 2	33.5 - 78.5	41/41	9273 - 9961	0.010/0.010
B $^2\Sigma^+$ - X $^2\Sigma^+$	0 - 0	0.5 - 104.5	344/350	20109 - 20645	0.023/0.050
B $^2\Sigma^+$ - X $^2\Sigma^+$	0 - 1	1.5 - 78.5	222/227	19380 - 19682	0.023/0.042
B $^2\Sigma^+$ - X $^2\Sigma^+$	0 - 2	2.5 - 49.5	69/164	18602 - 18732	0.027/0.047
B $^2\Sigma^+$ - X $^2\Sigma^+$	1 - 0	1.5 - 86.5	245/265	21089 - 21507	0.024/0.047
B $^2\Sigma^+$ - X $^2\Sigma^+$	1 - 1	0.5 - 90.5	244/261	20129 - 20543	0.023/0.050
B $^2\Sigma^+$ - X $^2\Sigma^+$	1 - 2	1.5 - 87.5	116/253	19291 - 19593	0.027/0.050
B $^2\Sigma^+$ - X $^2\Sigma^+$	1 - 3	0.5 - 67.5	41/184	18591 - 18655	0.026/0.049
B $^2\Sigma^+$ - X $^2\Sigma^+$	2 - 0	12.5 - 55.5	99/143	22149 - 22361	0.026/0.047
B $^2\Sigma^+$ - X $^2\Sigma^+$	2 - 1	0.5 - 87.5	187/252	20973 - 21398	0.024/0.050
B $^2\Sigma^+$ - X $^2\Sigma^+$	2 - 2	3.5 - 82.5	155/208	20111 - 20448	0.026/0.049

Table 3.5 - continued

Band	Vib.	*J* range	V/A	Energy range (cm^{-1})	Unc. Mean/Max (cm^{-1})
11LaBe (Launila and Berg, 2011) continued					
B $^2\Sigma^+$ - X $^2\Sigma^+$	2 - 3	0.5 - 86.5	58/216	19183 - 19512	0.025/0.048
B $^2\Sigma^+$ - X $^2\Sigma^+$	2 - 4	0.5 - 75.5	173/196	18364 - 18592	0.024/0.044
B $^2\Sigma^+$ - X $^2\Sigma^+$	3 - 1	2.5 - 56.5	122/187	22024 - 22245	0.028/0.048
B $^2\Sigma^+$ - X $^2\Sigma^+$	3 - 2	1.5 - 78.5	206/218	20959 - 21293	0.024/0.050
B $^2\Sigma^+$ - X $^2\Sigma^+$	3 - 4	2.5 - 91.5	201/210	19170 - 19438	0.023/0.049
B $^2\Sigma^+$ - X $^2\Sigma^+$	3 - 5	1.5 - 66.5	137/148	18357 - 18533	0.023/0.036
B $^2\Sigma^+$ - X $^2\Sigma^+$	4 - 2	2.5 - 62.5	153/189	21887 - 22134	0.024/0.048
B $^2\Sigma^+$ - X $^2\Sigma^+$	4 - 3	4.5 - 78.5	89/210	20872 - 21198	0.025/0.049
B $^2\Sigma^+$ - X $^2\Sigma^+$	4 - 5	1.5 - 67.5	175/186	19183 - 19371	0.023/0.045
B $^2\Sigma^+$ - X $^2\Sigma^+$	4 - 6	5.5 - 58.5	109/112	18333 - 18479	0.023/0.048
B $^2\Sigma^+$ - X $^2\Sigma^+$	5 - 3	1.5 - 67.5	79/185	21778 - 22030	0.026/0.049
B $^2\Sigma^+$ - X $^2\Sigma^+$	5 - 4	8.5 - 72.5	161/186	20851 - 21108	0.024/0.049
B $^2\Sigma^+$ - X $^2\Sigma^+$	5 - 6	7.5 - 61.5	99/112	19141 - 19305	0.022/0.046
B $^2\Sigma^+$ - X $^2\Sigma^+$	5 - 7	5.5 - 44.5	78/78	18332 - 18432	0.022/0.035
B $^2\Sigma^+$ - X $^2\Sigma^+$	6 - 4	8.5 - 66.5	150/155	21731 - 21935	0.023/0.049
B $^2\Sigma^+$ - X $^2\Sigma^+$	6 - 5	9.5 - 70.5	112/113	20827 - 21025	0.024/0.049
B $^2\Sigma^+$ - X $^2\Sigma^+$	6 - 7	3.5 - 48.5	67/67	19141 - 19234	0.023/0.043
B $^2\Sigma^+$ - X $^2\Sigma^+$	7 - 5	6.5 - 63.5	123/127	21613 - 21842	0.023/0.048
B $^2\Sigma^+$ - X $^2\Sigma^+$	7 - 6	3.5 - 50.5	64/66	20825 - 20951	0.023/0.048
B $^2\Sigma^+$ - X $^2\Sigma^+$	8 - 6	23.5 - 47.5	50/50	21631 - 21756	0.022/0.026
PGOPHER_11LaBe (Launila and Berg, 2011)					
X $^2\Sigma^+$ - X $^2\Sigma^+$	0 - 0	0.5 - 1.5	1/1	1.2778 - 1.2778	1.00×10^{-6}/1.00×10^{-6}
X $^2\Sigma^+$ - X $^2\Sigma^+$	3 - 3	2.5 - 2.5	1/1	3.7361 - 3.7361	0.020/0.020
X $^2\Sigma^+$ - X $^2\Sigma^+$	4 - 4	1.5 - 2.5	2/2	2.4752 - 3.6942	0.020/0.020
X $^2\Sigma^+$ - X $^2\Sigma^+$	6 - 6	4.5 - 5.5	1/1	6.0201 - 6.0201	0.020/0.020
X $^2\Sigma^+$ - X $^2\Sigma^+$	7 - 7	6.5 - 8.5	2/2	9.5555 - 10.7476	0.020/0.020

Chapter 4

H_3^+ and its deuterated isotopologues

4.1 Overview

H_3^+ is known to form rapidly in H_2 gas following an ionisation event via the strongly exothermic reaction

$$H_2 + H_2^+ \longrightarrow H_3^+ + H \tag{4.1}$$

which occurs at essentially every collision. As H_2 is common in a variety of astronomical bodies, H_3^+ is often the dominant molecular ion. The first 30 years of H_3^+ astronomy has been comprehensively reviewed by Miller et al. (2020). H_3^+ formation is stimulated by cosmic ray ionisation of the interstellar medium and by collisions with fast electrons and other charged particles in planetary ionospheres. H_3^+ is also believed to form in the ionosphere of planets through the ionisation of H_2 by extreme ultraviolet radiation (Chadney et al., 2016). In gas giant ionospheres, H_3^+ acts as a coolant through efficient infrared (IR) emissions (Miller et al., 2000, 2010); indeed, it is thought that H_3^+ emissions are key to determining the stability limits in hot Jupiter exoplanets (Koskinen et al., 2007).

The infrared spectrum of H_3^+ has been extensively observed in giant planets in our solar system such as Jupiter (Drossart et al., 1989; Ballester et al., 1994; Miller et al., 1997; Rego et al., 2000; Moore et al., 2017), Saturn (Geballe et al., 1993; Stallard et al., 2008b,a), Uranus (Trafton et al., 1993; Lam et al., 1997; Trafton et al., 1999; Melin et al., 2019; Thomas et al., 2023) and is believed to be present in Neptune (Melin et al., 2011, 2018) although it is yet to be detected there. Its presence can be used as an effective temperature probe here and in other astrophysical settings (Gibbs and Fitzgerald, 2022). H_3^+ is similarly expected to be of importance in extrasolar giant planets (Chadney et al., 2016; Khodachenko et al., 2015), such as hot Jupiters (Lenz et al., 2016), and an even more prominent feature in the aurorae of brown dwarfs (Gibbs and Fitzgerald, 2022); however, it has so far defied observation on these objects.

H_3^+ has also been observed in the interstellar medium (ISM) via absorption in the infrared light of a background star (McCall et al., 1999; Goto et al., 2002; McCall et al., 2002; Goto et al., 2003; Oka et al., 2005; Oka, 2006; Goto et al., 2008), pre-stellar core (Goto et al., 2019) or galactic centre (Geballe et al., 1999, 2006) where it forms through cosmic ray ionisation (Geballe and Oka, 1996). Hence it is also used in this setting to trace the cosmic ray ionisation rate (Indriolo and McCall, 2012; Harju et al., 2017) and similarly primarily relies on IR emissions. These IR

bands lie well within the wavelength range of the instruments onboard the JWST.

In regions where the precursors to H_3^+ exist in deuterated forms, namely HD and D_2, equivalent reactions occur to that described in Eq. (4.1) resulting in the formation of the deuterated isotopologues H_2D^+, D_2H^+ and D_3^+ (Roberts et al., 2003; Merkt et al., 2022). At low temperatures fractionation drives the preferential formation of isotopically substituted H_3^+ (Hewitt et al., 2005); indeed, models by Walmsley et al. (2004) suggest that in certain very cold regions D_3^+ may be the dominant isotopologue of H_3^+! Spectra of H_2D^+ (Stark et al., 1999; Caselli et al., 2003) and D_2H^+ (Vastel et al., 2004) have been observed in interstellar space through pure rotational transitions which lie in the far infrared / THZ region. However, D_3^+ remains undetected, at least in part because its higher symmetry means that, like H_3^+, its pure rotational spectrum is very weak. Elsewhere, free electrons and H^- ions provided by the reactions of H_3^+ have been shown to play an important role in the atmospheres of cool white dwarfs (Saumon et al., 1994; Bergeron et al., 1997; Harris et al., 2004).

Line lists for H_3^+ (Kao et al., 1991; Neale et al., 1996) and the associated partition function (Neale and Tennyson, 1995; Ramanlal and Tennyson, 2004) have played a key role in the astronomical study of this important molecular ion. In this chapter the updates to the MiZATeP H_3^+ line list of Mizus et al. (2017) and the older ST H_2D^+ line list of Sochi and Tennyson (2010) are described, adapted from their initial publication in Bowesman et al. (2023). This was done using updated versions of the MARVEL networks produced by the work of Furtenbacher et al. (2013b) and Furtenbacher et al. (2013a). New line lists for D_2H^+ and D_3^+ are presented, for which empirical energy levels are also used to improve the accuracy of the transition frequencies between key levels.

4.2 Method

The triatomic discrete variable representation (DVR) nuclear motion code DVR3D (Tennyson et al., 2004) has been used in the preparation of the line lists presented here to compute initial energy levels for H_3^+ and its deuterated isotopologues, as well as Einstein A-coefficients for each transition. This code, which is based on the use of an exact nuclear motion kinetic energy operator, has been shown to be capable of giving highly accurate results for the H_3^+ system (Polyansky and Tennyson, 1999; Pavanello et al., 2012b). It is important to note that in the absence of any absolute measurements of transition intensities for the H_3^+ system, all models rely on computed values which are thought to be accurate (Farnik et al., 2002; Petrignani et al., 2014). It should be noted that DVR3D only provides assignments for the rigorous quantum numbers: J, rotationless parity e/f and the interchange symmetry for two identical atoms. This means that most states in the existing version of the MiZATeP H_3^+ (Mizus et al., 2017) and ST H_2D^+ (Sochi and Tennyson, 2010) line lists do not have full ro-vibrational assignments. This issue is partially addressed in this chapter.

MARVEL spectroscopic networks were constructed for H_3^+, H_2D^+ and D_2H^+ using available laboratory spectra in order to obtain empirical energy levels for each species. These empirical energy levels were then used to improve the calculated line lists, correcting for obs.-calc. shifts in levels where empirical energy levels were

available for comparison. All of the MARVEL networks discusses in this chapter were produced using MARVEL version 4.1 and the MARVEL input and energies files are available as part of the supplementary material of Bowesman et al. (2023).

4.3 MARVELised data sources

Spectroscopic networks have been constructed in the past for the molecules H_3^+ (Furtenbacher et al., 2013b), H_2D^+ and D_2H^+ (Furtenbacher et al., 2013a) but new transition data has since been published. These new data allow us to expand the level coverage of the networks and, in the case of new data that remeasures existing transitions, to improve the accuracy to which term energies are known. Recent high-resolution experiments have provided new THz transition data with uncertainties on the order of MHz or kHz, well within the part-per-billion regime. When all of the transitions that determine a level's term energy are consistent within their experimental uncertainties, the uncertainty on the final term energy will generally be on the same order as the smallest uncertainty of the transitions that define the level. In cases where the transitions are consistent and agree on the final term energy with a variation much smaller than the input transition uncertainties, the uncertainty on the final term energy will can be smaller than that of the input transitions. Given many of these new, kHz-accuracy transitions already have very small uncertainties, they are sensitive to tiny variances in the final term energies and hence the final uncertainties are rarely much smaller than the input uncertainties. These high-accuracy transition measurements are, regardless, more accurate than the existing transition data set and with their addition the accuracy of the final energies can be significantly improved, in some cases by a few orders of magnitude.

The MARVEL procedure requires all transitions within a network to be identified by the same set of quantum numbers. For this purpose, H_3^+ and its deuterated isotopologues can be divided into two groups: H_3^+ and D_3^+ are symmetric tops belonging to the D_{3h}(M) molecular symmetry group and H_2D^+ and D_2H^+ are asymmetric tops belonging to the C_{2v}(M) group. These groupings in turn dictate the set of good quantum numbers used to define the levels of the networks.

As symmetric tops, the molecules H_3^+ and D_3^+ are defined by two primary vibrational modes, symmetric stretching (ν_1) and bending (ν_2). The bending mode is degenerate however, and as such these species are also described by the vibrational angular momentum quantum number $l_2 = \nu_2, \nu_2 - 2, \ldots, -\nu_2 + 2, -\nu_2$. The energy levels of these species are identified instead by $L_2 = |l_2|$ in this work, as the assignment of the sign of l_2 can be very difficult. The rigorous rotational angular momentum quantum number J is used to define the rotational levels of these molecules. The projection of J along the molecular symmetry axis, k can be used to determine the parity of the energy levels, such that the total parity is the sign of $(-1)^k$ (Furtenbacher et al., 2013b). The quantum number k does not offer a complete description of the system however, due to Coriolis coupling between it and l_2. As such, the value $G = |g|$ is used, where $g = k - l_2$ (Hougen, 1962). This quantum number is important because, as members of the D_{3h}(M) symmetry group, the A_1', A_1'', A_2', A_2'' rovibronic symmetries only occur for these molecules when $G = 3n$, where n is an integer. In H_3^+ the A_1' and A_1'' symmetries do not exist however, as they are

Table 4.1: The rovibronic symmetries of the isotopologues of H_3^+ where g_{ns} is the nuclear spin statistical weight. For H_3^+ and D_3^+, Γ_{rve} are representations of the D_{3h} point group while for H_2D^+ and D_2H^+ they are for C_{2v}.

Γ_{rve}	Isomer	g_{ns}	Isomer	g_{ns}
	H_3^+		D_3^+	
A_1', A_1''	-	0	ortho	10
A_2', A_2''	ortho	4	para	1
E', E''	para	2	meta	8
	H_2D^+		D_2H^+	
A_1, A_2	para	3	ortho	12
B_1, B_2	ortho	9	para	6

determined to have 0 nuclear spin statistical weight (Watson, 1984). This difference arises from the nuclear spin I of the constituent atoms, which is $I = \frac{1}{2}$ for hydrogen and $I = 1$ for deuterium. Consequently H_3^+ consists of two nuclear spin isomers while D_3^+ has three (Watson et al., 1987); these are shown in Table 4.1.

Levels with equivalent vibrational, J and G assignments are differentiated by the $(u|l|m)$ U-notation of Watson (1994). u and l are used to identify the upper and lower energy levels of the same assignment, differing in their value of $K = |k|$, and m is used when such a distinction is irrelevant as only one value of K can exist that produces the same G. As such, the energy levels of the species H_3^+ and D_3^+ are identified by the quantum number set $(\nu_1, \nu_2, L_2, J, G, U, K, \Gamma_{rve})$.

As asymmetric tops, H_2D^+ and D_2H^+ are defined by the symmetric stretching, bending and anti-symmetric stretching vibrational quantum numbers ν_1, ν_2 and ν_3. The quantum number J and its projections onto the C_2 axis and the axis perpendicular to the C_2 axis in the plane of the molecule, K_a and K_c, are the standard ones for labelling the rotational states of an asymmetric top.

For both asymmetric tops, the total parity is the sign of $(-1)^{K_c}$. A similar expression is used to identify the nuclear spin isomers of each asymmetric top, such that they are labelled ortho when it is positive and para when negative. For H_2D^+ this expression is $(-1)^{\nu_3+K_a}$ and for D_2H^+ it is $(-1)^{\nu_3+K_a+K_c}$. The ortho and para nuclear spin isomers identify the rovibronic symmetry group of the molecule, A_1, A_2, B_1 or B_2, as shown in Table 4.1. Hence, the energy levels of the species H_2D^+ and D_2H^+ are identified by the quantum number set $(\nu_1, \nu_2, \nu_3, J, K_a, K_c, \Gamma_{rve})$.

Transitions between nuclear spin isomers are forbidden, meaning networks constructed from observational transitions will be split into separate components for each isomer. Given MARVEL determines the energies of each level relative to the lowest energy level in the network, which is defined as 0, this presents a problem as any levels of a different nuclear spin isomer to that of the zero-energy level will not have their energies defined. This is avoided by the introduction of "magic" numbers; forbidden transitions were added to the networks to connect the lowest levels of each nuclear spin isomer to each other using synthetic transitions derived from calculated energies. This enables the determination of all energies for connected levels within the networks, relative to the zero-energy level. For D_3^+

this treatment was not needed as the energies were determined through the use of effective Hamiltonian calculations.

4.3.1 H_3^+ network

The MARVEL study of H_3^+ conducted by Furtenbacher et al. (2013b) combined transition data from 26 sources into a single network and served as the starting point for the new network presented here. Since then, six new sets of high-accuracy spectra have been reported (Berg et al., 2012; Hodges et al., 2013; Perry et al., 2015; Jusko et al., 2016; Guan et al., 2018; Markus and McCall, 2019) and are detailed below:

12BeWoPe (Berg et al., 2012): 3 R-branch transitions in the visible region are provided that had not been included from other sources.

13HoPeJeSi (Hodges et al., 2013): 10 R-branch transitions in the ν_2 band with MHz and sub-MHz accuracy are reported. All of these transitions had been previously reported in other sources (Oka, 1981; McKellar and Watson, 1998) but are presented here at higher accuracy.

15PeHoMaKo (Perry et al., 2015): A further 10 R-branch transitions in the ν_2 band are reported with MHz and sub-MHz accuracy. All of the transitions from this source had been observed previously (Oka, 1981; Lindsay et al., 2001; Wu et al., 2013).

16JuKoScAs (Jusko et al., 2016): 5 measurements of low-J R-branch transitions in the ν_2 band are provided, all with sub-MHz accuracy. These transitions had also been observed by Hodges et al. (2013).

18GuChLiPe (Guan et al., 2018): Transition frequencies for 12 R-branch and 4 Q-branch transitions in the ν_2 band are presented. The majority are reported with sub-MHz accuracy. All of the transitions in this source had also been observed in other experiments (Lindsay and McCall, 2001; Hodges et al., 2013; Perry et al., 2015; Jusko et al., 2016; Perry et al., 2016).

19MaMc (Markus and McCall, 2019): The largest of the new H_3^+ data sources, providing 36 measurements of transitions in the $\nu_2 \leftarrow 0$ band, 15 transitions in the $2\nu_2^2 \leftarrow \nu_2$ band and 7 transitions in the $2\nu_2^2 \leftarrow 0$ band. The data comprises a selection of P-, Q- and R-branch transitions with uncertainties of 4 MHz. All of the reported transitions had been observed in prior studies (Watson et al., 1984; Majewski et al., 1987; Bawendi et al., 1990; Xu et al., 1990; Uy et al., 1994; McKellar and Watson, 1998; Guan et al., 2018; Markus et al., 2018).

In total there were 102 new transitions to be added to the existing set of 1 610 transitions and a further 7 transitions that had been missed from old sources in the original MARVEL compilation. 7 transitions had their assignment corrected based on updated assignments provided in subsequent papers. A further 9 transitions were re-assigned based on apparent mixing identified through comparison with the empirical MARVEL energies. 2 transition assignments were updated based on suggestions provided by Jaquet (2022). Sarka and Poirier (2022) provided a series of assignments for H_3^+ which were used to correct the assignments of 41 transitions and to assign 22 previously unassigned transitions. A further three unassigned transitions from the literature were assigned based on comparison with the MARVEL energy levels. The new transition assignments are detailed in Table 4.2. The transitions updated in

Table 4.2: New transition assignments for transitions from the literature that previously had no assignment or were missing an upper state assignment. Assignments to transitions from Lindsay et al. (2001) were determined through comparison between the empirical energy levels determined by MARVEL, while transitions from Morong et al. (2009) were assigned based on assignments produced using the code SCALIT (Sarka and Poirier, 2022).

Wavenumber (cm^{-1})	v_1'	v_2'	L_2'	J'	G'	U'	K'	Γ_{rve}'	v_1''	v_2''	L_2''	J''	G''	U''	K''	Γ_{rve}''	Source
3 104.125(10)	2	0	0	6	1	m	1	E″	1	0	0	6	2	m	2	E′	Lindsay et al. (2001)
3 182.605(5)	1	2	2	5	2	u	0	E′	0	2	0	5	1	m	1	E″	Lindsay et al. (2001)
3 235.521(5)	1	2	2	7	5	u	3	E″	1	1	1	6	5	1	6	E′	Lindsay et al. (2001)
10 329.307(10)	0	4	2	7	3	u	1	A_2''	0	0	0	6	6	m	6	A_2'	Morong et al. (2009)
10 462.405(10)	0	5	1	5	6	m	5	A_2''	0	0	0	6	6	m	6	A_2'	Morong et al. (2009)
10 496.287(10)	2	2	2	6	8	m	6	E′	0	0	0	5	5	m	5	E″	Morong et al. (2009)
10 573.997(10)	0	4	4	5	0	m	4	A_2'	0	0	0	4	3	m	3	A_2''	Morong et al. (2009)
10 639.058(10)	0	5	1	5	0	m	1	A_2''	0	0	0	5	0	m	5	A_2'	Morong et al. (2009)
10 666.604(10)	0	5	1	5	3	1	4	A_2'	0	0	0	5	3	m	3	A_2''	Morong et al. (2009)
10 827.764(10)	0	6	0	3	0	m	0	A_2'	0	1	1	2	0	m	1	A_2''	Morong et al. (2009)
11 036.111(10)	0	5	1	7	6	1	7	A_2''	0	0	0	6	6	m	6	A_2'	Morong et al. (2009)
11 046.569(10)	0	5	1	6	5	1	6	E′	0	0	0	5	5	m	5	E″	Morong et al. (2009)
11 048.996(10)	0	5	1	5	4	1	5	E″	0	0	0	4	4	m	4	E′	Morong et al. (2009)
11 114.628(10)	2	2	2	6	3	u	1	A_2''	0	0	0	5	0	m	5	A_2'	Morong et al. (2009)
11 265.189(10)	1	5	3	3	0	m	3	A_2''	0	1	1	2	3	m	2	A_2'	Morong et al. (2009)
11 331.112(10)	0	5	5	5	0	m	5	A_2''	0	0	0	6	6	m	6	A_2'	Morong et al. (2009)
11 556.914(10)	0	5	3	5	3	m	0	A_2'	0	0	0	4	3	m	3	A_2''	Morong et al. (2009)
11 947.074(10)	2	3	1	5	6	m	5	A_2''	0	0	0	6	6	m	6	A_2'	Morong et al. (2009)
12 116.353(10)	0	6	0	3	3	m	3	A_2''	0	0	0	3	0	m	0	A_2'	Morong et al. (2009)
12 331.180(10)	1	4	0	5	0	m	0	A_2'	0	0	0	4	3	m	3	A_2''	Morong et al. (2009)
12 502.614(10)	0	6	2	2	0	m	2	A_2'	0	0	0	3	3	m	3	A_2''	Morong et al. (2009)
12 536.621(10)	1	4	2	4	3	m	1	A_2''	0	0	0	3	0	m	0	A_2'	Morong et al. (2009)
13 056.013(10)	0	6	2	2	3	m	1	A_2''	0	0	0	1	0	m	0	A_2'	Morong et al. (2009)
13 597.367(10)	0	6	4	1	3	m	1	A_2''	0	0	0	1	0	m	0	A_2'	Morong et al. (2009)
13 676.446(10)	0	7	1	1	0	m	1	A_2''	0	0	0	1	0	m	0	A_2'	Morong et al. (2009)

this way all involved levels with relatively high energies, in a region where accurate determination of the vibrational state can be challenging. In total, 59 transitions from the original network were reassigned and an additional 8 had their assignment corrected due to digitisation errors from their original sources. The inclusion of the new transitions and the reassignments described here allowed for the validation of 19 transitions that had previously failed validation.

The final set of 1 719 transitions were passed through MARVEL for validation, with 1 656 being validated; these transitions are summarised in Table 4.12. The network is divided into 39 components, the largest of which comprises 1 580 transitions which determine 703 empirical energy levels. Of the remaining components: two consist of 6 transitions; one of 5 transitions; two of 4 transitions; three of 3 transitions; 12 of 2 transitions and the remaining 18 of single transitions. As these minor components are not connected to the primary component the energies of the levels within them are not determined relative to the zero-energy level and are hence not considered further.

4.3.2 H_2D^+ network

A MARVEL network for H_2D^+ was originally produced by Furtenbacher et al. (2013a) and contained transition data from 13 sources. Since then, two new sets of transition measurements have been published by Jusko et al. (2016, 2017).

16JuKoScAs (Jusko et al., 2016): Transitions frequencies for 11 ν_1 band transitions are reported with MHz and sub-MHz accuracy. This source provides signifi-

cantly higher accuracy measurements of transitions previously observed by Amano (1985).

17JuToMuGh (Jusko et al., 2017): 3 pure-rotation transition measurements are provided with sub-MHz or kHz accuracy.

These two new sources and a "magic" forbidden transition to connect the nuclear spin isomers, derived from effective Hamiltonian calculations using molecular constants from Amano (2006), brought the total number of transitions for H_2D^+ to 210; these are summarised in Table 4.13. 208 transitions were validated successfully by MARVEL, yielding a final network comprising 7 components, the largest of which contained 200 transitions that determine 109 unique energy levels. For the remaining 6 components, one contained 3 transitions while the rest are single transition components; these disconnected components are not considered further here.

4.3.3 D_2H^+ network

The D_2H^+ MARVEL network was originally published by Furtenbacher et al. (2013a) and was constructed using transition data from 9 sources. Four new sets of transition data have subsequently been published (Jusko et al., 2016, 2017; Yu. et al., 2017; Markus et al., 2019) and have now been added to the existing network.

16JuKoScAs (Jusko et al., 2016): This source provides 10 transitions frequencies observed with sub-MHz accuracy. 8 of these transitions had been previously observed by Lubic and Amano (1984).

17JuToMuGh (Jusko et al., 2017): 3 ground state pure-rotation transition measurements are provided with kHz accuracy.

17YuPeAmMa (Yu. et al., 2017): This source reports 5 ground state pure-rotation transitions with sub-MHz accuracy. 4 of these transitions had not been reported in other sources, with the other also being observed by Jusko et al. (2017).

19MaKoMc (Markus et al., 2019): Transition frequencies for 37 ν_1 band transitions are provided with MHz accuracy. 10 of the transitions in this source are new and had not been reported elsewhere, while the rest had been observed by Lubic and Amano (1984); Jusko et al. (2016).

With the addition of 55 new transition measurements, the new network contains 210 transitions. Two existing transitions that had digitisation errors in their transition frequencies were updated to the correct values. A "magic" forbidden transition is included to connect the otherwise distinct ortho and para components of the network, using a frequency calculated by Yu. et al. (2017). The final set of D_2H^+ transition data is summarised in Table 4.14. All of the transitions in the network were validated by MARVEL, yielding a primary network component containing 200 transitions which define 115 unique energy levels. The rest of the transitions are present in 7 disconnected components, one of which contains 3 transitions, another 2 transitions and the remainder are single transition components.

4.4 Line list calculations

4.4.1 Updated H_3^+ and H_2D^+

While the core of the line lists were computed using DVR3D, Sarka et al. (2021); Sarka and Poirier (2022) performed calculations using the variational nuclear motion programs ScalIT (Chen and Poirier, 2006a,b, 2010a,b; Petty and Poirier, 2014), and GENIUSH (Mátyus et al., 2009; Fabri et al., 2011); these were leveraged to give full quantum number designations. The full approach applied is detailed by Sarka and Poirier (2022) but a quick summary of the main steps is provided below.

First, using Jacobi coordinates ScalIT calculations were carried out in the four blocks of the G_4 permutation-inversion (PI) symmetry group. Due to the very high convergence accuracy, the full G_{12} PI group labels (Γ_{rve}) were easily assigned unambiguously using the $\Gamma(G_{12}/D_{3h}) \downarrow G_4$ correlation table.

Next, calculations were repeated with the code GENIUSH with slightly lower accuracy, but still sufficient to match the energy levels with the ScalIT ones. After the vibrational states were labelled (v_1, v_2, L_2), vibrational parent labels were semi-automatically assigned to rovibrational states using the rigid rotor decomposition scheme (RRD) implemented in GENIUSH (Mátyus et al., 2010). The RRD overlaps of GENIUSH also help to assign the rotational quantum numbers (J, G, U, K), as the symmetric top rigid rotor functions are labelled by K. Using this method it was possible to label an additional 1 525 states in the MiZATeP H_3^+ line list with the $(v_1, v_2, L_2, J, G, U, K, \Gamma_{\text{rve}})$ quantum number set.

The energies of the existing H_3^+ and H_2D^+ line lists were updated with empirical energies where they were known. For levels with matching assignments in both the states files and corresponding Marvel network, the term energies and their uncertainties were set to the values determined by the Marvel procedure. For the levels that did not exist within the molecules' Marvel network, the calculated term energies were retained and estimates for their uncertainties were calculated as follows

$$\Delta\tilde{E} = \begin{cases} 0.1, & \text{if } \tilde{E} < 2000 \\ \lfloor \tilde{E}/2000 \rfloor / 10, & \text{otherwise.} \end{cases} \tag{4.2}$$

This differs from the uncertainty estimation given in Eq. (2.37), which is generally intended for diatomics and scales as a function of the individual level's quantum number assignment. Analysis of the known obs.-calc. values for these molecules showed that the accuracy of the potential energy surfaces decreased more as a function of energy than they did specifically J, hence this form was more appropriate here.

4.4.2 New line lists

New line lists were computed for the D_2H^+ and D_3^+ molecular ions. Both calculations used the highly accurate global *ab initio* PES, together with adiabatic and relativistic correction surfaces, computed by Pavanello et al. (2012b,a), which were also used for the MiZATeP H_3^+ line list. The high-accuracy dipole moment surface (DMS) obtained for the H_3^+ system was used (Petrignani et al., 2014) to calculate transition intensities. This DMS was obtained by fitting 7 parameters to a polynomial form written in terms of effective charges, see Röhse et al. (1994). This DMS was centred

on the centre-of-mass ensuring the correct treatment of the centre-of-charge – centre-of-mass displacement which leads to D_2H^+ (and H_2D^+) having a permanent dipole moment.

The DVR3D program suite (Tennyson et al., 2004) was used to compute the final line lists. As part of this project a new module was added to this suite which converts DVR3D results to the ExoMol format (Tennyson et al., 2013) comprising a states and trans file, and allowing spectra to be easily generated using ExoCross (Yurchenko et al., 2018). The module reads the energy levels and Einstein coefficients from DVR3D, requiring as input from the user the molecular symmetry, C_s or C_{2v}, and the nuclear statistic weight for each symmetry. The program, called LINELIST, is available as part of the DVR3D program suite from the ExoMol GitHub pages.

As with H_3^+ and H_2D^+, the calculated term energies of D_2H^+ were updated with empirical values from the new MARVEL network where available. Likewise, the unchanged calculated energies of the new D_2H^+ and D_3^+ line lists had uncertainties estimated using Eq. (4.2).

4.4.3 D_2H^+ nuclear motion calculations

DVR3D nuclear motion calculations were performed with 31, 31, and 50 grid points for two radial and one angular scattering coordinates. The calculations used Morse-like oscillators with parameters 3.1, 0.1, and 0.006 for the r_1 (D – D) radial coordinate, and spherical oscillators with parameters 0, 0, and 0.016 for the r_2 (H – D_2) scattering coordinate. The dimension of the final vibrational Hamiltonians were set to 5000. Calculations included all levels up to 15 000 cm^{-1} for $J \leq 25$. The DVR3DRJZ module was used to compute 1500 vibrational basis functions which were passed to theROTLEV3 module to perform the rotational step of the calculation. Following the specification of Polyansky and Tennyson (1999), rotational reduced masses $m_H = 1.007276$ Da and $m_D = 2.013553$ Da were used for the rotational motion and vibrational reduced masses $m_H = 1.007537$ Da and $m_D = 2.013814$ Da were used for the vibrational motion. This formulation has been shown to allow for non-adiabatic effects in the calculation, with the rotational and vibrational masses applying non-adiabatic corrections to their respective kinetic energy operators (Moss, 1996). Under this scheme, rotational reduced masses are set based on nuclear masses and vibrational reduced masses are set based on atomic masses. Corrections utilising a similar approach have been applied to calcualtions for other molecules, such as those for H_2O by Schwenke (2001). The resulting D_2H^+ MiZo line list is complete up to a temperature of 2000 K.

4.4.4 D_3^+ nuclear motion calculations

DVR3D calculations for D_3^+ were performed using the same size grids and Hamiltonians as those specified for D_2H^+ above. The calculations used Morse-like oscillators with parameters 2.6, 0.1, and 0.006 for the r_1 coordinate, and spherical oscillators with parameters 0, 0, and 0.016 for the r_2 coordinate. Nuclear masses equal to $m_D = 2.013553$ Da were used for all calculations.

The DMS of Petrignani et al. (2014) was used in the calculation of the D_3^+ transition frequencies and the final data set contains all levels below 15 500 cm^{-1} with $J \leq 15$. The new D_3^+ MiZo line list is complete up to a temperature of 800 K.

Table 4.3: Statistics for the new line lists, detailing: the maximum J value for each; the maximum temperature up to which the line list is complete; the maximum lower state energy involved in a transition; the maximum upper state energy involved in a transition; the total number of transitions and the total number of transitions between MARVELised states.

Species	J_{max}	T_{max} (K)	E_{low} (cm^{-1})	E_{high} (cm^{-1})	No. Trans	No. MARVELised Trans
H_3^+	37	5 000	25 189.709 34	42 000.743 57	127 542 657	17 147
H_2D^+	20	1 750	6 988.914 26	18 496.216 69	22 164 810	895
D_2H^+	25	2 000	8 253.939 82	34 838.528 61	2 290 235 000	905
D_3^+	15	800	2 639.965 60	17 234.642 27	36 078 183	0

Statistics for all of the line lists presented here are given in Table 4.3.

4.4.5 D_3^+ effective Hamiltonian calculations

There have been significantly fewer observations of D_3^+ spectra than of the three other isotopologues considered here. As such, there was insufficient data to build a well-connected MARVEL network to be used to refine the calculated energies. In lieu of this, effective Hamiltonian constants from Watson et al. (1987) and Amano et al. (1994) were used to calculate energies for the states in the range $J = 0 - 15$, up to a maximum energy of 2676.387 cm^{-1}. These calculations were performed using the program PGOPHER (Western, 2017) which also provides full state assignments for the levels it computes. Hence full quantum number assignments were determined via this method for 282 levels within the bands for which constants were available: 188 levels in the 000 band (ν_1, ν_2, L_2); 2 levels in the 010 band; 105 in the 011 band; 22 in the 100 band. The majority of the levels assigned through this method have $J < 10$. Further assignments were done manually for states at higher energies with the aid of the vibrational band origins published by Amano et al. (1994) and the assigned hot and overtone bands published by Alijah et al. (1995). 1045 additional states were assigned this way and a breakdown of the assigned bands is given in Table 4.4.

These assignments were added to the calculated states file, as otherwise the only assignments were the rigorous quantum numbers provided by DVR3D: J, rotationless parity e/f and the interchange symmetry of two of the D atoms.

4.4.6 States files

New states files are provided for each of the four H_3^+ isotopologues considered here and are formatted using the standard outlined by Tennyson et al. (2013). H_3^+ and D_3^+ are identified using the same set of quantum numbers and hence their states files contain the same columns. Excerpts from the H_3^+ and D_3^+ states files are provided in Table 4.5. Similarly, the states files for H_2D^+ and D_2H^+ contain the same set of quantum number columns and an excerpt for each of them are shown in Table 4.6.

Following the scheme outlined in Section 2.4.6, all entries in the new states files are marked with a source tag, indicating the method that was used to determine the final term energy for that level Only three of the source tags used in ExoMol line lists were incorporated in the line lists discussed in this chapter: "Ma" for MARVELised energies, "EH" for energies from effective Hamiltonian calculations and "Ca" for

Table 4.4: The assigned vibrational bands of the D_3^+ states file, detailing the J and energy ranges of each band.

ν_1	ν_2	L_2	Count	Energy range (cm^{-1})	J range
0	0	0	256	0 - 4753	0 - 15
0	1	1	380	1835 - 6300	0 - 15
0	2	0	99	3531 - 6830	0 - 15
0	2	2	253	3646 - 7551	0 - 15
0	3	1	11	5214 - 5513	0 - 3
0	3	3	6	5401 - 5513	0 - 1
0	4	0	1	6774	0
0	4	2	2	6860 - 6860	0
0	4	4	2	7170 - 7170	0
0	5	1	2	8298 - 8298	0
0	5	3	2	8376 - 8600	0
0	5	5	2	8791 - 8791	0
0	6	0	1	9696	0
0	6	2	2	9731 - 9731	0
1	0	0	140	2301 - 5436	0 - 15
1	1	1	99	4060 - 7800	0 - 14
1	2	0	4	5712 - 5756	0 - 1
1	2	2	4	5796 - 6169	0 - 4
1	3	1	2	7368 - 7368	0
1	3	3	2	7454 - 7536	0
1	4	0	1	8864	0
1	4	2	2	9031 - 9031	0
1	4	4	2	9163 - 9163	0
2	0	0	36	4555 - 5178	0 - 5
2	1	1	2	6237 - 6237	0
2	2	0	1	7831	0
2	2	2	2	7894 - 7894	0
2	3	1	2	9424 - 9424	0
2	3	3	2	9463 - 9555	0
3	0	0	1	6761	0
3	1	1	2	8366 - 8366	0
3	2	0	1	9896	0
3	2	2	2	9943 - 9943	0
4	0	0	1	8921	0

Table 4.5: Excerpts from the H_3^+ and D_3^+ states files, using the format defined by Tennyson et al. (2013). Note that the zero-energy level of H_3^+ with A_1' symmetry does not exist and hence has "nan" entries for its lifetime and isomer. Any row for which the ν_1, ν_2, L_2, G, U or K assignment is not known will likewise have "nan" entries in these columns.

i	$\tilde{E}$	$g_{\rm tot}$	J	unc	τ	Parity	$\Gamma_{\rm rve}$	No.	Isomer	ν_1	ν_2	L_2	G	U	K	Source Tag
						H_3^+										
1	0.000 000	0	0	0.000 000	nan	e	A1'	1	nan	0	0	0	0	m	0	Ma
2	2 521.410 484	2	0	0.000 133	8.4474e-03	e	E'	1	p	0	1	1	1	m	0	Ma
3	4 998.052 947	2	0	0.010 004	2.4871e-03	e	E'	2	p	0	2	2	2	m	0	Ma
4	5 554.061 000	2	0	0.010 000	7.3144e-03	e	E'	3	p	1	1	1	1	m	0	Ca
5	7 005.974 780	2	0	0.010 000	3.1660e-03	e	E'	4	p	0	3	1	1	m	0	Ca
6	7 870.229 810	2	0	0.010 000	2.5047e-03	e	E'	5	p	1	2	2	2	m	0	Ca
7	8 488.013 160	2	0	0.010 000	6.6336e-03	e	E'	6	p	2	1	1	1	m	0	Ca
8	9 113.041 390	2	0	0.010 000	2.0836e-03	e	E'	7	p	0	4	2	2	m	0	Ca
9	9 653.699 850	2	0	0.010 000	1.1122e-03	e	E'	8	p	1	3	1	1	m	0	Ca
10	9 997.183 130	2	0	0.010 000	1.0631e-03	e	E'	9	p	0	4	4	4	m	0	Ca
						D_3^+										
1	0.000 000	10	0	0.000 000	inf	+	A1'	1	o	0	0	0	0	m	0	EH
2	2 301.198 553	10	0	0.100 000	9.6693e+00	+	A1'	2	o	1	0	0	0	m	0	Ca
3	3 530.665 453	10	0	0.100 000	2.4171e-02	+	A1'	3	o	0	2	0	0	m	0	Ca
4	4 554.794 932	10	0	0.100 000	3.2217e+00	+	A1'	4	o	2	0	0	0	m	0	Ca
5	5 400.959 293	10	0	0.100 000	6.7375e-03	+	A1'	5	o	0	3	3	3	m	0	Ca
6	5 711.982 115	10	0	0.100 000	1.4546e-02	+	A1'	6	o	1	2	0	0	m	0	Ca
7	6 761.183 630	10	0	0.100 000	1.3900e+00	+	A1'	7	o	3	0	0	0	m	0	Ca
8	6 774.131 925	10	0	0.100 000	8.2880e-03	+	A1'	8	o	0	4	0	0	m	0	Ca
9	7 453.959 812	10	0	0.100 000	7.3275e-03	+	A1'	9	o	1	3	3	3	m	0	Ca
10	8 375.558 874	10	0	0.100 000	6.3728e-03	+	A1'	10	o	0	5	3	3	m	0	Ca

i: State counting number;
$\tilde{E}$: Term value (in cm^{-1});
$g_{\rm tot}$: Total state degeneracy;
J: Total angular momentum quantum number;
unc: Estimated uncertainty of energy level (in cm^{-1});
τ: Radiative lifetime (in seconds);
Parity: H_3^+ uses e/f rotationless parity and D_3^+ uses $+/-$ total parity;
$\Gamma_{\rm rve}$: D_{3h} symmetry group;
No.: Symmetry group block counting number;
Isomer: Nuclear spin isomer;
ν_1: Symmetric stretching quantum number;
ν_2: Bending quantum number;
L_2: Vibrational angular momentum quantum number;
G: Absolute value of $k - l_2$;
U: U-notation of Watson (1994);
K: Rotational angular momentum quantum number;
Source Tag: The method used to generate the term value; "Ma" for MARVELised energies, "EH" for energies from effective Hamiltonian calculations and "Ca" for energies calculated using DVR3D.

Table 4.6: Excerpts from the H_2D^+ and D_2H^+ states files, using the format defined by Tennyson et al. (2013). Any row for which the ν_1, ν_2, ν_3, K_a or K_c assignment is not known will have "nan" entries in these columns.

i	$\tilde{E}$	$g_{\rm tot}$	J	unc	τ	+/-	$\Gamma_{\rm rve}$	No.	Isomer	ν_1	ν_2	ν_3	K_a	K_c	Source Tag
						H_2D^+									
1	0.000 000 0	3	0	0.000 000 0	inf	+	A1	1	p	0	0	0	0	0	Ma
2	2 205.877 112 7	3	0	0.005 000 0	5.7143e-02	+	A1	2	p	0	1	0	0	0	Ma
3	2 992.502 235 7	3	0	0.000 005 0	1.8706e-02	+	A1	3	p	1	0	0	0	0	Ma
4	4 287.473 200 0	3	0	0.200 000 0	1.8812e-02	+	A1	4	p	0	2	0	0	0	Ca
5	4 602.619 640 0	3	0	0.200 000 0	3.1868e-03	+	A1	5	p	0	0	2	0	0	Ca
6	5 039.766 610 0	3	0	0.200 000 0	1.9520e-02	+	A1	6	p	1	1	0	0	0	Ca
7	5 877.257 410 0	3	0	0.200 000 0	1.0870e-02	+	A1	7	p	2	0	0	0	0	Ca
8	6 287.667 112 7	3	0	0.002 000 0	6.4627e-03	+	A1	8	p	0	3	0	0	0	Ma
9	6 645.700 870 0	3	0	0.300 000 0	2.5443e-03	+	A1	9	p	0	1	2	0	0	Ca
10	6 991.578 112 7	3	0	0.002 000 0	9.4938e-03	+	A1	10	p	1	2	0	0	0	Ma
						D_2H^+									
1	0.000 000 0	12	0	0.000 000 0	inf	+	A1	1	o	0	0	0	0	0	Ma
2	1 968.162 264 8	12	0	0.005 000 0	1.9317e-02	+	A1	2	o	0	1	0	0	0	Ma
3	2 736.975 496 9	12	0	0.000 004 0	1.1633e-02	+	A1	3	o	1	0	0	0	0	Ma
4	3 821.208 167 0	12	0	0.100 000 0	1.2227e-02	+	A1	4	o	nan	nan	nan	nan	nan	Ca
5	4 042.772 164 8	12	0	0.000 900 0	1.2305e-02	+	A1	5	o	0	0	2	0	0	Ma
6	4 648.758 740 0	12	0	0.200 000 0	6.4298e-03	+	A1	6	o	nan	nan	nan	nan	nan	Ca
7	5 385.352 227 0	12	0	0.200 000 0	6.0840e-03	+	A1	7	o	nan	nan	nan	nan	nan	Ca
8	5 579.192 822 0	12	0	0.200 000 0	8.0766e-03	+	A1	8	o	nan	nan	nan	nan	nan	Ca
9	6 008.516 310 0	12	0	0.300 000 0	4.8418e-03	+	A1	9	o	nan	nan	nan	nan	nan	Ca
10	6 432.559 670 0	12	0	0.300 000 0	6.6492e-03	+	A1	10	o	nan	nan	nan	nan	nan	Ca

i: State counting number;
$\tilde{E}$: Term value (in cm^{-1});
$g_{\rm tot}$: Total state degeneracy;
J: Total angular momentum quantum number;
unc: Estimated uncertainty of energy level (in cm^{-1});
τ: Radiative lifetime (in seconds);
+/−: Total parity;
$\Gamma_{\rm rve}$: C_{2v} symmetry group;
No.: Symmetry group block counting number;
Isomer: Nuclear spin isomer;
ν_1: Symmetric stretching quantum number;
ν_2: Bending quantum number;
ν_3: Asymmetrical stretching quantum number;
K_a: Rotational angular momentum quantum number;
K_c: Rotational angular momentum quantum number;
Source Tag: The method used to generate the term value; "Ma" for MARVELised energies, "EH" for energies from effective Hamiltonian calculations and "Ca" for energies calculated using DVR3D.

Table 4.7: Excerpts from the trans files for the MiZo line lists for D_2H^+ and D_3^+.

D_2H^+			D_3^+		
f	i	A_{fi} (s^{-1})	f	i	A_{fi} (s^{-1})
1 401	1	3.30142477E-03	226	16	5.65667085E-09
1 402	2	2.19499998E-03	229	16	2.93922054E-02
3	1 402	1.59575873E-01	216	226	1.30736782E-07
1 403	2	1.80478736E-03	1 023	226	4.95756630E-07
3	1 403	4.59507405E-02	1 025	226	5.90452177E-07
1 404	2	9.63358275E-02	1 028	226	6.58440901E-02
1 404	3	3.99647847E-03	2	212	1.03419866E-01
1 405	4	2.49561352E-03	1 013	212	2.22162053E-02
5	1 405	2.09336332E-03	229	216	3.39285830E-02
6	1 405	3.28445005E-01	1 043	216	4.03805710E-07

f: The upper state counting number from the corresponding states file.
i: The lower state counting number from the corresponding states file.
A_{fi}: The Einstein A coefficient.

energies calculated using DVR3D. For all levels marked "Ca" in all four states files an uncertainty estimate was calculated using Eq. (4.2). The H_3^+, H_2D^+ and D_2H^+ line lists contain a mix of "Ma" and "Ca" levels, while the D_3^+ line list is a mix of "EH" and "Ca" levels.

All new and updated states files were ordered on increasing J, Γ_{rve} and energy. The existing H_2D^+ states file was already formatted this way, while the states file for H_3^+ was not and hence was reformatted. This meant that the state counting numbers for H_3^+ assigned to each level were reassigned and accordingly the references to these values in the corresponding trans file were updated. Excerpts from the trans files for the new D_2H^+ and D_3^+ line lists can be seen in Table 4.7.

In general, all molecular states should be characterised by three rigorous quantum numbers: J, parity and the overall symmetry, which also determines the nuclear spin state (ortho/para/meta). All calculations have J and parity rigorously determined; due to the full treatment by DVR3D of the C_{2v} symmetry, the symmetry and nuclear spin statistics are also correctly determined for H_2D^+ and D_2H^+. This is not the case for H_3^+ and D_3^+ however, as the program does not include a full treatment for a D_{3h} Hamiltonian. The symmetry was initially output for all molecular species considered here under C_{2v} symmetry but was subsequently mapped to the appropriate D_{3h} representation for H_3^+ and D_3^+ for states with quantum number assignments. Due to the nuclear spin statistical weight of the A_1', A_1'' symmetries in H_3^+ being 0, it was possible to map all of the C_{2v} symmetries to the appropriate D_{3h} representation (Mizus et al., 2017). This is not the case for D_3^+ however, as all three nuclear spin isomers have non-zero nuclear spin statistical weights and hence exist. Instead, where D_{3h} symmetry and quantum number assignment was not carried out, the states retain the C_{2v} symmetries output by DVR3D. These C_{2v} symmetries are given as lower-case in the states file, to avoid confusion between the A_1 and A_2 irreducible representations under C_{2v} symmetry (formatted as "a1" and "a2") and

the A_1', A_1'', A_2' and A_2'' irreducible representations under D_{3h} symmetry.

4.4.7 Partition functions

Calculating the partition functions of the new line lists requires the determination of the total degeneracy of each state considered, as show in Eq. (4.3):

$$z = \sum_i g_{\text{tot},i} exp\left(-\frac{E_i}{k_B T}\right), \tag{4.3}$$

where g_{tot} is the total degeneracy of the ith level, E_i its energy, k_B is the Boltzmann constant and T is the temperature. The total degeneracy of a level depends directly on the nuclear spin statistical weight, g_{ns}:

$$g_{\text{tot}} = g_{\text{ns}} (2J + 1), \tag{4.4}$$

following the ExoMol and HITRAN convention of including the full nuclear spin degeneracy in the partition functions (Simeckova et al., 2006).

Nuclear spin statistics are important for understanding the molecules considered here, particularly in determining the possible nuclear spin permutations that can exist. Under Fermi statistics a wavefunction must be antisymmetric with respect to the interchange of two indistinguishable fermions. This applies to the three protons comprising H_3^+, each with $I = \frac{1}{2}$, which can only be arranged such that:

$$\Gamma_{\text{ns}} = 4A_1' \oplus 2E' \tag{4.5}$$

When the products of these symmetries are taken with the possible D_{3h} irreducible representations to yield the total symmetry, $\Gamma_{\text{int}} = \Gamma_{\text{rve}} \otimes \Gamma_{\text{ns}}$, only the combinations which yield $\Gamma_{\text{int}} = A_2'$ and A_2'' are allowed (Herzberg, 1991). This is because the A_2' and A_2'' representations are the only representations in this symmetry corresponding to internal wavefunctions that are antisymmetric on interchange of two fermions (Bunker and Jensen, 2006). Hence, when determining the nuclear spin statistical weights the number of nuclear spin functions that yield each symmetry and considered. This can be seen in the numerical factors present in the representations given in Eq. (4.5), which are reflected in the g_{ns} values given in Table 4.1. For D_3^+ however, each Deuterium atom has $I = 1$ and is a boson, meaning additional representations corresponding to internal wavefunctions that are symmetric on interchange of two atoms can occur and give rise to the "meta" nuclear spin isomer.

The mappings of the C_{2v} representations output by DVR3D to the full D_{3h} symmetry are complete for all states presented in the H_3^+ line list, but not for the states of D_3^+. Hence, the appropriate statistical weights to use when determining the degeneracy of the D_3^+ states left with C_{2v} symmetries must also be considered. As the D_{3h} representations A_1', A_1'', A_2', A_2'', E', E'' correspond to A_1, A_2, B_2, B_1, $A_1 \oplus B_2$, $A_2 \oplus B_1$ respectively under C_{2v} symmetry, population weighted average statistical weights for each C_{2v} representation can be calculated. These are calculated knowing that approximately two thirds of all D_3^+ levels will be E' and E'', due to the constraint that A_1', A_1'', A_2' and A_2'' levels only occur when $G = 3n$, where n is an integer; see also Berblinger et al. (1992). Accordingly, for the A_1 and A_2 representations in C_{2v}

Table 4.8: Adjusted nuclear spin statistical weights for the levels of D_3^+ for which C_{2v} symmetries are used.

Γ_{rve}	g_{ns}
A_1, A_2	6
B_1, B_2	3

symmetry, one third will be A_1' or A_1'' under D_{3h} symmetry while the remaining two thirds will be E′ and E″. The equivalent population ratio is true for B_1 and B_2 states and the corresponding A_2' and A_2'' representations. These population ratios are then weighted using the weights from Table 4.1, yielding the g_{ns} values shown in Table 4.8. These adjusted weights were used to calculate the total degeneracies of the states of the D_3^+ line list for which C_{2v} symmetries are used and are included in the new states file.

Partition functions are given in Table 4.9 for a series of temperatures up to the value of T_{max} for each line list. Partition functions for D_3^+ had previously been calculated by Ramanlal and Tennyson (2004) and their values are in close agreement with those presented here. For H_2D^+ however, the partition functions differ from those given by Sochi and Tennyson (2010). This is due to the different nuclear spin statistical weights used in their earlier work that did not consider the spin of the Deuterium atom. The degeneracies given in the H_2D^+ line list have been updated to use the nuclear spin statistical weights quoted in Table 4.1 and are thus consistent with the partition function computed using Eq. (4.3) and the same convention.

4.5 Spectra

4.5.1 Rotational spectra

Purely rotational transitions within the vibrational ground state are important for detections of H_3^+ and particularly its deuterated isotopologues in the interstellar medium. This is due to the low temperatures in such regions driving the majority of the level populations to low-energy states. Predicted transition frequencies for such transitions are given in Table 4.10 for H_3^+ and D_3^+ and in Table 4.11 for H_2D^+ and D_2H^+, based on the term energies derived from the MARVELised line lists presented here. While the purely rotational transitions of H_3^+ are "forbidden" due to the lack of a permanent electric dipole moment, it is believed that a small, temporary dipole moment can be induced due to the distortion of the molecule from equilibrium geometry under rotation about the C_2 molecular axis (Pan and Oka, 1986; Miller and Tennyson, 1988a).

The D_3^+ states file contains 43 extremely long-lived states with radiative lifetimes greater than 10^{10} s and can be considered meta-stable. In the extreme case, two states are calculated to have radiative lifetimes greater than 10^{18} s, a duration greater than the current age of the universe. All of these meta-stable states are in the vibrational ground state and have $G = J$ or $G = J - 1$. The same is true for the meta-stable states of H_3^+, though only one of their radiative lifetimes is in excess of 10^{10} s. In both species, this can cause molecules to become "trapped" in these states in collision free environments with consequences for both laboratory measurements (Kreckel

Table 4.9: The partition functions for each new line list, calculated for a range of temperatures up to each line list's maximum temperature, given in Table 4.3.

Temp. (K)	H_3^+	H_2D^+	D_2H^+	D_3^+
10	$6.000\,0\times10^{-4}$	$3.018\,1\times10^{0}$	$1.215\,3\times10^{1}$	$1.023\,5\times10^{1}$
50	$2.021\,5\times10^{0}$	$1.514\,1\times10^{1}$	$3.735\,5\times10^{1}$	$2.717\,5\times10^{1}$
100	$7.397\,2\times10^{0}$	$4.535\,4\times10^{1}$	$9.727\,8\times10^{1}$	$6.909\,5\times10^{1}$
200	$2.073\,3\times10^{1}$	$1.260\,4\times10^{2}$	$2.672\,1\times10^{2}$	$1.908\,5\times10^{2}$
300	$3.760\,9\times10^{1}$	$2.293\,7\times10^{2}$	$4.875\,6\times10^{2}$	$3.490\,4\times10^{2}$
400	$5.765\,0\times10^{1}$	$3.523\,1\times10^{2}$	$7.505\,3\times10^{2}$	$5.385\,8\times10^{2}$
500	$8.058\,1\times10^{1}$	$4.935\,7\times10^{2}$	$1.054\,9\times10^{3}$	$7.602\,2\times10^{2}$
600	$1.064\,0\times10^{2}$	$6.539\,1\times10^{2}$	$1.404\,8\times10^{3}$	$1.018\,8\times10^{3}$
700	$1.353\,3\times10^{2}$	$8.357\,2\times10^{2}$	$1.808\,0\times10^{3}$	$1.321\,5\times10^{3}$
800	$1.678\,3\times10^{2}$	$1.042\,6\times10^{3}$	$2.274\,6\times10^{3}$	$1.676\,1\times10^{3}$
900	$2.044\,2\times10^{2}$	$1.278\,7\times10^{3}$	$2.816\,2\times10^{3}$	
1 000	$2.457\,8\times10^{2}$	$1.548\,9\times10^{3}$	$3.445\,6\times10^{3}$	
1 250	$3.747\,8\times10^{2}$	$2.408\,7\times10^{3}$	$5.496\,7\times10^{3}$	
1 500	$5.508\,9\times10^{2}$	$3.606\,9\times10^{3}$	$8.435\,1\times10^{3}$	
1 750	$7.893\,8\times10^{2}$	$5.251\,0\times10^{3}$	$1.256\,3\times10^{4}$	
2 000	$1.108\,6\times10^{3}$		$1.824\,2\times10^{4}$	
3 000	$3.703\,2\times10^{3}$			
4 000	$1.023\,9\times10^{4}$			
5 000	$2.417\,7\times10^{4}$			

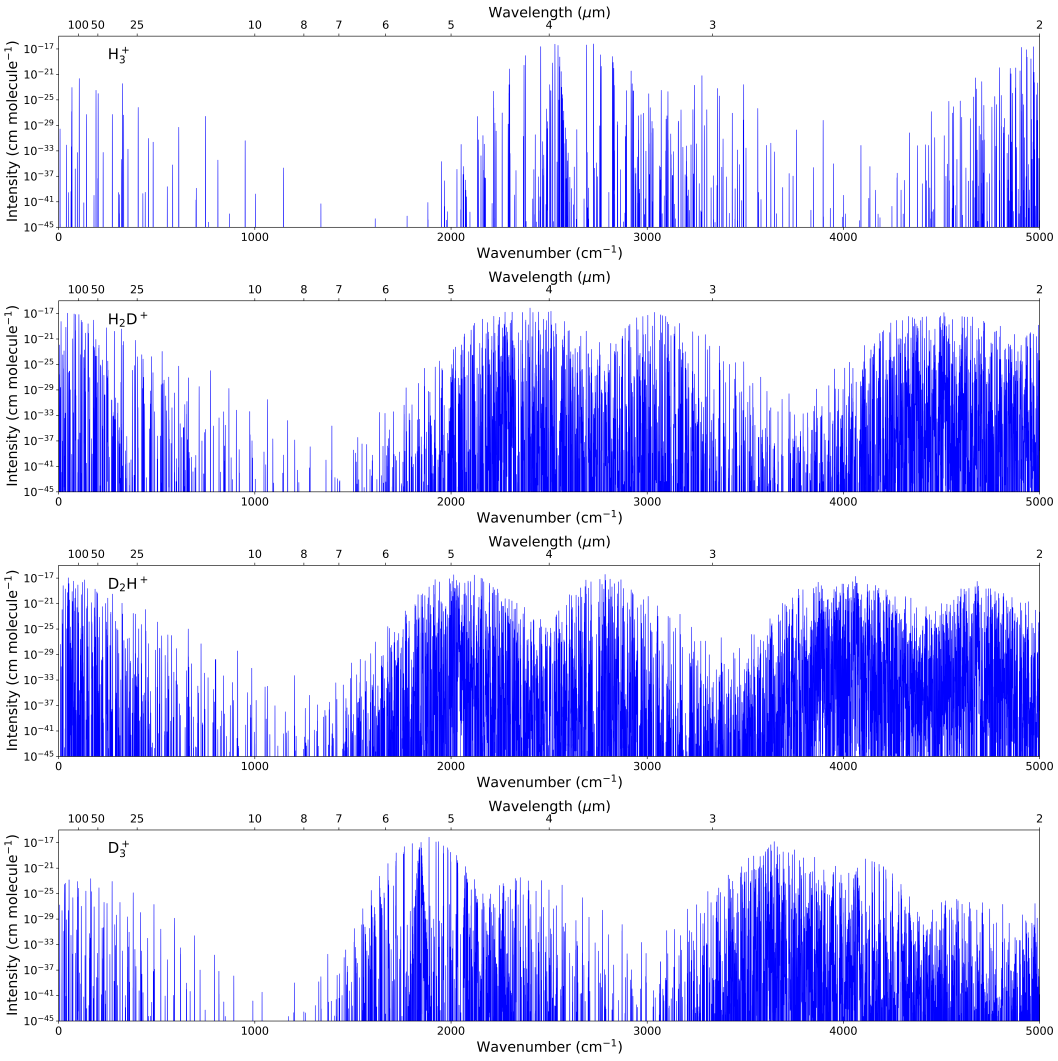
et al., 2004) and for possible maser action.

4.5.2 Mid and far infrared spectra

Fig. 4.1 shows example stick spectra for H_3^+ and its deuterated isotopologues up to 5 000 cm^{-1}, primarily in the infrared region. These spectra were generated using the program ExoCross (Yurchenko et al., 2018) and were computed for a temperature of 35 K, to simulate the conditions of the ISM where it has been observed (Geballe and Oka, 1996). The predicted far-IR transitions frequencies listed in Tables 4.10 and 4.11 that are expected to be of importance in the ISM fall within this range. Fig. 4.2 similarly shows the spectra computed at 1 000 K over the same wavelength range, to simulate conditions seen in Jupiter's ionosphere, though this can vary (Moore et al., 2017). This covers several wavelength ranges where H_3^+ has been observed in Jupiter's aurorae, such as the K band region centred at 2.2 μm (Uno et al., 2014) and the L band centred on 3.5 μm (Baron et al., 1991). This also covers the wavelength regions observed using the Jupiter infrared Auroral Mapper (JIRAM) instrument onboard NASA's Juno spacecraft (Dinelli et al., 2019; Migliorini et al., 2019) and those covered by the Near infrared Camera (NIRCam) long-wavelength channel onboard JWST.

Comparisons between computed spectra and real observations cannot be made for H_2D^+, D_2H^+ and D_3^+, as no measured transition intensities have been published. McKellar and Watson (1998) presented infrared absorption spectra of the ν_2 funda-

Fig. 4.1: Infrared spectra for H_3^+ and its deuterated isotopologues, computed using the program ExoCross (Yurchenko et al., 2018) at 35 K up to 5000 cm^{-1} (2 μm).

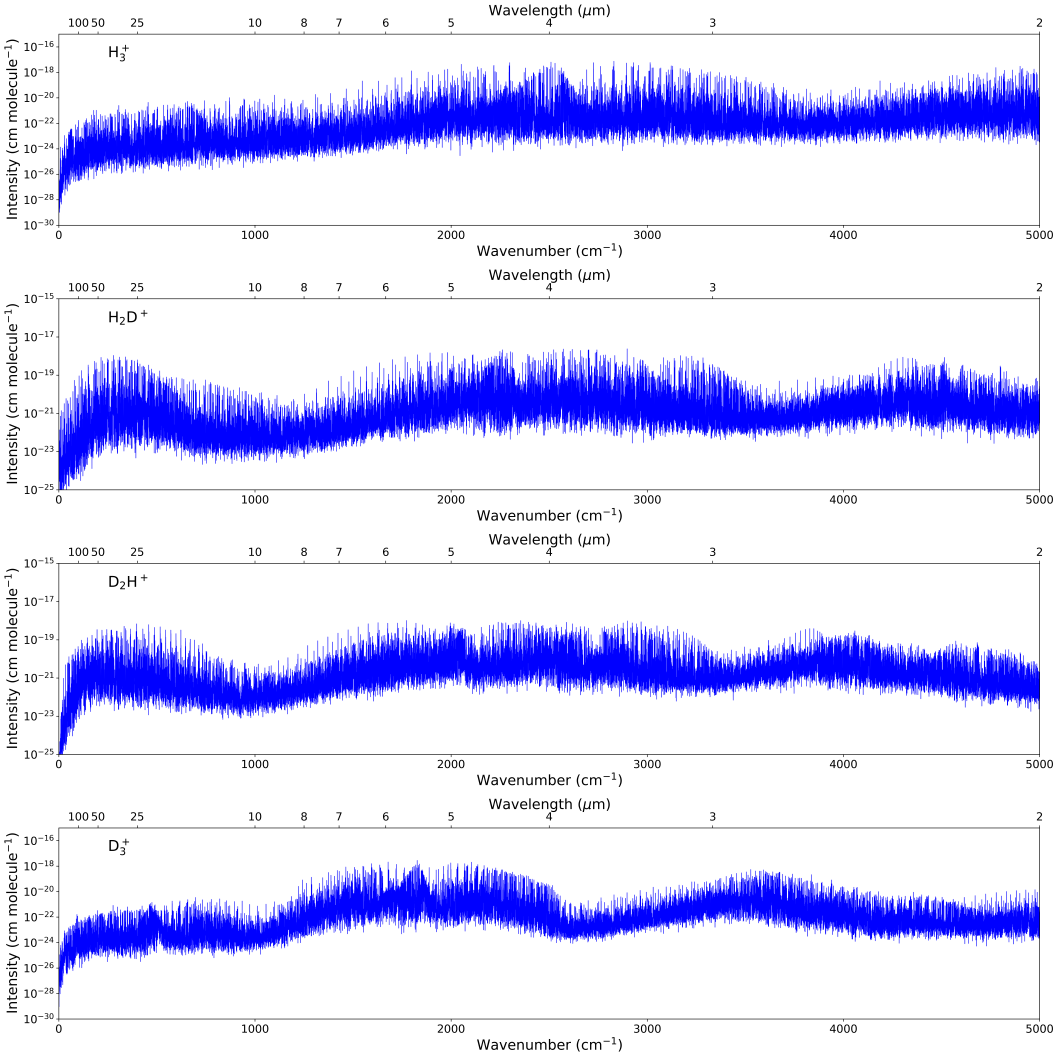


mental band of H_3^+ and provided integrated intensities, which were well reproduced by the original line list (Mizus et al., 2017).

4.6 Summary

Three MARVEL networks for H_3^+, H_2D^+ and D_2H^+ have been updated to include all currently published spectroscopic data for these molecules. Variational nuclear motion calculations have also been performed using the program DVR3D for D_2H^+ and D_3^+ to produce the new MiZo line lists. The empirical energy levels derived from the MARVEL networks have been used to update the calculated levels of their respective molecules. This allowed for the subset of transitions involving these MARVELised energies to be determined to much higher accuracy, making the use of these line lists well suited for high-resolution spectroscopy. The D_3^+ calculations have been combined with a set of energies derived from effective Hamiltonian calculations computed using experimentally determined molecular constants. Given

Fig. 4.2: Infrared spectra for H_3^+ and its deuterated isotopologues, computed using the program ExoCross (Yurchenko et al., 2018) at 1 000 K up to 5000 cm^{-1} (2 μm).



these effective Hamiltonian constants were derived from transitions in infrared bands, the new D_3^+ line list is best suited for infrared studies. Overall, the new D_3^+ line list is of lower resolution than the other three, due to the lack of MARVELised energy levels.

Table 4.10: Predicted pure-rotation transition wavenumbers and Einstein A coefficients for transitions involving low-energy lower levels for H_3^+ and D_3^+. For all upper and lower levels included here, $v_1 = v_2 = L_2 = 0$. Values quoted in brackets for energies are the uncertainty in the last digit.

		Upper Level						Lower Level					
Wavenumber (cm^{-1})	A_{fi} (s^{-1})	J	G	U	K	Γ_{rve}	Term Energy (cm^{-1})	J	G	U	K	Γ_{rve}	Term Energy (cm^{-1})
						H_3^+							
105.176 39(37)	4.2570×10^{-7}	2	2	m	2	E′	169.297 39(37)	1	1	m	1	E″	64.121 000
68.054 81(37)	5.6141×10^{-7}	2	1	m	1	E″	237.352 195(50)	2	2	m	2	E′	169.297 39(37)
325.465 35(40)	3.4982×10^{-5}	3	1	m	1	E″	494.762 74(14)	2	2	m	2	E′	169.297 39(37)
190.665 48(40)	1.7422×10^{-5}	3	2	m	2	E′	428.017 68(39)	2	1	m	1	E″	237.352 195(50)
201.528 43(29)	7.3590×10^{-5}	3	0	m	0	A_2'	516.880 36(23)	3	3	m	3	A_2''	315.351 92(18)
66.745 06(42)	2.6423×10^{-6}	3	1	m	1	E″	494.762 74(14)	3	2	m	2	E′	428.017 68(39)
405.556 23(42)	3.2067×10^{-4}	4	1	m	1	E″	833.573 91(14)	3	2	m	2	E′	428.017 68(39)
7.274 31(27)	2.5602×10^{-9}	4	4	m	4	E′	502.037 05(23)	3	1	m	1	E″	494.762 74(14)
273.706 56(44)	1.7953×10^{-4}	4	2	m	2	E′	768.469 30(42)	3	1	m	1	E″	494.762 74(14)
						D_3^+							
53.300 0(28)	1.3067×10^{-8}	2	2	m	2	E′	85.621 0(20)	1	1	m	1	E″	32.321 0(20)
33.747 0(28)	1.6552×10^{-8}	2	1	m	1	E″	119.368 0(20)	2	2	m	2	E′	85.621 0(20)
163.728 0(28)	1.0739×10^{-6}	3	1	m	1	E″	249.349 0(20)	2	2	m	2	E′	85.621 0(20)
96.544 0(28)	5.5135×10^{-7}	3	2	m	2	E′	215.912 0(20)	2	1	m	1	E″	119.368 0(20)
29.281 0(28)	3.1041×10^{-8}	3	-3	m	3	A_1''	159.868 0(20)	2	0	m	0	A_1'	130.587 0(20)
100.599 0(28)	2.1970×10^{-6}	3	0	m	0	A_2'	260.466 0(20)	3	3	m	3	A_2''	159.867 0(20)
272.690 0(28)	1.4422×10^{-5}	4	0	m	0	A_1'	432.558 0(20)	3	-3	m	3	A_1''	159.868 0(20)
33.437 0(28)	8.0083×10^{-8}	3	1	m	1	E″	249.349 0(20)	3	2	m	2	E′	215.912 0(20)
205.660 0(28)	1.0260×10^{-5}	4	1	m	1	E″	421.572 0(20)	3	2	m	2	E′	215.912 0(20)
5.666 0(28)	3.0205×10^{-10}	4	4	m	4	E′	255.015 0(20)	3	1	m	1	E″	249.349 0(20)
139.082 0(28)	5.7366×10^{-6}	4	2	m	2	E′	388.431 0(20)	3	1	m	1	E″	249.349 0(20)

Table 4.11: Predicted pure-rotation transition wavenumbers and Einstein A coefficients for transitions involving low-energy lower levels for H_2D^+ and D_2H^+. For all upper and lower levels included here, $\nu_1 = \nu_2 = \nu_3 = 0$. Values quoted in brackets for the transition frequencies are the uncertainty in the last digit.

		Upper Level					Lower Level				
Wavenumber (cm^{-1})	A_{fi} (s^{-1})	J	K_a	K_c	Γ_{rve}	Term Energy (cm^{-1})	J	K_a	K_c	Γ_{rve}	Term Energy (cm^{-1})
						H_2D^+					
45.701 112 7(4)	4.0400×10^{-3}	1	0	1	A_2	45.701 112 7(4)	0	0	0	A_1	0.000 000 0
85.951 350(33)	3.0300×10^{-2}	2	0	2	A_1	131.652 463(33)	1	0	1	A_2	45.701 112 7(4)
178.156 6(36)	1.6600×10^{-2}	2	2	0	A_1	223.857 7(36)	1	0	1	A_2	45.701 112 7(4)
12.422 639(14)	1.2200×10^{-4}	1	1	0	B_2	72.452 486(10)	1	1	1	B_1	60.029 846(10)
78.829 277(23)	1.8800×10^{-2}	2	1	2	B_2	138.859 124(21)	1	1	1	B_1	60.029 846(10)
103.482 549(23)	4.2400×10^{-2}	2	1	1	B_1	175.935 034(21)	1	1	0	B_2	72.452 486(10)
87.002 1(36)	3.2700×10^{-3}	2	2	1	A_2	218.654 5(36)	2	0	2	A_1	131.652 463(33)
119.762 2(20)	8.5300×10^{-2}	3	0	3	A_2	251.414 6(20)	2	0	2	A_1	131.652 463(33)
244.688 4(70)	4.7600×10^{-2}	3	2	1	A_2	376.340 9(70)	2	0	2	A_1	131.652 463(33)
37.075 911(30)	1.0700×10^{-3}	2	1	1	B_1	175.935 034(21)	2	1	2	B_2	138.859 124(21)
115.201 469(33)	7.3200×10^{-2}	3	1	3	B_1	254.060 593(26)	2	1	2	B_2	138.859 124(21)
319.484 3(70)	2.3600×10^{-2}	3	3	1	B_1	458.343 4(70)	2	1	2	B_2	138.859 124(21)
150.225 2(20)	1.5900×10^{-1}	3	1	2	B_2	326.160 2(20)	2	1	1	B_1	175.935 034(21)
283.894 5(70)	3.7500×10^{-2}	3	3	0	B_2	459.829 6(70)	2	1	1	B_1	175.935 034(21)
5.203 2(50)	1.1300×10^{-5}	2	2	0	A_1	223.857 7(36)	2	2	1	A_2	218.654 5(36)
136.123 8(79)	7.7800×10^{-2}	3	2	2	A_1	354.778 3(70)	2	2	1	A_2	218.654 5(36)
27.556 9(41)	9.5600×10^{-6}	3	0	3	A_2	251.414 6(20)	2	2	0	A_1	223.857 7(36)
152.483 2(79)	1.1200×10^{-1}	3	2	1	A_2	376.340 9(70)	2	2	0	A_1	223.857 7(36)
103.363 7(73)	8.2700×10^{-3}	3	2	2	A_1	354.778 3(70)	3	0	3	A_2	251.414 6(20)
151.38(10)	1.8100×10^{-1}	4	0	4	A_1	402.80(10)	3	0	3	A_2	251.414 6(20)
329.972(10)	6.7000×10^{-2}	4	2	2	A_1	581.386(10)	3	0	3	A_2	251.414 6(20)
527.62(10)	4.6500×10^{-3}	4	4	0	A_1	779.04(10)	3	0	3	A_2	251.414 6(20)
72.099 7(20)	4.1900×10^{-3}	3	1	2	B_2	326.160 2(20)	3	1	3	B_1	254.060 593(26)
149.618 9(53)	1.7400×10^{-1}	4	1	4	B_2	403.679 5(53)	3	1	3	B_1	254.060 593(26)
205.769 0(70)	3.1700×10^{-3}	3	3	0	B_2	459.829 6(70)	3	1	3	B_1	254.060 593(26)
391.51(10)	5.2800×10^{-2}	4	3	2	B_2	645.57(10)	3	1	3	B_1	254.060 593(26)
						D_2H^+					
49.254 264 8(2)	3.3014×10^{-3}	1	1	1	A_2	49.254 264 8(2)	0	0	0	A_1	0.000 000 0
23.071 309(14)	5.0885×10^{-4}	1	1	0	B_2	57.989 629(10)	1	0	1	B_1	34.918 320(10)
75.341 734(30)	1.0592×10^{-2}	2	1	2	B_2	110.260 054(28)	1	0	1	B_1	34.918 320(10)
52.463 752 2(33)	2.0691×10^{-3}	2	0	2	A_1	101.718 017 0(33)	1	1	1	A_2	49.254 264 8(2)
132.809 827(10)	4.4605×10^{-2}	2	2	0	A_1	182.064 091(10)	1	1	1	A_2	49.254 264 8(2)
121.174 679(68)	4.4481×10^{-2}	2	2	1	B_1	179.164 308(67)	1	1	0	B_2	57.989 629(10)
34.646 073 1(47)	1.2985×10^{-3}	2	1	1	A_2	136.364 090 1(34)	2	0	2	A_1	101.718 017 0(33)
98.311 007 2(57)	2.4763×10^{-2}	3	1	3	A_2	200.029 024 2(47)	2	0	2	A_1	101.718 017 0(33)
68.904 254(73)	4.5854×10^{-3}	2	2	1	B_1	179.164 308(67)	2	1	2	B_2	110.260 054(28)
85.840 024(73)	1.4620×10^{-2}	3	0	3	B_1	196.100 078(67)	2	1	2	B_2	110.260 054(28)
185.781 201(73)	5.4468×10^{-2}	3	2	1	B_1	296.041 254(67)	2	1	2	B_2	110.260 054(28)
45.700 001(11)	2.2792×10^{-3}	2	2	0	A_1	182.064 091(10)	2	1	1	A_2	136.364 090 1(34)
146.951 256(94)	6.2260×10^{-2}	3	2	2	A_1	283.315 346(94)	2	1	1	A_2	136.364 090 1(34)
72.137 151(95)	1.7139×10^{-3}	3	1	2	B_2	251.301 459(67)	2	2	1	B_1	179.164 308(67)
17.964 933(11)	5.6565×10^{-6}	3	1	3	A_2	200.029 024 2(47)	2	2	0	A_1	182.064 091(10)
55.201 381(95)	3.5511×10^{-3}	3	1	2	B_2	251.301 459(67)	3	0	3	B_1	196.100 078(67)
121.151 1(50)	5.0954×10^{-2}	4	1	4	B_2	317.251 2(50)	3	0	3	B_1	196.100 078(67)
83.286 322(94)	8.5394×10^{-3}	3	2	2	A_1	283.315 346(94)	3	1	3	A_2	200.029 024 2(47)
115.707 967(94)	4.3474×10^{-2}	4	0	4	A_1	315.736 992(94)	3	1	3	A_2	200.029 024 2(47)
44.739 796(95)	2.9105×10^{-3}	3	2	1	B_1	296.041 254(67)	3	1	2	B_2	251.301 459(67)
168.163 8(50)	8.7250×10^{-2}	4	2	3	B_1	419.465 3(50)	3	1	2	B_2	251.301 459(67)
115.734 01(13)	1.5816×10^{-2}	4	1	3	A_2	399.049 356(97)	3	2	2	A_1	283.315 346(94)
240.072 0(50)	2.4471×10^{-1}	4	3	1	A_2	523.387 3(50)	3	2	2	A_1	283.315 346(94)
21.209 9(50)	6.8544×10^{-6}	4	1	4	B_2	317.251 2(50)	3	2	1	B_1	296.041 254(67)

4.A H_3^+ MARVEL data

Table 4.12: Components of the updated H_3^+ MARVEL network. The network is broken down by the transition data sources and the vibrational bands contained within them, given in the form v_1', v_2', L_2' - v_1'', v_2'', L_2''. For each band, the transition energy and total angular momentum J ranges are provided, along with the mean and maximum uncertainties for these transitions. The total number of transitions validated and accessed by MARVEL (V/A) are also provided.

Vib.	J range	V/A	Energy range (cm^{-1})	Uncertainty Mean/Max (cm^{-1})
80Oka (Oka, 1980)				
011 - 000	0 - 4	14/15	2457 - 2918	0.013/0.015
81Oka (Oka, 1981)				
011 - 000	0 - 6	27/30	2457 - 3030	0.010/0.010
84WaFoMcBe (Watson et al., 1984)				
011 - 000	0 - 7	46/46	2217 - 3030	0.010/0.010
84WaFoMcBe_CD (Watson et al., 1984)				
000 - 000	1 - 4	5/5	173 - 596	0.010/0.012
87MaMaMcJo (Majewski et al., 1987)				
011 - 000	0 - 10	110/113	1798 - 3193	0.010/0.020
89MaFeWaMi (Majewski et al., 1989)				
022 - 000	1 - 12	44/50	4540 - 5094	0.017/0.041
90BaReOk (Bawendi et al., 1990)				
011 - 000	3 - 9	14/14	2468 - 2889	0.010/0.010
020 - 011	1 - 6	14/14	2395 - 2685	0.010/0.010
022 - 011	0 - 8	68/68	2090 - 2945	0.010/0.040
111 - 011	5 - 6	2/2	2741 - 2854	0.010/0.010
111 - 100	1 - 4	21/21	2089 - 2771	0.010/0.010
90NaItSuTa (Nakanaga et al., 1990)				
011 - 000	0 - 3	11/12	2457 - 2762	0.010/0.010
90XuGaOk (Xu et al., 1990)				
022 - 000	1 - 10	34/34	4557 - 5094	0.011/0.040
91LeVeCaOk (Lee et al., 1991)				
031 - 000	1 - 5	3/4	6866 - 6878	0.012/0.017
92XuRoGaOk (Xu et al., 1992)				
011 - 000	5 - 13	30/30	2419 - 3291	0.010/0.014
022 - 011	3 - 7	9/10	2893 - 3215	0.010/0.010
022 - 100	6 - 7	1/1	2980 - 2980	0.010/0.010
100 - 000	4 - 7	9/9	2454 - 3282	0.010/0.010
111 - 011	0 - 6	21/21	2437 - 3229	0.010/0.010
120 - 022	4 - 5	1/1	2990 - 2990	0.010/0.010
211 - 111	2 - 3	1/1	3006 - 3006	0.010/0.010
94MaMcSaWa (Majewski et al., 1994)				
011 - 000	5 - 14	67/67	1844 - 3643	0.014/0.050
020 - 011	1 - 10	27/27	1934 - 3024	0.013/0.050
022 - 000	2 - 8	9/11	4435 - 4795	0.017/0.030
022 - 011	1 - 10	57/63	1869 - 3293	0.013/0.040
022 - 100	5 - 6	1/2	2836 - 2836	0.010/0.010
031 - 011	n/a	0/1	nan - nan	nan/nan

Table 4.12 - continued

Vib.	J range	V/A	Energy range (cm^{-1})	Uncertainty Mean/Max (cm^{-1})
94MaMcSaWa (Majewski et al., 1994) continued				
031 - 020	1 - 7	2/2	2260 - 3002	0.010/0.010
033 - 011	3 - 4	2/2	4553 - 4721	0.020/0.030
033 - 022	3 - 7	3/4	2028 - 3241	0.010/0.010
100 - 000	7 - 11	4/4	3024 - 3277	0.010/0.010
120 - 022	6 - 7	1/1	3206 - 3206	0.010/0.010
122 - 020	9 - 10	1/1	2943 - 2943	0.010/0.010
122 - 022	n/a	0/1	nan - nan	nan/nan
94UyGaJaOk (Uy et al., 1994)				
011 - 000	1 - 16	73/73	2691 - 3579	0.011/0.040
100 - 000	8 - 10	2/2	3412 - 3441	0.010/0.010
94VeCaGuJo (Ventrudo et al., 1994)				
031 - 000	1 - 5	14/15	6807 - 7266	0.017/0.040
97DiNePoTe (Dinelli et al., 1997)				
000 - 020	n/a	0/1	nan - nan	nan/nan
011 - 000	6 - 14	14/16	2396 - 3269	0.012/0.040
020 - 011	4 - 10	9/10	2622 - 2998	0.013/0.040
020 - 100	9 - 10	1/1	2893 - 2893	0.010/0.010
022 - 011	4 - 13	17/24	2413 - 3240	0.010/0.010
022 - 100	4 - 6	2/4	2571 - 2709	0.010/0.010
031 - 020	1 - 9	9/9	2458 - 2977	0.010/0.010
031 - 022	4 - 6	2/2	2680 - 2709	0.010/0.010
033 - 022	0 - 9	19/20	2484 - 3061	0.010/0.010
100 - 000	8 - 8	1/1	2471 - 2471	0.010/0.010
111 - 011	4 - 7	5/9	2661 - 3203	0.020/0.030
111 - 100	4 - 11	7/7	2458 - 3294	0.013/0.030
120 - 022	2 - 6	2/2	2852 - 3052	0.010/0.010
120 - 111	4 - 6	2/2	2714 - 2817	0.025/0.040
122 - 111	2 - 7	7/7	2403 - 3022	0.010/0.010
211 - 200	1 - 6	3/3	2416 - 2654	0.010/0.010
00McOk (McCall and Oka, 2000)				
120 - 000	3 - 4	1/1	8038 - 8038	0.010/0.010
122 - 000	1 - 5	27/27	7785 - 8163	0.014/0.040
211 - 000	4 - 6	2/2	8053 - 8123	0.010/0.010
01LiMc (Lindsay and McCall, 2001)				
011 - 000	6 - 7	1/1	2956 - 2956	0.010/0.010
020 - 011	7 - 10	3/3	2902 - 2977	0.017/0.030
020 - 100	8 - 9	1/1	3003 - 3003	0.010/0.010
022 - 011	3 - 8	4/4	2601 - 2953	0.015/0.020
022 - 100	5 - 7	3/3	2844 - 2980	0.010/0.010
031 - 020	3 - 7	2/2	2596 - 2716	0.010/0.010
033 - 022	0 - 5	4/4	2469 - 2579	0.010/0.010
100 - 000	7 - 8	1/1	2957 - 2957	0.030/0.030
111 - 011	5 - 9	9/9	2437 - 3000	0.010/0.010
111 - 100	1 - 9	4/4	2575 - 2902	0.010/0.010
120 - 022	4 - 6	2/2	2976 - 2990	0.010/0.010
120 - 111	5 - 6	1/1	2817 - 2817	0.010/0.010

Table 4.12 - continued

Vib.	J range	V/A	Energy range (cm^{-1})	Uncertainty Mean/Max (cm^{-1})
01LiMc (Lindsay and McCall, 2001) continued				
122 - 111	1 - 6	8/8	2497 - 2893	0.015/0.030
211 - 111	4 - 6	2/2	2891 - 2903	0.010/0.010
211 - 200	5 - 6	1/1	2654 - 2654	0.010/0.010
01LiMc_MAGIC (Lindsay and McCall, 2001)				
000 - 000	0 - 1	3/3	22.839 - 86.960	1.00×10^{-9}/1.00×10^{-9}
01LiRaOk (Lindsay et al., 2001)				
011 - 000	4 - 16	96/96	3008 - 3596	0.008/0.045
020 - 011	8 - 13	6/6	2998 - 3283	0.007/0.015
020 - 100	9 - 10	1/1	3111 - 3111	0.010/0.010
022 - 011	4 - 12	75/75	3007 - 3527	0.007/0.040
022 - 100	7 - 9	4/4	3101 - 3269	0.013/0.035
031 - 020	5 - 8	2/2	3003 - 3134	0.005/0.005
033 - 022	5 - 6	1/1	3076 - 3076	0.010/0.010
100 - 000	4 - 11	22/22	3024 - 3575	0.009/0.045
111 - 011	0 - 9	24/25	3009 - 3443	0.006/0.015
111 - 100	6 - 10	14/14	3024 - 3296	0.006/0.010
120 - 020	6 - 7	1/1	3063 - 3063	0.015/0.015
120 - 022	5 - 6	2/2	3018 - 3052	0.005/0.005
122 - 020	5 - 5	1/1	3183 - 3183	0.005/0.005
122 - 111	6 - 7	2/2	3022 - 3236	0.005/0.005
200 - 100	6 - 8	3/3	3077 - 3104	0.008/0.010
03GoMcOk (Gottfried et al., 2003)				
051 - 000	1 - 4	7/7	11019 - 11576	0.011/0.015
053 - 000	1 - 3	2/2	11044 - 11247	0.010/0.010
055 - 000	1 - 3	5/5	11572 - 11854	0.010/0.010
062 - 000	1 - 1	1/1	12419 - 12419	0.010/0.010
142 - 000	1 - 2	1/1	12246 - 12246	0.020/0.020
231 - 000	1 - 3	3/3	12222 - 12254	0.013/0.020
311 - 000	1 - 3	3/3	11112 - 11504	0.010/0.010
04MiKrWePl (Mikosch et al., 2004)				
031 - 000	1 - 3	3/3	7193 - 7241	0.015/0.026
04OkEp (Oka and Epp, 2004)				
011 - 000	1 - 7	20/20	2530 - 3182	0.011/0.020
022 - 000	1 - 7	10/11	4777 - 4987	0.015/0.054
04OkEp_CD (Oka and Epp, 2004)				
000 - 000	1 - 10	68/69	7.255 - 1696	0.011/0.022
08KrBiRePe (Kreckel et al., 2008)				
051 - 000	1 - 2	2/2	11229 - 11244	0.010/0.010
055 - 000	0 - 2	4/4	11594 - 11882	0.010/0.010
062 - 000	1 - 2	5/5	12419 - 13072	0.011/0.014
142 - 000	1 - 2	2/2	12019 - 12087	0.010/0.010
144 - 000	1 - 2	1/1	12898 - 12898	0.010/0.010
231 - 000	0 - 1	1/1	12239 - 12239	0.010/0.010
311 - 000	0 - 2	4/4	11259 - 11511	0.010/0.010
322 - 000	1 - 2	1/1	13333 - 13333	0.010/0.010

Table 4.12 - continued

Vib.	J range	V/A	Energy range (cm^{-1})	Uncertainty Mean/Max (cm^{-1})
08VeLeAgBe (Velilla et al., 2008)				
051 - 000	1 - 3	4/4	10730 - 10790	0.010/0.010
062 - 000	1 - 3	2/2	12503 - 13056	0.010/0.010
142 - 000	3 - 4	1/1	12658 - 12658	0.010/0.010
144 - 000	1 - 2	1/1	12898 - 12898	0.010/0.010
222 - 000	1 - 3	4/4	10726 - 10779	0.010/0.010
09MoGoOk (Morong et al., 2009)				
042 - 000	6 - 7	1/1	10329 - 10329	0.010/0.010
044 - 000	2 - 5	4/4	10367 - 10574	0.010/0.010
051 - 000	0 - 7	38/39	10462 - 11619	0.010/0.015
053 - 000	1 - 5	9/9	10657 - 11954	0.010/0.010
055 - 000	1 - 6	19/19	11331 - 12321	0.010/0.010
060 - 000	3 - 3	1/1	12116 - 12116	0.010/0.010
060 - 011	2 - 3	1/1	10828 - 10828	0.010/0.010
062 - 000	1 - 3	4/4	12419 - 13056	0.014/0.025
064 - 000	1 - 1	1/1	13597 - 13597	0.010/0.010
071 - 000	1 - 1	1/1	13676 - 13676	0.010/0.010
140 - 000	3 - 5	3/3	11563 - 12331	0.010/0.010
142 - 000	1 - 4	5/5	12102 - 12658	0.010/0.010
144 - 000	1 - 2	1/1	12898 - 12898	0.010/0.010
153 - 011	2 - 3	1/1	11265 - 11265	0.010/0.010
220 - 000	4 - 5	1/1	11114 - 11114	0.010/0.010
222 - 000	0 - 6	32/33	10322 - 11115	0.010/0.010
231 - 000	1 - 6	7/7	11947 - 12525	0.011/0.020
311 - 000	1 - 6	11/11	10875 - 11892	0.010/0.010
12BeWoPe (Berg et al., 2012)				
144 - 000	1 - 2	1/1	12882 - 12882	0.005/0.005
231 - 000	1 - 2	1/1	12589 - 12589	0.005/0.005
233 - 000	1 - 2	1/1	12620 - 12620	0.005/0.005
12CrHoSiPe (Crabtree et al., 2012)				
011 - 000	1 - 2	1/1	2726 - 2726	0.004/0.004
12PaAdAlZo (Pavanello et al., 2012b)				
051 - 000	0 - 1	2/2	10799 - 10832	0.005/0.005
062 - 000	0 - 1	1/1	12413 - 12413	0.010/0.010
071 - 000	0 - 1	1/1	13638 - 13638	0.005/0.005
082 - 000	0 - 1	1/1	15059 - 15059	0.005/0.005
162 - 000	1 - 2	2/2	15130 - 15450	0.005/0.005
164 - 000	1 - 2	1/1	15643 - 15643	0.005/0.005
222 - 000	1 - 2	1/1	10752 - 10752	0.005/0.005
231 - 000	1 - 2	3/3	12374 - 12589	0.008/0.010
233 - 000	1 - 2	1/1	12620 - 12620	0.005/0.005
251 - 000	1 - 1	1/1	15717 - 15717	0.005/0.005
342 - 000	1 - 2	1/1	16506 - 16506	0.005/0.005
13HoPeJeSi (Hodges et al., 2013)				
011 - 000	1 - 5	10/10	2691 - 2894	2.40×10^{-5}/4.51×10^{-5}

Table 4.12 - continued

Vib.	J range	V/A	Energy range (cm^{-1})	Uncertainty Mean/Max (cm^{-1})
13WuLiLiSh (Wu et al., 2013)				
011 - 000	1 - 4	12/12	2518 - 2918	3.14×10^{-4}/1.00×10^{-3}
15PeHoMaKo (Perry et al., 2015)				
011 - 000	3 - 7	10/10	2895 - 3030	6.93×10^{-5}/1.30×10^{-4}
16JuKoScAs (Jusko et al., 2016)				
011 - 000	1 - 3	5/5	2691 - 2823	1.08×10^{-5}/2.20×10^{-5}
18GuChLiPe (Guan et al., 2018)				
011 - 000	1 - 6	16/16	2530 - 3015	5.20×10^{-5}/3.00×10^{-4}
19MaMc (Markus and McCall, 2019)				
011 - 000	0 - 6	36/36	2217 - 3008	1.67×10^{-4}/6.33×10^{-4}
022 - 000	1 - 4	7/7	4968 - 5094	2.16×10^{-4}/6.45×10^{-4}
022 - 011	0 - 5	15/15	2474 - 2945	1.48×10^{-4}/2.16×10^{-4}

Table 4.13: Components of the updated H_2D^+ MARVEL network. The network is broken down by the transition data sources and the vibrational bands contained within them, given in the form ν_1', ν_2', ν_3' - ν_1'', ν_2'', ν_3''. For each band, the transition energy and total angular momentum J ranges are provided, along with the mean and maximum uncertainties for these transitions. The total number of transitions validated and accessed by MARVEL (V/A) are also provided.

Vib.	J range	V/A	Energy range (cm^{-1})	Uncertainty Mean/Max (cm^{-1})
84AmWa (Amano and Watson, 1984)				
100 - 000	0 - 5	26/27	2841 - 3179	0.002/0.004
84BoDeDeDe (Bogey et al., 1984)				
000 - 000	1 - 1	1/1	12.423 - 12.423	6.67×10^{-6}/6.67×10^{-6}
84WaCoPeWo (Warner et al., 1984)				
000 - 000	1 - 1	1/1	12.423 - 12.423	3.34×10^{-6}/3.34×10^{-6}
85Amano (Amano, 1985)				
100 - 000	0 - 5	37/37	2839 - 3208	0.006/0.040
85SaKaHi (Saito et al., 1985)				
000 - 000	2 - 2	1/1	5.2032 - 5.2032	1.23×10^{-6}/1.23×10^{-6}
86FoMcPeWa (Foster et al., 1986a)				
001 - 000	0 - 5	42/42	2109 - 2602	0.006/0.042
010 - 000	0 - 7	31/31	1838 - 2537	0.004/0.005
02FaDaKo (Farnik et al., 2002)				
002 - 000	1 - 2	1/1	4538 - 4538	0.002/0.002
011 - 000	0 - 2	3/3	4423 - 4513	8.67×10^{-4}/0.001
020 - 000	1 - 2	4/4	4271 - 4394	0.001/0.002
05AmHi (Amano and Hirao, 2005)				
000 - 000	1 - 3	2/3	12.423 - 21.563	1.31×10^{-6}/1.67×10^{-6}
06Amano (Amano, 2006)				
000 - 000	1 - 3	3/3	85.9513 - 115	2.72×10^{-5}/3.34×10^{-5}
06Amano_MAGIC (Amano, 2006)				
000 - 000	0 - 1	1/1	60.030 - 60.030	1.00×10^{-5}/1.00×10^{-5}
06HlKoPlKo (Hlavenka et al., 2006a)				
021 - 000	0 - 2	3/3	6459 - 6491	0.021/0.031
07AsHuMuKu (Asvany et al., 2007)				
021 - 000	0 - 3	9/9	6341 - 6589	0.002/0.002
030 - 000	0 - 1	4/4	6242 - 6331	0.002/0.002
100 - 000	0 - 2	5/5	2947 - 3164	0.004/0.005
120 - 000	0 - 2	7/7	6946 - 7106	0.002/0.002
08AsRiMuWi (Asvany et al., 2008)				
000 - 000	0 - 1	1/1	45.701 - 45.701	6.67×10^{-7}/6.67×10^{-7}
09YoMaMoTa (Yonezu et al., 2009)				
000 - 000	0 - 3	8/8	5.2032 - 115	3.27×10^{-5}/2.01×10^{-4}
16JuKoScAs (Jusko et al., 2016)				
100 - 000	0 - 2	11/11	2887 - 3095	2.66×10^{-5}/1.50×10^{-4}
16JuKoScAs_CD (Jusko et al., 2016)				
000 - 000	0 - 2	4/4	66.4066 - 132	6.75×10^{-5}/1.51×10^{-4}
17JuToMuGh (Jusko et al., 2017)				
000 - 000	0 - 2	3/3	12.423 - 45.701	1.19×10^{-6}/3.07×10^{-6}

Table 4.14: Components of the updated D_2H^+ MARVEL network. The network is broken down by the transition data sources and the vibrational bands contained within them, given in the form v_1', v_2', v_3' - v_1'', v_2'', v_3''. For each band, the transition energy and total angular momentum J ranges are provided, along with the mean and maximum uncertainties for these transitions. The total number of transitions validated and accessed by MARVEL (V/A) are also provided.

Vib.	J range	V/A	Energy range (cm^{-1})	Uncertainty Mean/Max (cm^{-1})
84LuAm (Lubic and Amano, 1984)				
100 - 000	0 - 6	34/34	2638 - 2990	0.005/0.005
86FoMcWa (Foster et al., 1986b)				
001 - 000	0 - 5	35/35	1916 - 2291	0.005/0.005
010 - 000	0 - 6	53/53	1782 - 2280	0.004/0.005
90PoMc (Polyansky and McKellar, 1990)				
010 - 000	3 - 4	1/1	2276 - 2276	0.005/0.005
02FaDaKoPo (Farnik et al., 2002)				
002 - 000	0 - 2	6/6	3994 - 4066	6.17×10^{-4}/9.00×10^{-4}
011 - 000	0 - 2	6/6	3983 - 4122	0.002/0.004
020 - 000	0 - 2	4/4	3847 - 3887	0.003/0.004
03HiAm (Hirao and Amano, 2003)				
000 - 000	1 - 1	1/1	23.071 - 23.071	6.00×10^{-7}/6.00×10^{-7}
05AmHi (Amano and Hirao, 2005)				
000 - 000	0 - 2	3/3	23.071 - 49.254	1.00×10^{-5}/1.00×10^{-5}
06HlPlBa (Hlavenka et al., 2006b)				
102 - 000	0 - 3	3/3	6534 - 6536	0.005/0.005
07AsHuMuKu (Asvany et al., 2007)				
102 - 000	0 - 2	5/5	6467 - 6536	0.005/0.005
111 - 000	0 - 1	1/1	6581 - 6581	0.005/0.005
120 - 000	0 - 1	1/1	6482 - 6482	0.005/0.005
08AsRiMuWi (Asvany et al., 2008)				
000 - 000	0 - 1	1/1	49.254 - 49.254	5.00×10^{-7}/5.00×10^{-7}
16JuKoScAs (Jusko et al., 2016)				
100 - 000	0 - 2	10/10	2684 - 2866	8.80×10^{-6}/2.60×10^{-5}
17JuToMuGh (Jusko et al., 2017)				
000 - 000	0 - 2	3/3	23.071 - 49.254	2.08×10^{-7}/3.34×10^{-7}
17YuPeAmMa (Yu. et al., 2017)				
000 - 000	1 - 3	5/5	34.646 - 98.311	3.34×10^{-6}/3.34×10^{-6}
17YuPeAmMa_MAGIC (Yu. et al., 2017)				
000 - 000	0 - 1	1/1	34.918 - 34.918	1.00×10^{-5}/1.00×10^{-5}
19MaKoMc (Markus et al., 2019)				
100 - 000	0 - 5	37/37	2588 - 2928	6.83×10^{-5}/1.15×10^{-4}

Chapter 5

Vanadium Monoxide

5.1 Overview

Vanadium monoxide ($^{51}V^{16}O$) is known to exist in cool dwarfs due to its strong absorption spectra, where it is primarily observed in the near infrared (Keenan and Schroeder, 1952; Spinrad and Younkin, 1966; Wing et al., 1967; Spinrad and Wing, 1969; Kirkpatrick et al., 1991, 1993b,a; Cushing et al., 2005; Lançon et al., 2007; Rajpurohit et al., 2012; Liimets et al., 2022) and visible regions (Kamiński et al., 2010; Tylenda et al., 2011; Rajpurohit et al., 2014; Loebman et al., 2014) through rovibronic transitions in the A $^4\Pi$–X $^4\Sigma^-$, B $^4\Pi$–X $^4\Sigma^-$ and C $^4\Sigma^-$–X $^4\Sigma^-$ bands (Kirkpatrick et al., 1995; Sharp and Burrows, 2007). The strengths of these bands are used in the assignment of spectral classification to late M and early L dwarfs (Bernath, 2009). It has also been observed in the envelopes of supergiants (Fawley, 1977), red hypergiants such as VY CMa (Wallerstein, 1971; Humphreys et al., 2019; Dinh-V-Trung et al., 2022), asymptotic giant branch stars such as VX Sgr (Lockwood and Wing, 1982), Mira variables (Merrill et al., 1962; Wing and Lockwood, 1973; Castelaz et al., 2000; Goranskii and Barsukova, 2007; Kamiński et al., 2009; Tylenda et al., 2011), in circumstellar gas around protostars (Hillenbrand et al., 2012) and in protoplanetary disks (Ali-Dib et al., 2014). VO is also believed to be present in the atmospheres of hot and ultra-hot Jupiter exoplanets (Showman et al., 2009; Gandhi and Madhusudhan, 2019; Changeat et al., 2022; Coulombe et al., 2023) where some models suggest it acts as a driver of thermal inversions at high altitudes (Hubeny et al., 2003; Fortney et al., 2008; Lothringer et al., 2018). In both brown dwarfs and exoplanets, it is believed to be a strong source of opacities (Sharp and Burrows, 2007). Other studies argue that atmospheric cold traps could instead lead to the depletion of VO from the upper atmospheres (Spiegel et al., 2009), though this may not be the case in hotter atmospheres (Haynes et al., 2015; Evans et al., 2016). It is believed to be present in the likes of WASP-121b (Evans et al., 2016, 2017, 2018; Tsiaras et al., 2018; Goyal et al., 2020), WASP-18b (Coulombe et al., 2023) and HD 209458b (Désert et al., 2008; Showman et al., 2009; Schwarz et al., 2015) due to low-resolution studies, with the detection of atomic vanadium suggesting it is available to form gaseous species such as VO (Hoeijmakers et al., 2020); others suggest the presence of atomic Vanadium implies the VO has undergone thermal dissociation (Ben-Yami et al., 2020).

VO is a well-studied open shell diatomic molecule. The electronic structure

of VO has long been the subject of research, with many early investigations aiming to characterise the X $^4\Sigma^-$ ground state (Carlson and Moser, 1966; Kasai, 1968; Pykavy and van Wullen, 2003) and subsequent work focusing on its wealth of low-lying excited states (Veseth, 1975; Bauschlicher and Langhoff, 1986; Broclawik and Borowski, 2001; Miliordos and Mavridis, 2007; Uzunova et al., 2008; Jiang et al., 2021). As with other 3*d* transition metal oxides, the complex electronic structure of VO gives rise to complicated and dense spectra (Dolg et al., 1987; Merer, 1989; Bakalbassis et al., 1996; Bridgeman and Rothery, 2000; Uzunova et al., 2008; Kulik and Marzari, 2010). For VO, these complexities are the result of the three open-shell electrons, arising from the 23 electrons of Vanadium, five of which are unpaired, split over seven orbitals and the (3dσ + 3dπ) bond with Oxygen of triple bond character (Bauschlicher and Langhoff, 1986; Hübner et al., 2015; McKemmish et al., 2016a). In the ground state and some of the excited states, this bond is of triple bond character owing to covalent interactions between the V (3dσ) + O (2pσ) electrons and an ionic component from the donation of electrons from the O (2pπ) orbitals to the empty V (3dπ) orbitals (Miliordos and Mavridis, 2007; Gentleman et al., 2019). The bonding can be considered as in part between two neutral atoms and in part between two slightly charged ions (Bauschlicher and Maitre, 1995). The excited states arise either from excitations of the non-bonding V (4s) electron or excitations of likewise non-bonding electrons in the V (3dδ) orbital, hence the equilibrium bond lengths of all the electronic states considered here are similar. The problem is further complicated both by the large number of strong resonances between the densely packed electronic states (Lagerqvist and Selin, 1957; Cheung et al., 1982a; Merer et al., 1987; Merer, 1989; Cheung et al., 1994; Adam et al., 1995; Hopkins et al., 2009) and the need to consider hyperfine splittings in a number of key states (Hocking et al., 1981; Cheung et al., 1982a; Suenram et al., 1991; Adam et al., 1995; Flory and Ziurys, 2008; Döring et al., 2022). While polyatomic vanadium oxides have been analysed for their material properties (Calatayud et al., 2001; Du et al., 2008), with many forms being semiconductors (Hu et al., 2023) with potential supercapacitor applications (Gamal et al., 2024), VO is stable at high temperatures and occurs primarily in the gas phase.

A high-temperature, rovibronic and hyperfine-unresolved ExoMol line list for VO was produced by McKemmish et al. (2016b), which considered 13 of the lowest electronic states and was computed based on empirically-determined Morse-oscillator potentials for most states and *ab initio* coupling curves from MRCI calculations (McKemmish et al., 2016a). Dubbed the VOMYT line list after the author's initials, this line list had failed to provide a detection of VO in an exoplanet atmosphere (Hoeijmakers et al., 2020; Merritt et al., 2020, 2021; de Regt et al., 2022; Johnson et al., 2023), until a claim by a recent study of WASP-76b (Pelletier et al., 2023). A contributing factor to these non-detections is likely the omission of hyperfine couplings from the spectroscopic model and hence no hyperfine splittings in the spectra generated from it. Hyperfine effects are believed to be important in VO due to the large nuclear spin on the ^{51}V atom of $I = \frac{7}{2}$ and due to it having one of the largest magnetic dipole moments of any stable nucleus (Stone, 2005). These effects split spectral lines into multiple hyperfine components which in extreme

cases can be separated by more than 0.5 cm^{-1} and considerably change the structure of observed line profiles. The presence of these effects in the rovibronic spectra of VO has been known for some time (Richards and Barrow, 1968b), with the energy level splitting being largest in the X $^4\Sigma^-$ ground state. This results in substantially blended spectra for any bands transitioning to the ground state when observed below hyperfine resolution (Merer, 1989). As such, proper treatment of hyperfine effects is necessary to produce a VO line list well suited to a versatile range of high-resolution studies.

One issue that required addressing was the separation between the doublet and quartet states, which, while known approximately due to *ab initio* calculations, was not known to experimental accuracy. Hopkins et al. (2009) recorded an intercombination 2 $^2\Pi$–X $^4\Sigma^-$ band spectrum for VO however, though it had not initially been assigned. A series of new assignments to the 2 $^2\Pi$–X $^4\Sigma^-$ bands originally measured by Hopkins et al. (2009) are presented here, which allowed for the connection of the doublet and quartet states into a single spectroscopic network and for the determination of their energies on the same energy scale.

Fig. 5.1 details the known and predicted low-lying electronic states of VO, highlighting those considered explicitly in this work. Perturbation theory-based effective Hamiltonians have been extensively used to represent the energy levels of VO (Cheung et al., 1982a,b; Merer et al., 1987; Huang et al., 1992; Cheung et al., 1994; Adam et al., 1995; Karlsson et al., 1997; Ram et al., 2002; Ram and Bernath, 2005; Flory and Ziurys, 2008; Hopkins et al., 2009). However, given the large number of observed perturbations in the spectra of VO and the large number of electronic state crossing seen in *ab initio* potential calculations, effective Hamiltonian calculations are unlikely to adequately characterise the perturbations and resonances (Tennyson et al., 2016a), see Section 2.1.

VO is a considerably more complicated system than many of the other diatomics studied by the ExoMol project previously and a number of preparatory steps were undertaken to facilitate the production of a new hyperfine-resolved line list. Section 5.3 presents a MARVEL study that was performed for rovibronic transitions between 13 of the 15 electronic states considered here, adapted from its publication in Bowesman et al. (2022), obtaining 4 402 hyperfine-resolved energy levels and a further 4 712 hyperfine-unresolved levels. These MARVEL networks were subsequently extended with the newly available experimental results of Döring et al. (2022). Qu et al. (2022a) developed a fully hyperfine-resolved version of the workhorse variational diatomic nuclear motion program DUO (Yurchenko et al., 2016b); they used this program to develop a hyperfine-resolved model for the VO electronic ground state (Qu et al., 2022b), which is expanded here to include additional hyperfine-resolved electronic states. Qu et al. (2023) also developed a preliminary, hyperfine-unresolved, 11 electronic state model for VO. These steps all provided essential input for the work presented here. Section 5.4.1 presents the comprehensive model of 15 low-lying electronic states of VO that was constructed to facilitate the production of a new line list, adapted from its publication (Bowesman et al., 2024b). The output of this new model was MARVELised, and predicted shifts were fit to produce a hybrid line list fit for use in high-resolution studies. The dipoles for three crucial electronic bands

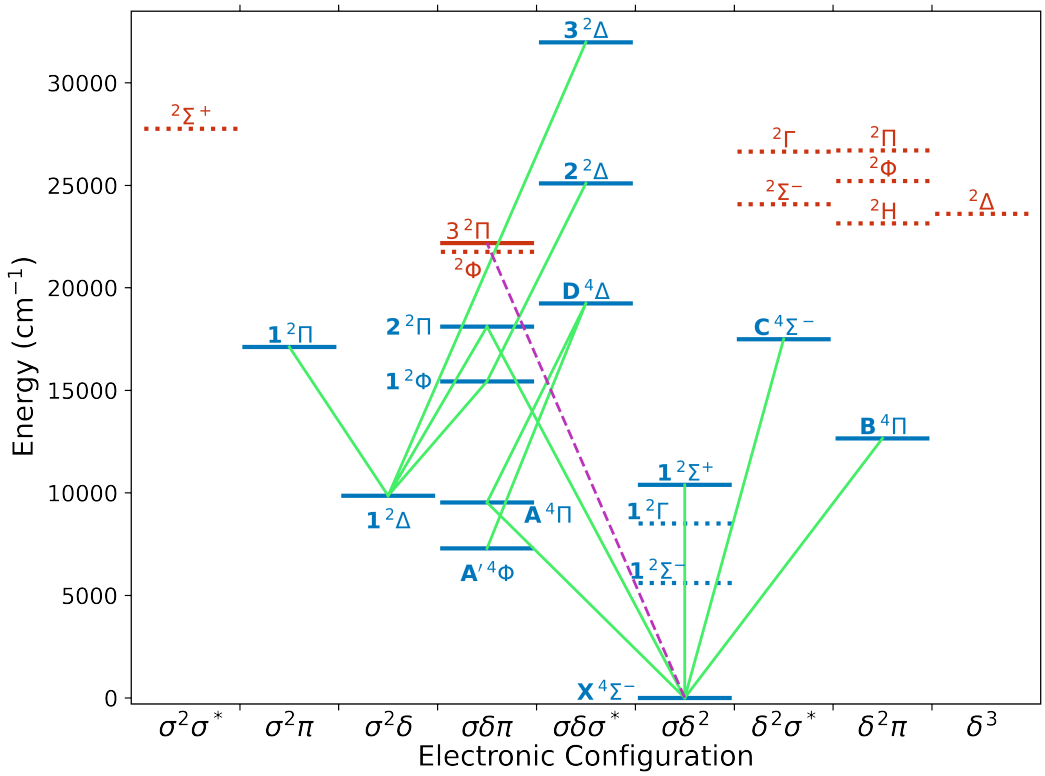


Fig. 5.1: Electronic states of $^{51}V^{16}O$ and the observed transitions between them, arranged based on their dominant electron configuration. States marked in blue are included in the new line list and those in red are not. States marked with a solid horizontal line are known from experiment while those marked with a dotted line are from *ab initio* calculations. The 3 $^2\Pi$ state was observed by Hopkins et al. (2009) through 3 $^2\Pi$–X $^4\Sigma^-$ bands that are unassigned and are marked in purple. Energies for the unobserved, *ab initio* doublets are taken from the calculations of Hübner et al. (2015).

were also adjusted based on experimental lifetime measurements of Karlsson et al. (1997) and the results of this update are adapted from their publication in Bowesman et al. (2024a).

5.2 Experimental data sources

The electronic structure of VO has been discussed at great length in the literature over the years (Carlson and Moser, 1966; Kasai, 1968; Veseth, 1975; Bauschlicher and Langhoff, 1986; Dolg et al., 1987; Merer, 1989; Bridgeman and Rothery, 2000; Calatayud et al., 2001; Broclawik and Borowski, 2001; Pykavy and van Wullen, 2003; Mackrodt et al., 2004; Du et al., 2006; Miliordos and Mavridis, 2007; Du et al., 2008; Uzunova et al., 2008; Kulik and Marzari, 2010; Hübner et al., 2015; Gentleman et al., 2019; Merriles et al., 2020; Jiang et al., 2021). This substantial coverage ensured any outdated transition assignments relating to fine structure or electronic state designation present in older sources could easily be updated and relabelled using the specified quantum numbers. Some sources that were considered when collecting data to build the spectroscopic networks were ultimately not included, either because their reported transitions did not include complete assignments or because their transitions were only reported qualitatively and without individual transitions wavenumbers (Mahanti, 1935; Lagerqvist and Selin, 1957; Richards and Barrow, 1968a; Laud and Kalsulka, 1968; Dyke et al., 1985). Others exclusively report measurements of perturbed transitions where the perturbing state has not been identified (Cheung et al., 1981). Multiple data sources report transitions affected by the internal hyperfine perturbations arising from a crossing between the F_2 and F_3 fine structure components discovered by Richards and Barrow (1968a). With experimental data that is hyperfine resolved it is possible to fully assign such perturbations, though there are also instances of Doppler-limited observations where these internal hyperfine perturbations have been assigned (Cheung et al., 1982b; Adam et al., 1995). Internal hyperfine and unconfirmed electronic state perturbations are differentiated in the MARVEL input file by appending '_PH' and '_PE' respectively to the end of the electronic state label.

5.2.1 MARVELised data sources

To construct a MARVEL network for VO, a consistent set of quantum number labelling was introduced for all transitions data. Each state was labelled by its electronic state term symbol, a fine structure configuration (F_1, F_2, F_3 or F_4), the projection of the total electronic angular momentum Ω, total parity (+/-), vibrational quantum number v and total angular momentum quantum number J. Observed VO transitions involve states best described by Hund's case (b) couplings in the observed $\Lambda = 0$, $^4\Sigma^-$ and $^2\Sigma^+$ states, including the ground state, or by case (a) coupling otherwise. Even where case (b) is used however, there are instances at low J where this breaks down and is better described by case (a) (Cheung et al., 1982a). Because of this, both Ω and fine structure are provided even though one is in most cases redundant.

Hyperfine-resolved transitions are also identified by the additional quantum number F. Typically, given MARVEL requires all states to have the same set of quantum number labels, these F values would either have to be removed or these transitions separated into another network. At the start of this work there were

no assigned intercombination bands in the literature and none of the doublet state transitions had been observed with hyperfine resolution, hence three networks were initially constructed. The first network comprised all hyperfine-resolved quartet transitions; the second contained hyperfine-unresolved quartets and the third contained the (hyperfine-unresolved) doublet transitions. Section 5.2.3 discusses the assignment of the 2 $^2\Pi$–X $^4\Sigma^-$ band system spectra which allowed for the creation of a single, unified network of hyperfine-unresolved transitions. The hyperfine-resolved transitions were used both for deperturbation to supplement the unified hyperfine-unresolved network and to produce a separate, hyperfine-resolved network.

The following 14 data sources provide data that are included in the spectroscopic network of VO described here:

57LaSe: Lagerqvist and Selin (1957) report 1 168 measured R- and P-branch C $^4\Sigma^-$–X $^4\Sigma^-$ transitions, 28 of which are perturbed by an unconfirmed electronic state. These branches are provided with the subscripts 'a' and 'b' in place of fine structure notation as this was not explicitly determined in the original work. It was confirmed that these subscripts corresponded to the F_3 and F_2 fine structure components respectively through the analysis of combination differences and by checking their consistency with the rest of the MARVEL network.

81HoMeMi: Hocking et al. (1981) provide 48 hyperfine-resolved C $^4\Sigma^-$–X $^4\Sigma^-$ transition measurements.

82ChHaMe: Cheung et al. (1982a) provide measurements for 2 834 hyperfine-resolved C $^4\Sigma^-$–X $^4\Sigma^-$ transitions, 17 of which are perturbed by an unconfirmed electronic state. Their observations included a number of internal hyperfine perturbations which they were able to fully assign.

82ChTaMe: Cheung et al. (1982b) report 1 058 A $^4\Pi$–X $^4\Sigma^-$ transition measurements, 7 of which exhibit internal hyperfine perturbations.

87MeHuChTa: Merer et al. (1987) provide 1 289 measurements for transitions involving quartet states, split between the D $^4\Delta$–A′ $^4\Phi$ (980 transitions, 2 of which are perturbed) and D $^4\Delta$–A $^4\Pi$ (309) bands. They also give measurements for 1 139 doublet transitions split between the 1 $^2\Pi$–1 $^2\Delta$ (885), 2 $^2\Pi$–1 $^2\Delta$ (81) and 2 $^2\Delta$–1 $^2\Phi$ (173) bands. Of these, 744 quartet and 411 doublet transitions are reported with unresolved Λ-doubling and hence had no parity assignment. Such transitions were entered into the MARVEL input file twice with both applicable upper and lower state total parity (+/-) combinations.

91SuFrLoGi: Suenram et al. (1991) report three very high accuracy measurements of hyperfine transitions within the X $^4\Sigma^-$ ground state.

94ChHaHuHu: Cheung et al. (1994) provide measurements for 471 B $^4\Pi$–X $^4\Sigma^-$ transitions, 7 of which are perturbed by the 1 $^2\Sigma^+$, $v = 3$ state. This perturbing state was initially labelled the a $^2\Sigma^+$ state but was updated to be consistent with the naming scheme for the other doublet electronic states, where each electronic state symmetry is numbered sequentially starting from the lowest energy instance.

95AdBaBeBo: Adam et al. (1995) provide two sets of data: 3 534 hyperfine-resolved and 776 hyperfine-unresolved B $^4\Pi$–X $^4\Sigma^-$ transitions. 14 of the hyperfine-resolved and 8 of the hyperfine-unresolved transitions are perturbed by the 1 $^2\Sigma^+$, $v = 2$ state, in addition to 22 further hyperfine-unresolved transitions perturbed by

an unknown state. As with the data of Cheung et al. (1994) the perturbing state was updated from its initial a $^2\Sigma^+$ label.

97KaLiLuSa: Karlsson et al. (1997) report 47 measured A $^4\Pi$–X $^4\Sigma^-$ transitions.

02RaBeDaMe: Ram et al. (2002) provide 218 measurements of transitions in the 1 $^2\Phi$–1 $^2\Delta$ band with no observed Λ-doubling and hence no parity assignment. As with the data from Merer et al. (1987), these transitions were each entered twice with both applicable upper and lower state parity combinations.

05RaBe: Ram and Bernath (2005) report 166 transitions in the 3 $^2\Delta$–1 $^2\Delta$ band with no observed Λ-doubling. Again, each transition was input twice with both applicable upper and lower state parity combinations.

08FlZi: Flory and Ziurys (2008) report 224 ground state, pure rotation X $^4\Sigma^-$–X $^4\Sigma^-$ hyperfine transitions. They observed the effects of the same internal hyperfine perturbation described by other sources but were able to fully assign the affected transitions. Four of these very high-accuracy transitions were inconsistent with hyperfine transitions from Cheung et al. (1982a) and Adam et al. (1995). Through comparisons with the ground state hyperfine calculations of Qu et al. (2022a) it was determined that the four transitions from this source were incorrect and had likely been misassigned.

08SrBaRaBa: Sriramachandran et al. (2008) provide measurements for 68 C $^4\Sigma^-$–X $^4\Sigma^-$ transitions observed in sunspot spectra. These measurements are assigned based on the data of Lagerqvist and Selin (1957), and as such also reported R- and P-branch transitions with 'a' and 'b' subscripts; their assignments were also updated to F_3 and F_2 fine structure components respectively. 11 of these transitions, all in the (0,2) band, had been reported with the incorrect R-/P-branch labelling and were corrected here.

09HoHaMa: Hopkins et al. (2009) observed crucial spin-forbidden intercombination transitions in the 2 $^2\Pi$–X $^4\Sigma^-$ band system that connect the quartet components of the spectroscopic network to the doublets via the transitions involving the 2 $^2\Pi$ state reported by Merer et al. (1987). The original spectra recorded by Hopkins et al. (2009) was revisited and assigned as part of this work to ensure the key connection between spin components of the VO network was correct; this assignment process is discussed in Section 5.2.3. Assignments for transitions involving the 2 $^2\Pi_{3/2}$, $v = 0$ state could be validated against the doublet data of Merer et al. (1987), whereas the 2 $^2\Pi_{1/2}$ bands had no other observations to compare against. This meant that while combination differences could be checked for the level energies of the 2 $^2\Pi_{3/2}$ spin-orbit component between sources, the 2 $^2\Pi_{1/2}$ component could only be ensured to be self-consistent. In total, 190 transitions were assigned in these spectra. An unassigned 3 $^2\Pi$–X $^4\Sigma^-$ band system is also reported, though no attempt was made to assign these spectra as they do not provide further connections to the rest of the doublet network.

22DoFuGi: Döring et al. (2022) presented 1 439 hyperfine-resolved ground state rovibrational transitions in the X $^4\Sigma^-$-X $^4\Sigma^-$ (1,0) and (2,1) bands. The high-resolution data was provided with an experimental uncertainty of 5×10^{-4} cm^{-1} and provided the majority of the experimental knowledge of the hyperfine-resolved

levels of the X $^4\Sigma^-$, $v = 1, 2$ states. These data were kindly made available after the publication of the initial MARVEL study and was crucial in the accurate determination of ground state energies and hence for fitting the hyperfine-resolved spectroscopic model. While the cited reference for this source is a conference talk, the full publication will be forthcoming.

While the initial MARVEL study of Bowesman et al. (2022) was constructed using MARVEL version 3.0, the final updated network discussed here was produced using version 4.1.

5.2.2 Connecting the doublet and quartet manifolds

5.2.3 New spectra assignment

Assignments of the spectra reported by Hopkins et al. (2009) were carried out by first performing rough calculations to provide an initial estimate for the transition frequencies. These estimates were produced for every expected set of P-, Q- and R-branch transitions in the observed bands and were generated using molecular constants published by Hopkins et al. (2009). These predictions were calculated using Eqs. (1) and (2) of Hopkins et al. (2009), and were only dependent on the rotational constant B_v, the centrifugal distortion constant D_v, the spin-orbit coupling constant A_v and the Ω-doubling constant p_v and as such minor deviations from the predicted values were to be expected.

Rotational branch assignments in this section make use of the ${}^{\Delta N}\Delta J_{F_n' F_n''}$ notation. Here $\Delta J = J' - J'' = -1, 0, +1$ which take the "P", "Q" and "R" shorthand respectively and the F_n numerical subscripts refer to the upper and lower state fine structure components. Due to the upper state being a doublet and the lower state a quartet, containing two and four fine structure components and hence as many possible N values for each J, the ΔN notation is extended. The $\Delta N = N' - N''$ notation uses lowercase letters and can take values from "n", corresponding to $\Delta N = -3$, to "t", with $\Delta N = +3$.

When assigning transitions in the 2 $^2\Pi_{1/2}$–X $^4\Sigma^-$ (0,0) band, it was possible to make assignments to at least one transition in 11 out of the 12 possible P-, Q- and R-branches. It was only the $^{q}P_{11}$ branch where it was not possible to assign any transitions, due to the initial predictions showing the band to start around 18 048 cm^{-1} and reflect back on itself at a band head at 18 050 cm^{-1}. Similarly, the predictions showed the $^{q}Q_{12}$ branch forming a band head at around 18 046 cm^{-1}. In this case the branch reflects back on itself twice, explaining the extremely blended, high intensity feature observed on the lower energy side of the band origin. As such it was only possible to confidently assign the first transition in this branch. These features can be seen in Fig. 5.2, along with the rest of the final assignments to the 2 $^2\Pi_{1/2}$–X $^4\Sigma^-$ (0,0) spectrum. With some coverage of almost all branches, 103 transitions in the 2 $^2\Pi_{1/2}$–X $^4\Sigma^-$ (0,0) spectrum were assigned with individual transitions frequencies provided in Table 5.1.

Upon reanalysing the 2 $^2\Pi_{3/2}$–X $^4\Sigma^-$ (0,0) data, lines from the $^{t}R_{21}$, $^{s}Q_{21}$, $^{s}R_{22}$, $^{q}P_{22}$, $^{p}P_{23}$ and $^{o}P_{24}$ branches were identified and assigned. The $^{r}P_{21}$ branch was predicted to fall near the heavily congested band origin and similarly the $^{r}Q_{22}$ and $^{r}R_{23}$ branches were both reflected at their band heads near the origin, significantly

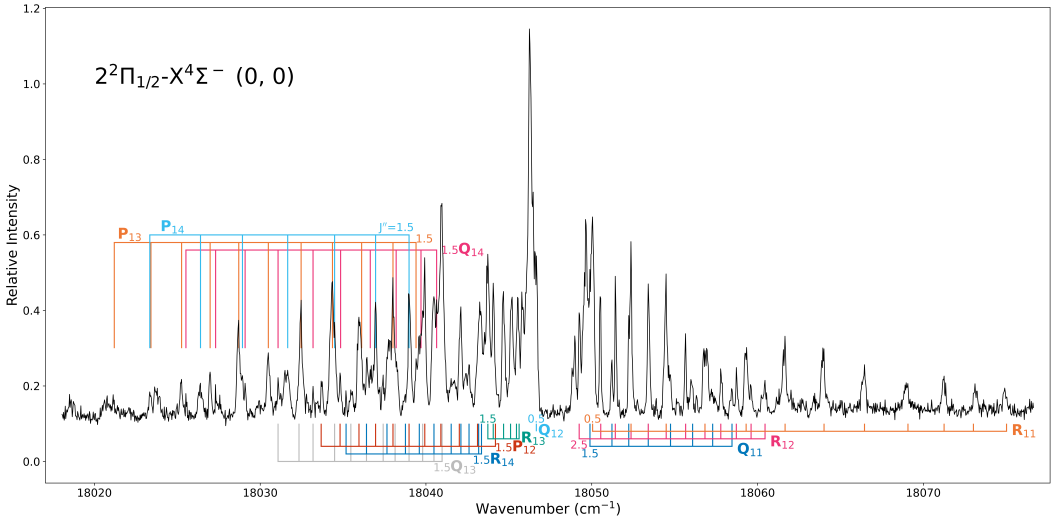


Fig. 5.2: Assigned branches of the 2 $^2\Pi_{1/2}$–X $^4\Sigma^-$ (0,0) spectrum measured by Hopkins et al. (2009). Each branch is marked with the lowest value of J″ in the series. Molecular constants fit to this spectrum are given in Table 5.2.

overlapping one another and making individual line assignments impossible at this resolution. As such, further high-resolution study near the band origin would be needed to confidently assign these branches. The $^qQ_{23}$, $^qR_{24}$ and $^pQ_{24}$ branches were similarly blended or too weak to assign. The transitions of the six assigned branches of the 2 $^2\Pi_{3/2}$–X $^4\Sigma^-$ (0,0) system are shown in Fig. 5.3. Some branches rapidly became much weaker and were obscured by transitions from other branches, as can be seen with the $^pP_{23}$ branch and the more extensively assigned, stronger $^oP_{24}$ branch. As such, only 56 transitions from the 2 $^2\Pi_{3/2}$–X $^4\Sigma^-$ (0,0) spectrum were assigned; these are given in Table 5.1.

While assigning the 2 $^2\Pi_{3/2}$–X $^4\Sigma^-$ (0,0) spectrum, a discrepancy was noticed in the $^tR_{21}$ and $^oP_{24}$ branches for lines between $J'' = 7.5 - 11.5$. For both branches, lines in this region appear at slightly higher wavenumbers than their predicted positions, shifted by up to ~0.75 cm^{-1}. This shift appears suddenly at $J'' = 7.5$, after which predictions gradually tend back to being consistent with observations, lining up well again at $J'' = 11.5$. The $^tR_{21}$ branch could be assigned beyond this, where observed line centres begin to shift to slightly lower wavenumbers than their predicted values and are assigned up to $J'' = 13.5$. Above this point, transitions in these bands are too weak to assign. Comparing against calculated term energies for the lower, X $^4\Sigma^-$ state, these two branches displayed obs.-calc. residuals as a function of J'' that sharply increase at $J'' = 7.5$ before gradually returning to scatter about zero. It is likely that these transitions are perturbed by another nearby state, but it was not clear which. While the C $^4\Sigma^-$, $v = 1$ state is nearby and can be seen in Fig. 5.3, the relevant J levels are not close enough.

The final spectrum to be assigned was that of a 2 $^2\Pi_{1/2}$–X $^4\Sigma^-$ (1,0) band. Here considerably fewer assignments were made than in the previous spectra as the majority of the branches that were not obscured in band heads were too heavily blended to confidently make any assignments. As such, assignments were only

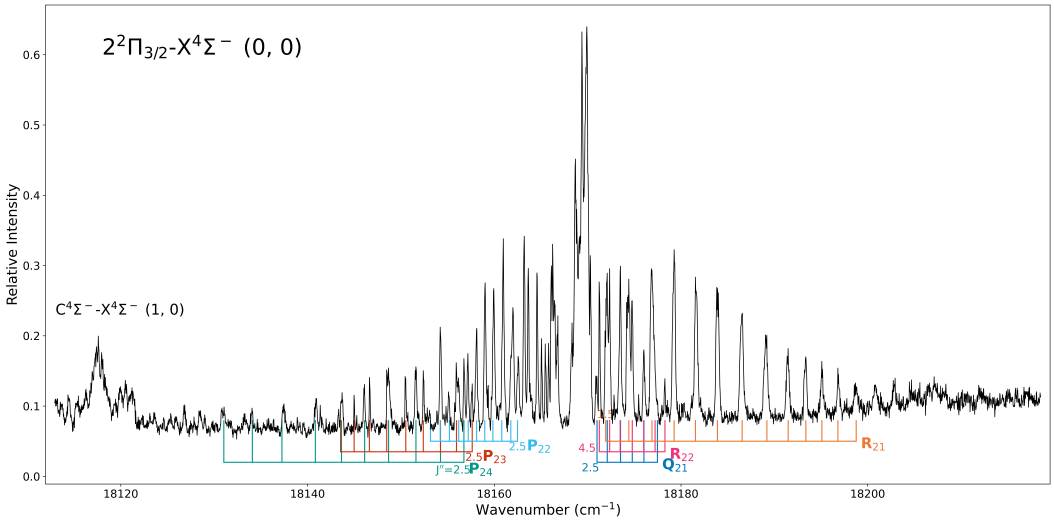


Fig. 5.3: Assigned branches of the 2 $^2\Pi_{3/2}$–X $^4\Sigma^-$ (0,0) spectrum measured by Hopkins et al. (2009). Each branch is marked with the lowest value of J′′ in the series. Molecular constants fit to this spectrum are given in Table 5.2. The unresolved profile of the C $^4\Sigma^-$–X $^4\Sigma^-$ (1,0) band is marked on the left edge of the plot.

made to transitions in the $^sR_{11}$, $^rQ_{11}$ and $^rR_{12}$ branches, all of which lie to the blue of the band origin where the spectrum is significantly less dense, as can be seen in Fig. 5.4. The 34 lines assigned to this band must be considered less reliable as they have fewer transitions to compare combination differences with or for the MARVEL procedure to evaluate their consistency against. While this higher vibrational band does not increase the connectivity between the quartet and doublet components of the network, it does provide information on the 2 $^2\Pi$ state vibrational excitation energy, which is useful for *ab initio* calculations and spectroscopic models.

The 2 $^2\Pi_{3/2}$ system took two attempts to assign in order to produce consistent data, whereas it only took a single attempt to assign a set of self-consistent transitions to both vibrational bands of the 2 $^2\Pi_{1/2}$ component. The majority of lines in these spectra are blended to some degree, especially lines to the red of the band origins; a conservative base uncertainty of 0.2 cm^{-1} was used for all newly assigned transitions. MARVEL and the method of combination differences were used to check the consistency of the final assignments by ensuring that the standard deviation of the energy of a given level was less than the uncertainty of the constituent transitions that defined that level.

5.2.4 Unresolved doublet spin-orbit separations

As the doublet and quartet networks were only initially connected through one spin-orbit component of the 2 $^2\Pi$ state, half of the doublet network was still unconnected. This was because all of the sources reporting doublet transitions exclusively observed P- and R-branch transitions, which for Merer et al. (1987) and Ram et al. (2002) had $\Delta\Omega = \pm 1$ and for Ram and Bernath (2005) $\Delta\Omega = 0$. This meant the 1 $^2\Delta_{3/2}$, 1 $^2\Pi_{1/2}$, 1 $^2\Phi_{5/2}$, 2 $^2\Delta_{3/2}$ and 3 $^2\Delta_{3/2}$ states were not connected to the quartet states via the newly assigned intercombination transitions observed by Hopkins et al. (2009)

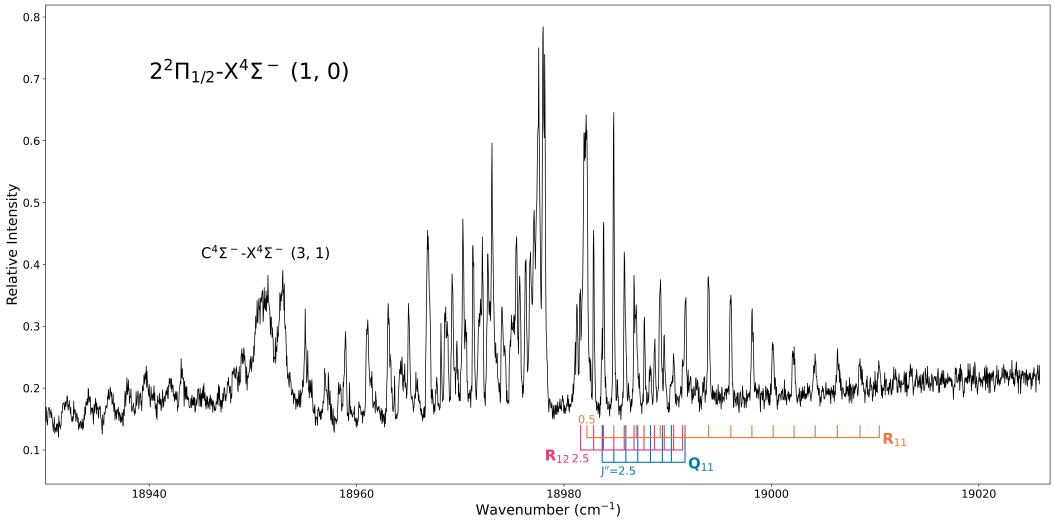


Fig. 5.4: Assigned branches of the 2 $^2\Pi_{1/2}$–X $^4\Sigma^-$ (1,0) spectrum measured by Hopkins et al. (2009). Each branch is marked with the lowest value of J′′ in the series. Molecular constants fit to this spectrum are given in Table 5.2. The unresolved profile of the C $^4\Sigma^-$–X $^4\Sigma^-$ (3, 1) band is marked on the plot.

and were split into two subgraphs based on their parity. This was rectified through the addition of calculated transition wavenumbers for both e→f and f→e parity Q_{21} (5.5) transitions in the 1 $^2\Delta$–1 $^2\Delta$ (0,0) band. These were derived from levels in the VOMYT line list, effectively estimating the spin-orbit splitting in the 1 $^2\Delta$ state which has not yet been observationally determined (Ram et al., 2002; Ram and Bernath, 2005). These were input as 356.596842 cm^{-1} for the Q_{21ef} (5.5) transition and 356.596837 cm^{-1} for Q_{21fe} (5.5). Both transitions are provided in the MARVEL input file with the source tag VOMYT_MAGIC. The 1 $^2\Delta$ state was chosen as it is both the lowest energy doublet state observed and the state involved in the most transitions within the doublet network. The value of $J = 5.5$ was chosen as it was the lowest value of J for which both parity levels in each spin-orbit component existed within the doublet data. This connection represents a weak point in the network and would benefit from observations involving the newly assigned 2 $^2\Pi_{1/2}$ state, such as the unobserved 2 $^2\Pi_{1/2}$—1 $^2\Delta_{3/2}$ band.

5.2.5 Effective Hamiltonian parameters for doublet states

Molecular constants were determined from effective Hamiltonian fits to the newly assigned spectra using the effective Hamiltonian form used by Ram et al. (2002), Ram and Bernath (2005) and Hopkins et al. (2009),

$$\begin{aligned} E(J) =& T_v + B_v J(J+1) - D_v (J(J+1))^2 + H_v (J(J+1))^3 \\ & \pm \frac{1}{2}\left(p_v \left(J+\frac{1}{2}\right) + p_{D_v} \left(J+\frac{1}{2}\right)^3 \right), \end{aligned} \tag{5.1}$$

where T_v is the origin of the v vibrational band, B_v is the rotational constant, D_v the quartic distortion to the rotation, H_v the sextic distortion to the rotation, p_v is the

Table 5.1: Assigned transitions of the 2 $^2\Pi$–X $^4\Sigma^-$ spectra reported by Hopkins et al. (2009) and reanalysed in this work.

					2 $^2\Pi_{1/2}$–X $^4\Sigma^-$ (0,0)						
J''	$^sR_{11}$	$^rQ_{11}$	$^rR_{12}$	$^qQ_{12}$	$^pP_{12}$	$^qR_{13}$	$^pQ_{13}$	$^oP_{13}$	$^pR_{14}$	$^oQ_{14}$	$^nP_{14}$
0.5	18050.05			18046.66							
1.5	18052.37	18049.89			18044.19	18043.73	18040.97	18039.40	18043.35	18040.64	18038.98
2.5	18054.49	18051.22	18049.24		18043.11	18044.06	18040.48	18038.01	18043.18	18039.70	18036.96
3.5	18056.83	18052.23	18050.54		18042.01	18044.68	18039.80	18036.12	18042.60	18038.20	18034.49
4.5	18059.31	18053.41	18051.42		18040.90	18045.10	18038.98	18034.36	18042.11	18036.64	18031.66
5.5	18061.66	18054.75	18052.37		18039.93	18045.46	18038.14	18032.47	18041.52	18034.85	18028.93
6.5	18064.01	18056.08	18053.41		18038.98	18045.62	18037.42	18030.49	18040.48	18033.19	18026.40
7.5	18066.45	18057.29	18054.49		18038.01		18036.41	18028.71	18039.60	18031.08	18023.34
8.5	18069.07	18058.46	18055.66		18036.96		18035.47	18026.98	18038.76	18029.09	
9.5	18071.25		18056.83		18035.96		18034.49	18025.26	18037.65	18027.31	
10.5	18073.02		18057.78		18034.82		18033.19	18023.41	18036.41	18025.52	
11.5	18075.02		18058.72		18033.68		18032.34	18021.20	18035.18		
12.5			18059.61				18031.08				
13.5			18060.45								

	2 $^2\Pi_{3/2}$–X $^4\Sigma^-$ (0,0)							2 $^2\Pi_{1/2}$–X $^4\Sigma^-$ (1,0)		
J''	$^tR_{21}$	$^sQ_{21}$	$^sR_{22}$	$^qP_{22}$	$^pP_{23}$	$^oP_{24}$	J''	$^sR_{11}$	$^rQ_{11}$	$^rR_{12}$
0.5							0.5	18982.21		
1.5	18171.93						1.5	18984.80		
2.5	18174.41	18171.01		18162.49	18157.64	18156.75	2.5	18986.97	18983.69	18981.60
3.5	18176.89	18172.10		18161.77	18155.95	18154.24	3.5	18989.28	18984.80	18982.86
4.5	18179.27	18173.52	18171.25	18160.81	18154.24	18151.61	4.5	18991.69	18985.96	18983.80
5.5	18181.55	18174.78	18172.36	18159.85	18152.40	18148.68	5.5	18993.93	18987.11	18984.80
6.5	18183.90	18176.03	18173.49	18158.98	18150.52	18146.11	6.5	18996.09	18988.34	18985.81
7.5	18186.55	18177.48	18174.78	18158.11	18148.77	18143.64	7.5	18998.12	18989.49	18986.75
8.5	18189.20		18176.00	18157.21	18146.63	18140.84	8.5	19000.17	18990.36	18987.72
9.5	18191.48		18177.22	18156.19	18144.99	18137.26	9.5	19002.19	18991.67	18988.73
10.5	18193.37		18178.28	18155.20	18142.87	18134.09	10.5	19004.22		18989.67
11.5	18195.09			18154.21		18131.03	11.5	19006.35		18990.57
12.5	18196.81			18153.16			12.5	19008.55		18991.44
13.5	18198.77						13.5	19010.40		

Ω-doubling constant and p_{D_v} the cubic distortion to the Ω-doubling. It should be noted that while the construction of the effective Hamiltonian in Eq. (5.1) is different to that of the standard implementation in programs like PGOPHER (Western, 2017) and while the rotational terms are similar, the Ω-doubling terms are not. The fits were corroborated to ensure the empirical energies determined through MARVEL were reproduced to a reasonable accuracy. In the 2 $^2\Pi_{3/2}$, $v = 0$ state, the constants also reproduce the higher-J levels known from the data of Merer et al. (1987) well, though the perturbed levels at $J = 50.5, 51.5, 62.5, 63.5, 64.5$ were excluded from the fit. These constants are tabulated in Table 5.2. The value of D_v was kept constant for the 2 $^2\Pi_{1/2}$ state, with a value of 6×10^{-7} cm^{-1} as attempts to float it yielded very high standard deviation results. This is likely because D_v scales with J^4 and the spectra being fit went no higher than $J = 14.5$ in the 2 $^2\Pi_{1/2}$, $v = 0, 1$ states, leaving it very poorly determined. Additional observations to higher J would help to better constrain the value of this constant. With the doublet network connected to the quartet ground state via the 2 $^2\Pi_{3/2}$–X $^4\Sigma^-$ (0,0) data, T_v values could be determined for the other doublet states. The resulting values are consistent with the relative doublet T_v energy differences reported in the literature, where absolute determination of the energy scale had not been possible due to the missing doublet-quartet connection (Merer et al., 1987; Ram et al., 2002; Ram and Bernath, 2005). Values were fit for the rotational constant B_v and the quartic centrifugal distortion

Table 5.2: Molecular constants (cm^{-1}) for the doublet states of VO contained with the Marvel network, including the 2 $^2\Pi$ states observed in the newly assigned 2 $^2\Pi$–X $^4\Sigma^-$ spectra. Values provided in parentheses are the standard deviation in units of the last digit; entries without standard deviations were fixed in the fit.

State	v	T_v	B_v	$10^7 \times D_v$	$10^{11} \times H_v$	p_v	p_{D_v}
1 $^2\Delta_{3/2}$	0	9684.106(14)	0.550790(70)	6.01(80)	−4.2(24)		
1 $^2\Delta_{3/2}$	1	10676.980(19)	0.546732(81)	7.27(83)	−8.7(24)		
1 $^2\Delta_{5/2}$	0	10040.7413(31)	0.552050(18)	2.93(25)	−48.7(94)		
1 $^2\Phi_{5/2}$	0	15223.558(11)	0.518948(29)	5.91(13)			
1 $^2\Phi_{7/2}$	0	15592.41964(99)	0.520613 3(31)	6.251(18)			
1 $^2\Pi_{1/2}$	0	16940.523(12)	0.518550(30)	6.18(14)		$2.901(36)\times10^{-2}$	-3.87×10^{-7}[a]
1 $^2\Pi_{1/2}$	1	17867.809(11)	0.515299(30)	6.39(14)		$3.040(37)\times10^{-2}$	-3.60×10^{-7}[a]
1 $^2\Pi_{1/2}$	2	18785.930(31)	0.511792(89)	5.68(49)		$3.62(21)\times10^{-2}$	$-6.0(17)\times10^{-6}$
1 $^2\Pi_{1/2}$	3	19694.193(19)	0.508507(75)	6.94(57)		$3.374(55)\times10^{-2}$	
1 $^2\Pi_{3/2}$	0	17188.4518(16)	0.521 1118(50)	6.627(28)		$-5.1(14)\times10^{-4}$	$8.0(11)\times10^{-7}$
1 $^2\Pi_{3/2}$	1	18115.4449(29)	0.518076(14)	6.80(12)			
2 $^2\Pi_{1/2}$	0	18048.052(25)	0.52177(28)	6.00[b]		$3.39(96)\times10^{-2}$	$1.59(71)\times10^{-4}$
2 $^2\Pi_{1/2}$	1	18980.000(80)	0.52011(75)	6.00[b]		$-4.79(11)\times10^{-3}$	
2 $^2\Pi_{3/2}$	0	18167.7181(64)	0.526394(20)	5.72(12)			
2 $^2\Delta_{3/2}$	0	24859.569(12)	0.487904(35)	3.78(18)			
2 $^2\Delta_{5/2}$	0	25148.1529(27)	0.491 6903(91)	6.634(57)			
3 $^2\Delta_{3/2}$	0	31721.867(13)	0.493505(33)	7.01(15)			
3 $^2\Delta_{5/2}$	0	32015.5504(48)	0.495531(52)	65.7(11)			

a: Values fixed to those provided by Ram and Bernath (2005).
b: Values kept fixed in the fit.

constant D_v for all state; values for the sextic centrifugal distortion constant H_v and the Ω-doubling constants p_v and p_{D_v} were fit where possible.

It is noted in the literature (Cheung et al., 1982a; Hopkins et al., 2009) that the levels of the 2 $^2\Pi$, $v = n$ states are very close to those of C $^4\Sigma^-$, $v = n+1$; an example of this can be seen in the far left of Fig. 5.3 where the unresolved C $^4\Sigma^-$–X $^4\Sigma^-$ (1,0) band approaches the edge of the 2 $^2\Pi_{3/2}$–X $^4\Sigma^-$ (0,0) spectrum. Similarly, the unresolved C $^4\Sigma^-$–X $^4\Sigma^-$ (3,1) band can be seen slightly closer to the 2 $^2\Pi_{1/2}$–X $^4\Sigma^-$ (1,0) band centre in Fig. 5.4. This supports the theory that the 2 $^2\Pi$ state is responsible for the electronic perturbations observed in the C $^4\Sigma^-$–X $^4\Sigma^-$ transitions included in the Marvel network (Lagerqvist and Selin, 1957; Cheung et al., 1982a). Unfortunately, the assignments of the 2 $^2\Pi$–X $^4\Sigma^-$ spectra do not extend to sufficiently high values of J to match those of the perturbed transitions, so this cannot be explicitly confirmed through these observations.

5.3 Marvel networks

Two spectroscopic networks for VO were produced using the Marvel procedure, one with resolved hyperfine structure and one without; these are presented here. Unlike in previous Marvel studies, where the number of hyperfine-resolved transitions has been orders of magnitude less than that of hyperfine-unresolved transitions, such as for AlO in Section 3.2.2 and elsewhere (Tennyson et al., 2010; Yurchenko et al., 2018b; Darby-Lewis et al., 2019; Bowesman et al., 2021; Furtenbacher et al., 2022), the VO data analysed in this work consisted of a much more even split; 49.7% of transition data is hyperfine resolved. As such, the Marvel procedure yielded hyperfine-resolved and unresolved networks with a similar number of final energy

levels. Hence, two distinct networks were produced in order to preserve the level coverage provided by both. While the aim was to ultimately have hyperfine resolution of all states, the hyperfine-unresolved data was the only source of experimental information on many of the electronic states.

The Marvel input files are made available as part of the supplementary material of Bowesman et al. (2024b) along with the output energy files obtained for both networks. The final networks contain the updated perturbation assignment detailed in Section 5.4.4 and were computed using Marvel version 4.1.

5.3.1 Hyperfine-resolved network

The full set of 8 082 transitions were passed through Marvel for validation; 41 transitions were invalidated as they were found to be inconsistent with the rest of the network, considerably beyond their initial uncertainties. As expected, 20 of the invalidated transitions are from the largest data source in this network (Cheung et al., 1982a), accounting for half of the invalidated transitions. The 17 other invalidated transitions were from Adam et al. (1995), the next largest hyperfine-resolved data source, and then 4 from Flory and Ziurys (2008). All of the data comprising this network is summarised in Table 5.12. The final hyperfine-resolved network hence consists of 8 041 validated transitions, split between 152 components. The largest of these components comprises 6 452 transitions that determine 5 702 unique energy levels. This is an increase from the published Marvel study (Bowesman et al., 2022), which validated 6 603 transitions and obtained a primary component consisting of 6 452 transitions and 4 402 energy levels. The increase comes primarily from new levels in the previously missing X $^4\Sigma^-$ $v = 1, 2$ states, where the experimental results of Döring et al. (2022) added 865 and 413 new levels respectively. The extended level coverage also allowed for previously unconnected components of the network to be joined up, adding an additional 2 levels in the B $^4\Pi$ state and 6 in the C $^4\Sigma^-$ state. Of the remaining network components, the next largest consist of only 3 transitions, followed by a further eight components containing only 2 transitions. The remaining 142 components each consist of a single transition between two energy levels, with no connection to the zero-energy level. This spectroscopic network connects hyperfine-resolved levels in the X $^4\Sigma^-$, B $^4\Pi$, C $^4\Sigma^-$ and 1 $^2\Sigma^+$ states.

5.3.2 Hyperfine-unresolved network

Validated transitions from the hyperfine-resolved network were deperturbed to yield equivalent hyperfine-unresolved transition frequencies, totalling 1 150 deperturbed transitions. The hyperfine-resolved data of Döring et al. (2022) contributed an additional 204 deperturbed levels to the 946 computed as part of the initial Marvel study (Bowesman et al., 2022). 99 and 77 O- and S-branch hyperfine transitions were excluded from the deperturbation process, due to the $|\Delta J| \leq 1$ constraint on the $6j$-symbol in Eq. (2.27). All levels involved in the excluded transitions were also involved in at least one P-, Q- or R- branch transition, hence this constraint did not reduce the total number of levels in the network.

The deperturbed transitions were combined with the 8 194 hyperfine-unresolved transitions, yielding 9 344 total transitions that were then passed through Marvel

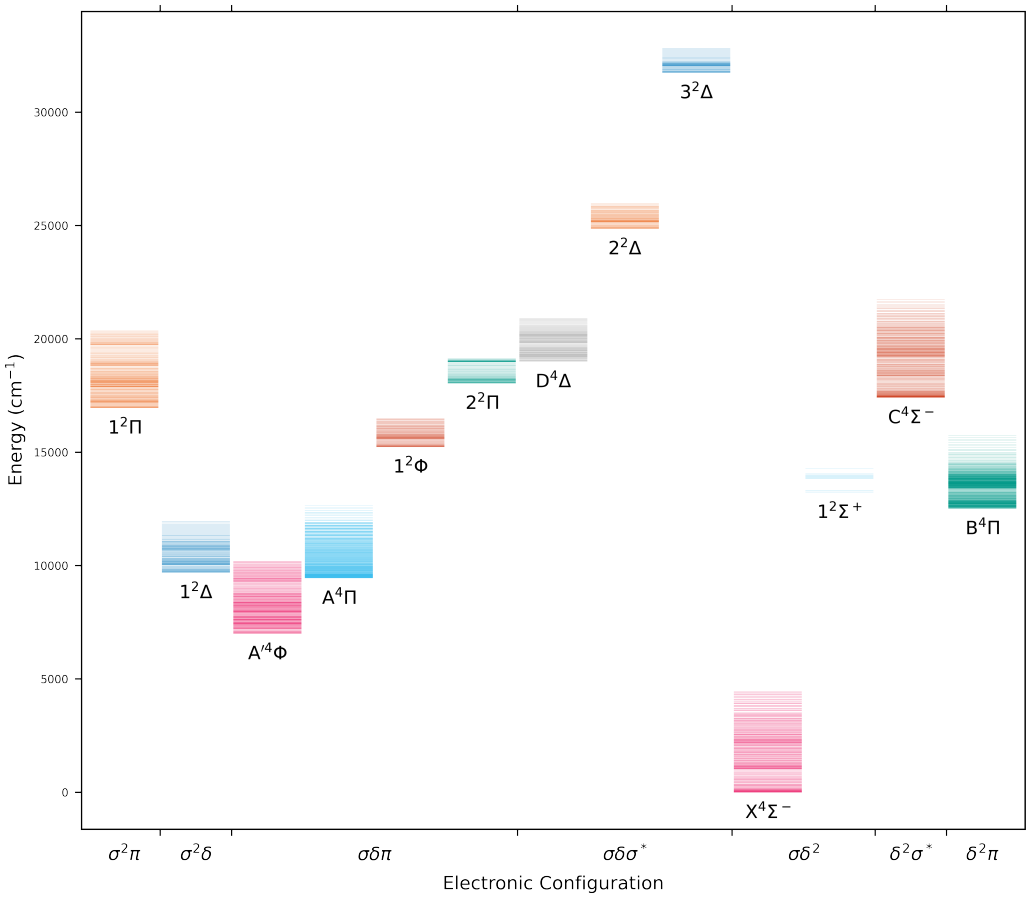


Fig. 5.5: Levels of $^{51}V^{16}O$ in the hyperfine-unresolved network, grouped by electronic state and ordered by increasing T_0 values for each electron configuration. Each horizontal line represents an energy level in that electronic state.

for validation; these are summarised in Table 5.13. All transitions from Hocking et al. (1981), Cheung et al. (1982a), Suenram et al. (1991), Flory and Ziurys (2008) and Döring et al. (2022) contained within the hyperfine-unresolved network have been deperturbed, while the data of Adam et al. (1995) is a mixture: 41.1% of the transitions accessed and 41.3% of those validated by Marvel for this source are deperturbed. The deperturbed transitions involve 820 unique energy levels, 262 of which were not present in any hyperfine-unresolved transition data.

54 of the input transitions were invalidated due to having optimal uncertainties determined by the Marvel procedure significantly greater than their input uncertainty and due to being in poor agreement with energies determined via combination differences. The largest number of invalidated transitions come from Merer et al. (1987), which is also the largest source of hyperfine-unresolved data. The final hyperfine-unresolved network hence contains 9 290 validated transitions divided into 121 components, the largest of which consists of 9 110 transitions that determine 4 813 energy levels. This is an increase on the 9 087 validated hyperfine-unresolved transitions of the original Marvel study, which were also split across 121 compo-

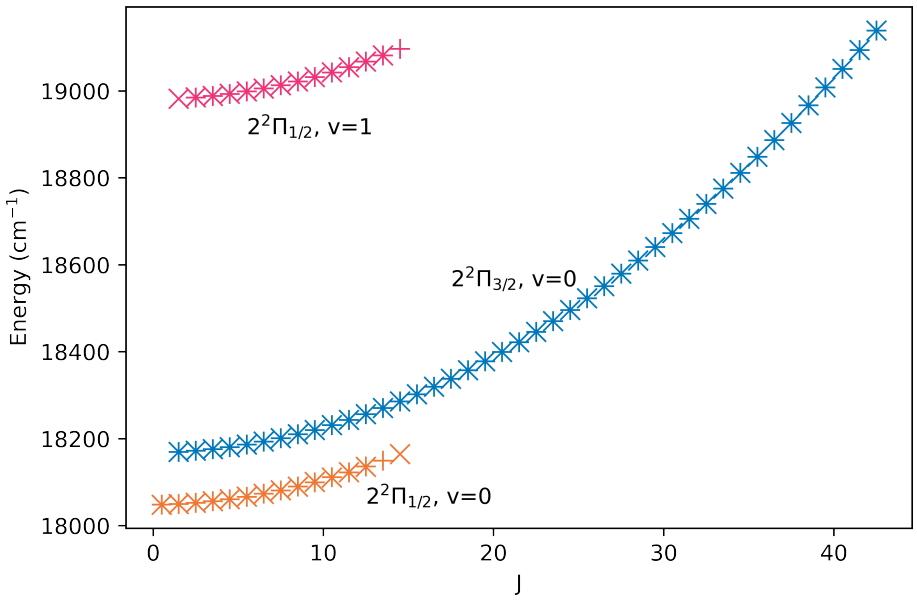


Fig. 5.6: Energy levels of the 2 $^2\Pi$ system determined by MARVEL as part of the hyperfine-unresolved network. Levels are marked with a '+' or 'x' based on their +/- total parity assignment, respectively.

nents, the largest of which consisted of 8 907 transitions and contained 4 712 energy levels. Of the remaining components in this network, six consist of 4 transitions, a further nine consist of 2 transitions and the remaining 105 are single-transitions components. A breakdown of the electronic states included in this network is shown in Fig. 5.5. The energy levels of the 2 $^2\Pi$ state that were determined through MARVEL analysis are shown in Fig. 5.6.

The exceptionally large maximum transition uncertainties in the data of Cheung et al. (1982a) and some bands of Adam et al. (1995) seen in Table 5.13 are the result of the uncertainty scaling applied to a select few deperturbed hyperfine transitions, where the majority of the hyperfine components were absent from the data and those that were present were heavily skewed. Given the scaling factors defined in Eq. (2.30) and Eq. (2.31), this has resulted in 8 and 12 transitions from these two sources with uncertainties above 1 cm^{-1}, all of which were validated by MARVEL.

The mean degree of the final energy levels determined by MARVEL, meaning the average number of transitions that define each level, is 3.79. 864 energy levels in the network are only defined by one transition and are hence less reliable. These levels primarily occur in the B $^4\Pi$ state (31.0%) followed by the X $^4\Sigma^-$ (15.6%), A $^4\Pi$ (13.0%) and A′ $^4\Phi$ (10.6%) states.

5.4 Spectroscopic Model

To construct an initial form for the new spectroscopic model, the 11 potential energy curves (PECs) for the X $^4\Sigma^-$, A′ $^4\Phi$, A $^4\Pi$, B $^4\Pi$, C $^4\Sigma^-$, D $^4\Delta$, 1 $^2\Delta$, 1 $^2\Sigma^+$, 1 $^2\Phi$, 1 $^2\Pi$ and 2 $^2\Pi$ states were taken from Qu et al. (2023) and those for the 1 $^2\Gamma$ and 1 $^2\Sigma^-$ states from McKemmish et al. (2016b). The 1 $^2\Sigma^-$ and 1 $^2\Gamma$ states

are sometimes referred to as "dark" states, in that they are not observed directly in spectra, though they are known to exist through *ab initio* calculations and their spin-orbit interactions with other states. PECs for the 2 $^2\Delta$ and 3 $^2\Delta$ states were added based on the fitted effective Hamiltonian parameters given in Table 5.2. An illustration of these electronic states and their energies is given in Fig. 5.1, along with the observed electronic bands. Most of the *ab initio* diagonal and off-diagonal spin-orbit and L_x curves calculated by McKemmish et al. (2016a) were included, unless they had been refit by Qu et al. (2023), in which case the updated versions were included instead. This includes all of the spin-rotation and spin-spin curves. The hyperfine coupling curves calculated by Qu et al. (2022b) for the X $^4\Sigma^-$ were also used. The dissociation energy of VO has been experimentally measured using a variety of techniques (Mahanti, 1935; Farber et al., 1972; Jones and Gole, 1976; Berkowitz et al., 1957; Balducci et al., 1983; Gentleman et al., 2019) but here the value of 52 790 cm^{-1} determined by Merriles et al. (2020) is adopted; since all the electronic states considered go the same limit this value is used to constrain the asymptotes of all states.

It should be noted that while the 11 electronic state model of Qu et al. (2023) gave a good description of the term energies, the model only included two spin-orbit couplings. Given that spin-orbit coupling facilitates intensity borrowing between coupled states, a model with a more complete description of the spin-orbit couplings between the electronic states of VO was necessary for the ultimate goal of constructing a new line list.

5.4.1 Duo model

The model was computed using the program Duo (Yurchenko et al., 2016b) over a grid of 4001 points arranged between 1.2 and 4.0 Å. The rotational basis extends up to $J = 153.5$, so as to compute levels up to $F = 150$. An energy cutoff was imposed at 45 000 cm^{-1} to make the calculation feasible and the vibrational basis size for each electronic state was set accordingly and are given in Table 5.3. This is the same energy cutoff used in the calculation of the existing VOMYT line list (McKemmish et al., 2016b). At high energies close to dissociation the density of states increases significantly as sequential vibrational states interact with one another. In order to ensure the vibrational levels below the energy cutoff had accurate energies, each state's vibrational basis was set to extended beyond the energy cutoff.

The model was refined against the empirical Marvel energy levels obtained in Section 5.3.1 and Section 5.3.2. Refinement was initially carried out in two stages: first the potentials and couplings were fit against only the hyperfine-unresolved Marvel energy levels, with the Duo hyperfine coupling modules turned off. All of the 15 electronic state potentials, 3 spin-rotation and 6 spin-spin coupling curves were refined at this stage. 10 of the 11 diagonal spin-orbit coupling curves were refined; the diagonal spin-orbit coupling of the 1 $^2\Gamma$ state was left with its original *ab initio* form due to a lack of observational data to fit against. 18 of the 28 off-diagonal spin-orbit coupling curves were also refined, including all of those that had been fit by Qu et al. (2022b, 2023).

The 15 PECs were represented using analytical forms, 14 of which were represented by extended Morse oscillators (EMO) (Lee et al., 1999; Seto, 2000; Huang,

Table 5.3: Potential minima, T_e, and equilibrium bond lengths, r_e, of all 15 states included in the spectroscopic model. These values are rounded to 3 decimal places; the full values are available in the Duo input file included with the supplementary material of Bowesman et al. (2024b). The vibrational basis size for each state, v_{max}, and the maximum value of v for each state that occurs below the energy cutoff of 45 000 cm^{-1}, v_{cutoff}, are also provided.

State	T_e (cm^{-1})	r_e (Å)	v_{max}	v_{cutoff}
X $^4\Sigma^-$	0.000	1.589	75	66
1 $^2\Sigma^-$	5 604.265	1.574	65	56
A′ $^4\Phi$	7 289.736	1.625	65	55
1 $^2\Gamma$	8 503.438	1.577	64	50
A $^4\Pi$	9 529.978	1.635	65	52
1 $^2\Delta$	9 861.072	1.581	64	53
1 $^2\Sigma^+$	10 392.666	1.590	64	54
B $^4\Pi$	12 656.367	1.641	60	49
1 $^2\Phi$	15 438.229	1.627	54	40
1 $^2\Pi$	17 116.891	1.630	54	39
C $^4\Sigma^-$	17 492.985	1.672	55	43
2 $^2\Pi$	18 106.524	1.623	54	47
D $^4\Delta$	19 241.935	1.686	45	26
2 $^2\Delta$	25 093.236	1.677	44	30
3 $^2\Delta$	31 976.453	1.672	35	21

2001) of the form

$$V(r) = T_e + (A_e - T_e)\left[1 - \exp\left(-\sum_{i=0}^{N} B_i \xi_p^i (r - r_e)\right)\right]^2, \tag{5.2}$$

where $A_e - T_e = D_e$ is the dissociation energy, A_e is the corresponding asymptote, T_e is the potential minimum, r_e is the equilibrium distance of the PEC, and ξ_p is the Šurkus variable (Šurkus et al., 1984) given by

$$\xi_p = \frac{r^p - r_e^p}{r^p + r_e^p}. \tag{5.3}$$

All of the PECs in this model represented using the form given by Eq. (5.2) have $N = 2$ or 3. The PEC of the 1 $^2\Gamma$ state was represented with a standard Morse oscillator, due to a lack of experimental data for this state to be fit against. The T_e and r_e values used for each state are shown in Table 5.3; the individual p values and B_i parameters are given in the Duo input file provided in the supplementary material of Bowesman et al. (2024b).

The spin-orbit coupling curves presented by Qu et al. (2023) were represented

using polynomials of the form

$$V(r) = \sum_{i=0}^{N} a_i (r - r_e)^i \tag{5.4}$$

while those of McKemmish et al. (2016a,b) were a series of discreet *ab initio* grid points. To refine these spin-orbit coupling curves, all of the *ab initio* forms were fit to analytical representations. While the polynomial representations of Eq. (5.4) are adequate when fitting to energies arising from a wide range of r values, the VO MARVEL data generally occupies low vibrational states. This means that the experimentally known states primarily reside low-down in their respective potentials. Consequently, while these fits are well defined at values of r close to the potential minimums at their respective r_e values, they are poorly constrained towards the edges of the calculation and lead to over-fitting. This was especially true towards the 4.0 Å end of the grid, where the polynomial representations of the spin-orbit couplings had a tendency to extrapolate to extremely high values. As the aim was to produce a line list up to close to dissociation, analytical representations that did not produce unrealistically large magnitudes for the spin-orbit couplings at large or small r were required. To achieve this, spin-orbit couplings were instead fit to a functional form suggested by Le Roy (2017)

$$F(r) = \left(1 - \xi_p\right) \sum_{k=0}^{N} B_k \xi_p^k + \xi_p B_\infty, \tag{5.5}$$

where B_∞ is an asymptote reached as $r \to \infty$ and ξ_p is given in Eq. (5.3). By constraining the value of this asymptote it was easy to avoid spin-orbit couplings which extrapolated to extreme values. All of the refined spin-orbit coupling curves were represented with the form given in Eq. (5.5), as well as one of the spin-rotation and one of the spin-spin coupling curves. The diagonal spin-orbit coupling curves are shown in Fig. 5.7 and the off-diagonal curves in Fig. 5.8. Several of the curves shown in Fig. 5.8 appear almost flat; these curves are the unchanged *ab initio* curves of McKemmish et al. (2016a). Though the refined spin-orbit couplings are in many cases considerably changed from their initial *ab initio* forms, the resultant model reproduces empirical term energies much more accurately.

While the use of the analytic representation given by Eq. (5.5) was helpful in avoiding extrapolation to high magnitude spin-orbit couplings at large-r, some couplings still tend to large values on the order of hundreds of wavenumbers at the low-r limit. While these are likely not representative of the true magnitudes of the various couplings at those bond lengths, the low-r configurations generally correspond to positions in the respective potentials with very high energies, sometimes above the dissociation limit. As such, these few couplings with doubtful low-r extrapolations should not impact the overall quality of the model. Indeed, these couplings are of these forms as their values closer to the equilibrium bond length were crucial in obtaining a good fit to experimental data. The region of roughly $r = 1.4 - 1.9$ Å was the most important for the fit, as varying the values of the couplings outside

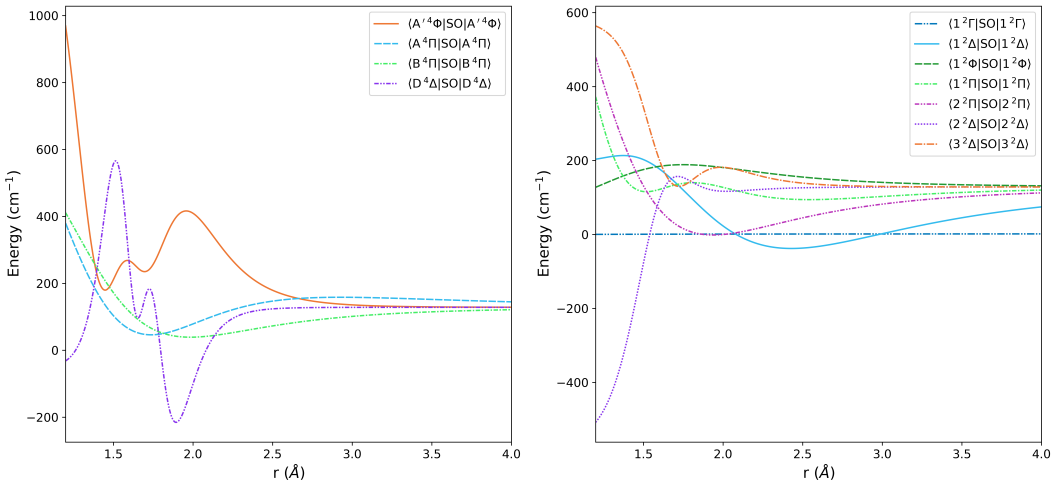


Fig. 5.7: Diagonal spin-orbit coupling curves of $^{51}V^{16}O$ included in this model. The left plot shows the spin-orbit coupling curves for the quartet states and the right plot the curves for the doublets.

this range had minimal effect on the fitted energy residuals. This range was smaller for states with fewer empirical energy levels to fit to, such as in the $2\ ^2\Delta$ and $3\ ^2\Delta$ states where only a very small region of the relevant coupling curves around their respective equilibrium bond lengths had any impact on the quality of the fit.

5.4.2 Hyperfine couplings

Qu et al. (2022b) produced an empirical, hyperfine-resolved model for the X $^4\Sigma^-$ ground state of VO using the hyperfine coupling modules of Duo (Qu et al., 2022a) - see Section 2.1.1 for detail on the available hyperfine coupling terms. As is standard in the formalism of Duo, these couplings are implemented as radial functions of the bond length r (Å) and can be constructed using a variety of analytical representations (Yurchenko et al., 2016b). Of the seven possible hyperfine coupling terms, the Fermi contact, b_F, the diagonal nuclear electric quadrupole, $eQq0$, nuclear spin-orbit interaction, a, electron spin nuclear spin dipole-dipole interactions, c and d, and the nuclear spin-rotation interaction c_i were considered in this model. This excludes the $eQq2$ term which was expected to be small and had not been included in published experimental fits to hyperfine-resolved data.

After a satisfactory fit had been achieved for the hyperfine-unresolved data, determined based on the global root-mean-square error (RMSE), hyperfine couplings were added to the model. Refinement was then carried out against the 5 702 hyperfine-resolved Marvel energy levels, which only cover the X $^4\Sigma^-$, B $^4\Pi$, C $^4\Sigma^-$ and 1 $^2\Sigma^+$ states. While this stage primarily involved fitting of the various hyperfine coupling curves, small changes were also made to the electronic state potentials, spin-rotation and spin-spin coupling curves of these states.

Initial forms for the hyperfine coupling curves of the X $^4\Sigma^-$ state were taken from the ground state hyperfine-resolved model of Qu et al. (2022b), which consisted of Fermi contact, nuclear electric quadrupole, electron spin - nuclear spin dipole-dipole (c) and nuclear spin-rotation coupling curves. For the hyperfine couplings

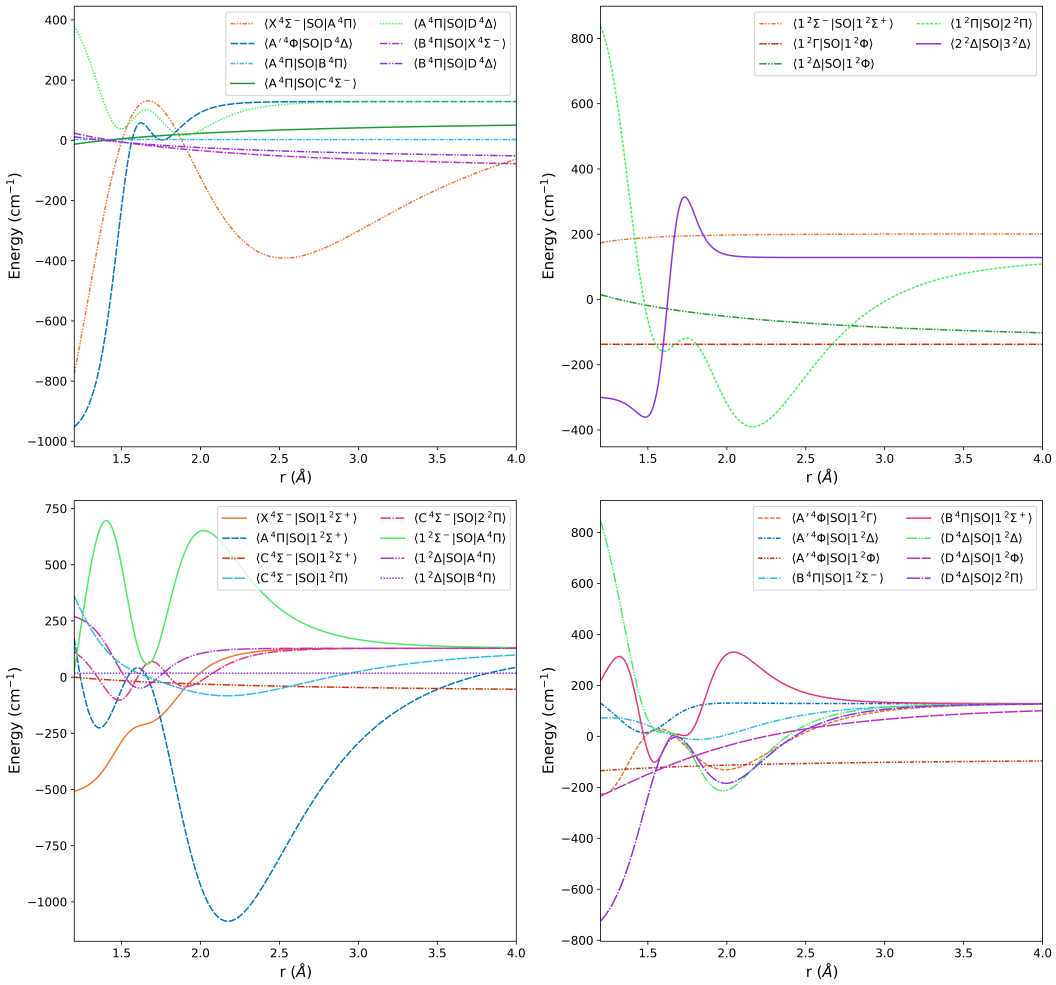


Fig. 5.8: Off-diagonal spin-orbit coupling curves of $^{51}V^{16}O$ included in this model. The upper plot shows the spin-orbit couplings between different quartet states, the middle plot those between different doublet states and the bottom two plots those between quartet and doublet states, split up to avoid crowding the plot.

of the B $^4\Pi$ and C $^4\Sigma^-$ states, initial values for the couplings were set based on the values obtained via effective Hamiltonian fits to hyperfine-resolved experiments (Cheung et al., 1982a; Adam et al., 1995). Both of these states were fit with all of the same class of couplings as the X $^4\Sigma^-$ state, except for the B $^4\Pi$ state which was fit with additional nuclear spin-orbit and electron spin - nuclear spin dipole-dipole (d) couplings as they were deemed necessary in the experimental fits (Adam et al., 1995).

The initial forms for all of the hyperfine couplings were polynomial representations described by Eq. (5.4). As with other couplings in the model, it was again necessary in some cases to instead use the representation given by Eq. (5.5) to avoid unreasonable extrapolation at large-r. The final forms of each coupling used in this model are shown in Fig. 5.9. Though the Fermi contact parameter was expected to be the dominant hyperfine coupling parameter for the ground state, it was ultimately necessary to fit a much larger nuclear electric quadrupole interaction to reproduce

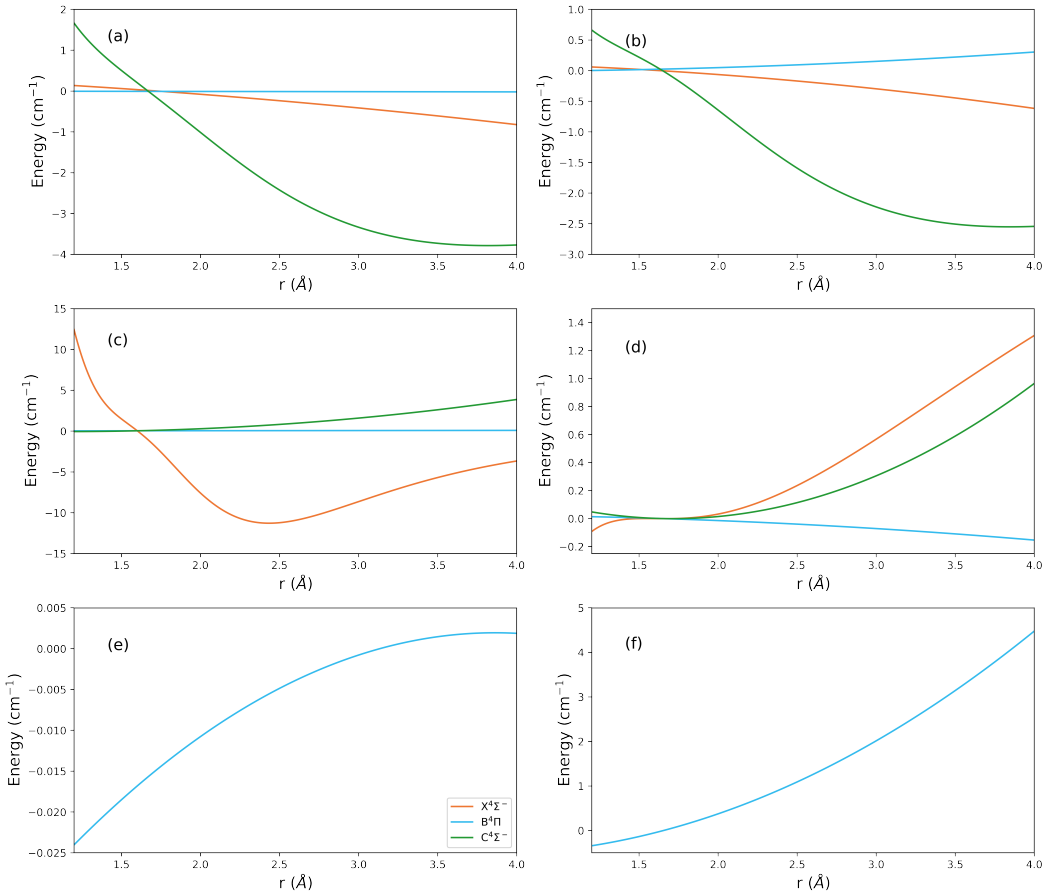


Fig. 5.9: Six hyperfine coupling curves included in the new VO spectroscopic model: (a) Fermi contact parameter, b_F; (b) Diagonal nuclear electric quadrupole interaction, $eQq0$; (c) Nuclear spin-orbit interaction, a; (d) Nuclear spin-rotation interaction, c_i; (e) Electron spin nuclear spin dipole-dipole interaction, c; (f) Electron spin nuclear spin dipole-dipole interaction, d.

experimental energies. This is perhaps an artefact of the fit used for this empirical model, rather than being indicative of the relative size of these two interactions.

The program Duo was developed in part to fit model parameters to hyperfine-unresolved energies, but the fitting of hyperfine coupling parameters is a yet to be fully implemented in the code. The fitting in this worked utilised a custom python wrapper that executed the Duo code up to the computation of hyperfine-resolved energy eigenvalues before terminating the program. The wrapper then matched the energies on an input list of hyperfine-resolved energy levels and calculated obs.-calc. residuals before modifying the parameters in the Duo input file and calling the Duo executable again. The parameters to be fit were flagged with the word "fit" at the end of the relevant line in the input file, much like in the regular Duo fitting procedure, but with the addition of an optional text string of the format "(x_1,x_2)" where x_1 and x_2 are lower and upper bounds for the parameter. This allowed for the parameters of the extremely sensitive hyperfine couplings to be bounded, avoiding the fitting procedure determining optimal but nonphysical values. The fitting utilised

Table 5.4: Observed minus calculated RMSE for the experimentally derived, hyperfine-resolved MARVEL energies and their values calculated using DUO, for each vibronic state.

State	v	F range	RMSE (cm^{-1})	No. energies
X $^4\Sigma^-$	0	0 - 47	0.060	1 270
	1	0 - 36	0.150	865
	2	5 - 34	0.183	413
1 $^2\Sigma^+$	2	35 - 43	0.819	13
B $^4\Pi$	0	1 - 46	0.229	1 841
C $^4\Sigma^-$	0	1 - 48	0.126	1 287
Overall			0.169	5 689

a Levenberg-Marquardt Trust Region Reflective non-linear least-squares algorithm (Moré, 1978) to minimise the residuals, as the parameters of Eqs. (5.4) and (5.5) are decidedly non-linear. Attempts were made to use the basin-hopping algorithm which aims to find the global minimum through randomised exploration of the parameter space (Wales and Doye, 1997), specifically designed for finding the minima of complex potential energy surfaces (Wales and Scheraga, 1999) but were found to be too slow to converge on a viable set of parameters. Other derivative-free algorithms such as COBYLA (Constrained Optimisation BY Linear Approximations) which had been used in the fitting of the ground state hyperfine-resolved model of Qu et al. (2022b) and the Nelder-Mead method (Nelder and Mead, 1965) were tested but faced the same problem. The fitting was performed using the LMFIT (Newville et al., 2015) and SCIPY (Virtanen et al., 2020) python libraries. The finalisation of the hyperfine refinement module is forthcoming and will be made available via GitHub when complete.

5.4.3 Results

Though VO is a diatomic molecule, the inclusion of a large number of electronic states and a multitude of couplings results in a fairly complex Hamiltonian which, when combined with the expansion of the basis set under hyperfine coupling, requires a considerable amount of computation power to solve. Hence, the final model required 1.3 TB of high-performance RAM to compute the 3 410 598 states present below the 45 000 cm^{-1} cutoff. The final model contains three states with full hyperfine resolution, the X $^4\Sigma^-$, B $^4\Pi$ and C $^4\Sigma^-$ states, and 12 states without, the A′ $^4\Phi$, A $^4\Pi$, 1 $^2\Delta$, 1 $^2\Sigma^+$, 1 $^2\Phi$, 1 $^2\Pi$, 2 $^2\Pi$, D $^4\Delta$, 2 $^2\Delta$ and 3 $^2\Delta$ states. While the 1 $^2\Sigma^+$ has observed hyperfine-splitting through its perturbations to the B $^4\Pi$ state (Cheung et al., 1994; Adam et al., 1995), its energy level coverage is sparse and insufficient to meaningfully fit any hyperfine couplings to. Hence in the 12 states without hyperfine couplings, any apparent hyperfine splitting is induced through coupling to the X $^4\Sigma^-$, B $^4\Pi$ or C $^4\Sigma^-$ states.

Table 5.4 shows the obs.-calc. energy root-mean-square error (RMSE) for the newly computed hyperfine-resolved DUO model, calculated against the known hyperfine-resolved MARVEL levels. Table 5.5 gives the same comparison for all of the hyperfine-unresolved MARVEL levels. In this comparison, hyperfine-unresolved

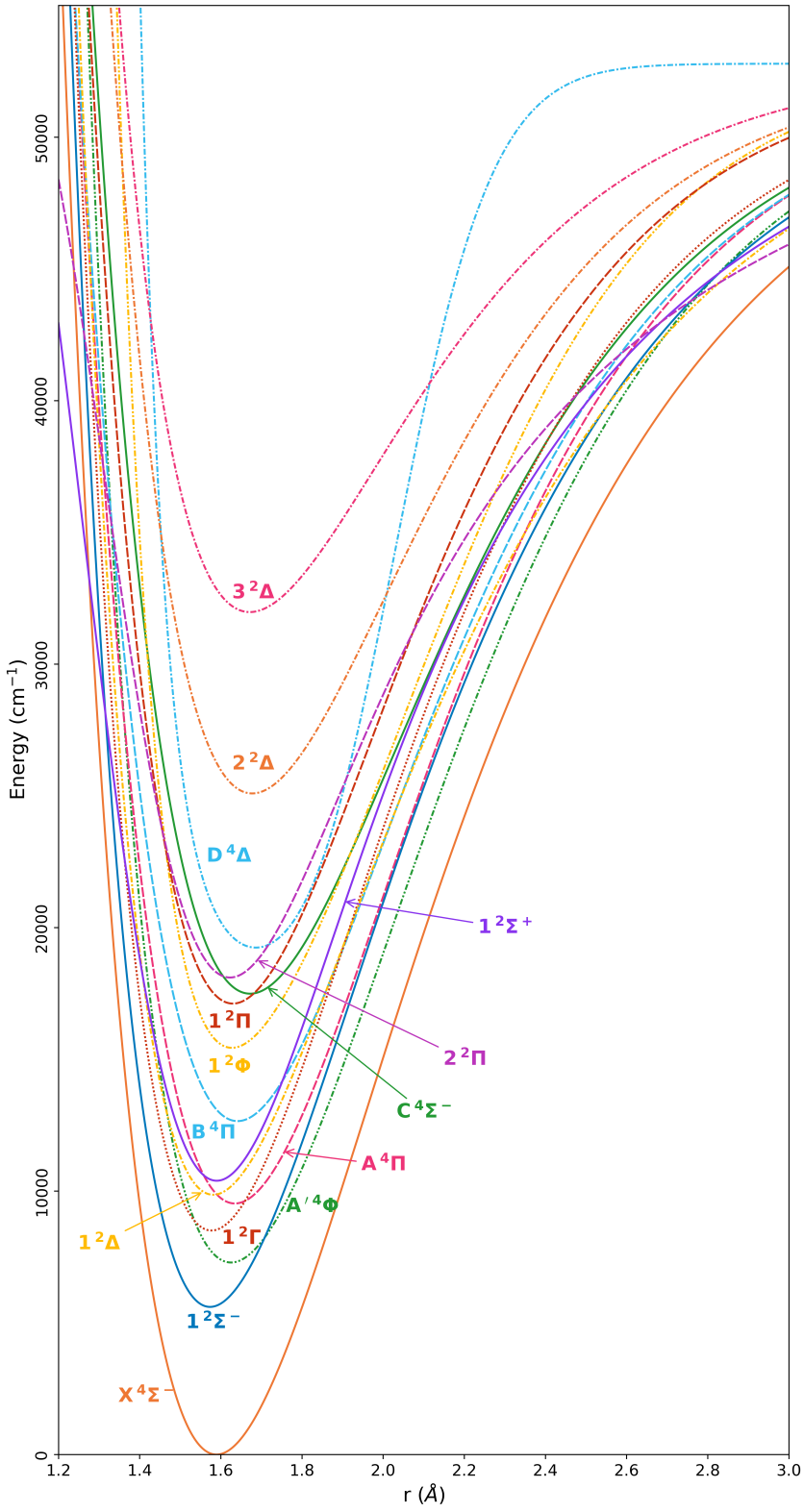


Fig. 5.10: 15 potential energy curves of $^{51}V^{16}O$ included in this model, after refinement against empirical MARVEL energy levels. Calculations were done over an internuclear distance range of 1.2 to 4.0 Å; all states tend to the same dissociation asymptote.

Table 5.5: Observed minus calculated RMSE between the experimentally derived, hyperfine-unresolved MARVEL energies and the energies of their equivalent hyperfine components calculated using DUO, for each vibronic state.

State	v	F range	RMSE (cm^{-1})	No. energies
X $^4\Sigma^-$	0	48 - 83	0.244	832
	1	37 - 83	0.282	940
	2	35 - 71	0.232	520
A′ $^4\Phi$	0	0 - 55	0.234	2 240
	1	1 - 51	0.420	1 600
	2	10 - 46	0.337	848
A $^4\Pi$	0	0 - 82	0.276	4 316
1 $^2\Delta$	0	0 - 50	0.200	1 320
	1	5 - 51	0.190	640
1 $^2\Sigma^+$	2	47 - 61	0.272	24
	3	24 - 33	0.117	16
B $^4\Pi$	0	47 - 82	0.443	744
	1	0 - 46	0.351	2 080
1 $^2\Phi$	0	1 - 50	0.061	1 296
1 $^2\Pi$	0	1 - 50	0.121	1 296
	1	0 - 50	0.135	1 168
	2	5 - 46	0.185	552
	3	5 - 39	0.147	440
C $^4\Sigma^-$	0	49 - 84	0.737	518
	1	9 - 83	0.811	1 062
	2	11 - 76	1.242	739
2 $^2\Pi$	0	0 - 68	1.355	900
	1	0 - 33	0.451	240
D $^4\Delta$	0	0 - 55	0.649	2 460
	1	1 - 45	0.450	1 592
2 $^2\Delta$	0	0 - 48	0.126	1 264
3 $^2\Delta$	0	3 - 50	0.081	848
Global			0.470	30 495

MARVEL levels are compared against all of their equivalent hyperfine components. This also includes levels from the X $^4\Sigma^-$, B $^4\Pi$ and C $^4\Sigma^-$ states with either higher F or v quantum numbers than those covered by the hyperfine-resolved data. Consequently, the RMSE of hyperfine-unresolved data for the X $^4\Sigma^-$, B $^4\Pi$ and C $^4\Sigma^-$ states shown in Table 5.5 is noticeably worse than that of the hyperfine-resolved data in Table 5.4. The high RMSE values of the hyperfine-unresolved C $^4\Sigma^-$, $v = 1, 2$ and 2 $^2\Pi$, $v = 0$ data are the result of a small number of poorly fit levels where these states perturb one another.

It is notable that, excluding the limited data on the 1 $^2\Sigma^+$ state, none of the doublets have observed hyperfine-splittings. This is perhaps not surprising however, as some observations of the doublet states in the 1 $^2\Pi$–1 $^2\Delta$ and 2 $^2\Pi$–1 $^2\Delta$ bands

(Merer et al., 1987) and all of the published observations of the 2 $^2\Delta$–1 $^2\Phi$, 1 $^2\Phi$–1 $^2\Delta$ and 3 $^2\Delta$–1 $^2\Delta$ bands (Merer et al., 1987; Ram et al., 2002; Ram and Bernath, 2005) were unable to resolve Λ-doubling.

Duo assigns quantum number labels to the hyperfine-resolved states it calculates under Hund's case (a_β) coupling. Due to the large number of spin-orbit couplings present in the model, the labelling of Ω values is sometimes wrong. This can be corrected however, such as through manual inspection of plots of the calculated energy as a function of F for each vibronic band. While this problem also occurs without hyperfine coupling, a new issue is the assignment of the label J, which is no longer rigorous under hyperfine coupling. Accordingly, in cases such as the internal hyperfine perturbations of the X $^4\Sigma^-$ state observed in the literature (Richards and Barrow, 1968a; Cheung et al., 1982a,b; Adam et al., 1995; Flory and Ziurys, 2008), J is sometimes mislabelled by Duo but can be easily corrected in post-processing.

It should be noted that a smaller vibrational basis size was used when fitting this model, as this allowed for the calculation of term energies within approximately 15 minutes per iteration. The time for each iteration increased significantly with the number of parameters being fit: small refinements were doable in under 10 minutes per iteration for 1-3 parameters, while fits to a sensitive spin-orbit coupling curves, such as the $\langle$C $^4\Sigma^-|SO|$ 2 $^2\Pi\rangle$ coupling, often also required the simultaneous fitting of both electronic state potentials directly involved in the interaction. This was because without allowing the PECs to be modified, the fit would either explode to extreme values or fail to escape the initial local minimum. In such cases, in was necessary to float more than 10 parameters at once and could take in excess of 40 minute per iteration. This use of the smaller vibrational basis size was necessary then, as it took roughly 5 000 hours or over 200 days of near-continuous fitting, parallelised across a minimum of 32 cores on either the UCL theory computing cluster or the DiRAC Data Intensive service at Leicester high-performance cluster, to obtain the final parameter set. In total, 332 model parameters were fit over the course of this work.

A series of final fits were done to the ground state hyperfine coupling curves using the full ground state vibrational basis size in order to ensure that the fit was converged, taking approximately one hour per iteration. For comparison, one iteration with the full vibrational basis size used in the complete model would take 12 hours to compute. The final fits to the ground state hyperfine coupling curves were essential to ensure that the quality of the fit was retained for the final product. The final model, in the form of an input file for the program Duo, is given as supporting information alongside the publication of the model discussed here (Bowesman et al., 2024b).

5.4.4 Perturbations

Perturbations to the B $^4\Pi$, $v = 0, 1$–X $^4\Sigma^-$ bands by the 1 $^2\Sigma^+$, $v = 2, 3$ states were identified by Merer and co-workers (Cheung et al., 1994; Adam et al., 1995) and comprise the only experimental knowledge of the 1 $^2\Sigma^+$ state. Perturbations to the C $^4\Sigma^-$, $v = 0, 1, 2$ states observed in C $^4\Sigma^-$–X $^4\Sigma^-$ bands by Lagerqvist and Selin (1957) and Cheung et al. (1982a) had remained unassigned, however. Through analysis of the spectroscopic model described here and its full labelling of the states

it computes, it was possible to assign the perturbations to the C $^4\Sigma^-$, $v = 1$ (F_2) state at $J = 50.5 - 51.5$ to the 2 $^2\Pi_{3/2}$, $v = 0$ state, as well as those seen in the C $^4\Sigma^-$, $v = 1$ (F_3) state at $J = 62.5 - 64.5$. Similarly, the perturbations to the C $^4\Sigma^-$, $v = 2$ (F_3) state at $J = 25.5 - 27.5$ arise from the 2 $^2\Pi_{3/2}$, $v = 1$ state. These new assignments are provided in the MARVEL input file given in the supplementary materials of Bowesman et al. (2024b,a). The perturbations to C $^4\Sigma^-$, $v = 0$ at $J = 24.5, 38.5, 73.5 - 76.5$ remain unidentified. The electronic perturbation to the D $^4\Delta$–A′ $^4\Phi$ (0, 0) band observed by Merer et al. (1987) likewise remains unassigned. Further experimental measurements targeting the as of yet unobserved electronic states of VO would likely enable the identification of these perturbing states.

5.4.5 Transition dipole moments

To compute the Einstein A coefficients contained in the trans file portion of the line list, required to calculate intensities, the original dipole moment curves of McKemmish et al. (2016a) calculated using the program MOLPRO were used (Werner et al., 2015, 2020). The transition dipole moment curves were initially kept the same, though after calculating final state lifetimes for the new line list there was disagreement between the calculated lifetimes of the A $^4\Pi$, B $^4\Pi$ and C $^4\Sigma^-$ states and the experimental measurements made by Karlsson et al. (1997). These measurements only concerned the lifetimes of $v = 0$ levels in these electronic states and the $v = 1$ levels in the B $^4\Pi$ and C $^4\Sigma^-$ states. Accordingly, there was not sufficient information to fully refit the dipoles. Instead, the transition dipole moments between these three states and the X $^4\Sigma^-$ ground state were scaled. This involved multiplying these three *ab initio* dipole moment curves by scalar values, taken as the ratio between the calculated lifetimes and the experimental lifetimes for each state. While these states can transition to states other than the ground state, the A $^4\Pi$–X $^4\Sigma^-$, B $^4\Pi$–X $^4\Sigma^-$ and C $^4\Sigma^-$–X $^4\Sigma^-$ bands are the primary decay channels for each of the upper states, as evidenced by being the three strongest electronic bands in the spectra of VO. The dipoles for each of these bands were scaled by factors of 1.94, 1.58 and 1.33 respectively and can be found in the DUO input file included in the supplementary material of Bowesman et al. (2024a).

The final intensity distributions in spectra generated from the new line list will differ for two additional reasons. Firstly, the dipole moment curves in the VOMYT model (McKemmish et al., 2016b) had mistakenly been entered in Λ-representation, rather than the Cartesian form appropriate for MOLPRO outputs. This has been corrected and results in an increase in the intensities of transitions between upper and lower states both with $\Lambda \geq 1$ and $\Delta\Lambda = \pm 1$ by a factor of 2 (Whiting et al., 1980). Secondly, the spin-orbit coupling curves, which allow for intensity borrowing between states proportional to the magnitude of the coupling, were refit. The change in the strengths of these couplings should result in a slight shift in the distribution of intensities between electronic bands.

5.5 Hybrid line list

As described in Section 2.4.1, levels had their calculated energies replaced with MARVEL values where they were available. This was done directly for the hyperfine-resolved levels of the X $^4\Sigma^-$, B $^4\Pi$, C $^4\Sigma^-$ and $1^2\Sigma^+$ states. For states with levels

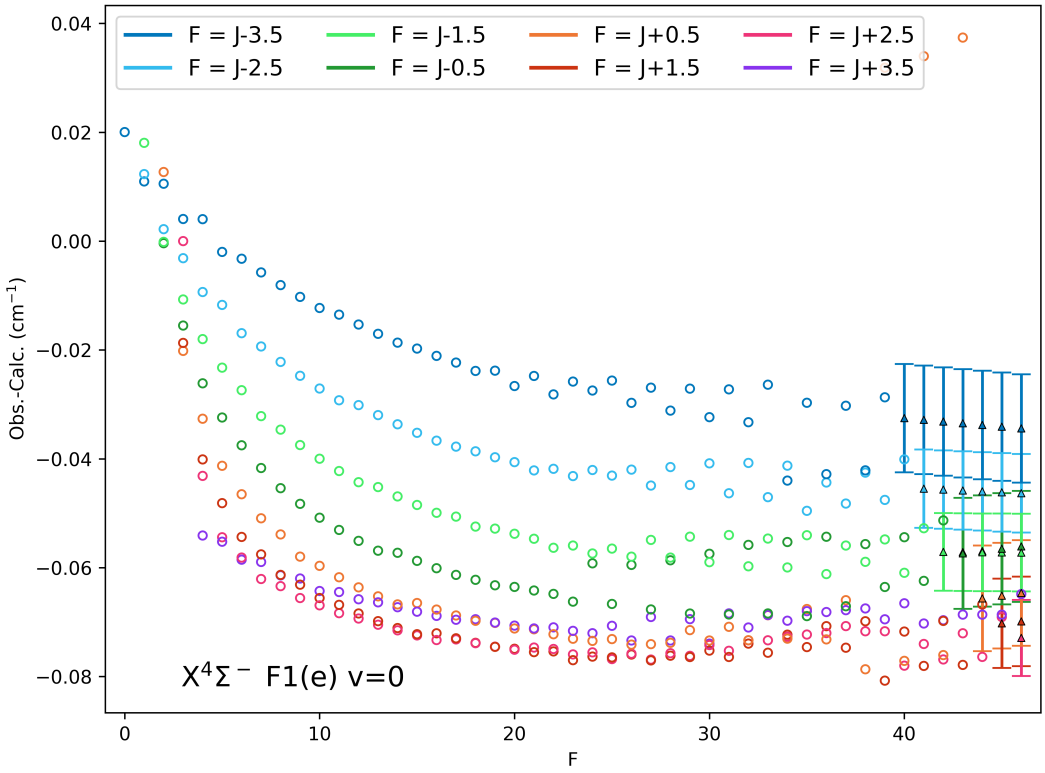


Fig. 5.11: X $^4\Sigma^-$ F1(e) $v = 0$ obs.-calc. values for the MARVEL data, marked with "o". The predicted energy shifts fit to the data are shown marked with triangles and their accompanying estimated uncertainty.

only known from experiment without hyperfine resolution, the hyperfine-unresolved energy value was used for all hyperfine components of each level.

Predicted shifts were fit to fill in the gaps between MARVEL energy levels, where some F values were missing. These synthetic obs.-calc. shifts were determined independently for every combination of electronic state, v, Ω and rotationless party that existed in the MARVEL data, as a function of F and J. The implementation was such that the dependence on J was only to enable a different numerical dependence on F to be fit for each hyperfine component, i.e.: each $F - J$ value. An example of the different fits obtained for each hyperfine component is shown in Fig. 5.11. Uncertainties for the energies corrected with the interpolative form of predicted shifts were set using Eq. (2.33) and those with extrapolated shifts using Eq. (2.35), using $a = 0.0001$ cm^{-1}

For the remaining calculated levels in the states file, an uncertainty value was estimated using Eq. (2.38), where the scaling factors took the values $a = 0.001$ cm^{-1} and $b = 0.05$ cm^{-1}. In cases where calculated energies were replaced with MARVEL or predicted shift energies, the original calculated term energies are retained in the final column of the states file.

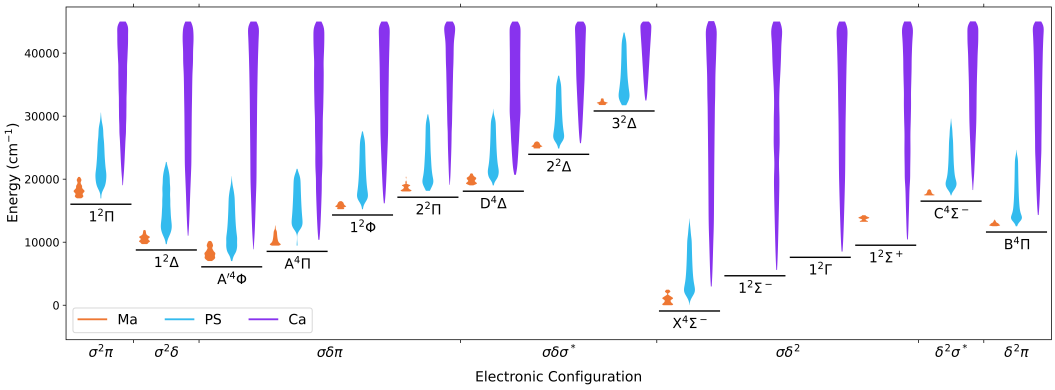


Fig. 5.12: Distribution of MARVELised ("Ma"), predicted shift ("PS") and variationally calculated ("Ca") energy levels in each state of the new line list, grouped based on electron configuration.

5.5.1 New line list

A new line list, consisting of a states file and series of trans files, is now made available via the ExoMol website and are formatted following the ExoMol standard (Tennyson et al., 2013). The states file consists of a series of term energies with associated uncertainties, each with a rigorous F and +/- total parity assignment and labelling for other identifies such as electronic state, vibrational band and J. These latter quantum number labels are provided based on the largest contributions to the wavefunction for each state as computed by DUO. An excerpt from the new states file is provided in Table 5.6. While the fourth column in the ExoMol standard is usually J and g_{tot} is calculated as $(2J+1)\times g_{ns}$, under hyperfine coupling the rigorous quantum number is instead F and $g_{tot} = 2F+1$. This is in keeping with the HITRAN format (Simeckova et al., 2006), such that the total degeneracy of the hyperfine-unresolved level is recouped through the combination of the degeneracies of the individual hyperfine-resolved components. The fifth and sixth columns contain the uncertainty on the term energies and each level's radiative lifetime, calculated using ExoCROSS (Yurchenko et al., 2018), in keeping with the updated ExoMol format (Tennyson et al., 2023). While the updated ExoMol states file specification also includes the option of a column for Landé g-factors, these had not been implemented in the DUO hyperfine modules at the time of calculation. Were the DUO code updated to include this functionality they could then be computed using the hyperfine-resolved spectroscopic model for VO and added to the line list, should the need arise to consider the effect of magnetic fields on the spectra of VO.

As has been used in other recent ExoMol line lists, a "Source Tag" column is provided to indicate the method used to produce each final term value - see Section 2.4.6 for possible values. The final line list consists of 28 760 MARVELised levels, labelled with "Ma"; 105 566 levels energies adjusted have been based on obs.-calc. predicted shifts and are labelled "PS"; 3 276 272 levels are labelled "Ca" and retain their energies as calculated by DUO. The distribution of these levels among each electronic state is shown in Fig. 5.12. The number of MARVELised levels is greater than the number of MARVEL energies obtained in Sections 5.3.1

Table 5.6: Excerpt from the $^{51}V^{16}O$ states file, using the format defined by Tennyson et al. (2013, 2023).

i	$\tilde{E}$	g_{tot}	F	unc	τ	$+/-$	e/f	J	State	v	Λ	Σ	Ω	Source Tag	$\tilde{E}_{calc}$
1	10.764 111	1	0	0.002 646	1.3052E+04	+	f	3.5	X(4SIGMA-)_4Sigma-	0	0	0.5	0.5	Ma	10.773 921
2	18.286 612	1	0	0.002 646	5.4524E+03	+	f	3.5	X(4SIGMA-)_4Sigma-	0	0	1.5	1.5	Ma	18.329 941
3	1 012.490 751	1	0	0.014 945	5.2807E-02	+	f	3.5	X(4SIGMA-)_4Sigma-	1	0	0.5	0.5	PS	1 012.367 510
4	1 020.007 393	1	0	0.001 500	5.2805E-02	+	f	3.5	X(4SIGMA-)_4Sigma-	1	0	1.5	1.5	Ma	1 019.925 017
5	2 003.704 567	1	0	0.009 312	2.6738E-02	+	f	3.5	X(4SIGMA-)_4Sigma-	2	0	0.5	0.5	PS	2 003.948 182
6	2 011.289 305	1	0	0.006 908	2.6739E-02	+	f	3.5	X(4SIGMA-)_4Sigma-	2	0	1.5	1.5	PS	2 011.485 588
7	2 985.497 918	1	0	0.280 311	1.8054E-02	+	f	3.5	X(4SIGMA-)_4Sigma-	3	0	0.5	0.5	Ca	2 985.497 918
8	2 992.995 747	1	0	0.280 311	1.8056E-02	+	f	3.5	X(4SIGMA-)_4Sigma-	3	0	1.5	1.5	Ca	2 992.995 747
9	3 956.999 417	1	0	0.330 311	1.3718E-02	+	f	3.5	X(4SIGMA-)_4Sigma-	4	0	0.5	0.5	Ca	3 956.999 417
10	3 964.443 764	1	0	0.330 311	1.3720E-02	+	f	3.5	X(4SIGMA-)_4Sigma-	4	0	1.5	1.5	Ca	3 964.443 764

i: State counting number;
$\tilde{E}$: Term value (in cm^{-1});
g_{tot}: Total state degeneracy, $2F+1$;
F: Final angular momentum, $F = J + I$;
unc: Estimated uncertainty of energy level (in cm^{-1});
τ: Radiative lifetime (in seconds);
$+/-$: Total parity;
e/f: Rotationless parity;
J: Total electron angular momentum;
State: Electronic state;
v: vibrational quantum number;
Λ: Projection of the electron orbital angular momentum;
Σ: Projection of the electron spin;
Ω: Projection of the total angular momentum, $\Omega = \Lambda + \Sigma$;
Source Tag: The method used to generate the term value; "Ma" for MARVELised energies, "PS" for energies from predicted shifts and "Ca" for energies calculated using DUO;
$\tilde{E}_{calc}$: The original energy calculated by DUO.

and 5.3.2 as the hyperfine-unresolved MARVEL energies were used for all hyperfine components of the hyperfine-unresolved electronic states. Using the same energy and uncertainty for each hyperfine component is valid for these hyperfine-unresolved states, given according to experiment, the uncertainties in the hyperfine-unresolved MARVEL levels is set such that it is greater than the magnitude of their hyperfine splitting else they would have been resolved (Lagerqvist and Selin, 1957; Cheung et al., 1982b; Merer et al., 1987; Cheung et al., 1994; Adam et al., 1995; Karlsson et al., 1997; Ram et al., 2002; Ram and Bernath, 2005; Sriramachandran et al., 2008; Hopkins et al., 2009).

The trans files consist of a list of upper and lower state counting numbers, referencing the new states file, and an Einstein A coefficient giving the transition probability between the two states. Given the large number of transitions computed as part of the new line list, the trans files are provided as a series of archives each covering transitions within a 500 cm^{-1} range. An excerpt from one of the new trans files is given in Table 5.7.

The total number of transitions calculated as part of the new line list is 58 904 173 243. The total number of MARVELised transitions, being the number

Table 5.7: Excerpt from the $^{51}V^{16}O$ trans file, using the format defined by Tennyson et al. (2013). The below data come from the trans file detailing transitions between 0 - 500 cm^{-1}.

f	i	A_{fi} (s^{-1})
328	6 864	5.6380E-08
598	7 659	5.7151E-07
975	8 772	7.4097E-11
382	7 023	2.9118E-18
166	6 387	3.0935E-07
59	6 069	1.3400E-37
490	7 341	5.2938E-24
652	7 818	1.0421E-12
1 029	8 931	7.0662E-13
219	6 546	1.6189E-12

f: The upper state counting number from the corresponding states file.
i: The lower state counting number from the corresponding states file.
A_{fi}: The Einstein A coefficient.

Table 5.8: Number of levels and transitions calculated as part of the new line list for $^{51}V^{16}O$, including the number of MARVELised transitions, where both upper and lower energy levels have been MARVELised, and the number of transitions where the upper and lower energy levels have either MARVEL or predicted shift energies.

No. states	No. transitions	No. MARVELised transitions	No. MARVELised and PS transitions
3 410 598	58 904 173 243	12 987 450	90 787 509

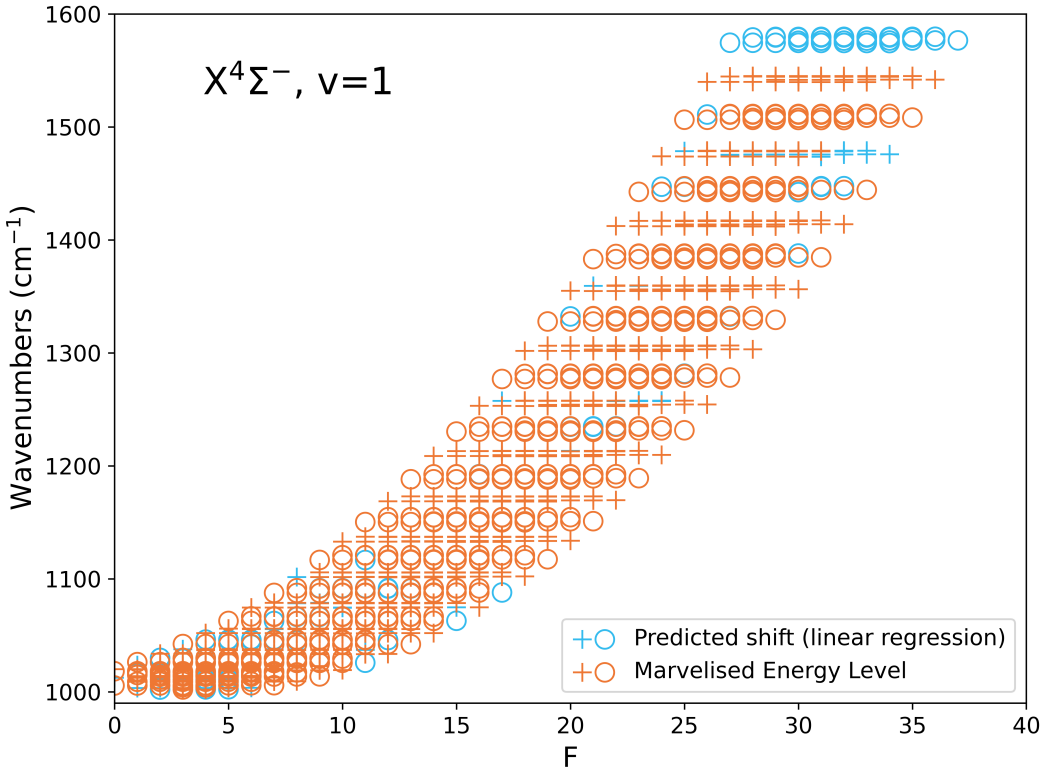


Fig. 5.13: Combination of MARVELised and predicted shift energy levels in the X $^4\Sigma^-$, $v = 1$ state. Levels with positive total parity are marked with a "+" and those with negative total parity with "o".

of transitions with both upper and lower states having MARVELised energies, is 12 987 450. This represents a very significant increase on the 8 082 hyperfine-resolved and 9 344 hyperfine-unresolved experimental transitions used to determine the MARVEL energies and serves as a strong example of the power the MARVEL technique has to predict new transitions frequencies with experimental accuracy. Also considering transitions between energy levels that have been adjusted with predicted shifts, the number of transitions that are known to a reasonably high accuracy increases to 90 787 509. These are summarised in Table 5.8. An example of the distribution of the predicted shift energies amongst the MARVEL energies of the X $^4\Sigma^-$, $v = 1$ state can be seen in Fig. 5.13. Fig. 5.14 shows the contributions to the overall cross-section from transitions between each possible combination of upper and lower level source tags, highlighting how the most intense transitions all involve at least one MARVELised or predicted shift energy level. Transitions between calculated levels provide the largest contribution at small cross sections, which is to be expected as levels involved in weaker transitions are less likely to be observed experimentally and hence not present in the MARVEL data set.

5.5.2 Partition functions

Partition function for the new line list were calculated over a range of temperatures using the program ExoCross (Yurchenko et al., 2018) and are shown in Table 5.9.

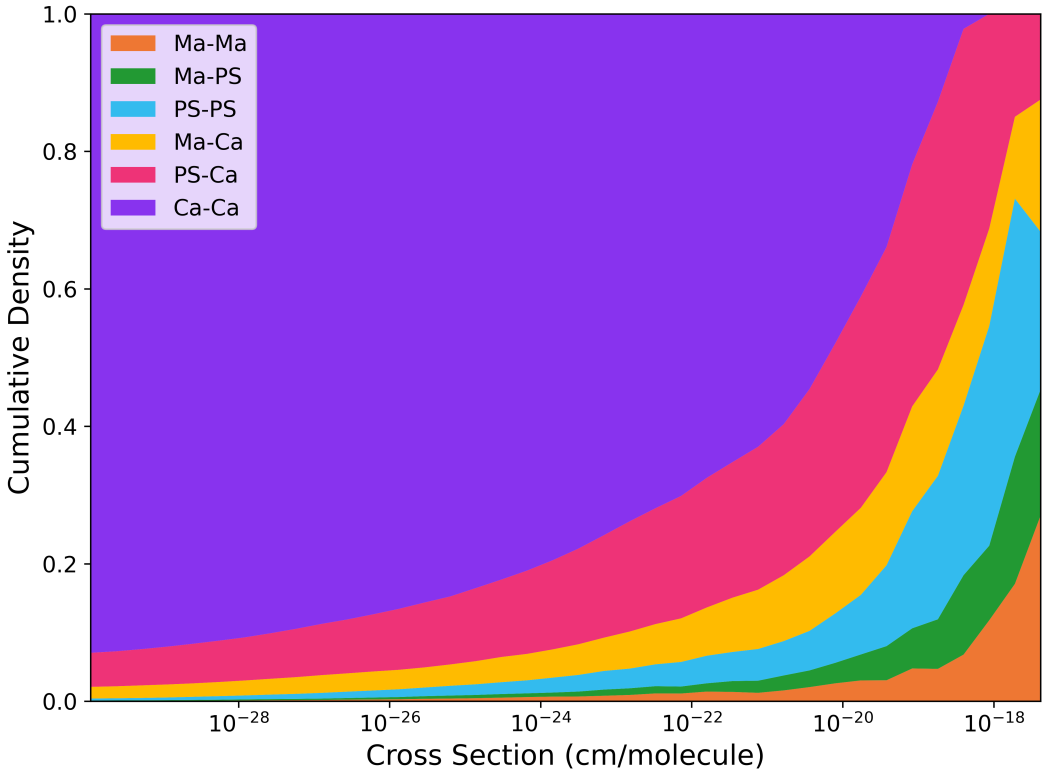


Fig. 5.14: Probability density of transitions being between levels with each combination of source tags at a given intensity, in the spectrum of $^{51}V^{16}O$ at 2 000 K computed using ExoCross (Yurchenko et al., 2018). Transitions are grouped irrespective of which source tag belongs to the upper and lower energy level. "Ma" denotes a MARVELised energy level; "PS" denotes a predicted shift energy level and "Ca" an energy calculated by DUO.

The difference between these values and the partition function of the VOMYT line list (McKemmish et al., 2016b) increases with temperature and have separated by 5% at approximately 5 400 K. Though there are over five times as many levels in the new line list than in VOMYT (638 958 levels) the total degeneracies of the levels of VOMYT, which neglect hyperfine effects, are a factor of $g_{\text{ns}} = (2I+1) = 8$ larger. Moreover, the VOMYT line list contains all states up to $J = 197.5$ with energies below 50 000 cm^{-1}, meaning approximately 216 619 levels (33.9% of total) exist outside of the scope of the new line list. The number of levels is approximate as a J cutoff of 150.5 was taken for a comparison, whereas the new line list contains levels up to $F = 150$, meaning a small subset of levels with $J = 151.5 - 153.5$ are present. The contribution of these extra high-energy levels to the overall partition function will become more prominent at higher temperatures as their level population increases, accounting for most of the divergence between the two line lists. It is possible to calculate partition functions for the levels in VOMYT that are beyond the scope of the new line list and add them to the hyperfine-resolved partition functions to produce a more equivalent comparison. This is shown in Table 5.9, where the adjusted partition function is in much better agreement with the VOMYT line list.

Table 5.9: Partition functions of $^{51}V^{16}O$ calculated over a range of temperatures for the new line list presented here. The partition functions of the VOMYT line list are given as reference, along with the contribution to the partition function from levels outside the scope of the new line list. An adjusted partition function for the new line list, with the added contribution from the VOMYT levels outside the quantum number and energy scope, is given for a more accurate comparison.

	Partition Function			
Temp. (K)	New	VOMYT	ΔPF	Adjusted
100	3.9097×10^{3}	3.9152×10^{3}	0.0000×10^{0}	3.9097×10^{3}
200	7.9850×10^{3}	7.9905×10^{3}	0.0000×10^{0}	7.9850×10^{3}
300	1.2154×10^{4}	1.2160×10^{4}	0.0000×10^{0}	1.2154×10^{4}
400	1.6588×10^{4}	1.6593×10^{4}	0.0000×10^{0}	1.6588×10^{4}
500	2.1423×10^{4}	2.1428×10^{4}	0.0000×10^{0}	2.1423×10^{4}
600	2.6740×10^{4}	2.6745×10^{4}	0.0000×10^{0}	2.6740×10^{4}
700	3.2581×10^{4}	3.2586×10^{4}	0.0000×10^{0}	3.2581×10^{4}
800	3.8971×10^{4}	3.8976×10^{4}	0.0000×10^{0}	3.8971×10^{4}
900	4.5926×10^{4}	4.5930×10^{4}	2.0000×10^{-4}	4.5926×10^{4}
1 000	5.3460×10^{4}	5.3462×10^{4}	1.4000×10^{-3}	5.3460×10^{4}
1 500	1.0037×10^{5}	1.0035×10^{5}	9.4060×10^{-1}	1.0037×10^{5}
2 000	1.6556×10^{5}	1.6554×10^{5}	2.9106×10^{1}	1.6559×10^{5}
2 500	2.5621×10^{5}	2.5642×10^{5}	2.6255×10^{2}	2.5647×10^{5}
3 000	3.8289×10^{5}	3.8429×10^{5}	1.2726×10^{3}	3.8416×10^{5}
3 500	5.5822×10^{5}	5.6325×10^{5}	4.2959×10^{3}	5.6251×10^{5}
4 000	7.9548×10^{5}	8.0901×10^{5}	1.1469×10^{4}	8.0695×10^{5}
5 000	1.5069×10^{6}	1.5670×10^{6}	5.2019×10^{4}	1.5589×10^{6}
6 000	2.6073×10^{6}	2.7879×10^{6}	1.6032×10^{5}	2.7677×10^{6}
7 000	4.1620×10^{6}	4.5870×10^{6}	3.8568×10^{5}	4.5476×10^{6}
8 000	6.2072×10^{6}	7.0536×10^{6}	7.8170×10^{5}	6.9889×10^{6}
9 000	8.7519×10^{6}	1.0245×10^{7}	1.3982×10^{6}	1.0150×10^{7}
10 000	1.1782×10^{7}	1.4186×10^{7}	2.2754×10^{6}	1.4058×10^{7}

Indeed, this adjusted partition function never deviates from the VOMYT partition function by more than 1%. Given the equivalence of the total degeneracies used in the line lists, this approximates the partition functions that would be obtained were the hyperfine-resolved model to be calculated up to $J = 197.5$.

Other partition functions for VO exist in the literature, often based on theoretical calculations with some adjustments owing to experiments but ultimately differing considerably from those of the new line list. For example, the partition functions of Sauval and Tatum (1984) are ~35% larger at 1 000 K than they are for both the VOMYT and the new HyVO line lists, with the difference decreasing until reaching approximate agreement at 5 000 K and falling off to ~25% smaller at 9 000 K. Similarly, the partition functions of Barklem and Collet (2016) are slightly larger at low temperatures of $T < 100$ K but fall off rapidly at higher temperatures to ~40% of the values presented in Table 5.9 at 5 000 K and diverging further beyond that.

It can be noted that the first level to appear in the states file, shown in Table 5.6, with $F = 0$, does not have zero energy as it is not the zero-energy level. In the absence of hyperfine resolution, the lowest energy level in the system is the $J = 0.5$, e parity level in the F_1 fine structure component of the X $^4\Sigma^-$, $v = 0$ ground state. When hyperfine couplings are included, this level gives rise to two F levels with F = 3 and 4, of which $F = 3$ is lowest and hence the zero-energy level, i.e.: defined as the energy zero in the line list.

5.6 Discussion

The model presented here is extensive in its coverage of 15 electronic states; however, *ab initio* electronic structure calculations indicate that there are a significant number of additional electronic states that are not observed. Hübner et al. (2015) calculate a further 9 doublet states between 21 000 - 28 000 cm^{-1}, below the observed 3 $^2\Delta$ state. They also report 4 additional quartet states between 31 000 - 45 000 cm^{-1} and 6 sextet states between 24 000 - 32 000 cm^{-1}. Indeed, according to Wigner-Witmer correlation (Herzberg, 1989) each of the two dissociation channels below the VO ionisation energy of 58 380 cm^{-1} (Luo et al., 2015) should correlate to 36 electronic states: the O(^{3}P) + V(3d^{3}4s^2,^{4}F) asymptote to two Σ^+, one Σ^-, three Π, three Δ, two Φ and one Γ state each of doublet, quartet and sextet multiplicity; the O(^{3}P) + V(3d^{4}4s^1,^{6}D) asymptote to one Σ^+, two Σ^-, three Π, two Δ and one Φ state each of doublet, quartet, sextet and octet multiplicity. It is likely that the higher dissociation channels will also give rise to further electronic states below the energy cut-off. Hence, it is apparent that this model, while complex for a variational model of its kind, is an empirical description of a much larger problem. Consequently, the empirical nature of the spin-orbit couplings used in this model could lead to erroneous intensity borrowing for transitions arising from energy levels outside of the empirical MARVEL data set.

Couplings to the D $^4\Delta$ state by some of the other electronic states not considered here could explain why it was necessary to fit a much steeper potential for this state in the model, as can be seen in Fig. 5.10. This explanation is perhaps incomplete however, as the *ab initio* calculations of Hübner et al. (2015) and later calculations by others using the same methodology (Sun et al., 2023) found the C $^4\Sigma^-$ state had a higher T_e than the D $^4\Delta$ state and instead adiabatically correlated to the O(^{3}P) + V(3d^{4}4s^1,^{6}D) asymptote. Given their state ordering is not in agreement with experimental data, the original O(^{3}P) + V(3d^{3}4s^2,^{4}F) dissociation channel for the C $^4\Sigma^-$ state as calculated by McKemmish et al. (2016a) was retained, which is the same as all other states in the model.

36 of the 44 possible diagonal and off-diagonal spin-orbit coupling curves between the 13 lowest electronic states of the model were included. The missing 8 coupled states that were too far apart that no relevant empirical data existed to constrain the fit against, meaning any attempts to fit them either diverged or resulted in significant over-fitting. The 2 $^2\Delta$ and 3 $^2\Delta$ states were each modelled with a diagonal spin-orbit coupling curve and an off-diagonal spin-orbit coupling between them. To fully couple these states to the other 13 would have required an additional 8 off-diagonal spin-orbit terms each. Given this would significantly increase the

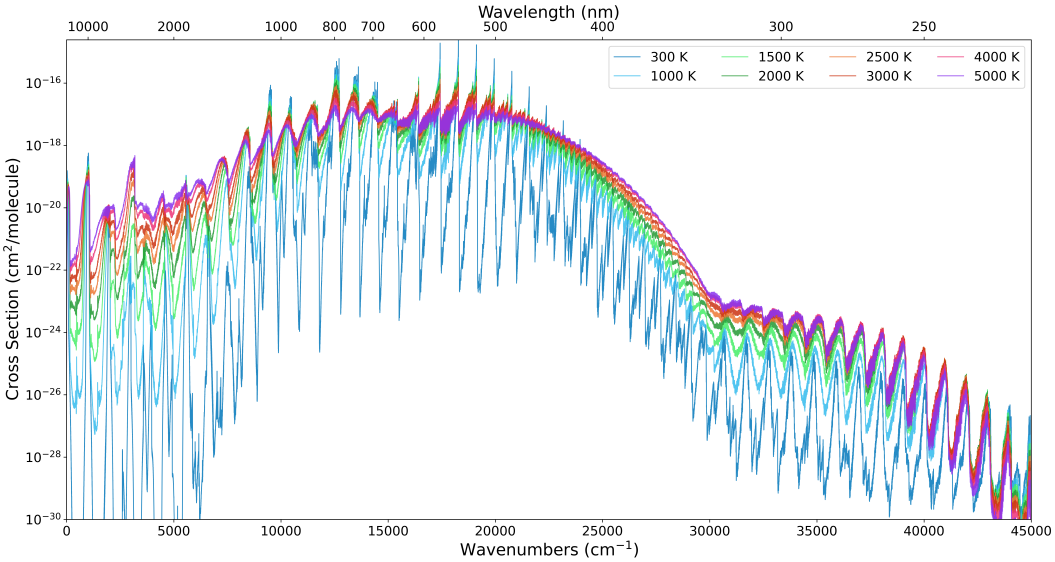


Fig. 5.15: Absorption spectra of $^{51}V^{16}O$ at a variety of temperatures up to 5 000 K, computed using the program ExoCross (Yurchenko et al., 2018) between 0-45 000 cm^{-1}. These spectra were computed using Gaussian line profiles with a half-width half-maximum of 0.2 cm^{-1}.

degree of correlation in the model, as well as there being a lack of empirical energy levels from other electronic states in proximity to these high-energy states meaning refinement would likely only result in over-fitting, no attempt was made to include these 16 extra terms. This was also a contributing factor in why the transition dipole moments for these states were not computed and included in the model: fully coupling and determining intensities for these two states would have significantly increased the complexity of an already intricate model, without necessarily providing much contribution to the resultant spectra.

5.6.1 Spectra

An example of the absorption spectrum generated from the new line list can be seen in Fig. 5.15, computed using the program ExoCross (Yurchenko et al., 2018) for a variety of temperature up to 5 000 K. This covers the main B $^4\Pi$–X $^4\Sigma^-$ and C $^4\Sigma^-$–X $^4\Sigma^-$ bands, which are expected to be the strongest features for observation in exoplanet atmospheres.

Given the lack of dipole moment curves for the 2 $^2\Delta$ and 3 $^2\Delta$ states in the new model, there are 51 dipole allowed electronic bands where $\Delta S = 0$, $\Delta\Lambda = 0, \pm 1$ (24 quartet-to-quartet, and 27 doublet-to-doublet) though these selection rules are not rigorous, unlike the $\Delta F = 0, \pm 1$ and parity change selection rules. Consequently, a further 50 spin-forbidden bands between doublet and quartet states and 68 bands with $|\Delta\Lambda \geq 2|$ occur, facilitated through state mixing and intensity borrowing via spin-orbit coupling. Of these possible electronic bands, 99 different bands (32 dipole allowed, 31 spin-forbidden and 36 forbidden) provide contributions to the overall cross section on the order of 10^{-25} cm^2/molecule or larger at 2 200 K. It can be seen in Fig. 5.16 however, which shows the individual electronic bands responsible

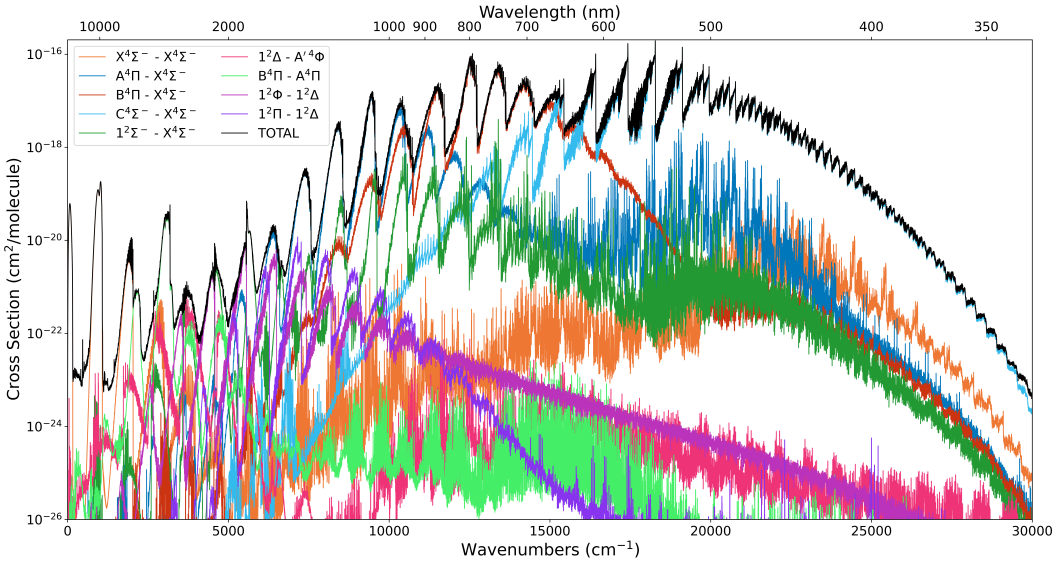


Fig. 5.16: Decomposition of the absorption spectrum of $^{51}V^{16}O$ at 2200 K computed using the program ExoCross (Yurchenko et al., 2018), between 0-30 000 cm^{-1}. The individual contributions to the overall spectrum from several of the strongest electronic bands that contribute to the majority of the most prominent features are shown. The spectrum was computed using Gaussian line profiles with a half-width half-maximum of 1 cm^{-1}.

for the main features in the spectrum of VO, that the spectrum is dominated by the A $^4\Pi$–X $^4\Sigma^-$, B $^4\Pi$–X $^4\Sigma^-$ and C $^4\Sigma^-$–X $^4\Sigma^-$ bands in the near-infrared and visible regions, in agreement with the bands reported in astronomical observations (Kirkpatrick et al., 1993b, 1995; Kamiński et al., 2010; Tylenda et al., 2011). Though some of the bands that are shown to provide large contributions to the overall cross section below 15 000 cm^{-1} seem to show an increase in their contributions at higher wavenumbers, this is most likely due to the mislabelling of states in higher vibrational bands as a result of state mixing. The primary feature from 30 000-45 000 cm^{-1} appears to be the forbidden D $^4\Delta$–X $^4\Sigma^-$ band, though state mixing at these higher energies means this is unclear.

While the strength of the C $^4\Sigma^-$–X $^4\Sigma^-$ band system decreases relative to the B $^4\Pi$–X $^4\Sigma^-$ system as temperature increases, it still remains the strongest component of VO spectra up to 5 000 K, as seen in Fig. 5.15. Given VO is believed to exist in hot-Jupiter exoplanets across temperature ranges of approximately 1 500–2 800 K, consistent with its characterisation of late M and early L dwarf spectra, the C $^4\Sigma^-$–X $^4\Sigma^-$ (0,0) band head should be the single most prominent feature in its spectra. Due to the MARVELisation procedure, this band is known to very high accuracy. The MARVELised transition frequencies across all vibrational bands of the C $^4\Sigma^-$–X $^4\Sigma^-$ system have a mean uncertainty of 0.0045 cm^{-1}, meaning the predicted line positions are accurate to a mean instrumental resolving power of approximately $\bar{R} = 4\,000\,000$. Above this resolving power, deviations in the line positions arising from the limits on the uncertainties in the MARVEL energy levels would be resolvable. Similarly, the MARVELised B $^4\Pi$–X $^4\Sigma^-$ transition frequencies have a mean uncertainty of 0.0041

cm^{-1}, which given their position in the infrared corresponds to an accuracy up to a resolving power of $\bar{R} = 3\,000\,000$.

For other important electronic bands where one or more electronic state is not hyperfine resolved, the uncertainty in the line positions are larger but still well suited for high-resolution studies. This includes the strong A $^4\Pi$–X $^4\Sigma^-$ band with a mean uncertainty in the transition frequencies of 0.064 cm^{-1}, hence accurate up to resolving powers of $\bar{R} = 140\,000$. Some of the other important features in the spectrum of VO, such as the B $^4\Pi$–A $^4\Pi$ system with its prominent peak around 3 000 cm^{-1} and the 1 $^2\Phi$–1 $^2\Delta$ system with its contributions to the peaks from 3 500–6 500 cm^{-1} shown in Fig. 5.16, have larger mean uncertainties in their transition frequencies: 0.064 cm^{-1} and 0.31 cm^{-1} respectively. This means the new line list has comparatively limited accuracy for these bands, with deviations from the predicted line positions becoming resolvable at resolving powers of $\bar{R} = 49\,000$ and $\bar{R} = 17\,000$. This is owing to the lower accuracy of the empirical MARVEL energies derived from hyperfine-unresolved transition data. Indeed, some of the experimental data for the 1 $^2\Phi$ state was not of sufficiently high-resolution to resolve parity splitting, so the derived MARVEL energies are less accurate.

5.6.2 Hyperfine effects

Though the number of energy levels is increased by approximately a factor of 8 under hyperfine coupling, due to the splitting of each J into F values in the range $|J - I| \leq F \leq J + I$, the increase in the number of transitions is much greater - approximately a factor of 64. This is a result of how the hyperfine coupling $F = J + I$ allows for transitions forbidden under the dipole selection rule $\Delta J = 0, \pm 1$ to occur, as the selection rule transforms to $\Delta F = 0, \pm 1$. Consequently, transitions up to $|\Delta J| = 8$ are facilitated by the nuclear spin $I = \frac{7}{2}$ of the ^{51}V atom. Despite this, it has been shown in earlier work on the hyperfine-resolved ground state of VO by Qu et al. (2022b) that Einstein A coefficients and hence transition intensities decrease rapidly above $|\Delta J| = 3$; transitions with $\Delta J = 0, \pm 1, \pm 2, \pm 3$ have intensities on the same order. Experimental measurements have only been reported up to $|\Delta J| = 2$, however (Cheung et al., 1982a, 1994; Adam et al., 1995; Karlsson et al., 1997). Though propensity rules favour transitions with $\Delta F = \Delta J$, those where $\Delta F \neq \Delta J$ do occur (Cheung et al., 1982a; Suenram et al., 1991; Adam et al., 1995; Flory and Ziurys, 2008; Döring et al., 2022) and are referred to as hyperfine satellites. It can be seen in Fig. 5.17 that as the difference between ΔF and ΔJ become larger, transitions get weaker. Given the new line list comprises just over 59 billion transitions, modifications were made to the hyperfine modules of the DUO code (Qu et al., 2022a) to parallelise the computation of Einstein A coefficients, in order to significantly reduce the computation time.

Considering how the new line list compares to hyperfine-unresolved transitions, what would have previously been considered a single $\Delta J = 0$ Q-branch transition now exists as 22 hyperfine transitions - 8 transitions with $\Delta F = 0$ and 7 each for $\Delta F = \pm 1$. While the number of hyperfine transitions decreases as $|\Delta J|$ increases, down to 1 for $|\Delta J| = 8$, the single feature you would expect to see in a hyperfine-unresolved spectrum becomes spread out due to hyperfine coupling. An example of the 21 components comprising a standard R-branch transitions are shown in

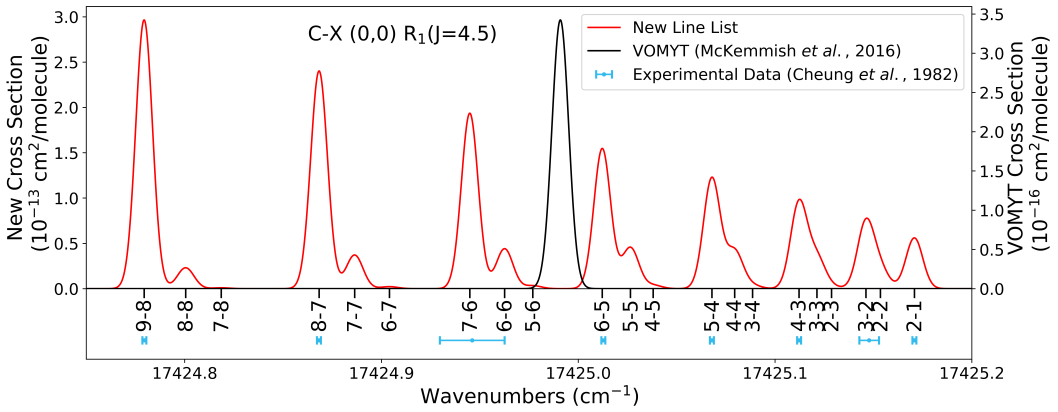


Fig. 5.17: $C\,^4\Sigma^- – X\,^4\Sigma^-$ (0, 0) R_1 ($J = 4.5$) transitions in the absorption spectrum of $^{51}V^{16}O$ computed using the program ExoCross (Yurchenko et al., 2018) at 2 200 K. The spectra were generated using Gaussian line profiles with HWHM of 0.005 cm^{-1} and are marked with their $F' \leftarrow F''$ values. Note that the new, hyperfine resolved spectrum in red use the left-hand axis and the VOMYT spectra in black uses the right-hand axis. Transitions with $\Delta F = +1$ are the strongest, as is expected for $\Delta J = +1$ transition, with $\Delta F = 0$ transitions being weaker but still noticeable, and those with $\Delta F = -1$ being heavily blended and difficult to distinguish. This coincides with the experimental observations for these transitions recorded by Cheung et al. (1982a), shown in blue in the bottom panel, who only observed $\Delta F = +1$ transitions. The higher uncertainty in the $7 \leftarrow 6$ transition was due to severe blending leading to an initial misassignment to the $6 \leftarrow 6$ transition.

Fig. 5.17. It should be noted that the difference in the cross sections of the hyperfine transitions of the new line list compared to those of VOMYT are due to changes in the underlying potential energy, coupling and transition dipole moment curves of the spectroscopic model and not simply due to the introduction of hyperfine couplings. The total integrated cross section of a given transition is conserved upon the introduction of hyperfine couplings and the splitting of the transitions into its hyperfine components. In the known experimental data for the $C\,^4\Sigma^- – X\,^4\Sigma^-$ and $B\,^4\Pi – X\,^4\Sigma^-$ systems, the hyperfine components of what would be considered a single transition in the absence of hyperfine couplings have a median spread over 0.198 and 0.188 cm^{-1} respectively. For both systems approximately 45% of experimental transitions have hyperfine splitting between 0.2–0.4 cm^{-1}, with a tail off up to ~0.6 cm^{-1}. Consequently, and given the positions of these band systems, these hyperfine splittings will start to be resolvable at resolving powers of $R \approx 30\,000$. While at temperatures such as 2 200 K the Doppler-broadened line profiles of these bands will have half width at half maximum (HWHM) values of $\approx 0.025 – 0.035$ cm^{-1}, Fig. 5.18 shows how multiple rotational bands overlap and individual hyperfine transitions are significantly blended. Consequently, the convolution of individual line profiles is decidedly non-Gaussian and the overall cross section differs greatly from that of the spectrum without hyperfine effects (Qu et al., 2022b). Given high-resolution cross-correlation studies aim for a resolving power of $R = 100\,000$ for a reliable detection, the inclusion of hyperfine effects is hence necessary for a line list

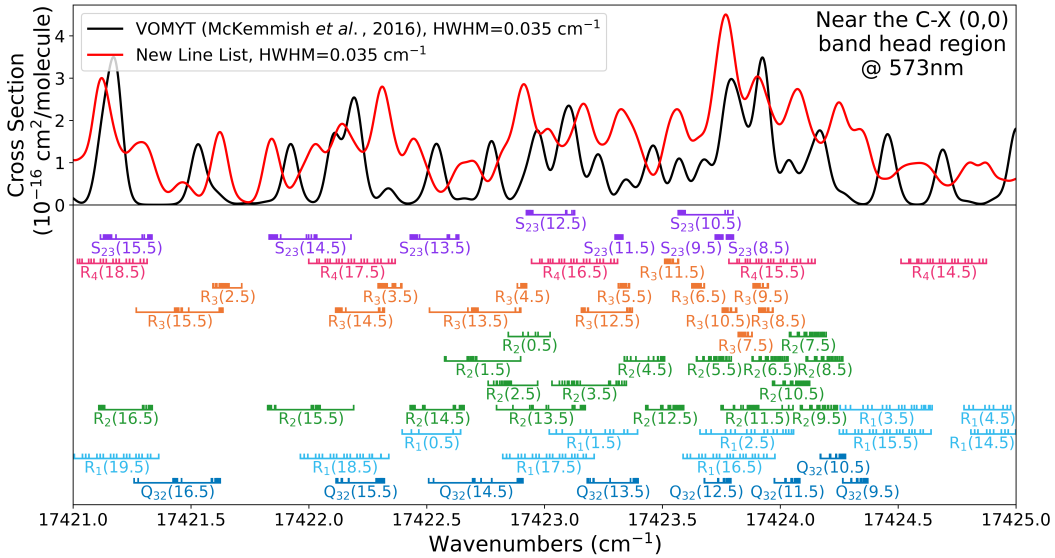


Fig. 5.18: Closeup near the C $^4\Sigma^-$–X $^4\Sigma^-$ (0, 0) band head in the absorption spectra of $^{51}V^{16}O$, computed using the program ExoCross (Yurchenko et al., 2018) at 2 200 K. The spectra were generated using Gaussian line profiles with HWHM of 0.035 cm^{-1} to demonstrate that the complicated arrangement of line positions and their individual intensities are very different in the new line list compared to that of the older VOMYT line list (McKemmish et al., 2016b). Rotational assignments to the strongest transitions in this region are marked in the bottom panel, with the number in brackets being the lower state J assignment. Stick marks are used to identify each hyperfine component of a rotational transition: the 63 rotational transitions shown here comprise 1 250 hyperfine components. The new line list contains a total of 1 309 241 hyperfine transitions in the 4 cm^{-1} range shown in this plot.

to be used with such high-resolution techniques. Moreover, it is possible that failure to consider hyperfine effects in the spectra of $^{51}V^{16}O$, with their impact on the overall cross section and broadening of spectral features, may lead to the mischaracterisation of the thermal broadening present in exoplanet spectra. This could in turn lead to the improper determination of physical properties such as atmospheric temperature during an exoplanet retrieval.

5.6.3 VOMYT Comparisons

Individual transitions in the new line list appear quite differently to those in the VOMYT line list, not just because of the splitting of transitions into multiple hyperfine components, but also due to the redistribution of intensities. As shown in Fig. 5.17, while the hyperfine transitions are spread across ≈ 0.2 cm^{-1} either side of the equivalent C $^4\Sigma^-$–X $^4\Sigma^-$ (0,0) R_1 ($J = 4.5$) transition from VOMYT which neglects hyperfine effects, they are also significantly more intense. The C $^4\Sigma^-$–X $^4\Sigma^-$ (0,0) band overall is only slightly stronger in the new line list, but the intensities of individual transitions have been redistributed, as can be seen in Fig. 5.18. This is not surprising given the refitting of the electronic state potentials and couplings described in Section 5.4. In particular, considerable adjustments were made to the

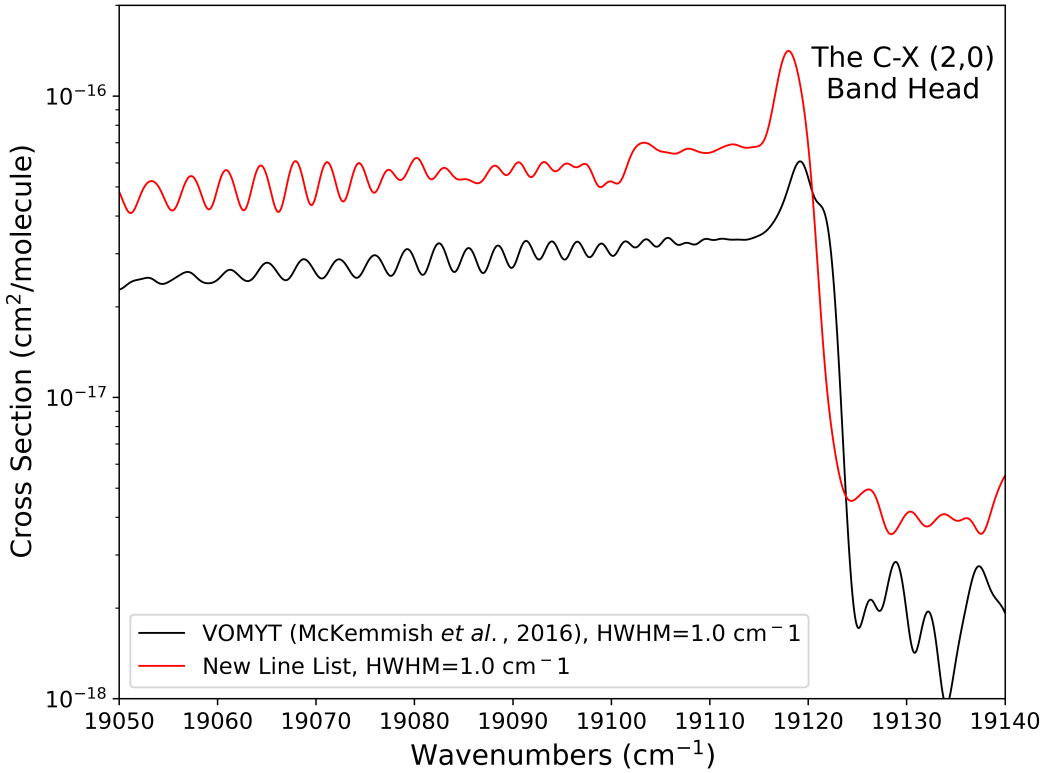


Fig. 5.19: C $^4\Sigma^-$–X $^4\Sigma^-$ (2, 0) band head in the absorption spectra of $^{51}V^{16}O$, computed using the program ExoCross (Yurchenko et al., 2018) at 2 200 K. The spectra were generated using Gaussian line profiles with HWHM of 1.0 cm^{-1}, showing an example of how many entire bands are shifted compared to the VOMYT line list (McKemmish et al., 2016b) at resolutions relevant to high-resolution studies.

off-diagonal spin-orbit couplings in the model that are principally responsible for the intensity borrowing between electronic states.

While the $(v', v'') = (0, 0)$ bands in the VOMYT model generally most accurately recreated experimental band head measurements, the new model is much better at reproducing the higher vibrational bands for which experimental data was available. Fig. 5.19 shows an example of the C $^4\Sigma^-$–X $^4\Sigma^-$ (2, 0) band, one of the strongest features in the spectrum of VO, which has shifted by several wavenumbers as a result of the refitting of the C $^4\Sigma^-$ state. Even in low resolution experiments that are not able to resolve the hyperfine structure, this change in position, intensity and shape will be noticeable, highlighting how the new line list is better suited for experiments at all resolutions.

Table 5.10 gives the mean lifetimes for the levels in each spin-orbit or fine structure component of each vibronic state, in the new line list and in VOMYT. As discussed in Section 5.4.5 the three dipole moment curves between the A $^4\Pi$, B $^4\Pi$ and C $^4\Sigma^-$ states and the ground state were scaled to bring the final vibronic lifetimes inline with the experimental values obtained by Karlsson et al. (1997). This dipole scaling is the primary cause of the difference in the lifetimes of these three states between the HyVO and VOMYT line lists and will have knock-on effects for other

Table 5.10: Mean radiative lifetimes in the first two vibrational bands of each state, compared against the VOMYT line list and experimental measurements of Karlsson et al. (1997). The lowest energy levels in the X $^4\Sigma^-$ state with infinite lifetimes were excluded from the calculations. The mean lifetimes of the VOMYT line list were calculated over levels with $J \leq 150.5$ for a more equivalent comparison to the $F \leq 150$ of the new HyVO line list.

	$v = 0$ mean lifetime (s)			$v = 1$ mean lifetime (s)		
State	HyVO	VOMYT	Experiment	HyVO	VOMYT	Experiment
$X^4\Sigma^-$	5.19×10^{4}	1.03×10^{5}		5.34×10^{-2}	5.32×10^{-2}	
$1^2\Sigma^-$	6.51×10^{-3}	1.69×10^{-1}		4.71×10^{-3}	7.49×10^{-2}	
$A'^4\Phi$	9.61×10^{1}	7.63×10^{1}		9.16×10^{-2}	8.98×10^{-2}	
$1^2\Gamma$	3.43×10^{0}	3.66×10^{1}		7.07×10^{-2}	7.41×10^{-2}	
$A^4\Pi$	5.82×10^{-6}	2.29×10^{-5}	5.8×10^{-6}	5.88×10^{-6}	2.34×10^{-5}	
$1^2\Delta$	5.15×10^{-4}	2.78×10^{-3}		1.60×10^{-3}	5.53×10^{-3}	
$1^2\Sigma^+$	1.48×10^{-4}	1.89×10^{-4}		1.68×10^{-4}	2.71×10^{-4}	
$B^4\Pi$	4.03×10^{-7}	9.94×10^{-7}	3.74×10^{-7}	3.86×10^{-7}	9.71×10^{-7}	4.07×10^{-7}
$1^2\Phi$	2.88×10^{-5}	1.97×10^{-3}		2.60×10^{-5}	9.82×10^{-5}	
$1^2\Pi$	9.19×10^{-6}	1.18×10^{-4}		9.40×10^{-6}	6.25×10^{-5}	
$C^4\Sigma^-$	6.88×10^{-8}	1.18×10^{-7}	7.3×10^{-8}	6.80×10^{-8}	1.16×10^{-7}	6.3×10^{-8}
$2^2\Pi$	1.03×10^{-5}	1.53×10^{-4}		1.03×10^{-5}	1.21×10^{-4}	
$D^4\Delta$	1.22×10^{-5}	2.70×10^{-5}		1.09×10^{-5}	2.45×10^{-5}	

state lifetimes as a result of intensity borrowing through spin-orbit coupling.

The lifetimes of states with $v = 0$ in the new line list are on average almost 12 times smaller than they were in VOMYT, but this is skewed by several states. The 1 $^2\Pi$ and 2 $^2\Pi$, $v = 0$ states have lifetimes over ten times smaller in the new line list, likely because the VOMYT model did not include spin-orbit coupling to the C $^4\Sigma^-$, which provided a mechanism for the intensity stealing that facilitates the spin-forbidden 2 $^2\Pi$–X $^4\Sigma^-$ band observed by Hopkins et al. (2009). The 1 $^2\Phi$, $v = 0$ lifetimes are now almost 70 times smaller however, and are likely due to a combination of its refit electronic state potential and spin-orbit interactions and the correction to the transition dipole moments affecting states with $\Lambda \geq 1$ mentioned in Section 5.4.5. This is also likely the cause of the factor of 10 reduction in the 1 $^2\Gamma$ and factor of 25 reduction in the $1^2\Sigma^-$, $v = 0$ lifetimes.

Table 5.11 highlights the energy shifts between the new HyVO line list and the equivalent energies in the old VOMYT line list (McKemmish et al., 2016b). This comparison covers the vibronic states for which empirical MARVEL energies are known, i.e.: those which have been observed in experiment, plus the first vibrational states of the unobserved 1 $^2\Sigma^-$ and 1 $^2\Gamma$ states. The overall mean energy difference for these bands in the two line lists is 1.132 cm^{-1} and though this seems small, this is due to some bands being shifted up and others down; the mean absolute energy difference is 13.467 cm^{-1}. This paints a clear picture of how the shapes and positions of many vibronic bands will appear differently in the new line list even at medium and low resolutions. Hence, even in bands where hyperfine splittings may not be resolvable, the new line list should obtain decidedly different results to that of the previous ExoMol line list and hopefully enable the reliable detection of VO

in exoplanet atmospheres.

Table 5.11: The mean and standard deviation energy differences between the new HyVO line list and the old VOMYT line list (McKemmish et al., 2016b) in the vibronic states for which MARVEL energies are known, plus the first vibrational bands of the unobserved $1\ ^2\Sigma^-$ and $1\ ^2\Gamma$ states.

		HyVO - VOMYT (cm^{-1})	
State	v	Mean	Std. Dev.
$X\ ^4\Sigma^-$	0	−0.084	0.294
	1	0.065	0.213
	2	−0.530	0.571
$1\ ^2\Sigma^-$	0	10.069	40.721
$A'\ ^4\Phi$	0	−15.712	22.620
	1	−15.117	22.878
	2	−10.706	34.264
$1\ ^2\Gamma$	0	−45.435	11.606
$A\ ^4\Pi$	0	9.576	14.866
$1\ ^2\Delta$	0	−1.608	63.860
	1	−9.478	54.695
$1\ ^2\Sigma^+$	2	−9.133	27.805
	3	−17.282	34.609
$B\ ^4\Pi$	0	−2.689	13.558
	1	4.090	13.546
$1\ ^2\Phi$	0	0.362	1.040
$1\ ^2\Pi$	0	0.651	8.025
	1	1.120	4.415
	2	1.035	9.006
	3	0.835	18.665
$C\ ^4\Sigma^-$	0	0.867	11.926
	1	8.875	20.590
	2	18.174	35.494
$2\ ^2\Pi$	0	51.649	47.499
	1	34.420	32.762
$D\ ^4\Delta$	0	0.546	6.164
	1	23.082	30.414

5.7 Summary

A new, high-resolution line list for $^{51}V^{16}O$ has been produced, intended to replace the existing ExoMol line list (McKemmish et al., 2016b). The new line list is based on the hyperfine-resolved spectroscopic model of Bowesman et al. (2024b) that well-describes 15 electronic states and is computed using the program DUO (Yurchenko et al., 2016b) with its recently added hyperfine coupling modules (Qu et al., 2022a). Based on earlier *ab initio* (McKemmish et al., 2016a; Qu et al., 2022b) and empirical (Qu et al., 2023) studies, this model was refined against empirical term

energies derived from the MARVEL procedure (Bowesman et al., 2022) to enable the accurate recreation of experimental transition measurements. The model presented here is unusually complex for a variational model, in terms of the number of potential energy and coupling curves involved, though such complexity is necessary to tackle the long-standing problem of VO observations in exoplanet atmospheres (Désert et al., 2008; Showman et al., 2009; Schwarz et al., 2015; Evans et al., 2018; Tsiaras et al., 2018; Goyal et al., 2020; Hoeijmakers et al., 2020; Ben-Yami et al., 2020; Merritt et al., 2020, 2021; Johnson et al., 2023; Coulombe et al., 2023; Pelletier et al., 2023). Accordingly, this new line list should enable the more reliable high-resolution detection of the molecule in both stellar and exoplanet atmospheres, which the previous line list was unable to facilitate due to the absence of hyperfine effects (de Regt et al., 2022).

Though the quality of fit to the VO MARVEL data shown in the hyperfine-unresolved, 11 electronic state model of Qu et al. (2023) is superior to the fits presented here in some vibronic bands, their model only included two off-diagonal spin-orbit coupling curves. The inclusion of 28 off-diagonal spin-orbit couplings in this work, as well as the new hyperfine couplings, significantly increases the degree of correlation between any given parameters in the model and accordingly, it took a long time to achieve the fit presented here. For comparison, the quality of the fit presented here is on the same order as those achieved for line lists involving other heavy metal oxides such as CaO (Yurchenko et al., 2016a), TiO (McKemmish et al., 2019), ZrO (Perri et al., 2023) and YO (Xu and Tennyson, 2023). None of these, however, involved as many electronic states and spin-orbit couplings and crucially, none considered hyperfine effects; indeed ^{40}Ca, ^{48}Ti and ^{90}Zr, the most abundant isotope in each case, are all spin zero nuclei.

5.A VO MARVEL data

Table 5.12: Components of the hyperfine-resolved MARVEL network for VO, broken down by data source and vibronic band. The energy and F ranges for the transitions in each band is provided, along with their mean and maximum uncertainty. The total number of transitions validated compared to those accessed by MARVEL (V/A) is also given.

Band	Vib.	F range	V/A	Energy range (cm^{-1})	Unc. Mean/Max (cm^{-1})
81HoMeMi (Hocking et al., 1981)					
C $^4\Sigma^-$-X $^4\Sigma^-$	0 - 0	24 - 34	48/48	17336 - 17354	0.008/0.029
82ChHaMe (Cheung et al., 1982a)					
C $^4\Sigma^-$-X $^4\Sigma^-$	0 - 0	0 - 51	2797/2817	17288 - 17427	0.004/0.200
91SuFrLoGi (Suenram et al., 1991)					
X $^4\Sigma^-$-X $^4\Sigma^-$	0 - 0	3 - 5	3/3	0.2863 - 0.3664	2.00×10^{-7}/2.00×10^{-7}
95AdBaBeBo (Adam et al., 1995)					
1 $^2\Sigma^+$-X $^4\Sigma^-$	2 - 0	35 - 44	14/14	12421 - 12432	0.002/0.002
B $^4\Pi_{-1/2}$-X $^4\Sigma^-$	0 - 0	2 - 52	1027/1030	12408 - 12536	7.73×10^{-4}/0.006
B $^4\Pi_{1/2}$-X $^4\Sigma^-$	0 - 0	1 - 45	872/876	12490 - 12593	8.52×10^{-4}/0.009
B $^4\Pi_{3/2}$-X $^4\Sigma^-$	0 - 0	0 - 44	901/906	12491 - 12661	0.001/0.033
B $^4\Pi_{5/2}$-X $^4\Sigma^-$	0 - 0	1 - 46	703/708	12575 - 12734	9.18×10^{-4}/0.010
08FlZi (Flory and Ziurys, 2008)					
$X^4\Sigma^-$-$X^4\Sigma^-$	0 - 0	3 - 21	220/224	9.7268 - 17.5154	1.67×10^{-6}/1.67×10^{-6}
22DoFuGi (Döring et al., 2022)					
X $^4\Sigma^-$-X $^4\Sigma^-$	1 - 0	0 - 36	1008/1008	1001 - 1032	5.01×10^{-4}/0.001
X $^4\Sigma^-$-X $^4\Sigma^-$	2 - 1	4 - 34	431/431	1000 - 1020	5.00×10^{-4}/5.00×10^{-4}

Table 5.13: Components of the hyperfine-unresolved MARVEL network for VO, broken down by data source and vibronic band. The range in energy and total angular momentum quantum number J for transitions in each band is provided, along with their mean and maximum uncertainty. The total number of transitions validated compared to those accessed by MARVEL (V/A) is also given.

Band	Vib.	J range	V/A	Energy range (cm^{-1})	Unc. Mean/Max (cm^{-1})
57LaSe (Lagerqvist and Selin, 1957)					
$2\ ^2\Pi_{3/2}$-X $^4\Sigma^-$	0 - 0	49.5 - 65.5	10/10	17967 - 18184	0.089/0.326
$2\ ^2\Pi_{3/2}$-X $^4\Sigma^-$	1 - 0	24.5 - 30.5	10/10	19020 - 19094	0.073/0.164
C $^4\Sigma^-$-X $^4\Sigma^-$	0 - 0	12.5 - 85.5	265/265	17026 - 17423	0.065/0.236
C $^4\Sigma^-$-X $^4\Sigma^-$	0 - 1	11.5 - 85.5	267/267	16028 - 16422	0.057/0.257
C $^4\Sigma^-$-X $^4\Sigma^-$	0 - 2	11.5 - 68.5	168/168	15284 - 15431	0.077/0.691
C $^4\Sigma^-$-X $^4\Sigma^-$	1 - 0	12.5 - 87.5	258/258	17868 - 18275	0.061/0.339
C $^4\Sigma^-$-X $^4\Sigma^-$	2 - 0	14.5 - 72.5	176/176	18771 - 19116	0.061/0.179
81HoMeMi (Hocking et al., 1981)					
C $^4\Sigma^-$-X $^4\Sigma^-$	0 - 0	27.5 - 30.5	6/6	17336 - 17354	0.045/0.070
82ChHaMe (Cheung et al., 1982a)					
C $^4\Sigma^-$-X $^4\Sigma^-$	0 - 0	0.5 - 47.5	367/367	17288 - 17427	0.183/12.529
82ChTaMe (Cheung et al., 1982b)					
A $^4\Pi_{-1/2}$-X $^4\Sigma^-$	0 - 0	4.5 - 89.5	197/197	9258 - 9481	0.015/0.254
A $^4\Pi_{-1/2}$-X $^4\Sigma^-$	0 - 1	8.5 - 67.5	114/114	8364 - 8481	0.017/0.251
A $^4\Pi_{1/2}$-X $^4\Sigma^-$	0 - 0	14.5 - 78.5	153/155	9312 - 9493	0.013/0.184
A $^4\Pi_{1/2}$-X $^4\Sigma^-$	0 - 1	20.5 - 66.5	69/69	8374 - 8476	0.010/0.103
A $^4\Pi_{3/2}$-X $^4\Sigma^-$	0 - 0	13.5 - 74.5	166/170	9290 - 9538	0.012/0.152
A $^4\Pi_{3/2}$-X $^4\Sigma^-$	0 - 1	9.5 - 54.5	71/72	8419 - 8514	0.012/0.077
A $^4\Pi_{5/2}$-X $^4\Sigma^-$	0 - 0	3.5 - 89.5	219/221	9262 - 9558	0.011/0.188
A $^4\Pi_{5/2}$-X $^4\Sigma^-$	0 - 1	7.5 - 33.5	53/53	8521 - 8558	0.012/0.057
87MeHuChTa (Merer et al., 1987)					
$1\ ^2\Pi_{1/2}$-$1\ ^2\Delta_{3/2}$	0 - 0	5.5 - 47.5	211/211	7160 - 7266	0.009/0.125
$1\ ^2\Pi_{1/2}$-$1\ ^2\Delta_{3/2}$	1 - 0	4.5 - 46.5	217/217	8057 - 8192	0.016/0.200
$1\ ^2\Pi_{1/2}$-$1\ ^2\Delta_{3/2}$	2 - 1	4.5 - 42.5	163/163	8031 - 8117	0.020/0.200
$1\ ^2\Pi_{1/2}$-$1\ ^2\Delta_{3/2}$	3 - 1	6.5 - 35.5	103/103	8962 - 9025	0.023/0.200
$1\ ^2\Pi_{3/2}$-$1\ ^2\Delta_{5/2}$	0 - 0	4.5 - 46.5	208/208	7048 - 7157	0.007/0.028
$1\ ^2\Pi_{3/2}$-$1\ ^2\Delta_{5/2}$	1 - 0	3.5 - 33.5	140/140	8008 - 8083	0.009/0.031
$2\ ^2\Delta_{3/2}$-$1\ ^2\Phi_{5/2}$	0 - 0	2.5 - 44.5	168/184	9568 - 9644	0.037/0.214
$2\ ^2\Delta_{5/2}$-$1\ ^2\Phi_{7/2}$	0 - 0	2.5 - 40.5	162/162	9483 - 9565	0.027/0.200
$2\ ^2\Pi_{3/2}$-$1\ ^2\Delta_{5/2}$	0 - 0	3.5 - 42.5	162/162	8063 - 8138	0.021/0.200
D $^4\Delta_{1/2}$-A $^4\Pi_{-1/2}$	0 - 0	4.5 - 27.5	37/37	9526 - 9557	0.076/0.313
D $^4\Delta_{3/2}$-A $^4\Pi_{1/2}$	0 - 0	7.5 - 39.5	153/153	9567 - 9632	0.025/0.200
D $^4\Delta_{5/2}$-A $^4\Pi_{3/2}$	0 - 0	3.5 - 29.5	63/66	9647 - 9688	0.048/0.507
D $^4\Delta_{7/2}$-A $^4\Pi_{5/2}$	0 - 0	4.5 - 30.5	115/116	9690 - 9740	0.018/0.200
D $^4\Delta_{1/2}$-A′ $^4\Phi_{3/2}$	0 - 0	2.5 - 40.5	192/192	11946 - 12016	0.015/0.200
D $^4\Delta_{1/2}$-A′ $^4\Phi_{3/2}$	0 - 1	4.5 - 28.5	70/70	11033 - 11067	0.005/0.005
D $^4\Delta_{1/2}$-A′ $^4\Phi_{3/2}$	1 - 0	4.5 - 28.5	96/96	12793 - 12833	0.007/0.024
D $^4\Delta_{3/2}$-A′ $^4\Phi_{5/2}$	0 - 0	7.5 - 41.5	107/107	11867 - 11928	0.016/0.200
D $^4\Delta_{3/2}$-A′ $^4\Phi_{5/2}$	0 - 1	10.5 - 20.5	38/38	10961 - 10987	0.008/0.054
D $^4\Delta_{3/2}$-A′ $^4\Phi_{5/2}$	1 - 0	4.5 - 27.5	73/73	12715 - 12764	0.014/0.302
D $^4\Delta_{5/2}$-A′ $^4\Phi_{7/2}$	0 - 0	7.5 - 51.5	242/242	11713 - 11863	0.011/0.222
D $^4\Delta_{5/2}$-A′ $^4\Phi_{7/2}$	0 - 1	9.5 - 48.5	204/204	10811 - 10929	0.012/0.243
D $^4\Delta_{5/2}$-A′ $^4\Phi_{7/2}$	1 - 0	13.5 - 36.5	78/78	12630 - 12685	0.022/0.200
D $^4\Delta_{5/2}$-A′ $^4\Phi_{7/2}$	1 - 2	13.5 - 42.5	168/168	10730 - 10836	0.010/0.087
D $^4\Delta_{7/2}$-A′ $^4\Phi_{9/2}$	0 - 0	12.5 - 47.5	164/164	11710 - 11795	0.010/0.200
D $^4\Delta_{7/2}$-A′ $^4\Phi_{9/2}$	0 - 1	18.5 - 43.5	82/82	10787 - 10848	0.008/0.020

Table 5.13 - continued

Band	Vib.	J range	V/A	Energy range (cm^{-1})	Unc. Mean/Max (cm^{-1})
87MeHuChTa (Merer et al., 1987) continued					
D $^4\Delta_{7/2}$-A′ $^4\Phi_{9/2}$	1 - 0	14.5 - 39.5	98/98	12529 - 12617	0.027/0.200
D $^4\Delta_{7/2}$-A′ $^4\Phi_{9/2}$	1 - 2	17.5 - 42.5	110/110	10677 - 10768	0.007/0.046
91SuFrLoGi (Suenram et al., 1991)					
X $^4\Sigma^-$-X $^4\Sigma^-$	0 - 0	0.5 - 1.5	1/1	0.3042 - 0.3042	5.95×10^{-6}/5.95×10^{-6}
94ChHaHuHu (Cheung et al., 1994)					
1 $^2\Sigma^+$-X $^4\Sigma^-$	3 - 0	27.5 - 29.5	3/3	13409 - 13413	0.020/0.020
B $^4\Pi_{-1/2}$-X $^4\Sigma^-$	1 - 0	3.5 - 40.5	108/112	13354 - 13409	0.014/0.147
B $^4\Pi_{1/2}$-X $^4\Sigma^-$	1 - 0	5.5 - 38.5	96/100	13360 - 13476	0.014/0.235
B $^4\Pi_{3/2}$-X $^4\Sigma^-$	1 - 0	5.5 - 42.5	93/97	13486 - 13556	0.011/0.214
B $^4\Pi_{5/2}$-X $^4\Sigma^-$	1 - 0	3.5 - 41.5	153/159	13534 - 13631	0.011/0.163
95AdBaBeBo (Adam et al., 1995)					
1 $^2\Sigma^+$-X $^4\Sigma^-$	2 - 0	37.5 - 58.5	13/13	12408 - 12433	0.335/2.250
B $^4\Pi_{-1/2}$-X $^4\Sigma^-$	0 - 0	1.5 - 61.5	382/383	12368 - 12536	0.074/2.250
B $^4\Pi_{1/2}$-X $^4\Sigma^-$	0 - 0	0.5 - 92.5	314/315	12213 - 12593	0.055/2.250
B $^4\Pi_{3/2}$-X $^4\Sigma^-$	0 - 0	0.5 - 53.5	257/258	12491 - 12661	0.038/0.562
B $^4\Pi_{5/2}$-X $^4\Sigma^-$	0 - 0	1.5 - 49.5	323/326	12575 - 12734	0.063/2.250
97KaLiLuSa (Karlsson et al., 1997)					
A $^4\Pi_{-1/2}$-X $^4\Sigma^-$	0 - 0	0.5 - 4.5	10/10	9453 - 9460	0.055/0.087
A $^4\Pi_{1/2}$-X $^4\Sigma^-$	0 - 0	0.5 - 6.5	20/20	9481 - 9498	0.050/0.050
A $^4\Pi_{3/2}$-X $^4\Sigma^-$	0 - 0	0.5 - 5.5	10/10	9516 - 9528	0.050/0.050
A $^4\Pi_{5/2}$-X $^4\Sigma^-$	0 - 0	1.5 - 5.5	7/7	9559 - 9568	0.086/0.241
02RaBeDaMe (Ram et al., 2002)					
1 $^2\Phi_{5/2}$-1 $^2\Delta_{3/2}$	0 - 0	6.5 - 47.5	224/224	5433 - 5548	0.004/0.021
1 $^2\Phi_{7/2}$-1 $^2\Delta_{5/2}$	0 - 0	2.5 - 41.5	212/212	5462 - 5561	0.004/0.018
05RaBe (Ram and Bernath, 2005)					
3 $^2\Delta_{3/2}$-1 $^2\Delta_{3/2}$	0 - 0	7.5 - 46.5	136/136	21866 - 22042	0.008/0.050
3 $^2\Delta_{3/2}$-1 $^2\Delta_{3/2}$	0 - 1	4.5 - 47.5	146/146	20877 - 21050	0.006/0.033
3 $^2\Delta_{5/2}$-1 $^2\Delta_{5/2}$	0 - 0	6.5 - 19.5	50/50	21932 - 21980	0.010/0.032
08FlZi (Flory and Ziurys, 2008)					
X $^4\Sigma^-$-X $^4\Sigma^-$	0 - 0	6.5 - 17.5	28/28	9.7287 - 17.5151	1.05×10^{-5}/1.95×10^{-5}
08SrBaRaBa (Sriramachandran et al., 2008)					
2 $^2\Pi_{3/2}$-X $^4\Sigma^-$	0 - 0	64.5 - 65.5	1/1	17971 - 17971	0.050/0.050
C $^4\Sigma^-$-X $^4\Sigma^-$	0 - 2	14.5 - 67.5	16/16	15289 - 15431	0.062/0.230
C $^4\Sigma^-$-X $^4\Sigma^-$	1 - 0	14.5 - 74.5	25/25	18008 - 18270	0.050/0.050
C $^4\Sigma^-$-X $^4\Sigma^-$	2 - 0	14.5 - 67.5	25/26	18771 - 19116	0.050/0.050
09HoHaMa (Hopkins et al., 2009)					
2 $^2\Pi_{1/2}$-X $^4\Sigma^-$	0 - 0	0.5 - 14.5	101/101	18021 - 18075	0.217/0.570
2 $^2\Pi_{1/2}$-X $^4\Sigma^-$	1 - 0	0.5 - 14.5	33/33	18982 - 19010	0.213/0.431
2 $^2\Pi_{3/2}$-X $^4\Sigma^-$	0 - 0	1.5 - 14.5	56/56	18131 - 18199	0.250/0.708
22DoFuGi (Döring et al., 2022)					
X $^4\Sigma^-$-X $^4\Sigma^-$	1 - 0	0.5 - 32.5	134/134	1001 - 1032	0.036/0.487
X $^4\Sigma^-$-X $^4\Sigma^-$	2 - 1	7.5 - 30.5	70/70	1000 - 1020	0.055/0.562
VOMYT_MAGIC					
1 $^2\Delta_{5/2}$-1 $^2\Delta_{3/2}$	0 - 0	5.5 - 5.5	2/2	357 - 357	0.100/0.100

Chapter 6

Conclusion

6.1 Summary

Chapter 3 detailed the update of the calculated ATP line list of Patrascu et al. (2015) using empirical energy levels obtained through the MARVEL analysis of nine experimental data sources. These high-accuracy empirical energy levels were supported with energies calculated using effective Hamiltonians based on fits to experimental data, as well as the machine learning of observed minus calculated (obs.-calc.) energy differences used to predict energy shifts in levels not observed through experiment. The pseudo-experimental technique was employed to carry all of these energy shifts over to the energies of three other isotopologues of aluminium monoxide in lieu of their own experimental measurements, hence why this technique is sometimes called "isotopologue extrapolation" in other literature (Syme and McKemmish, 2021; Perri et al., 2023; Perri and McKemmish, 2023; McKemmish et al., 2024). These techniques were detailed in Section 2.4 and makeup the hybrid empirical-variational approach to line lists now commonly in use by the ExoMol group and elsewhere.

The update to the AlO line list should serve to future proof it for use with high-resolution studies, though it can be continuously updated with new MARVEL energies when they become available. While the existing ATP line list was successful in detecting AlO in the atmospheres of several exoplanets (von Essen et al., 2019; Chubb et al., 2020a) and has provided tentative results in others (Lewis et al., 2020; Sheppard et al., 2021; Colon et al., 2020) the new update should lead to more consistent results. Similarly, this work will enable the reliable study of AlO in the oxygen rich atmospheres of cool AGB, supergiant and hypergiant stars at high resolutions (Tenenbaum and Ziurys, 2009; Danilovich et al., 2020; Singh et al., 2022). The spectrum of aluminium monoxide is also of interest to plasma physicists, where it is observed through spontaneous emission in laser-induced plasma and can be used to track the time evolution the plasma constituents (Li et al., 2019). This technique can be used to map plasma temperatures (Surmick et al., 2019) and probe non-equilibrium chemistry (Chemin et al., 2023). While analysis showed that the calculated line positions of the ATP $^{27}Al^{16}O$ line list were not of sufficient accuracy for such applications (Parigger, 2023), the empirical energies included in the updated line list should likely remedy this. Indeed, the AlO in these experiments is excited to the B $^2\Sigma^+$ state using a laser, where it subsequently de-excites via fluorescence

down to the ground state; both of the relevant electronic states are well characterised by the MARVEL energies produced in Chapter 3.

As with AlO, an updated line list for four isotopologues of H_3^+ was detailed in Chapter 4, covering all of its deuterated permutations. No isotopologues containing tritium were considered as it is believed to be less abundant than deuterium, which already has a small relative abundance, between 0.028 and 0.001% (de Laeter et al., 2003). Empirical MARVEL energies for these molecules update the high-accuracy calculations of Mizus et al. (2017) and Sochi and Tennyson (2010) for H_3^+ and H_2D^+, respectively, and the newly calculated line list for D_2H^+ to the high-resolution ExoMol format. While the line list for D_3^+ is not of the same accuracy, owing to the lack of sufficient experimental data to obtain meaningful MARVEL energies, it is supplemented with effective Hamiltonian energies calculated from experimental constants. Hence, all four species have term energies with accompanying MARVEL uncertainties or uncertainty estimates. These new line lists will support ongoing studies of chemistry in the ISM and hopefully assist in the detection of H_3^+ in exoplanets.

The updated line lists for AlO and H_3^+ discussed in this work contain high accuracy energies, though the determined obs.-calc. energy values were small, indicating the original calculations were well done. The updates performed for these two data sets are nonetheless essential for ensuring these molecules can be well studied with high-resolution spectroscopy. Owing to the lack of consideration of hyperfine effects in these two molecules, the provision of isotopically substituted line lists through mass substitutions was straightforward. Conversely, the energy differences between the new VO line list and the calculated energies of the VOMYT line list are in many states large, as shown in Table 5.11. Additionally, the existing VOMYT line list did not consider the distinctive hyperfine structure of VO, which appears to be essential for high-resolution experiments. Hence, a brand-new spectroscopic model was produced rather than updating the existing one. The inclusion of hyperfine effects in this case makes the consideration of isotopic substitutions difficult. For example, the next most abundant isotope of vanadium, ^{50}V, has a nuclear spin of $I = 6$, and different nuclear magnetic dipole and electric quadrupole constants owing to different distortions to the nucleus. Accordingly, a simple mass substitution for this isotope will fail to capture the changes in the six different hyperfine interactions included within the model and would instead require refitting to experimental data which is not currently available. Thankfully, the relative abundances of this vanadium isotope are very small, roughly 0.25%. For the other stable isotopes of oxygen, ^{18}O has no nuclear spin and so should be computable with the same model but ^{17}O has $I = \frac{5}{2}$; DUO is not currently able to consider hyperfine interactions in diatomics where both atoms have non-zero nuclear spin. Thankfully, these isotopes also have small relative abundances, roughly 0.21% and 0.04% respectively (de Laeter et al., 2003), so the new line list presented here should be able to characterise the vast majority of VO spectra.

6.2 Future work

In the updated line lists for AlO, the newly added electronic states (C $^2\Pi_r$, D $^2\Sigma^+$, E $^2\Delta_i$ and F $^2\Sigma^+$), comprising 0.7% of the total entries in the $^{27}Al^{16}O$ states file, do not currently have any transitions associated with them. These could be produced however, with the addition of the relevant electronic state potential and transition dipole moment curves to the original ATP spectroscopic model (Patrascu et al., 2015). Since the initial publication of the work on AlO presented in Chapter 3, Bai et al. (2021) provided a 12 electronic state spectroscopic model for AlO using *ab initio* potential energy curves and transition dipole moments. This model covered six doublet and six quartet states correlating to the first dissociation energy and was later extended to include a further 4 doublets corresponding to the next dissociation energy (Bai et al., 2023) with the aim of acquiring better coverage in the UV. This extended model includes the C $^2\Pi_r$ and D $^2\Sigma^+$ state, among five other doublet states and six quartet states that have so far not been observed in experiment. While their model produces energies in worse agreement with the MARVEL data set than those of the ATP line list, their *ab initio* transition dipole moment curves could be added to the ATP spectroscopic model as their intensities were generally in good agreement, if slightly lower than those of the ATP line list (Bai et al., 2023). Their potential energy curves for the C $^2\Pi_r$ and D $^2\Sigma^+$ states could also serve as a good starting point for further refinement against the known MARVEL energies using the built-in fitting procedures in DUO (Yurchenko et al., 2016b). New *ab initio* calculations could be performed for the potential energy curves of the E $^2\Delta_i$ and F $^2\Sigma^+$ states to additionally incorporate them into the line list. Diagonal spin-orbit coupling curves for the C $^2\Pi_r$ state could be taken from the work of Bai et al. (2023) and calculated for the E $^2\Delta_i$ state, followed by minimal refinement against the small number of known empirical energy levels. Additional experimental measurements of transitions involving these higher lying states would allow for the determination of more empirical energy levels and subsequently the more thorough refinement of the *ab initio* curves. Experimental measurements involving the higher vibrational bands of these states would be particularly useful as they would better constrain the shapes of the potential energy curves and allow for more accurate extrapolation.

Hyperfine effects are known to be present in the spectra of H_3^+ and its deuterated isotopologues, due to the nuclear spin of the component protons and deuterons (Jensen et al., 1997). These hyperfine splittings have not yet been observed however in either an astrophysical setting or in the laboratory, hence why they were absent from the MARVEL dataset. Were experiments to be conducted to measure the hyperfine-resolved spectra of the species considered here, it would enable the construction of hyperfine-resolved MARVEL networks and subsequently line lists. Similarly, any further measurements of hyperfine-unresolved spectra could be added to the current MARVEL network to further constrain the resultant empirical energy levels and hence improve the accuracy of the line lists. In particular, additional measurements of hot bands would allow for more accurate constraints on higher vibrational bands and, ideally, better quantum number assignments for levels in these regions, where the density of states is very high. If a sufficiently large number of new spectra were observed for D_3^+ to form a well-connected MARVEL network,

it would be possible to further update the D_3^+ line list with MARVEL energies to a high-resolution standard.

Though the predicted shift technique detailed in Section 2.4.3 proved effective in the production of hybrid line lists for AlO and VO, it was not used for the isotopologues of H_3^+. In diatomics this technique was applied to predict synthetic obs.-calc. values for levels in spin-orbit components of vibronic states, though the application was not directly transferable to triatomics. It would be necessary to first test which quantum numbers the trends in the obs.-calc. values depend on, and this will likely differ between the species due to the different symmetries and hence quantum number schemes used. While it is likely that these trends will depend on both J and K or K_a and K_c, it may be that they more depend on a linear transform of these values, i.e.: $J - K$, as with the predicted shifts in the hyperfine-resolved energies of VO depending on $F - J$. A machine learning project to classify these effects would be enlightening.

While the levels of the X $^4\Sigma^-$, B $^4\Pi$ and C $^4\Sigma^-$ states of VO in the new line list are fully hyperfine-resolved, levels from other electronic states use hyperfine-unresolved term energies for all of their hyperfine components, due to limited experimental resolution. As such, hyperfine-resolved spectroscopic studies of important bands such as the A $^4\Pi$–X $^4\Sigma^-$ system would enable the further improvement of the line list by characterising the currently not quantified hyperfine splitting in the A $^4\Pi$ state. Merer et al. (1987) observed broadening due to hyperfine splittings in the A′ $^4\Phi$–D$^4\Delta$ band but were unable to assign individual hyperfine transitions due to limited experimental resolution available to them at the time. Additional hyperfine-resolved observations of such bands at the higher resolutions available in modern laboratories would allow for the inclusion of hyperfine couplings for even more electronic states. While the hyperfine-resolved levels of the 1 $^2\Sigma^+$ state have been observed via perturbations to the B $^4\Pi$ state, the hyperfine effects present in the rest of the doublet states of VO remain essentially unobserved. Indeed, most published observations of the doublet states had insufficient resolution to resolve parity splitting, let alone the smaller hyperfine splittings, and would all benefit from new high-resolution experiments.

If studies aim to observe VO further into the UV, calculations could be performed for transition dipole moments involving the 2 $^2\Delta$ and 3 $^2\Delta$ states to better characterise their contributions to the spectra in these regions. A full treatment of these two states in the current spectroscopic model would require the addition of 9 transition dipole moments and 16 off-diagonal spin-orbit couplings which, given the high-degree of correlation between the model parameters, would likely require extensive refinement. It might be necessary to include a considerable number of extra electronic states if one intended to properly model the UV spectrum of VO, to characterise its photodissociation spectrum for example. The same applies to AlO, where its photodissociation cross section may also be relevant in the atmospheres of both exoplanets and stars, requiring the extension of the current model to higher energies and electronic states.

Observations of higher vibrational bands of VO would allow for better constraints on the shapes of the electronic potentials and hence better extrapolation to

higher energies. The model presented here covers all of the experimentally observed states of VO, except for the 3 $^2\Pi$ state observed by Hopkins et al. (2009). Assignments to the 3 $^2\Pi$–X $^4\Sigma^-$ bands observed by them could be added to the MARVEL data and the current model subsequently extended to include the 3 $^2\Pi$ state. Band head measurements of bands involving higher vibrational states of the X $^4\Sigma^-$, B $^4\Pi$, C $^4\Sigma^-$ and 2 $^2\Pi$ states than were present in the fully assigned transition data were incorporated into the spectroscopic model refinement process. This ensured that the model extrapolated to these higher vibrational bands fairly well but would be more accurate if fully assigned transition data were available to be included in the MARVEL networks. Though the spectra from which these band head measurements were taken are published and available, they are too low resolution to make individual line assignments. Again, new high-resolution observations of these and additional bands would be of great benefit to the overall accuracy of the potential energy curves in the model and hence the spectra derived from it.

The roughly 59 billion transitions in the new VO line list are a considerable increase on the 277 million transitions that made up its predecessor, the VOMYT line list (McKemmish et al., 2016b). Owing to the significant increase in energy levels as a result of hyperfine coupling, the number of transitions in the new line list is closer to line lists of polyatomic molecules than it is other diatomics. With the current implementation of DUO and owing to the large number of electronic states and associated couplings, the spectroscopic model calculations required considerable computer resources and made use of the DiRAC Data Intensive service at Leicester high-performance cluster. While the VO line list could be extended to consider some of the additional known electronically excited states, particularly those lying at higher energies, the calculations using the new spectroscopic model would rapidly approach the memory limits of these computer resources. Accordingly, modifications to the code would likely be required before tackling larger and more complex systems; it may be necessary to restructure the program's memory management, rather than simply optimise parts of the calculation. Current implementations of polyatomic variational nuclear motion codes like TROVE (Yurchenko et al., 2007) deal with this issue by generating "checkpoint" files at various intervals that store intermediary data, avoiding having to hold multiple extremely large matrices in memory simultaneously. A similar implementation could be added to DUO, freeing up considerable amounts of memory currently used to hold the entire very large hyperfine-resolved basis set in memory.

Going beyond the work presented here on VO, it will likely be necessary to extend the capabilities of DUO and indeed variational nuclear motion codes for molecules consisting of a larger number of atoms to consider the general hyperfine case, where more than one atom has non-zero nuclear spin. Some studies, such as the recent work on aluminium hydride and aluminium deuteride by Yurchenko et al. (2024c), found that a treatment only considering the hyperfine effects arising from the atom with the largest nuclear spin in the molecule was sufficient, in this case $I = \frac{5}{2}$ for ^{27}Al, though this is not the case for many molecules of interest. For example, the two hydrogen atoms of H_2O have equivalent nuclear spin and hence both must be considered to accurately describe its hyperfine structure, which is known to have

applications in masers (Varshalovich et al., 2006). This is even more true in the case of $H_2{}^{17}O$, where the oxygen isotope also has non-zero nuclear spin (Melosso et al., 2021b). Likewise, the hyperfine structure is believed to be important in D_2O and HDO (Puzzarini et al., 2015; Cazzoli et al., 2015), NH_2D and ND_2H (Melosso et al., 2021a) and H_2S and HDS (Helgaker et al., 2013; Melosso et al., 2023), all of which are known to be of astrophysical significance. Before tackling larger molecules such as these, the hyperfine structure of several other 3d-transition metal bearing diatomics like ScH (Le and Steimle, 2011), CrH (Halfen and Ziurys, 2004) or CoH (Gordon et al., 2006) could be characterised, the first two of which are known to present in cool dwarfs and hot Jupiters (Braam et al., 2021; Flagg et al., 2023) and the latter in asymptotic giant branch stars (Agúndez, M. et al., 2020). Smaller molecules with less complicated electronic structures like NH also have observed hyperfine splittings (Perri and McKemmish, 2023). Some of these molecules have existing spectroscopic models (Lodi et al., 2015; Perri and McKemmish, 2023) that could be adapted to produce hyperfine-resolved line lists, much in the same manner that the hyperfine-unresolved VOMYT line list served as a comprehensive starting point for the construction of the new VO line list presented here. To achieve this, the hyperfine coupling terms presented in Section 2.1.1 would need to be modified to sum over the interactions with each nucleus, which would likely not be too computationally challenging as the majority of the individual interaction terms have already been implemented (Qu et al., 2022a).

As discussed in Section 2.1.1, other hyperfine coupling terms implementing Zeeman and diamagnetic interactions could be included in hyperfine-resolved models only if variational nuclear motion codes were modified to account for external magnetic fields, as many of the codes in use are field-free. Such additions would likely be necessary to fully model the behaviour of relevant molecules in the atmospheres of exoplanets with strong magnetic fields, where the weak-field approximation of Landé g-factors is no longer valid (Semenov et al., 2017). Indeed, a study of four hot Jupiters found magnetic field strengths ranging from $20-120$ Gauss, substantially larger than that of Jupiter's, which is known to be roughly 4 Gauss (Cauley et al., 2019). Given the strength of the auroral H_3^+ emissions observed from Jupiter, which is driven by its magnetic field, these planets may make good targets for testing whether similar processes occur outside of our solar system.

Hyperfine effects are also an important field of study for ultracold molecules, with many of the pertinent molecules under study being diatomics containing alkali or alkaline earth metals with large nuclear spins (Ran et al., 2010; Aldegunde and Hutson, 2018; Yang et al., 2022; Pang et al., 2023). Laser cooling experiments have more recently started to consider polyatomic molecular candidates, such as SrOH (Kozyryev et al., 2017), YbOH (Pilgram et al., 2021), CaOH (Anderegg et al., 2023) and even more complex molecules like $YbOCH_3$ (Augenbraun et al., 2021) where hyperfine resolution is believed to be necessary. These molecules will require variational nuclear motion codes for polyatomics to be updated to include hyperfine coupling modules, as codes such as TROVE (Yurchenko et al., 2007), which has been frequently used by the ExoMol group, and Everest (Mitrushchenkov, 2012), which allows for the calculation of excited electronic states, do not currently have this

capability. Indeed, a MARVELised line list for CaOH was computed by Owens et al. (2022b) but was not able to provide the hyperfine-resolved energy levels needed for these sorts of experiments. Many of these metal hydroxides are also of importance in the oxygen-rich envelopes of stars, such as AlOH which has been detected alongside its monoxide counterpart, AlO, in VY CMa (Tenenbaum and Ziurys, 2009, 2010).

The line lists presented here have been produced to the accuracy required for use with ground based high-resolution spectroscopy. Though the JWST continues to provide medium resolution exoplanet spectra and future space-based missions such as ARIEL will provide a further source of atmospheric data, ground-based observations will remain crucial. The high resolutions obtainable on ground-based instruments enable the more thorough characterisation of exoplanet atmospheres by probing a wider range of altitudes (Gandhi et al., 2020; Guilluy et al., 2022) and will be essential to corroborate retrieved abundances and derived physical properties. Corroboration of these data is essential, as current modelling of JWST spectra does not appear to reliably retrieve consistent abundances or isotope ratios (Petrus et al., 2023). To match the increasing rate of data acquisition these new telescopes will bring, continued laboratory measurements for future MARVEL studies will be required, along with much more data on pressure and collisional line broadening and line shift parameters which are currently severely lacking (Fortney et al., 2016, 2019). These abundances and broadening effects are crucial for understanding the chemical processes occurring within and for providing insights into the structures of exoplanet atmospheres (de Kok et al., 2014; Hedges and Madhusudhan, 2016; Brogi and Line, 2019).

While there are many existing line lists that are waiting to be updated to a high-resolution standard, there are even more molecules of interest to the astronomical community for which no line list has yet been provided. Many more diatomics containing 3d-transition metals are known to be important in stars and believed to be important in hot Jupiters. To provide a comprehensive data library for such targets, construction of line lists for the 3d-transition metal hydrides and oxides will be necessary (Decin et al., 2018), with potential for addressing their nitrides and sulphides afterwards. Of particular interest are FeH and FeO, though their electronic structures are even more complicated than that of VO as presented in Fig. 5.10 and will require computational improvements for adequate spectroscopic models to be feasibly computed. Beyond metal-bearing species, protonated noble gases and other ions are known to be important in regions such as molecular clouds (Güsten et al., 2019) and will need to be considered. So far, the ExoMol project has only considered cations, not anions, and these have all only been singularly ionised. Outside of astrophysics, high-accuracy line lists for alkali or alkaline earth metals diatomics are of interest to those studying ultra-cold molecules and laser cooling. The molecule BH is relevant to fusion research, where it is a candidate constituent for tokamak reactor walls; the capability to monitor its presence within the reactor is crucial to efficient operation. Similarly, the molecules WC and WB and polyatomic permutations of these atoms are also relevant due to the use of tungsten-based shielding for high-temperature superconductors in tokamaks (Windsor et al., 2021). In short, the list of important molecules yet to be considered is extensive and

continues to grow, requiring the continued efforts of many to tackle.

Bibliography

Abraham, A., Lynch, P., Glumac, N., 2023. On using ab initio calibration to fit temperature from AlO B-X emission. Proceedings of the Combustion Institute 39, 1249–1257. doi:10.1016/j.proci.2022.09.050.

Adam, A.G., Barnes, M., Berno, B., Bower, R.D., Merer, A.J., 1995. Rotational and hyperfine-structure in the B $^4\Pi$-X $^4\Sigma^-$ (0,0) band of VO at 7900 Å: Perturbations by the a $^2\Sigma^+$, v=2 level. J. Mol. Spectrosc. 170, 94–130. doi:10.1006/jmsp.1995.1059.

Agúndez, M., Martínez, J. I., de Andres, P. L., Cernicharo, J., Martín-Gago, J. A., 2020. Chemical equilibrium in AGB atmospheres: successes, failures, and prospects for small molecules, clusters, and condensates. Astron. Astrophys. 637, A59. doi:10.1051/0004-6361/202037496.

Al-Derzi, A.R. et al., 2021. An improved rovibrational linelist of formaldehyde, $H_2^{12}C^{16}O$. J. Quant. Spectrosc. Radiat. Transf. 266, 107563. doi:10.1016/j.jqsrt.2021.107563.

Al-Refaie, A.F., Yurchenko, S.N., Yachmenev, A., Tennyson, J., 2015. ExoMol line lists - VIII: A variationally computed line list for hot formaldehyde. Mon. Not. Roy. Astron. Soc. 448, 1704–1714. doi:10.1093/mnras/stv091.

Aldegunde, J., Hutson, J.M., 2018. Hyperfine structure of $^2\Sigma$ molecules containing alkaline-earth-metal atoms. Phys. Rev. A 97, 042505. doi:10.1103/PhysRevA.97.042505.

Ali-Dib, M., Mousis, O., Pekmezci, G.S., Lunine, J.I., Madhusudhan, N., Petit, J.M., 2014. Influence of the C/O ratio on titanium and vanadium oxides in protoplanetary disks. Astron. Astrophys. 561, A60. doi:10.1051/0004-6361/201321780.

Alijah, A., Wolniewicz, L., Hinze, J., 1995. Rotation-vibrational states of D_3^+ computed using hyperspherical harmonics. Mol. Phys. 85, 1125–1150. doi:10.1080/00268979500101711.

Amano, T., 1985. Difference-frequency laser spectroscopy of molecular ions with a hollow-cathode cell: Extended analysis of the ν_1 band of H_2D^+. J. Opt. Soc. Am. B 2, 790 – 793. doi:10.1364/JOSAB.2.000790.

Amano, T., 2006. Submillimetre-wave lines of H_2D^+ and D_2H^+ as probes into chemistry in cold dark clouds. Phil. Trans. Royal Soc. London A 364, 2943–2952. doi:10.1098/rsta.2006.1861.

Amano, T., Chan, M.C., Civis, S., McKellar, A.R.W., Majewski, W.A., Sadovskii, D., Watson, J.K.G., 1994. The infrared vibration-rotation spectrum of the D_3^+ molecular ion - extension to higher vibrational and rotational quantum numbers. Can. J. Phys. 72, 1007–1015. doi:10.1139/p94-132.

Amano, T., Hirao, T., 2005. Accurate rest frequencies of submillimeter-wave lines of H_2D^+ and D_2H^+. J. Mol. Spectrosc. 233, 7–14. doi:10.1016/j.jms.2005.05.008.

Amano, T., Watson, J.K.G., 1984. Observation of the ν_1 fundamental band of H_2D^+. J. Chem. Phys. 81, 2869–2871. doi:10.1063/1.448059.

Anderegg, L., Vilas, N.B., Hallas, C., Robichaud, P., Jadbabaie, A., Doyle, J.M., Hutzler, N.R., 2023. Quantum control of trapped polyatomic molecules for eEDM searches. Science 382, 665–668. doi:10.1126/science.adg8155.

Árendás, P., Furtenbacher, T., Császár, A.G., 2016. On spectra of spectra. J. Math. Chem. 54, 806–822. doi:10.1007/s10910-016-0591-1.

Arendas, P., Furtenbacher, T., Császár, A.G., 2020. From bridges to cycles in spectroscopic networks. Sci. Rep. 10, 19489. doi:10.1038/s41598-020-75087-5.

Asvany, O., Hugo, E., Schlemmer, S., Muller, F., Kuhnemann, F., Schiller, S., Tennyson, J., 2007. Overtone spectroscopy of H_2D^+ and D_2H^+ using laser induced reactions. J. Chem. Phys. 127, 154317. doi:10.1063/1.2794331.

Asvany, O., Ricken, O., Müller, H.S.P., Wiedner, M.C., Giesen, T.F., Schlemmer, S., 2008. High-Resolution Rotational Spectroscopy in a Cold Ion Trap: H_2D^+ and D_2H^+. Phys. Rev. Lett. 100, 233004. doi:10.1103/PhysRevLett.100.233004.

Augenbraun, B.L., Lasner, Z.D., Frenett, A., Sawaoka, H., Le, A.T., Doyle, J.M., Steimle, T.C., 2021. Observation and laser spectroscopy of ytterbium monomethoxide, $YbOCH_3$. Phys. Rev. A 103, 022814. doi:10.1103/PhysRevA.103.022814.

Augustovicova, L.D., Spirko, V., 2021a. Radial molecular property functions of CH in its ground electronic state. J. Quant. Spectrosc. Radiat. Transf. 272, 107809. doi:10.1016/j.jqsrt.2021.107809.

Augustovicova, L.D., Spirko, V., 2021b. Radial molecular property functions of the A $^2\Sigma^+$ state of hydroxyl. J. Quant. Spectrosc. Radiat. Transf. 266, 107530. doi:10.1016/j.jqsrt.2021.107530.

Bai, T., Qin, Z., Liu, L., 2021. Rate coefficients of the aluminium monoxide formation by radiative association. Mon. Not. Roy. Astron. Soc. 510, 1649–1656. doi:10.1093/mnras/stab3481.

Bai, T., Qin, Z., Liu, L., 2023. Ultraviolet spectroscopy of AlO from first principle. J. Quant. Spectrosc. Radiat. Transf. 302, 108587. doi:10.1016/j.jqsrt.2023.108587.

Bai, X., Steimle, T.C., 2020. The Stark Effect, Zeeman Effect, and Transition Dipole Moments for the B $^2\Sigma^+$–X $^2\Sigma^+$ Band of Aluminum Monoxide, AlO. Astrophys. J. 889, 147. doi:10.3847/1538-4357/ab6327.

Bakalbassis, E.G., Stiakaki, M.A.D., Tsipis, A.C., Tsipis, C.A., 1996. Ground and low-lying excited state properties of the first-row transition-metal oxide diatomics calculated by an improved ASED-MO model. Chem. Phys. 205, 389–399. doi:10.1016/0301-0104(95)00417-3.

Balducci, G., Gigli, G., Guido, M., 1983. Thermochemical properties of the gaseous molecules VO, VO2, and V2O4. J. Chem. Phys. 79, 5616–5622. doi:10.1063/1.445682.

Ballester, G.E., Miller, S., Tennyson, J., Trafton, L.M., Geballe, T.R., 1994. Lattitudinal temperature variations of Jovian H_3^+. Icarus 107, 189–194. doi:10.1006/icar.1994.1015.

Banerjee, D.P.K., Ashok, N.M., Launila, O., Davis, C.J., Varricatt, W.P., 2004. A search for radioactive Al-26 in the nova- like variable V4332 Sagittarii. Astrophys. J. 610, L29–L32. doi:10.1086/423171.

Banerjee, D.P.K., Varricatt, W.P., Ashok, N.M., Launila, O., 2003. Remarkable changes in the near-infrared spectrum of the Nova-like Variable V4332 Sagittari. Astrophys. J. 598, L31–L34. doi:10.1086/380389.

Banerjee, D.P.K., Varricatt, W.P., Mathew, B., Launila, O., Ashok, N.M., 2012. The A-X infrared bands of aluminum oxide in stars: Search and new detections. Astrophys. J. Lett. 753, L20. doi:10.1088/2041-8205/753/1/L20.

Barklem, P.S., Collet, R., 2016. Partition functions and equilibrium constants for diatomic molecules and atoms of astrophysical interest. Astron. Astrophys. 588, A96. doi:10.1051/0004-6361/201526961.

Barletta, P., Lombardi, M., Kievsky, A., 2004. Variational DVR Calculations. Few-Body Systems 34, 11–14. doi:10.1007/s00601-004-0023-9.

Baron, R., Joseph, R.D., Owen, T., Tennyson, J., Miller, S., Ballester, G.E., 1991. Imaging Jupiter's aurorae from H_3^+ emissions in the 3–4 μm band. Nature 353, 539–542. doi:10.1038/353539a0.

Bauschlicher, C.W., Langhoff, S.R., 1986. Theoretical-studies of the low-lying states of ScO, ScS, VO, and VS. J. Chem. Phys. 85, 5936–5942. doi:10.1063/1.451505.

Bauschlicher, C.W., Maitre, P., 1995. Theoretical-study of the first transition row oxides and sulfides. Theor. Chim. Acta. 90, 189–203. doi:10.1007/BF01113847.

Bawendi, M.G., Rehfuss, B.D., Oka, T., 1990. Laboratory observation of hot bands of H_3^+. J. Chem. Phys. 93, 6200–6209. doi:10.1063/1.458989.

Ben-Yami, M., Madhusudhan, N., Cabot, S.H.C., Constantinou, S., Piette, A., Gandhi, S., Welbanks, L., 2020. Neutral Cr and V in the Atmosphere of Ultra-hot Jupiter WASP-121 b. Astrophys. J. Lett. 897, L5. doi:10.3847/2041-8213/ab94aa.

Berblinger, M., Schlier, C., Tennyson, J., Miller, S., 1992. Accurate specific molecular state densities by phase space integration: II comparison with quantum calculations on H_3^+ and HD_2^+. J. Chem. Phys. 96, 6842–6849. doi:10.1063/1.462573.

Berg, M., Wolf, A., Petrignani, A., 2012. Visible transitions from ground state H_3^+ measured with high-sensitivity action spectroscopy. Phil. Trans. Royal Soc. London A 370, 5028–5040. doi:10.1098/rsta.2012.0017.

Bergeron, P., Ruiz, M.T., Leggett, S.K., 1997. The chemical evolution of cool white dwarfs and the age of the local galactic disk. Astrophys. J. Suppl. Ser. 108, 339–387. doi:10.1086/312955.

Berkowitz, J., Chupka, W.A., Inghram, M.G., 1957. Thermodynamics of the V-O system: Dissociation energies of VO and VO_2. J. Chem. Phys. 27, 87–90. doi:10.1063/1.1743723.

Bernath, P.F., 2009. Molecular astronomy of cool stars and sub-stellar objects. Int. Rev. Phys. Chem. 28, 681–709. doi:10.1080/01442350903292442.

Bernath, P.F., 2020. MoLLIST: Molecular Line Lists, Intensities and Spectra. J. Quant. Spectrosc. Radiat. Transf. 240, 106687. doi:10.1016/j.jqsrt.2019.106687.

Bescos, B., Morley, G., Urena, A.G., 1995. Chemiluminescence and reactivity of aluminum monoxide (alo) in the excited b $^2\sigma^+$ state. Chem. Phys. Lett. 244, 407–413. doi:10.1016/0009-2614(95)00949-5.

Birkby, J.L., 2018. Exoplanet Atmospheres at High Spectral Resolution. arXiv e-prints. doi:10.48550/arXiv.1806.04617, arXiv:1806.04617.

Birkby, J.L., 2018. Spectroscopic Direct Detection of Exoplanets. Handbook of Exoplanets, 1485–1508. doi:10.1007/978-3-319-55333-7_16.

Bogey, M., Demuynck, C., Denis, M., Destombes, J.L., Lemoine, B., 1984. Laboratory measurement of the 1_{10}-1_{11} submillimeter line of H_2D^+. Astron. Astrophys. 137, L15. URL: https://ui.adsabs.harvard.edu/abs/1984A&A...137L..15B.

Bol'shakov, A.A., Mao, X., Russo, R.E., 2017. Spectral emission enhancement by an electric pulse for LIBS and LAMIS. J. Anal. At. Spectrom. 32, 657–670. doi:10.1039/c6ja00436a.

Bowesman, C.A., Akbari, H., Hopkins, S., Yurchenko, S.N., Tennyson, J., 2022. Fine and hyperfine resolved empirical energy levels for VO. J. Quant. Spectrosc. Radiat. Transf. 289, 108295. doi:10.1016/j.jqsrt.2022.108295.

Bowesman, C.A. et al., 2023. ExoMol line lists - L: High-resolution line lists of H_3^+, H_2D^+, D_2H^+ and D_3^+. Mon. Not. Roy. Astron. Soc. 519, 6333–6348. doi:10.1093/mnras/stad050.

Bowesman, C.A., Qu, Q., McKemmish, L.K., Yurchenko, S.N., Tennyson, J., 2024a. ExoMol line lists – LV: Hyperfine-resolved molecular line list for vanadium monoxide ($^{51}V^{16}O$). Mon. Not. Roy. Astron. Soc. 529, 1321–1332. doi:10.1093/mnras/stae542.

Bowesman, C.A., Shuai, M., Yurchenko, S.N., Tennyson, J., 2021. A high resolution line list for AlO. Mon. Not. Roy. Astron. Soc. 508, 3181–3193. doi:10.1093/mnras/stab2525.

Bowesman, C.A., Yurchenko, S.N., Tennyson, J., 2024b. A hyperfine-resolved spectroscopic model for vanadium monoxide ($^{51}V^{16}O$). Mol. Phys. 122, e2255299. doi:10.1080/00268976.2023.2255299.

Braam, M., van der Tak, F.F.S., Chubb, K.L., Min, M., 2021. Evidence for chromium hydride in the atmosphere of hot Jupiter WASP-31b. Astron. Astrophys. 646, A17. doi:10.1051/0004-6361/202039509.

Brady, R.P., Yurchenko, S.N., Tennyson, J., Kim, G.S., 2024. ExoMol line lists – LVI. The SO line list, MARVEL analysis of experimental transition data and refinement of the spectroscopic model. Mon. Not. Roy. Astron. Soc. 527, 6675–6690. doi:10.1093/mnras/stad3508.

Brandl, B.R. et al., 2010. Instrument concept and science case for the mid-IR E-ELT imager and spectrograph METIS, in: McLean, I.S., Ramsay, S.K., Takami, H. (Eds.), Ground-based and Airborne Instrumentation for Astronomy III, International Society for Optics and Photonics. SPIE. p. 77352G. doi:10.1117/12.857346.

Bridgeman, A.J., Rothery, J., 2000. Periodic trends in the diatomic monoxides and monosulfides of the 3d transition metals. J. Chem. Soc. Dalton, 211–218. doi:10.1039/a906523g.

Broclawik, E., Borowski, T., 2001. Time-dependent DFT study on electronic states of vanadium and molybdenum oxide molecules. Chem. Phys. Lett. 339, 433–437. doi:10.1016/S0009-2614(01)00361-X.

Brogi, M., Line, M.R., 2019. Retrieving Temperatures and Abundances of Exoplanet Atmospheres with High-resolution Cross-correlation Spectroscopy. Astrophys. J. 157, 114. doi:10.3847/1538-3881/aaffd3.

Brown, J.M., Carrington, A., 2010. Rotational Spectroscopy of Diatomic Molecules. Cambridge Molecular Science, Cambridge University Press.

Bunker, P.R., Jensen, P., 2006. Molecular Symmetry and Spectroscopy, Second Edition. NRC Research Press, Ottawa, Canada.

Butler, P.A., 2020. Pear-shaped atomic nuclei. Proc. R. Soc. London, Ser. A 476, 20200202. doi:10.1098/rspa.2020.0202.

Calatayud, M., Silvi, B., Andres, J., Beltran, A., 2001. A theoretical study on the structure, energetics and bonding of VO_x^+ and VO_x (x=1-4) systems. Chem. Phys. Lett. 333, 493–503. doi:10.1016/S0009-2614(00)01287-2.

Carlson, K.D., Moser, C., 1966. Electronic ground state and wavefunctions for vanadium monoxide. J. Chem. Phys. 44, 3259–3265. doi:10.1063/1.1727221.

Caselli, P., van der Tak, F.F.S., Ceccarelli, C., Bacmann, A., 2003. Abundant H_2D^+ in the pre-stellar core L1544. Astron. Astrophys. 403, L37–L41. doi:10.1051/0004-6361:20030526.

Castelaz, M.W., Luttermoser, D.G., Piontek, R.A., 2000. Vanadium oxide in the spectra of Mira variables. Astrophys. J. 538, 341–345. doi:10.1086/309121.

Cauley, P.W., Shkolnik, E.L., Llama, J., Lanza, A.F., 2019. Magnetic field strengths of hot Jupiters from signals of star–planet interactions. Nature Astronomy 3, 1128–1134. doi:10.1038/s41550-019-0840-x.

Cazzoli, G., Lattanzi, V., Alonso, J.L., Gauss, J., Puzzarini, C., 2015. The hyperfine structure of the rotational spectrum of HDO and its extension to the THz region: accurate rest frequencies and spectroscopic parameters for astrophysical observations. Astrophys. J. 806, 100. doi:10.1088/0004-637X/806/1/100.

Chadney, J.M., Galand, M., Koskinen, T.T., Miller, S., Sanz-Forcada, J., Unruh, Y.C., Yelle, R.V., 2016. EUV-driven ionospheres and electron transport on extrasolar giant planets orbiting active stars. Astron. Astrophys. 587, A87. doi:10.1051/0004-6361/201527442.

Changeat, Q. et al., 2022. Five key exoplanet questions answered via the analysis of 25 hot-jupiter atmospheres in eclipse. Astrophys. J. Suppl. Ser. 260, 3. doi:10.3847/1538-4365/ac5cc2.

Chemin, A., Ross, A., Hermelin, S., Crozet, P., Motto-Ros, V., Ledoux, G., Dujardin, C., Amans, D., 2023. On the use of laser-induced fluorescence to probe the thermodynamic equilibrium in laser-generated plasmas. Spectroc. Acta Pt. B-Atom. Spectr. 205, 106685. doi:10.1016/j.sab.2023.106685.

Chen, W., Poirier, B., 2006a. Parallel Implementation of Efficient Preconditioned Linear Solver for Grid-based Applications in Chemical Physics: I. Block-Jacobi diagonalization. J. Comput. Phys. 219, 185–197. doi:10.1016/j.jcp.2006.04.012.

Chen, W., Poirier, B., 2006b. Parallel Implementation of Efficient Preconditioned Linear Solver for Grid-based Applications in Chemical Physics: II. QMR linear solver. J. Comput. Phys. 219, 198–209. doi:10.1016/j.jcp.2006.03.031.

Chen, W., Poirier, B., 2010a. Parallel Implementation of Efficient Preconditioned Linear Solver for Grid-based Applications in Chemical Physics: III. Improved parallel scalability for sparse matrix-vector products. J. Parallel Distrib. Comput. 70, 779–782. doi:10.1016/j.jpdc.2010.03.008.

Chen, W., Poirier, B., 2010b. Quantum Dynamics on Massively Parallel Computers: Efficient numerical implementation for preconditioned linear solvers and eigensolvers. J. Theoret. Comput. Chem. 9, 825. doi:10.1142/S021963361000602X.

Cheung, A.S.C., Hajigeorgiou, P.G., Huang, G., Huang, S.Z., Merer, A.J., 1994. Rotational Structure and Perturbations in the B $^4\Pi$–X $^4\Sigma^-$ (1, 0) Band of VO. J. Mol. Spectrosc. 163, 443–458. doi:10.1006/jmsp.1994.1039.

Cheung, A.S.C., Hansen, R.C., Lyyra, A.M., Merer, A.J., 1981. A novel electronic-hyperfine perturbation in the C $^4\Sigma^-$ state of VO. J. Mol. Spectrosc. 86, 526–533. doi:10.1016/0022-2852(81)90298-8.

Cheung, A.S.C., Hansen, R.C., Merer, A.J., 1982a. Laser Spectroscopy of VO-Analysis of the Rotational and Hyperfine Structure of the C $^4\Sigma^-$–X $^4\Sigma^-$ (O, O) band. J. Mol. Spectrosc. 91, 165–208. doi:10.1016/0022-2852(82)90039-X.

Cheung, A.S.C., Taylor, A.W., Merer, A.J., 1982b. Fourier-transform spectroscopy of VO: Rotational structure in the A $^4\Pi$–X $^4\Sigma^-$ system near 10 500 A. J. Mol. Spectrosc. 92, 391–409. doi:10.1016/0022-2852(82)90110-2.

Chubb, K.L. et al., 2018. MARVEL analysis of the measured high-resolution spectra of C_2H_2. J. Quant. Spectrosc. Radiat. Transf. 204, 42–55. doi:10.1016/j.jqsrt.2017.08.018.

Chubb, K.L., Min, M., Kawashima, Y., Helling, C., Waldmann, I., 2020a. Aluminium oxide in the atmosphere of hot Jupiter WASP-43b. Astron. Astrophys. 639, A3. doi:10.1051/0004-6361/201937267.

Chubb, K.L., Tennyson, J., Yurchenko, S.N., 2020b. ExoMol Molecular linelists – XXXVII: spectra of acetylene. Mon. Not. Roy. Astron. Soc. 493, 1531–1545. doi:10.1093/mnras/staa229.

Coles, P.A., , Yurchenko, S.N., Tennyson, J., 2019. ExoMol molecular line lists XXXV: a rotation-vibration line list for hot ammonia. Mon. Not. Roy. Astron. Soc. 490, 4638–4647. doi:10.1093/mnras/stz2778.

Colon, K.D. et al., 2020. An Unusual Transmission Spectrum for the Sub-Saturn KELT-11b Suggestive of a Subsolar Water Abundance. Astron. J. 160, 280. doi:10.3847/1538-3881/abc1e9.

Cook, R.L., De Lucia, F.C., 1971. Application of the Theory of Irreducible Tensor Operators to Molecular Hyperfine Structure. Am. J. Phys. 39, 1433–1454. doi:10.1119/1.1976693.

Corey, G.C., Tromp, J.W., 1995. Variational discrete variable representation. J. Chem. Phys. 103, 1812–1820. doi:10.1063/1.469755.

Coulombe, L.P. et al., 2023. A broadband thermal emission spectrum of the ultra-hot Jupiter WASP-18b. Nature. doi:10.1038/s41586-023-06230-1.

Coxon, J.A., Naxakis, S., 1985. Rotational analysis of the B $^2\Sigma^+ \rightarrow$ X $^2\Sigma^+$ system of the aluminum monoxide radical, AlO. J. Mol. Spectrosc. 111, 102–113. doi:10.1016/0022-2852(85)90073-6.

Crabtree, K.N., Hodges, J.N., Siller, B.M., Perry, A.J., Kelly, J.E., Jenkins, P.A., McCall, B.J., 2012. Sub-Doppler mid-infrared spectroscopy of molecular ions. Chem. Phys. Lett. 551, 1–6. doi:10.1016/j.cplett.2012.09.015.

Császár, A.G., Furtenbacher, T., 2011. Spectroscopic networks. J. Mol. Spectrosc. 266, 99 – 103. doi:10.1016/j.jms.2011.03.031.

Császár, A.G., Furtenbacher, T., Arendas, P., 2016. Small Molecules – Big Data. J. Phys. Chem. A 120, 8949–8969. doi:10.1021/acs.jpca.6b02293.

Cushing, M.C., Rayner, J.T., Vacca, W.D., 2005. An Infrared Spectroscopic Sequence of M, L, and T Dwarfs. Astrophys. J. 623, 1115. doi:10.1086/428040.

Danilovich, T. et al., 2020. Rotational Spectra of Vibrationally Excited AlO and TiO in Oxygen-rich Stars. Astron. J. 904, 110. doi:10.3847/1538-4357/abc079.

Darby-Lewis, D. et al., 2019. MARVEL analysis of the measured high-resolution spectra of NH. J. Mol. Spectrosc. 362, 69–76. doi:10.1016/j.jms.2019.06.002.

De Beck, E., Decin, L., Ramstedt, S., Olofsson, H., Menten, K.M., Patel, N.A., Vlemmings, W.H.T., 2017. Search for aluminium monoxide in the winds of oxygen-rich AGB stars. Astron. Astrophys. 598, A53. doi:10.1051/0004-6361/201628928.

Decin, L., Danilovich, T., Gobrecht, D., Plane, J.M.C., Richards, A.M.S., Gottlieb, C.A., Lee, K.L.K., 2018. Constraints on Metal Oxide and Metal Hydroxide Abundances in the Winds of AGB Stars: Potential Detection of FeO in R Dor. Astrophys. J. 855, 113. doi:10.3847/1538-4357/aaab6a.

Delahaye, T. et al., 2021. The 2020 edition of the GEISA spectroscopic database. J. Mol. Spectrosc. 380, 111510. doi:10.1016/j.jms.2021.111510.

Désert, J.M., Vidal-Madjar, A., Lecavelier des Etangs, A., Sing, D., Ehrenreich, D., Hébrard, G., Ferlet, R., 2008. TiO and VO broad band absorption features in the optical spectrum of the atmosphere of the hot-Jupiter HD 209458b. Astron. Astrophys. 492, 585–592. doi:10.1051/0004-6361:200810355.

Dinelli, B.M., Adriani, A., Mura, A., Altieri, F., Migliorini, A., Moriconi, M.L., 2019. JUNO/JIRAM's view of Jupiter's H_3^+ emissions. Phil. Trans. Royal Soc. London A 377, 20180406. doi:10.1098/rsta.2018.0406.

Dinelli, B.M., Neale, L., Polyansky, O.L., Tennyson, J., 1997. New assignments for the infrared spectrum of H_3^+. J. Mol. Spectrosc. 181, 142–150. doi:10.1006/jmsp.1996.7178.

Dinh-V-Trung, Bao, N.T.T., Tien, P.M., Hai, B.V., Minh, P.H., Khiem, L.H., 2022. High-resolution Linear Spectropolarimetry of Red Supergiant VY CMa: Identification of Atomic and Molecular Features. Astron. J. 164, 219. doi:10.3847/1538-3881/ac9237.

Dolg, M., Wedig, U., Stoll, H., Preuss, H., 1987. Ab initio pseudopotential study of the first row transition-metal monoxides and iron monohydride. J. Chem. Phys. 86, 2123–2131. doi:10.1063/1.452110.

Döring, E., Fuchs, G.W., Giesen, T., Breier, A.A., Blum, L., 2022. High-resolution infrared spectrum of the diatomic vanadium oxide, in: 2022 International Symposium on Molecular Spectroscopy, p. FG11. doi:10.15278/isms.2022.FG11.

Drossart, P. et al., 1989. Detection of H_3^+ on jupiter. Nature 340, 539–541. doi:10.1038/340539a0.

Du, Q., Wang, L., Shen, X.H., Gao, T., 2006. Study on potential energy functions and spectrum constants of $VO^{n\pm}$ (n=0, 1, 2). Acta Phys. Sin. 55, 6308–6314. doi:10.7498/aps.55.6308.

Du, Q., Wang, L., Shen, X.H., Wang, H.Y., Gao, T., Zheu, Z.H., 2008. Study of the structures and stabilities of the VO_x (x=1 approximate to 5) molecules by density functional theory. Acta Chim. Sin. 66, 23–30.

Dulieu, O., Kosloff, R., Masnou-Seeuws, F., Pichler, G., 1997. Quasibound states in long-range alkali dimers: Grid method calculations. J. Chem. Phys. 107, 10633–10642. doi:10.1063/1.474179.

Dyke, J.M., Gravenor, B.W.J., Hastings, M.P., Morris, A., 1985. High-temperature photoelectron-spectroscopy: The vanadium monoxide molecule. J. Phys. Chem. 89, 4613–4617. doi:10.1021/j100267a040.

Emery, G., 2006. Hyperfine Structure, in: Drake, G. (Ed.), Springer Handbook of Atomic, Molecular, and Optical Physics. Springer New York, New York, NY, pp. 253–260. doi:10.1007/978-0-387-26308-3_16.

Endres, C.P., Schlemmer, S., Schilke, P., Stutzki, J., Müller, H.S.P., 2016. The Cologne Database for Molecular Spectroscopy, CDMS, in the Virtual Atomic and Molecular Data Centre, VAMDC. J. Mol. Spectrosc. 327, 95–104. doi:10.1016/j.jms.2016.03.005.

von Essen, C., Mallonn, M., Welbanks, L., Madhusudhan, N., Pinhas, A., Bouy, H., Hansen, P.W., 2019. An optical transmission spectrum of the ultra-hot Jupiter WASP-33 b First indication of aluminum oxide in an exoplanet. Astron. Astrophys. 622, A71. doi:10.1051/0004-6361/201833837.

Evans, T.M. et al., 2018. An Optical Transmission Spectrum for the Ultra-hot Jupiter WASP-121b Measured with the Hubble Space Telescope. Astron. J. 156, 283. doi:10.3847/1538-3881/aaebff.

Evans, T.M. et al., 2017. An ultrahot gas-giant exoplanet with a stratosphere. Nature 548, 58–61. doi:10.1038/nature23266.

Evans, T.M. et al., 2016. Detection of H_2O and evidence for tio/vo in an ultra-hot exoplanet atmosphere. Astrophys. J. 822, L4. doi:10.3847/2041-8205/822/1/l4.

Fabri, C., Matyus, E., Császár, A.G., 2011. Rotating full- and reduced-dimensional quantum chemical models of molecules. J. Chem. Phys. 134, 074105. doi:10.1063/1.3533950.

Farber, M., Manuel Uy, O., Srivastava, R.D., 1972. Effusion-Mass Spectrometric Determination of the Heats of Formation of the Gaseous Molecules V_4O_{10}, V_4O_8, VO_2, and VO. J. Chem. Phys. 56, 5312–5315. doi:10.1063/1.1677037.

Farnik, M., Davis, S., Kostin, M.A., Polyansky, O.L., Tennyson, J., Nesbitt, D.J., 2002. Beyond the Born-Oppenheimer approximation: High-resolution overtone spectra of H_2D^+ and D_2H^+. J. Chem. Phys. 116, 6146–6158. doi:10.1063/1.1458244.

Fast, A., Meek, S.A., 2021. Frequency comb referenced spectroscopy of A–X 0–0 transitions in SH. J. Chem. Phys. 154, 114304. doi:10.1063/5.0042552.

Fawley, W.M., 1977. On the near-infrared excesses of very cool supergiants. Astrophys. J. 218, 181–194. doi:10.1086/155669.

Feng, Y., Zhu, Z., 2019. Rotationless radiative lifetimes and transition probabilities of the seven lowest-lying doublet states of the AlO radical. J. Quant. Spectrosc. Radiat. Transf. 231, 37–48. doi:10.1016/j.jqsrt.2019.04.007.

Fisher, C., Hoeijmakers, H.J., Kitzmann, D., Márquez-Neila, P., Grimm, S.L., Sznitman, R., Heng, K., 2020. Interpreting High-resolution Spectroscopy of Exoplanets using Cross-correlations and Supervised Machine Learning. The Astronomical Journal 159, 192. doi:10.3847/1538-3881/ab7a92.

Flagg, L. et al., 2023. ExoGemS Detection of a Metal Hydride in an Exoplanet Atmosphere at High Spectral Resolution. Astrophys. J. Lett. 953, L19. doi:10.3847/2041-8213/ace529.

Flory, M.A., Ziurys, L.M., 2008. Submillimeter-wave spectroscopy of VN ($X\ ^3\Delta_r$) and VO ($X\ ^4\Sigma^-$): A study of the hyperfine interactions. J. Mol. Spectrosc. 247, 76–84. doi:10.1016/j.jms.2007.09.007.

Flygare, W.H., 1974. Magnetic interactions in molecules and an analysis of molecular electronic charge distribution from magnetic parameters. Chemical Reviews 74, 653–687. doi:10.1021/cr60292a003.

Fortney, J.J., Dawson, I, R., Komacek, T.D., 2021. Hot Jupiters: Origins, Structure, Atmospheres. J. Geophys. Res. 126, e2020JE006629. doi:10.1029/2020JE006629.

Fortney, J.J., Lodders, K., Marley, M.S., Freedman, R.S., 2008. A Unified Theory for the Atmospheres of the Hot and Very Hot Jupiters: Two Classes of Irradiated Atmospheres. Astrophys. J. 678, 1419–1435. doi:10.1086/528370.

Fortney, J.J. et al., 2016. The Need for Laboratory Work to Aid in The Understanding of Exoplanetary Atmospheres. arXiv e-prints. doi:10.48550/arXiv.1602.06305, arXiv:1602.06305.

Fortney, J.J. et al., 2019. The Need for Laboratory Measurements and Ab Initio Studies to Aid Understanding of Exoplanetary Atmospheres. arXiv e-prints. arXiv:1905.07064.

Foster, S.C., McKellar, A.R.W., Peterkin, I.R., Watson, J.K.G., Pan, F.S., Crofton, M.W., Altman, R.S., Oka, T., 1986a. Observation and analysis of the ν_2 and ν_3 fundamental bands of the H_2D^+ ion. J. Chem. Phys. 84, 91–99. doi:10.1063/1.450137.

Foster, S.C., McKellar, A.R.W., Watson, J.K.G., 1986b. Observation and analysis of the ν_2 and ν_3 fundamental bands of the D_2H^+ ion. J. Chem. Phys. 85, 664–670. doi:10.1063/1.451841.

Frosch, R.A., Foley, H.M., 1952. Magnetic Hyperfine Structure in Diatomic Molecules. Phys. Rev. 88, 1337–1349. doi:10.1103/PhysRev.88.1337.

Furtenbacher, T., Árendás, P., Mellau, G., Császár, A.G., 2014. Simple molecules as complex systems. Sci. Rep. 4, 4654. doi:10.1038/srep04654.

Furtenbacher, T., Coles, P.A., Tennyson, J., Yurchenko, S.N., Yu, S., Drouin, B., Tóbiás, R., Császár, A.G., 2020a. Empirical rovibrational energy of ammonia up to 7500 cm^{-1}. J. Quant. Spectrosc. Radiat. Transf. 251, 107027. doi:10.1016/j.jqsrt.2020.107027.

Furtenbacher, T., Császár, A.G., 2012. MARVEL: measured active rotational-vibrational energy levels. II. Algorithmic improvements. J. Quant. Spectrosc. Radiat. Transf. 113, 929–935. doi:10.1016/j.jqsrt.2012.01.005.

Furtenbacher, T., Császár, A.G., Tennyson, J., 2007. MARVEL: measured active rotational-vibrational energy levels. J. Mol. Spectrosc. 245, 115–125. doi:10.1016/j.jms.2007.07.005.

Furtenbacher, T., Hegedus, S.T., Tennyson, J., Császár, A.G., 2022. Analysis of the measured high-resolution doublet rovibronic spectra of ^{12}CH and ^{16}OH. Phys. Chem. Chem. Phys. 24, 19287. doi:10.1039/D2CP02240K.

Furtenbacher, T., Szidarovszky, T., Fábri, C., Császár, A.G., 2013a. MARVEL analysis of the rotational-vibrational states of the molecular ions H_2D^+ and D_2H^+. Phys. Chem. Chem. Phys. 15, 10181–10193. doi:10.1039/c3cp44610g.

Furtenbacher, T., Szidarovszky, T., Mátyus, Edit Fábri, C., Császár, A.G., 2013b. Analysis of the Rotational-Vibrational States of the Molecular Ion H_3^+. J. Chem. Theory Comput. 9, 5471–5478. doi:10.1021/ct4004355.

Furtenbacher, T., Tóbiás, R., Tennyson, J., Polyansky, O.L., Császár, A.G., 2020b. W2020: A Database of Validated Rovibrational Experimental Transitions and Empirical Energy Levels of $H_2{}^{16}O$. J. Phys. Chem. Ref. Data 49, 033101. doi:10.1063/5.0008253.

Furtenbacher, T., Tóbiás, R., Tennyson, J., Polyansky, O.L., Kyuberis, A.A., Ovsyannikov, R.I., Zobov, N.F., Császár, A.G., 2020c. W2020: A Database of Validated Rovibrational Experimental Transitions and Empirical Energy Levels Part II. $H_2{}^{17}O$ and $H_2{}^{18}O$ with an Update to $H_2{}^{16}O$. J. Phys. Chem. Ref. Data 49, 043103. doi:10.1063/5.0030680.

Gamal, H., Elshahawy, A.M., Medany, S.S., Hefnawy, M.A., Shalaby, M., 2024. Recent advances of vanadium oxides and their derivatives in supercapacitor applications: A comprehensive review. Journal of Energy Storage 76, 109788. doi:10.1016/j.est.2023.109788.

Gandhi, S., Brogi, M., Webb, R.K., 2020. Seeing above the clouds with high-resolution spectroscopy. Mon. Not. Roy. Astron. Soc. 498, 194–204. doi:10.1093/mnras/staa2424.

Gandhi, S., Madhusudhan, N., 2019. New avenues for thermal inversions in atmospheres of hot Jupiters. Mon. Not. Roy. Astron. Soc. 485, 5817–5830. doi:10.1093/mnras/stz751.

Geballe, T.R., Goto, M., Usuda, T., Oka, T., McCall, B.J., 2006. The Interstellar Medium of IRAS 08572+3915 NW: H_3^+ and Warm High-Velocity CO. Astrophys. J. 644, 907. doi:10.1086/503763.

Geballe, T.R., Jagod, M.F., Oka, T., 1993. Detection of H_3^+ infrared-emission lines in Saturn. Astrophys. J. 408, L109–L112. doi:10.1086/186843.

Geballe, T.R., McCall, B.J., Hinkle, K.H., Oka, T., 1999. Detection of H_3^+ in the Diffuse Interstellar Medium: The Galactic Center and Cygnus OB2 Number 12. Astrophys. J. 510, 251. doi:10.1086/306580.

Geballe, T.R., Oka, T., 1996. Detection of H_3^+ in interstellar space. Nature 384, 334–335. doi:10.1038/384334a0.

Gentleman, A.S., Iskra, A., Köckert, H., Mackenzie, S.R., 2019. Photodissociation dynamics and the dissociation energy of vanadium monoxide, VO, investigated using velocity map imaging. Phys. Chem. Chem. Phys. 21, 15560–15567. doi:10.1039/C9CP02120E.

Gibbs, A., Fitzgerald, M.P., 2022. Limits on the Auroral Generation of H_3^+ in Brown Dwarf and Extrasolar Giant Planet Atmospheres with the Keck Near Infrared Echelle Spectrograph. Astron. J. 164. doi:10.3847/1538-3881/ac7718.

Goodlett, V.W., Innes, K.K., 1959. Hollow-Cathode Emission of the AlO Spectrum. Nature 183, 243–244. doi:10.1038/183243a0.

Goranskii, V.P., Barsukova, E.A., 2007. Comparative spectral analysis of the peculiar red novae V838 Mon and V4332 Sgr in quiescence after their outbursts. Astron. Rep. 51, 126–142. doi:10.1134/S1063772907020072.

Gordon, I.E., Le Roy, R.J., Bernath, P.F., 2006. Near infrared emission spectra of CoH and CoD. J. Mol. Spectrosc. 237, 11–18. doi:10.1016/j.jms.2006.02.011.

Gordon, I.E. et al., 2022. The HITRAN2020 molecular spectroscopic database. J. Quant. Spectrosc. Radiat. Transf. 277, 107949. doi:10.1016/j.jqsrt.2021.107949.

Goto, M., Geballe, T.R., Harju, J., Caselli, P., Sipila, O., Menten, K.M., Usuda, T., 2019. Search for H_3^+ isotopologues toward CRL2136 IRS 1. Astron. Astrophys. 632, A29. doi:10.1051/0004-6361/201936119.

Goto, M., McCall, B.J., Geballe, T.R., Usuda, T., Kobayashi, N., Terada, H., Oka, T., 2002. Absorption line survey of H_3^+ toward the Galactic center sources I. GCS 3-2 and GC IRS3. Publ. Astron. Soc. Japan 54, 951–961. doi:10.1093/pasj/54.6.951.

Goto, M., McCall, B.J., Geballe, T.R., Usuda, T., Kobayashi, N., Terada, H., Oka, T., 2003. Observation of Interstellar H_3^+ Using Subaru IRCS: The Galactic Center. ASP Conference Series 289, 189–193. URL: http://adsabs.harvard.edu/full/2003ASPC..289..189G.

Goto, M., Takano, S., Yamamoto, S., Ito, H., Saito, S., 1994. Microwave spectra of the AlO ($X\ ^2\Sigma^+$) radical in the v= 1 and 2 states. Chem. Phys. Lett. 227, 287–292. doi:10.1016/0009-2614(94)00820-5.

Goto, M. et al., 2008. Absorption line survey of H_3^+ toward the galactic center sources. II. Eight infrared sources within 30 Pc of the galactic center. Astrophys. J. 688, 306–319. doi:10.1086/591657.

Gottfried, J.L., McCall, B.J., Oka, T., 2003. Near-infrared spectroscopy of H_3^+ above the barrier to linearity. J. Chem. Phys. 118, 10890–10899. doi:10.1063/1.1575737.

Goyal, J.M. et al., 2020. A library of self-consistent simulated exoplanet atmospheres. Mon. Not. Roy. Astron. Soc. 498, 4680–4704. doi:10.1093/mnras/staa2300.

Guan, Y.C., Chang, Y.H., Liao, Y.C., Peng, J.L., Wang, L.B., Shy, J.T., 2018. Precision saturated absorption spectroscopy of H_3^+. J. Chem. Phys. 148, 124310. doi:10.1063/1.5017080.

Guilluy, G., Sozzetti, A., Giacobbe, P., Bonomo, A.S., Micela, G., 2022. On the synergy between Ariel and ground-based high-resolution spectroscopy. Experimental Astronomy 53, 655–677. doi:10.1007/s10686-021-09824-7.

Güsten, R. et al., 2019. Astrophysical detection of the helium hydride ion HeH^+. Nature 568, 357–359. doi:10.1038/s41586-019-1090-x.

Halfen, D.T., Ziurys, L.M., 2004. The Submillimeter Spectrum of CrH and CrD ($X^6\Sigma^+$). Astrophys. J. 611, L65. doi:10.1086/423426.

Harilal, S.S., Brumfield, B.E., Cannon, B.D., Phillips, M.C., 2016. Shock Wave Mediated Plume Chemistry for Molecular Formation in Laser Ablation Plasmas. Analytical Chemistry 88, 2296–2302. doi:10.1021/acs.analchem.5b04136.

Harilal, S.S., Murzyn, C.M., Phillips, M.C., Martin, J.B., 2020. Hyperfine structures and isotopic shifts of uranium transitions using tunable laser spectroscopy of laser ablation plumes. Spectroc. Acta Pt. B-Atom. Spectr. 169, 105828. doi:10.1016/j.sab.2020.105828.

Harju, J. et al., 2017. Detection of Interstellar Ortho-D_2H^+ with SOFIA. Astrophys. J. 840, 63. doi:10.3847/1538-4357/aa6c69.

Harris, G.J., Lynas-Gray, A., Miller, S., Tennyson, J., 2004. The Role of HeH^+ in Cool Helium-rich White Dwarfs. Astrophys. J. 617, L143–L146. doi:10.1086/427391.

Havalyova, I., Bozhinova, I., Pashov, A., Ross, A.J., Crozet, P., 2021. A coupled-channels model describing the low-lying $^2\Delta$, $^2\Sigma^+$ and $^2\Pi$ electronic states of nickel monohydride with experimental accuracy. J. Quant. Spectrosc. Radiat. Transf. 272, 107800. doi:10.1016/j.jqsrt.2021.107800.

Haynes, K., Mandell, A.M., Madhusudhan, N., Deming, D., Knutson, H., 2015. Spectroscopic Evidence for a Temperature Inversion in the Dayside Atmosphere of Hot Jupiter WASP-33b. Astrophys. J. 806, 146. doi:10.1088/0004-637X/806/2/146.

Hazi, A.U., Taylor, H.S., 1970. Stabilization Method of Calculating Resonance Energies: Model Problem. Phys. Rev. A 1, 1109–1120. doi:10.1103/PhysRevA.1.1109.

Hébert, G.R., Tyte, D.C., 1964. Intensity measurements on the A $^2\Sigma$–X $^2\Sigma$ system of aluminium oxide. Proceedings of the Physical Society 83, 629–634. doi:10.1088/0370-1328/83/4/316.

Hedges, C., Madhusudhan, N., 2016. Effect of pressure broadening on molecular absorption cross sections in exoplanetary atmospheres. Mon. Not. Roy. Astron. Soc. 458, 1427–1449. doi:10.1093/mnras/stw278.

Helgaker, T., Gauss, J., Cazzoli, G., Puzzarini, C., 2013. ^{33}S hyperfine interactions in H_2S and SO_2 and revision of the sulfur nuclear magnetic shielding scale. J. Chem. Phys. 139, 244308. doi:10.1063/1.4849177.

Herzberg, G., 1989. Molecular Spectra and Molecular Structure: I. Spectra of Diatomic Molecules. Krieger Publishing Company.

Herzberg, G., 1991. Molecular Spectra and Molecular Structure, Volume II: Infrared and Raman spectra of polyatomic molecules. Krieger Publishing Company.

Hewitt, A.J., Doss, N., Zobov, N.F., Polyansky, O.L., Tennyson, J., 2005. Deuterated water: Partition functions and equilibrium constant. Mon. Not. Roy. Astron. Soc. 356, 1123–1126. doi:10.1111/j.1365-2966.2004.08559.x.

Hillenbrand, L.A., Knapp, G.R., Padgett, D.L., Rebull, L.M., McGehee, P.M., 2012. Optical TiO and VO band emission in two embedded protostars: IRAS 04369+2539 and IRAS 05451+0037. Astron. J. 143, 37. doi:10.1088/0004-6256/143/2/37.

Hinkel, N.R., Unterborn, C.T., 2018. The Star–Planet Connection. I. Using Stellar Composition to Observationally Constrain Planetary Mineralogy for the 10 Closest Stars. Astrophys. J. 853, 83. doi:10.3847/1538-4357/aaa5b4.

Hirao, T., Amano, T., 2003. Laboratory Submillimeter-Wave Detection of D_2H^+: A New Probe into Multiple Deuteration? Astrophys. J. 597, L85–L87. doi:10.1086/379801.

Hlavenka, P., Korolov, I., Plasil, R., Varju, J., Kotrik, T., Glosik, J., 2006a. Near infrared second overtone cw-cavity ringdown spectroscopy of H_2D^+ ions. Czech. J. Phys. 56, B749–B760. doi:10.1007/s10582-006-0280-6.

Hlavenka, P., Plasil, R., Bano, G., Korolov, I., Ramanlal, J., Tennyson, J., Glosik, J., Gerlich, D., 2006b. Near infrared second overtone cw-cavity ringdown spectroscopy of the D_2H^+ ion. Int. J. Mass Spectrom. 255-256, 170–176. doi:10.1016/j.ijms.2006.02.002.

Hocking, W.H., Merer, A.J., Milton, D.J., 1981. Resolved hyperfine-structure in the C-X electronic-transition of VO: An internal hyperfine perturbation in the C $^4\Sigma^-$ state. Can. J. Phys. 59, 266–270. doi:10.1139/p81-035.

Hodges, J.N., Perry, A.J., Jenkins II, P.A., Siller, B.M., McCall, B.J., 2013. High-precision and high-accuracy rovibrational spectroscopy of molecular ions. J. Chem. Phys. 139, 164201. doi:10.1063/1.4825251.

Hoeijmakers, H.J. et al., 2020. Hot Exoplanet Atmospheres Resolved with Transit Spectroscopy (HEARTS) - IV. A spectral inventory of atoms and molecules in the high-resolution transmission spectrum of WASP-121 b. Astron. Astrophys. 641, A123. doi:10.1051/0004-6361/202038365.

Honjou, N., 2010. *Ab initio* study of the molecular vibrations and electronic structure of the X, B, D and F $^2\Sigma^+$ states of AlO. J. Molec. Struct. (THEOCHEM) 939, 59–64. doi:10.1016/j.theochem.2009.09.041.

Honjou, N., 2011. *Ab initio* study of band strengths for the F $^2\Sigma^+$–A $^2\Pi$ electronic transition of AlO. Comput. Theor. Chem. 978, 138–142. doi:10.1016/j.comptc.2011.10.006.

Honjou, N., 2014. *Ab initio* study of breakdown of the Condon approximation in the F $^2\Sigma^+$–A $^2\Pi$ electronic transition of AlO. Comput. Theor. Chem. 1027, 186–190. doi:10.1016/j.comptc.2013.11.002.

Honjou, N., 2015. *Ab initio* study of band strength distribution for the D $^2\Sigma^+$–A $^2\Pi$ transition of AlO and the effect of R dependence of the electronic transition moment on the distribution. Comp. Theor. Chem. 1054, 1–7. doi:10.1016/j.comptc.2014.11.019.

Hopkins, W.S., Hamilton, S.M., Mackenzie, S.R., 2009. The electronic spectrum of vanadium monoxide across the visible: New bands and new insight. J. Chem. Phys. 130, 144308. doi:10.1063/1.3104844.

Hougen, J.T., 1962. Classification of Rotational Energy Levels for Symmetric-Top Molecules. J. Chem. Phys. 37, 1433–1441. doi:10.1063/1.1733301.

Hu, P. et al., 2023. Vanadium Oxide: Phase Diagrams, Structures, Synthesis, and Applications. Chem. Rev. 123, 4353–4415. doi:10.1021/acs.chemrev.2c00546.

Huang, G.I., Merer, A.J., Clouthier, D.J., 1992. Intracavity laser spectroscopy of VO: Hyperfine parameters and electron configuration of the B $^4\Pi$ state. J. Mol. Spectrosc. 153, 32–40. doi:10.1016/0022-2852(92)90455-W.

Huang, X., Schwenke, D.W., Freedman, R.S., Lee, T.J., 2017. Ames-2016 Line Lists for 13 Isotopologues of CO_2: Updates, Consistency, and Remaining Issues. J. Quant. Spectrosc. Radiat. Transf. 203, 224–241. doi:10.1016/j.jqsrt.2017.04.026.

Huang, Y., 2001. Determining Analytical Potential Energy Functions of Diatomic Molecules by Direct Fitting. Master's thesis. Department of Chemistry, University of Waterloo. URL: http://hdl.handle.net/10012/1284. m. Sc. thesis.

Hubeny, I., Burrows, A., Sudarsky, D., 2003. A Possible Bifurcation in Atmospheres of Strongly Irradiated Stars and Planets. Astrophys. J. 594, 1011. doi:10.1086/377080.

Huber, P.J., Ronchetti, E.M., 2009. Robust Statistics, Second Edition. Wiley.

Hübner, O., Hornung, J., Himmel, H.J., 2015. The electronic structure of VO in its ground and electronically excited states: A combined matrix isolation and quantum chemical (MRCI) study. J. Chem. Phys. 143, 024309. doi:10.1063/1.4926393.

Humphreys, R.M. et al., 2019. The Unexpected Spectrum of the Innermost Ejecta of the Red Hypergiant VY CMa. Astrophys. J. Lett. 874, L26. doi:10.3847/2041-8213/ab11e5.

Indriolo, N., McCall, B.J., 2012. Investigating the Cosmic-Ray ionization rate in the galactic diffuse Interstellar Medium Through Observations of H_3^+. Astrophys. J. 745, 91. doi:10.1088/0004-637X/745/1/91.

Ito, H., 1994. Analysis of the A $^2\Pi_i$–X $^2\Sigma^+$ perturbations of the AlO radical. Can. J. Phys. 72, 1082–1086. doi:10.1139/p94-141.

Ito, H., Goto, M., 1994. Analysis of an anomalous vibrational dependence of the spin-rotation constants for AlO (X $^2\Sigma^+$). Chem. Phys. Lett. 227, 293–298. doi:10.1016/0009-2614(94)00821-3.

Jaquet, R., 2022. Investigation of the global second-derivative non-adiabatic contributions: Rovibrational energies of H_2^+, H_2, and prospects for H_3^+ (Part II). J. Mol. Spectrosc. 384, 111585. doi:10.1016/j.jms.2022.111585.

Jensen, P., Paidarová, I., Špirko, V., Sauer, S.P.A., 1997. Theoretical calculations of the hyperfine structure in the spectra of H_3^+ and its deuterated isotopomers. Mol. Phys. 91, 319–332. doi:10.1080/002689797171616.

Jiang, T., Chen, Y., Bogdanov, N.A., Wang, E., Alavi, A., Chen, J., 2021. A full configuration interaction quantum Monte Carlo study of ScO, TiO, and VO molecules. J. Chem. Phys., 164302. doi:10.1063/5.0046464.

Johnson, M.C. et al., 2023. The PEPSI Exoplanet Transit Survey (PETS). II. A Deep Search for Thermal Inversion Agents in KELT-20 b/MASCARA-2 b with Emission and Transmission Spectroscopy. Astron. J. 165, 157. doi:10.3847/1538-3881/acb7e2.

Johnson, S.E., Capelle, G., Broida, H.P., 1972. Laser Excited Fluorescence and Radiative Lifetimes of AlO (B $^2\Sigma^+$–X $^2\Sigma^+$). J. Chem. Phys. 56, 663–665. doi:10.1063/1.1676921.

Jones, H.R.A., Pavlenko, Y., Viti, S., Barber, R.J., Yakovina, L., Pinfold, D., Tennyson, J., 2005. Carbon monoxide in low-mass dwarf stars. Mon. Not. Roy. Astron. Soc. 358, 105–112. doi:10.1111/j.1365-2966.2005.08736.x.

Jones, R.W., Gole, J.L., 1976. Single collision oxidation of vanadium with NO_2 and O_2. J. Chem. Phys. 65, 3800–3802. doi:10.1063/1.433541.

Jozwiak, H., Cybulski, H., Grabowski, A., Wcislo, P., 2021. Hyperfine structure of the EF^{1}Sigma$_g^+$ state in H_2. Phys. Rev. A 104, 012808. doi:10.1103/PhysRevA.104.012808.

Jusko, P., Konietzko, C., Schlemmer, S., Asvany, O., 2016. Frequency comb assisted measurement of fundamental transitions of cold H_3^+, H_2D^+ and D_2H^+. J. Mol. Spectrosc. 319, 55–58. doi:10.1016/j.jms.2015.12.002.

Jusko, P., Toepfer, M., Mueller, H.S.P., Ghosh, P.N., Schlemmer, S., Asvany, O., 2017. Double resonance rotational action spectroscopy of cold H_2D^+ and D_2H^+. J. Mol. Spectrosc. 332, 33–37. doi:10.1016/j.jms.2016.09.013.

Kamada, T., Kawai, S., 1989. An algorithm for drawing general undirected graphs. Information Processing Letters 31, 7–15. doi:10.1016/0020-0190(89)90102-6.

Kamiński, T., Schmidt, M., Tylenda, R., 2010. V4332 Sagittarii: a circumstellar disc obscuring the main object. Astron. Astrophys. 522, A75. doi:10.1051/0004-6361/201014406.

Kamiński, T., Schmidt, M., Tylenda, R., Konacki, M., Gromadzki, M., 2009. KECK/HIRES spectroscopy of V838 Monocerotis in october 2005*. Astrophys. J. Suppl. Ser. 182, 33. doi:10.1088/0067-0049/182/1/33.

Kaminski, T., Schmidt, M.R., Menten, K.M., 2013. Aluminium oxide in the optical spectrum of VY Canis Majoris. Astron. Astrophys. 549, A6. doi:10.1051/0004-6361/201220650.

Kaminski, T. et al., 2016. An observational study of dust nucleation in Mira (o Ceti) I. Variable features of AlO and other Al- bearing species. Astron. Astrophys. 592, A42. doi:10.1051/0004-6361/201628664.

Kao, L., Oka, T., Miller, S., Tennyson, J., 1991. A table of astronomically important ro-vibrational transitions for the H_3^+ molecular ion. Astrophys. J. Suppl. Ser. 77, 317–329. doi:10.1086/191606.

Karlsson, L., Lindgren, B., Lundevall, C., Sassenberg, U., 1997. Lifetime measurements of the A $^4\Pi$, B $^4\Pi$, and C $^4\Sigma^-$ states of VO. J. Mol. Spectrosc. 181, 274–278. doi:10.1006/jmsp.1996.7173.

Kasai, P.H., 1968. ESR of VO in Argon matrix at 4°K: Establishment of its electronic ground state. J. Chem. Phys. 49, 4979. doi:10.1063/1.1669987.

Kato, H., 1993. Energy-Levels and Line-Intensities of Diatomic-Molecules – Application to Alkali-Metal Molecules. Bull. Chem. Soc. Japan 66, 3203–3234. doi:10.1246/bcsj.66.3203.

Keenan, P.C., Schroeder, L.W., 1952. An infrared system of bands of VO in M-type stars. Astrophys. J. 115, 82–88. doi:10.1086/145515.

Khodachenko, M.L., Shaikhislamov, I.F., Lammer, H., Prokopov, P.A., 2015. Atmosphere expansion and mass loss of close-orbit Giant exoplanets heated by stellar Xuv. II. Effects of planetary magnetic field; structuring of inner magnetosphere. Astrophys. J. 813, 50. doi:10.1088/0004-637X/813/1/50.

Kimblin, C., Trainham, R., Capelle, G.A., Mao, X., Russo, R.E., 2017. Characterization of laser-induced plasmas as a complement to high-explosive large-scale detonations. AIP Adv. 7, 095208. doi:10.1063/1.4999793.

Kirkpatrick, J.D., Henry, T.J., Liebert, J., 1993a. The unique spectrum of the brown dwarf candidate GD 165B and comparison to the spectra of other low-luminosity objects. Astrophys. J. 406, 701–707. doi:10.1086/172480.

Kirkpatrick, J.D., Henry, T.J., McCarthy, Jr., D.W., 1991. A standard stellar spectral sequence in the red/near-infrared - Classes K5 to M9. Astrophys. J. Suppl. Ser. 77, 417–440. doi:10.1086/191611.

Kirkpatrick, J.D., Henry, T.J., Simons, D.A., 1995. The solar neighborhood. 2: The first list of dwarfs with spectral types of M7 and cooler. Astron. J. 109, 797–807. doi:10.1086/117323.

Kirkpatrick, J.D., Kelly, D.M., Rieke, G.H., Liebert, J., Allard, F., Wehrse, R., 1993b. M dwarf spectra from 0.6 to 1.5 micron-A spectral sequence, model atmosphere fitting, and the temperature scale. Astrophys. J. 402, 643–654. doi:10.1086/172166.

Knecht, D.J., Pike, C.P., Murad, E., Rall, D.L.A., 1996. Interaction of solid-rocket exhaust with the atmosphere. J. Spacecrafts Rockets 33, 677–685. doi:10.2514/3.26820.

de Kok, R.J., Birkby, J., Brogi, M., Schwarz, H., Albrecht, S., de Mooij, E.J.W., Snellen, I.A.G., 2014. Identifying new opportunities for exoplanet characterisation at high spectral resolution. Astron. Astrophys. 561, A150. doi:10.1051/0004-6361/201322947.

Koskinen, T.T., Aylward, A.D., Miller, S., 2007. A stability limit for the atmospheres of giant extrasolar planets. Nature 450, 845–848. doi:10.1038/nature06378.

Kozin, I., Law, M.M., Tennyson, J., Hutson, J.M., 2004. New vibration-rotation code for tetraatomic molecules exhibiting wide-amplitude motion: Wavr4. Comput. Phys. Commun. 163, 117–131. doi:10.1016/j.cpc.2004.07.005.

Kozyryev, I., Baum, L., Matsuda, K., Augenbraun, B.L., Anderegg, L., Sedlack, A.P., Doyle, J.M., 2017. Sisyphus Laser Cooling of a Polyatomic Molecule. Phys. Rev. Lett. 118, 173201. doi:10.1103/PhysRevLett.118.173201.

Kramida, A., Ralchenko, Y., Reader, J., and NIST ASD Team, 2020. Development of NIST Atomic Databases and Online Tools. Atoms 8, 56. doi:10.3390/atoms8030056.

Kraus, D., Saykally, R.J., Bondybey, V.E., 2002. Cavity-Ringdown Spectroscopy Studies of the B $^2\Sigma^+ \leftarrow$ X $^2\Sigma^+$ System of AlO. ChemPhysChem 3, 364–366. doi:10.1002/1439-7641(20020415)3:4<364::AID-CPHC364>3.0.CO;2-G.

Kreckel, H., Bing, D., Reinhardt, S., Petrignani, A., Berg, M.H., Wolf, A., 2008. Chemical probing spectroscopy of H_3^+ above the barrier to linearity. J. Chem. Phys. 129, 164312. doi:10.1063/1.2994730.

Kreckel, H., Schwalm, D., Tennyson, J., Wolf, A., Zajfman, D., 2004. Rovibrational relaxation model for H_3^+. New J. Phys 6, 151. doi:10.1088/1367-2630/6/1/151.

Krishnamachari, S.L.N.G., Narasimham, N.A., Singh, M., 1966. A New Band System of AlO. Can. J. Phys. 44, 2513–2516. doi:10.1139/p66-204.

Kulik, H.J., Marzari, N., 2010. Systematic study of first-row transition-metal diatomic molecules: A self-consistent DFT+U approach. J. Chem. Phys. 133, 114103. doi:10.1063/1.3489110.

Labiano, A. et al., 2021. Wavelength calibration and resolving power of the JWST MIRI Medium Resolution Spectrometer. Astron. Astrophys. 656, A57. doi:10.1051/0004-6361/202140614.

de Laeter, J.R., Böhlke, J.K., Bièvre, P.D., Hidaka, H., Peiser, H.S., Rosman, K.J.R., Taylor, P.D.P., 2003. Atomic weights of the elements. Review 2000 (IUPAC Technical Report). Pure and Applied Chemistry 75, 683–800. doi:10.1351/pac200375060683.

Lagerqvist, A., Selin, L.E., 1957. Some infrared bands of vanadium oxide. Arkiv for Fysik 11, 429–430.

Lam, H.A., Miller, S., Joseph, R.D., Geballe, T.R., Trafton, L.M., Tennyson, J., Ballester, G.E., 1997. Variations in the H_3^+ emission of Uranus. Astrophys. J. 474, L73–L76. doi:10.1086/310424.

Lançon, A., Hauschildt, P.H., Ladjal, D., Mouhcine, M., 2007. Near-IR spectra of red supergiants and giants. Astron. Astrophys. 468, 205–220. doi:10.1051/0004-6361:20065824.

Larsson, M., 2008. H3 : the initiator of interstellar chemistry. International Journal of Astrobiology 7, 237–241. doi:10.1017/S1473550408004230.

Laud, B.B., Kalsulka, D.R., 1968. Emission spectrum of VO molecule. Indian J. Phys. 42, 61–71.

Launila, O., Banerjee, D.P.K., 2009. Rotational spectroscopy of AlO. Astron. Astrophys. 508, 1067–1072. doi:10.1051/0004-6361/200913274.

Launila, O., Berg, L.E., 2011. Spectroscopy of AlO: Combined analysis of the A $^2\Pi_i \rightarrow$ X $^2\Sigma^+$ and B $^2\Sigma^+ \rightarrow$ X $^2\Sigma^+$ transitions. J. Mol. Spectrosc. 265, 10–14. doi:10.1016/j.jms.2010.10.005.

Launila, O., Jonsson, J., 1994. Spectroscopy of AIO: Rotational Analysis of the A $^2\Pi_i$–X $^2\Sigma^+$ Transition in the 2-μm Region. J. Mol. Spectrosc. 168, 1–38. doi:10.1006/jmsp.1994.1257.

Le, A., Steimle, T.C., 2011. Optical Stark Spectroscopy of the $D^1\Pi$-$X^1\Sigma^+$(0,0) Band of Scandium Monohydride. J. Phys. Chem. A 115, 9370–9376. doi:10.1021/jp110838j.

Le Roy, R.J., 2017. Level: A computer program for solving the radial schrödinger equation for bound and quasibound levels. J. Quant. Spectrosc. Radiat. Transf. 186, 167 – 178. doi:10.1016/j.jqsrt.2016.05.028.

Le Roy, R.J., 2017. RKR1: a computer program implementing the first-order RKR method for determining diatomic molecule potential energy functions. J. Quant. Spectrosc. Radiat. Transf. 186, 158–166. doi:10.1016/j.jqsrt.2016.03.030.

Lee, E.G., Seto, J.Y., Hirao, T., Bernath, P.F., Le Roy, R.J., 1999. FTIR emission Spectra, Molecular Constants, and Potential Curve of Ground State GeO. J. Mol. Spectrosc. 194, 197–202. doi:10.1006/jmsp.1998.7789.

Lee, S.S., Ventrudo, B.F., Cassidy, D.T., Oka, T., Miller, S., Tennyson, J., 1991. Observation of the $3\nu_2 \leftarrow 0$ overtone band of H_3^+. J. Mol. Spectrosc. 145, 222–224. doi:10.1016/0022-2852(91)90365-H.

Lenz, L.F., Reiners, A., Seifahrt, A., Kaeufl, H.U., 2016. A CRIRES-search for H_3^+ emission from the hot Jupiter atmosphere of HD 209458 b. Astron. Astrophys. 589, A99. doi:10.1051/0004-6361/201525675.

Lewis, N.K. et al., 2020. Into the UV: The Atmosphere of the Hot Jupiter HAT-P-41b Revealed. Astrophys. J. Lett. 902, L19. doi:10.3847/2041-8213/abb77f.

Li, J., Xu, M., Li, X., Ma, Q., Zhao, N., Zhang, Q., Guo, L., Lu, Y., 2019. Laser-induced molecular fluorescence diagnosis of aluminum monoxide evolution in laser-induced plasma. Laser Physics Letters 16, 055701. doi:10.1088/1612-202X/ab1013.

Liimets, T. et al., 2022. V838 Mon: A slow waking up of Sleeping Beauty? Astron. Astrophys. 670, A13. doi:10.1051/0004-6361/202142959.

Lindsay, C.M., McCall, B.J., 2001. Comprehensive Evaluation and Compilation of H_3^+ Spectroscopy. J. Mol. Spectrosc. 210, 60–83. doi:10.1006/jmsp.2001.8444.

Lindsay, C.M., Rade, Jr, R.M., Oka, T., 2001. Survey of H_3^+ Transitions between 3000 and 4200 cm^{-1}. J. Mol. Spectrosc. 210, 51–59. doi:10.1006/jmsp.2001.8443.

Lockwood, G.W., Wing, R.F., 1982. The light and spectrum variations of VX Sgr, an exctremely cool supergiant. Mon. Not. Roy. Astron. Soc. 198, 385–404. doi:10.1093/mnras/198.2.385.

Lodi, L., Yurchenko, S.N., Tennyson, J., 2015. The calculated rovi-bronic spectrum of scandium hydride, ScH. Mol. Phys. 113, 1559–1575. doi:10.1080/00268976.2015.1029996.

Loebman, S.R. et al., 2014. The continued optical to mid-infrared evolution of V838 Monocerotis. Astron. J. 149, 17. doi:10.1088/0004-6256/149/1/17.

Lombardi, M., Barletta, P., Kievsky, A., 2004. Variational estimates using a discrete variable representation. Phys. Rev. A 70, 032503. doi:10.1103/PhysRevA.70.032503.

Londhe, C.T., Sunanda, K., Saksena, M.D., Behere, S.H., 2010. Franck-Condon factors and r-centroids of B-X, C-X and C-A band systems of AlO molecule. J. Mol. Spectrosc. 263, 178–182. doi:10.1016/j.jms.2010.07.013.

Londhe, C.T., Undre, P.B., 2020. Rotational Temperature of AlO Molecule from Fourier Transform Spectrum of the 0-1 band of B $^2\Sigma^+$–X $^2\Sigma^+$ System. J. Phys. Conf. Ser. 1644, 012063. doi:10.1088/1742-6596/1644/1/012063.

Lothringer, J.D., Barman, T., Koskinen, T., 2018. Extremely Irradiated Hot Jupiters: Non-oxide Inversions, H^- Opacity, and Thermal Dissociation of Molecules. Astrophys. J. 866, 27. doi:10.3847/1538-4357/aadd9e.

Lubic, K.G., Amano, T., 1984. Observation of the ν_1 fundamental band of D_2H^+. Can. J. Phys. 62, 1886–1888. doi:10.1139/p84-232.

Luo, Z., Chang, Y.C., Huang, H., Ng, C.Y., 2015. Rotationally Selected and Resolved State-to-State Photoelectron Study of Vanadium Monoxide Cation $VO^+(X^3\Sigma^-; v^+ = 0\text{-}3)$. J. Phys. Chem. A 119, 11162–11169. doi:10.1021/acs.jpca.5b09458.

Lynas-Gray, A.E., Miller, S., Tennyson, J., 1995. Infra red transition intensities for water: a comparison of *ab initio* and fitted dipole moment surfaces. J. Mol. Spectrosc. 169, 458–467. doi:10.1006/jmsp.1995.1038.

Mackrodt, W.C., Middlemiss, D.S., Owens, T.G., 2004. Hybrid density functional theory study of vanadium monoxide. Phys. Rev. B 69, 115119. doi:10.1103/PhysRevB.69.115119.

Madhusudhan, N., 2019. Exoplanetary Atmospheres: Key Insights, Challenges, and Prospects. Ann. Rev. Astron. Astrophys 57, 617–663. doi:10.1146/annurev-astro-081817-051846.

Mahanti, P.C., 1935. The Band Spectrum Of Vanadium Oxide. Proc. Phys. Soc. 47, 433. doi:10.1088/0959-5309/47/3/308.

Mahieu, J.M., Jacquniot, D., Schamps, J., Hall, J.A., 1975. Spin doubling in the observed $^2\Sigma^+$ states of AlO. J. Phys. B-At. Mol. Opt. Phys. 8, 308–312. doi:10.1088/0022-3700/8/2/020.

Majewski, W., Marshall, M.D., McKellar, A., Johns, J., Watson, J., 1987. Higher rotational lines in the ν_2 fundamental of the H_3^+ molecular ion. J. Mol. Spectrosc. 122, 341–355. doi:10.1016/0022-2852(87)90009-9.

Majewski, W.A., Feldman, P.A., Watson, J.K.G., Miller, S., Tennyson, J., 1989. Laboratory observation of the $2\nu_2$ band of the H_3^+ molecular ion. Astrophys. J. 347, L51–L54. doi:10.1086/185605.

Majewski, W.A., McKellar, A.R.W., Sadovskii, D., Watson, J.K.G., 1994. New observations and analysis of the infrared vibration–rotation spectrum of H_3^+. Can. J. Phys. 72, 1016–1027. doi:10.1139/p94-133.

Man, P.P., 2013. Cartesian and Spherical Tensors in NMR Hamiltonians. Concepts in Magnetic Resonance Part A 42, 197–244. doi:10.1002/cmr.a.21289.

Mandelshtam, V.A., Ravuri, T.R., Taylor, H.S., 1993. Calculation of the density of resonance states using the stabilization method. Phys. Rev. Lett. 70, 1932–1935. doi:10.1103/PhysRevLett.70.1932.

Markus, C.R., Kocheril, P.A., McCall, B.J., 2019. Sub-Doppler rovibrational spectroscopy of the ν_1 fundamental band of D_2H^+. J. Mol. Spectrosc. 355, 8–13. doi:10.1016/j.jms.2018.11.005.

Markus, C.R., McCall, B.J., 2019. Highly accurate experimentally determined energy levels of H_3^+. J. Chem. Phys. 150, 214303. doi:10.1063/1.5099454.

Markus, C.R., McCall, B.J., Schrader, A.W., Esposito, A.M., Kocheril, P.A., 2018. Sub-Doppler spectroscopy of the ν_2 fundamental band and first hot band of the H_3^+ cation, in: 73^{rd} International Symposium on Molecular Spectroscopy, p. MG09. doi:10.15278/isms.2018.MG09.

Mátyus, E., Czakó, G., Császár, A.G., 2009. Toward black-box-type full- and reduced-dimensional variational (ro)vibrational computations. J. Chem. Phys. 130, 134112. doi:10.1063/1.3076742.

Mátyus, E., Fábri, C., Szidarovszky, T., Czakó, G., Allen, W.D., Császár, A.G., 2010. Assigning quantum labels to variationally computed rotational-vibrational eigenstates of polyatomic molecules. J. Chem. Phys. 133, 034113. doi:10.1063/1.3451075.

Mayor, M., Queloz, D., 1995. A Jupiter-mass companion to a solar-type star. Nature 378, 355–359. doi:10.1038/378355a0.

McCall, B.J., Geballe, T.R., Hinkle, K.H., Oka, T., 1999. Observations of H_3^+ in dense molecular clouds. Astrophys. J. 522, 338–348. doi:10.1086/307637.

McCall, B.J. et al., 2002. Observations of H_3^+ in the diffuse interstellar medium. Astrophys. J. 567, 391–406. doi:10.1086/338380.

McCall, B.J., Oka, T., 2000. Combination band spectroscopy of H_3^+. J. Chem. Phys. 113, 3104–3110. doi:10.1063/1.1287142.

Mcdonald, J.K., Innes, K.K., 1969. A low-lying excited electronic state of AlO molecule and ground-state dissociation energy. J. Mol. Spectrosc. 32, 501–510. doi:10.1016/0022-2852(69)90014-9.

McDonald, J.K., Innes, K.K., Goodlett, V.W., Tolbert, T.W., 1969. A regular $^2\Pi$ state of the AlO molecule. J. Mol. Spectrosc. 32, 511–512. doi:10.1016/0022-2852(69)90015-0.

McKellar, A., Watson, J., 1998. The Infrared Spectrum of H_3^+ Revealed. J. Mol. Spectrosc. 191, 215–217. doi:10.1006/jmsp.1998.7613.

McKemmish, L.K., Bowesman, C.A., Kefala, K., Perri, A.N., Syme, A.M., Yurchenko, S.N., Tennyson, J., 2024. A hybrid approach to generating diatomic line lists for high resolution studies of exoplanets and other hot astronomical objects: Updates to ExoMol MgO, VO and TiO line lists. RAS Tech. Instr. (Submitted).

McKemmish, L.K., Masseron, T., Hoeijmakers, J., Pérez-Mesa, V.V., Grimm, S.L., Yurchenko, S.N., Tennyson, J., 2019. ExoMol Molecular line lists – XXXIII. The spectrum of Titanium Oxide. Mon. Not. Roy. Astron. Soc. 488, 2836–2854. doi:10.1093/mnras/stz1818.

McKemmish, L.K. et al., 2017. MARVEL analysis of the measured high-resolution spectra of $^{48}Ti^{16}O$. Astrophys. J. Suppl. Ser. 228, 15. doi:10.3847/1538-4365/228/2/15.

McKemmish, L.K., Syme, A.M., Borsovszky, J., Yurchenko, S.N., Tennyson, J., Furtenbacher, T., Csaszar, A.G., 2020. Incorportating new experiments in diatomic spectral databases: An update to the $^{12}C_2$ MARVEL database and ExoMol line list of $^{12}C_2$. Mon. Not. Roy. Astron. Soc. 497, 1081–1097. doi:10.1093/mnras/staa1954.

McKemmish, L.K., Yurchenko, S.N., Tennyson, J., 2016a. Ab initio calculations to support accurate modelling of the rovibronic spectroscopy calculations of vanadium monoxide (VO). Mol. Phys. 114, 3232–3248. doi:10.1080/00268976.2016.1225994.

McKemmish, L.K., Yurchenko, S.N., Tennyson, J., 2016b. ExoMol line lists – XVIII. The high-temperature spectrum of VO. Mon. Not. Roy. Astron. Soc. 463, 771–793. doi:10.1093/mnras/stw1969.

Melin, H., Fletcher, L.N., Stallard, T.S., Johnson, R.E., O'Donoghue, J., Moore, L., Donnelly, P.T., 2018. The quest for H_3^+ at Neptune: deep burn observations with NASA IRTF iSHELL. Mon. Not. Roy. Astron. Soc. 474, 3714–3719. doi:10.1093/mnras/stx3029.

Melin, H. et al., 2019. The H_3^+ ionosphere of Uranus: decades-long cooling and local-time morphology. Phil. Trans. Royal Soc. London A 377, 20180408. doi:10.1098/rsta.2018.0408.

Melin, H., Stallard, T., Miller, S., Lystrup, M.B., Trafton, L.M., Booth, T.C., Rivers, C., 2011. New limits on H_3^+ abundance on Neptune using Keck NIRSPEC. Mon. Not. Roy. Astron. Soc. 410, 641–644. doi:10.1111/j.1365-2966.2010.17468.x.

Mellor, T., Owens, A., Yurchenko, S.N., Tennyson, J., 2022. ExoMol line lists – LI. Rvibronic molecular line list for thioformaldehyde (H_2CS). Mon. Not. Roy. Astron. Soc. 520, 1997–2008. doi:10.1093/mnras/stad111.

Melosso, M. et al., 2021a. Improved centrifugal and hyperfine analysis of ND2H and NH2D and its application to the spectral line survey of L1544. J. Mol. Spectrosc. 377, 111431. doi:10.1016/j.jms.2021.111431.

Melosso, M., Diouf, M.L., Bizzocchi, L., Harding, M.E., Cozijn, F.M.J., Puzzarini, C., Ubachs, W., 2021b. Hyperfine-Resolved Near-Infrared Spectra of $H_2^{17}O$. J. Phys. Chem. A 125, 7884–7890. doi:10.1021/acs.jpca.1c05681.

Melosso, M., Jiang, N., Gauss, J., Puzzarini, C., 2023. Hyperfine-resolved spectra of HDS together with a global ro-vibrational analysis. J. Chem. Phys. 158, 174310. doi:10.1063/5.0148810.

Merer, A.J., 1989. Spectroscopy of the diatomic 3d transition-metal oxides. Annu. Rev. Phys. Chem. 40, 407–438. doi:10.1146/annurev.pc.40.100189.002203.

Merer, A.J., Huang, G., Cheung, A.S.C., Taylor, A.W., 1987. New quartet and doublet electronic-transitions in the near-infrared emission-spectrum of VO. J. Mol. Spectrosc. 125, 465–503. doi:10.1016/0022-2852(87)90110-X.

Merkt, F., Hoeveler, K., Deiglmayr, J., 2022. Reactions of H_2, HD, and D_2 with H_2^+, HD^+, and D_2^+: Product-Channel Branching Ratios and Simple Models. J. Phys. Chem. Lett. doi:10.1021/acs.jpclett.1c03374.

Merriles, D.M., Sevy, A., Nielson, C., Morse, M.D., 2020. The bond dissociation energy of VO measured by resonant three-photon ionization spectroscopy. J. Chem. Phys. 153, 024303. doi:10.1063/5.0014006.

Merrill, P.W., Deutsch, A.J., Keenan, P.C., 1962. Absorption Spectra of M-Type Mira Variables. Astrophys. J. 136, 21. doi:10.1086/147348.

Merritt, S.R. et al., 2021. An inventory of atomic species in the atmosphere of WASP-121b using UVES high-resolution spectroscopy. Mon. Not. Roy. Astron. Soc. 506, 3853–3871. doi:10.1093/mnras/stab1878.

Merritt, S.R. et al., 2020. Non-detection of TiO and VO in the atmosphere of WASP-121b using high-resolution spectroscopy. Astron. Astrophys. 636, A117. doi:10.1051/0004-6361/201937409.

Migliorini, A. et al., 2019. H_3^+ characteristics in the Jupiter atmosphere as observed at limb with Juno/JIRAM. Icarus 329, 132–139. doi:10.1016/j.icarus.2019.04.003.

Mikosch, J., Kreckel, H., Wester, R., Plašil, R., Glosík, J., Gerlich, D., Schwalm, D., Wolf, A., 2004. Action spectroscopy and temperature diagnostics of H_3^+ by chemical probing. J. Chem. Phys. 121, 11030–11037. doi:10.1063/1.1810512.

Miliordos, E., Mavridis, A., 2007. Electronic structure of vanadium oxide. Neutral and charged species, $VO^{0,\pm}$. J. Phys. Chem. A 111, 1953–1965. doi:10.1021/jp067451b.

Miller, S. et al., 2000. The role of H_3^+ in planetary atmospheres. Phil. Trans. Royal Soc. London A 358, 2485–2502. doi:10.1098/rsta.2000.0662.

Miller, S., Achilleos, N., Ballester, G.E., Lam, H.A., Tennyson, J., Geballe, T.R., Trafton, L.M., 1997. Mid-to-low lattitude H_3^+ emission from Jupiter. Icarus 130, 57–67. doi:10.1006/icar.1997.5813.

Miller, S., Geballe, T.R., Stallard, T., Tennyson, J., 2020. Thirty years of H_3^+ astronomy. Rev. Mod. Phys. 92, 035003. doi:10.1103/RevModPhys.92.035003.

Miller, S., Stallard, T., Melin, H., Tennyson, J., 2010. H_3^+ cooling in planetary atmospheres. Faraday Discuss. 147, 283–291. doi:10.1039/C004152C.

Miller, S., Tennyson, J., 1987. First principles calculation of the molecular constants of H_3^+, H_2D^+, D_2H^+ and D_3^+. J. Mol. Spectrosc. 126, 183–192. doi:10.1016/0022-2852(87)90089-0.

Miller, S., Tennyson, J., 1988a. Calculated rotational and ro-vibrational transitions in the spectrum of H_3^+. Astrophys. J. 335, 486–490. doi:10.1086/166941.

Miller, S., Tennyson, J., 1988b. Calculation of the high angular momentum dissociation limit for H_3^+ and H_2D^+. Chem. Phys. Lett. 145, 117–120. doi:10.1016/0009-2614(88)80161-1.

Miller, S., Tennyson, J., 1988c. Overtone bands of H_3^+: first principle calculations. J. Mol. Spectrosc. 128, 530–539. doi:10.1016/0022-2852(88)90168-3.

Miller, S., Tennyson, J., Sutcliffe, B.T., 1989. First principles calculation of rotational and ro-vibrational line strengths: Spectra for H_2D^+ and D_2H^+. Mol. Phys. 66, 429–456. doi:10.1080/00268978900100211.

Mitrushchenkov, A.O., 2012. A new general renner-teller (including $\varepsilon \gtrsim 1$) spectroscopic formalism for triatomic molecules. J. Chem. Phys. 136, 024108. URL: https://doi.org/10.1063/1.3672162, doi:10.1063/1.3672162.

Mizus, I.I., Alijah, A., Zobov, N.F., Kyuberis, A.A., Yurchenko, S.N., Tennyson, J., Polyansky, O.L., 2017. ExoMol molecular line lists XX: a comprehensive line list for H_3^+. Mon. Not. Roy. Astron. Soc. 468, 1717–1725. doi:10.1093/mnras/stx502.

Moore, L. et al., 2017. Variability of Jupiter's IR H_3^+ aurorae during Juno approach. Geophys. Res. Lett. 44, 4513–4522. doi:10.1002/2017GL073156.

Moré, J.J., 1978. The Levenberg-Marquardt algorithm: Implementation and theory, in: Watson, G.A. (Ed.), Numerical Analysis, Springer Berlin Heidelberg, Berlin, Heidelberg. pp. 105–116. doi:10.1007/BFb0067700.

Morong, C.P., Gottfried, J.L., Oka, T., 2009. H_3^+ as the benchmark for rigorous ab initio theory. J. Mol. Spectrosc. 255, 13–23. doi:10.1016/j.jms.2009.02.010.

Moss, R.E., 1996. On the adiabatic and nonadiabatic corrections in the ground electronic state of the hydrogen molecular cation. Mol. Phys. 89, 195–210. doi:10.1080/002689796174083.

Murzyn, C.M., Allen, D.J., Baca, A.N., Ching, M.L., Marinis, R.T., 2022. Tunable infrared laser absorption spectroscopy of aluminum monoxide A $^2\Pi_i$ - X $^2\Sigma^+$. J. Quant. Spectrosc. Radiat. Transf. 279, 108029. doi:10.1016/j.jqsrt.2021.108029.

Nakanaga, T., Ito, F., Sugawara, K., Takeo, H., Matsumura, C., 1990. Observation of infrared absorption spectra of molecular ions, H_3^+ and HN_2^+, by FTIR spectroscopy. Chemical Physics Letters 169, 269–273. doi:10.1016/0009-2614(90)85199-M.

Neale, L., Miller, S., Tennyson, J., 1996. Spectroscopic properties of the H_3^+ molecule: a new calculated linelist. Astrophys. J. 464, 516–520. doi:10.1086/177341.

Neale, L., Tennyson, J., 1995. A high temperature partition function for H_3^+. Astrophys. J. 454, L169–L173. doi:10.1086/309789.

Nelder, J.A., Mead, R., 1965. A Simplex Method for Function Minimization. The Computer Journal 7, 308–313. doi:10.1093/comjnl/7.4.308.

Neugart, R., Neyens, G., 2006. Nuclear Moments, in: Al-Khalili, J., Roeckl, E. (Eds.), The Euroschool Lectures on Physics with Exotic Beams, Vol. II. Springer Berlin Heidelberg, Berlin, Heidelberg, pp. 135–189. doi:10.1007/3-540-33787-3_4.

Newville, M., Stensitzki, T., Allen, D.B., Ingargiola, A., 2015. LMFIT: Non-Linear Least-Square Minimization and Curve-Fitting for Python. doi:10.5281/zenodo.598352.

Oka, T., 1980. Observation of the Infrared Spectrum of H_3^+. Phys. Rev. Lett. 45, 531–534. doi:10.1103/PhysRevLett.45.531.

Oka, T., 1981. A search for interstellar H_3^+. Phil. Trans. Royal Soc. London A 303, 543–549. doi:10.1098/rsta.1981.0223.

Oka, T., 2006. Interstellar H_3^+. Proc. Natl. Acad. Sci. U. S. A. 103, 12235–12242. doi:10.1073/pnas.0601242103.

Oka, T., Epp, E., 2004. The nonthermal rotational distribution of H_3^+. Astrophys. J. 613, 349–354. doi:10.1086/423030.

Oka, T., Geballe, T.R., Goto, M., Usuda, T., McCall, B.J., 2005. Hot and diffuse clouds near the galactic center probed by metastable H_3^+. Astrophys. J. 632, 882–893. doi:10.1086/432679.

Owen, A.B., 2007. A robust hybrid of lasso and ridge regression, in: Prediction and discovery. Amer. Math. Soc., Providence, RI. volume 443 of *Contemp. Math.*, pp. 59–71. doi:10.1090/conm/443/08555.

Owens, A., Dooley, S., McLaughlin, L., Tan, B., Zhang, G., Yurchenko, S.N., Tennyson, J., 2022a. ExoMol line lists – XLV. Rovibronic molecular line lists of calcium monohydride (CaH) and magnesium monohydride (MgH). Mon. Not. Roy. Astron. Soc. 511, 5448–5461. doi:10.1093/mnras/stac371.

Owens, A., Mitrushchenkov, A., Yurchenko, S.N., Tennyson, J., 2022b. ExoMol line lists – XLVII. Rovibronic molecular line list of the calcium monohydroxide radical (CaOH). Mon. Not. Roy. Astron. Soc. 516, 3995–4002. doi:10.1093/mnras/stac2462.

Pan, F.S., Oka, T., 1986. Calculated forbidden rotational spectra of H_3^+. Astrophys. J. 305, 518–525. doi:10.1086/164264.

Pang, R. et al., 2023. Theoretical Investigation of Spectroscopic Properties of the Alkaline-Earth-Metal Monohydrides toward Laser Cooling and Magneto-Optical Trapping. ACS Omega 8, 19391–19401. doi:10.1021/acsomega.3c00352.

Parigger, C.G., 2023. On Analysis of Laser Plasma Aluminum Monoxide Emission Spectra. arXiv e-prints. doi:10.48550/arXiv.2305.02083, arXiv:2305.02083.

Parigger, C.G., Hornkohl, J.O., 2011. Computation of AlO B $^2\Sigma^+ \rightarrow$ X $^2\Sigma^+$ emission spectra. Spectroc. Acta Pt. A-Molec. Biomolec. Spectr. 81, 404–411. doi:10.1016/j.saa.2011.06.029.

Parmentier, V., Fortney, J.J., Showman, A.P., Morley, C., Marley, M.S., 2016. Transitions in the cloud composition of hot Jupiters. Astrophys. J. 828, 22. doi:10.3847/0004-637X/828/1/22.

Parmentier, Vivien et al., 2018. From thermal dissociation to condensation in the atmospheres of ultra hot Jupiters: WASP-121b in context. Astron. Astrophys. 617, A110. doi:10.1051/0004-6361/201833059.

Partridge, H., Langhoff, S.R., Lengsfield, B.H., Liu, B., 1983. Theoretical study of the AlO blue-green (B $^2\Sigma^+$–X $^2\Sigma^+$) band system. J. Quant. Spectrosc. Radiat. Transf. 30, 449–462. doi:10.1016/0022-4073(83)90108-5.

Partridge, H., Schwenke, D.W., 1997. The determination of an accurate isotope dependent potential energy surface for water from extensive ab initio calculations and experimental data. J. Chem. Phys. 106, 4618–4639. doi:10.1063/1.473987.

Patrascu, A.T., Hill, C., Tennyson, J., Yurchenko, S.N., 2014. Study of the electronic and rovibronic structure of the $X\ ^2\Sigma^+$ $A\ ^2\Pi$ and $B\ ^2\Sigma^+$ states of AlO. J. Chem. Phys. 141, 144312. doi:10.1063/1.4897484.

Patrascu, A.T., Tennyson, J., Yurchenko, S.N., 2015. ExoMol molecular linelists - IX: The spectrum of AlO. Mon. Not. Roy. Astron. Soc. 449, 3613–3619. doi:10.1093/mnras/stv507.

Pavanello, M. et al., 2012a. Calibration-quality adiabatic potential energy surfaces for H_3^+ and its isotopologues. J. Chem. Phys. 136, 184303. doi:10.1063/1.4711756.

Pavanello, M. et al., 2012b. Precision measurements and computations of transition energies in rotationally cold triatomic hydrogen ions up to the mid-visible spectral range. Phys. Rev. Lett. 108, 023002. doi:10.1103/PhysRevLett.108.023002.

Pavlenko, Y.V., Yurchenko, S.N., McKemmish, L.K., Tennyson, J., 2020. Analysis of the TiO isotopologues in stellar optical spectra. Astron. Astrophys. 42, A77. doi:10.1051/0004-6361/202037863.

Pedregosa, F. et al., 2011. Scikit-learn: Machine Learning in Python. Journal of Machine Learning Research 12, 2825–2830. URL: http://jmlr.org/papers/v12/pedregosa11a.html.

Pelletier, S. et al., 2023. Vanadium oxide and a sharp onset of cold-trapping on a giant exoplanet. Nature 619, 491–494. doi:10.1038/s41586-023-06134-0.

Perri, A.N., McKemmish, L.K., 2023. Full spectroscopic model and trihybrid experimental-perturbative-variational line list for NH. Mon. Not. Roy. Astron. Soc.

Perri, A.N., Taher, F., McKemmish, L.K., 2023. Full spectroscopic model and trihybrid experimental-perturbative-variational line list for ZrO. Mon. Not. Roy. Astron. Soc. 524, 4631–4641. doi:10.1093/mnras/stad2103.

Perry, A.J., Hodges, J.N., Markus, C.R., Kocheril, G.S., McCall, B.J., 2015. High-precision R-branch transition frequencies in the ν_2 fundamental band of H_3^+. J. Mol. Spectrosc. 317, 71–73. doi:10.1016/j.jms.2015.09.004.

Perry, A.J., McCall, B.J., Kocheril, G.S., Hodges, J.N., Markus, C.R., 2016. Highly accurate and precise infrared transition frequencies of the H_3^+ cation, in: 71^{st} International Symposium on Molecular Spectroscopy, p. MH03. doi:10.15278/isms.2016.MH03.

Petrignani, A. et al., 2014. Visible intensities of the triatomic hydrogen ion from experiment and theory. J. Chem. Phys. 141, 241104. doi:10.1063/1.4904440.

Petrus, S. et al., 2023. The JWST Early Release Science Program for Direct Observations of Exoplanetary Systems V: Do Self-Consistent Atmospheric Models Represent JWST Spectra? A Showcase With VHS 1256 b. arXiv e-prints. doi:10.48550/arXiv.2312.03852, arXiv:2312.03852.

Petty, C., Poirier, B., 2014. Using ScalIT for Performing Accurate Rovibrational Spectroscopy Calculations for Triatomic Molecules: A practical guide. Appl. Math. 5, 2756–2763. doi:10.4236/am.2014.517263.

Pickett, H.M., Poynter, R.L., Cohen, E.A., Delitsky, M.L., Pearson, J.C., Muller, H.S.P., 1998. Submillimeter, Millimeter, and Microwave Spectral Line Catalog. J. Quant. Spectrosc. Radiat. Transf. 60, 883–890. doi:10.1016/S0022-4073(98)00091-0.

Pilgram, N.H., Jadbabaie, A., Zeng, Y., Hutzler, N.R., Steimle, T.C., 2021. Fine and hyperfine interactions in ^{171}YbOH and ^{173}YbOH. J. Chem. Phys. 154, 244309. doi:10.1063/5.0055293.

Polyansky, O.L., Jensen, P., Tennyson, J., 1994. A spectroscopically determined potential energy surface for the ground state of $H_2{}^{16}O$: a new level of accuracy. J. Chem. Phys. 101, 7651–7657. doi:10.1063/1.468258.

Polyansky, O.L., Jensen, P., Tennyson, J., 1996. The potential energy surfaces of $H_2{}^{16}O$. J. Chem. Phys. 105, 6490–6497.

Polyansky, O.L., Kyuberis, A.A., Lodi, L., Tennyson, J., Ovsyannikov, R.I., Zobov, N., 2017. ExoMol molecular line lists XIX: high accuracy computed line lists for $H_2{}^{17}O$ and $H_2{}^{18}O$. Mon. Not. Roy. Astron. Soc. 466, 1363–1371. doi:10.1093/mnras/stw3125.

Polyansky, O.L., Kyuberis, A.A., Zobov, N.F., Tennyson, J., Yurchenko, S.N., Lodi, L., 2018. ExoMol molecular line lists XXX: a complete high-accuracy line list for water. Mon. Not. Roy. Astron. Soc. 480, 2597–2608. doi:10.1093/mnras/sty1877.

Polyansky, O.L., McKellar, A.R.W., 1990. Improved analysis of the infrared spectrum of D_2H^+. J. Chem. Phys. 92, 4039–4043. doi:10.1063/1.457817.

Polyansky, O.L., Tennyson, J., 1999. Ab initio calculation of the rotation-vibration energy levels of H_3^+ and its isotopomers to spectroscopic accuracy. J. Chem. Phys. 110, 5056–5064. doi:10.1063/1.478404.

Puzzarini, C., Cazzoli, G., Harding, M.E., Vázquez, J., Gauss, J., 2015. The hyperfine structure in the rotational spectra of $D_2^{17}O$ and $HD^{17}O$: Confirmation of the absolute nuclear magnetic shielding scale for oxygen. J. Chem. Phys. 142, 124308. doi:10.1063/1.4916068.

Pykavy, M., van Wullen, C., 2003. Multireference correlation calculations for the ground states of $VO^{+/0/-}$ using correlation consistent basis sets. J. Phys. Chem. A 107, 5566–5572. doi:10.1021/jp027264n.

Qu, Q., Yurchenko, S.N., Tennyson, J., 2021. ExoMol molecular line lists – XLII: Rovibronic molecular line list for the low-lying states of NO. Mon. Not. Roy. Astron. Soc. 504, 5768–5777. doi:10.1093/mnras/stab1154.

Qu, Q., Yurchenko, S.N., Tennyson, J., 2022a. A Method for the Variational Calculation of Hyperfine-Resolved Rovibronic Spectra of Diatomic Molecules. J. Chem. Theory Comput. 18, 1808–1820. doi:10.1021/acs.jctc.1c01244.

Qu, Q., Yurchenko, S.N., Tennyson, J., 2022b. A variational model for the hyperfine resolved spectrum of VO in its ground electronic state. J. Chem. Phys. 157, 124305. doi:10.1063/5.0105965.

Qu, Q., Yurchenko, S.N., Tennyson, J., 2023. An empirical spectroscopic model for eleven electronic states of VO. J. Mol. Spectrosc. 391, 111733. doi:10.1016/j.jms.2022.111733.

Rajpurohit, A.S., Reylé, C., Allard, F., Scholz, R.D., Homeier, D., Schultheis, M., Bayo, A., 2014. High-resolution spectroscopic atlas of M subdwarfs. Effective temperature and metallicity. Astron. Astrophys. 564, A90. doi:10.1051/0004-6361/201322881.

Rajpurohit, A.S., Reylé, C., Schultheis, M., Allard, F., Scholz, R., Homeier, D., 2012. Stellar parameters of M dwarfs from low and high-resolution spectra together with new model atmospheres, in: Boissier, S., de Laverny, P., Nardetto, N., Samadi, R., Valls-Gabaud, D., Wozniak, H. (Eds.), SF2A-2012: Proceedings of the Annual meeting of the French Society of Astronomy and Astrophysics, pp. 383–388. URL: https://ui.adsabs.harvard.edu/abs/2012sf2a.conf..383R.

Ram, R.S., Bernath, P.F., 2005. Emission spectroscopy of a new $^2\Delta$–$1\ ^2\Delta$ system of VO. J. Mol. Spectrosc. 229, 57–62. doi:10.1016/j.jms.2004.08.014.

Ram, R.S., Bernath, P.F., Davis, S.P., Merer, A.J., 2002. Fourier Transform Emission Spectroscopy of a New $^2\Phi$–$1\ ^2\Delta$ System of VO. J. Mol. Spectrosc. 211, 279–283. doi:10.1006/jmsp.2001.8510.

Ramanlal, J., Tennyson, J., 2004. Deuterated hydrogen chemistry: partition functions, equilibrium constants and transition intensities for the H_3^+ system. Mon. Not. Roy. Astron. Soc. 354, 161–168. doi:10.1111/j.1365-2966.2004.08178.x.

Ran, H., Aldegunde, J., Hutson, J.M., 2010. Hyperfine structure in the microwave spectra of ultracold polar molecules. New Journal of Physics 12, 043015. doi:10.1088/1367-2630/12/4/043015.

Ran, P., Hou, H., Luo, S.N., 2017. Molecule formation induced by non-uniform plume-air interactions in laser induced plasma. J. Anal. At. Spectrom. 32, 2254–2262. doi:10.1039/c7ja00287d.

Rego, D., Miller, S., Achilleos, N., Prangé, R., Joseph, R., 2000. Latitudinal Profiles of the Jovian IR Emissions of H_3^+ at 4 μm with the NASA Infrared Telescope Facility: Energy Inputs and Thermal Balance. Icarus 147, 366–385. doi:10.1006/icar.2000.6444.

de Regt, S., Kesseli, A.Y., Snellen, I.A.G., Merritt, S.R., Chubb, K.L., 2022. A quantitative assessment of the VO line list: Inaccuracies hamper high-resolution VO detections in exoplanet atmospheres. Astron. Astrophys. 661, A109. doi:10.1051/0004-6361/202142683.

Rey, M., Nikitin, A.V., Babikov, Y.L., Tyuterev, V.G., 2016. TheoReTS – An information system for theoretical spectra based on variational predictions from molecular potential energy and dipole moment surfaces. J. Mol. Spectrosc. 327, 138–158. doi:10.1016/j.jms.2016.04.006.

Richards, D., Barrow, R.F., 1968a. New type of perturbation caused by a magnetic hyperfine interaction observed in ground state of VO. Nature 219, 1244–1245. doi:10.1038/2191244a0.

Richards, D., Barrow, R.F., 1968b. Nuclear hyperfine interactions in diatomic molecules and ground state of VO. Nature 217, 842. doi:10.1038/217842a0.

Roberts, H., Herbst, E., Millar, T.J., 2003. Enhanced Deuterium Fractionation in Dense Interstellar Cores Resulting from Multiply Deuterated H_3^+. Astrophys. J. 591, L41. doi:10.1086/376962.

Röhse, R., Kutzelnigg, W., Jaquet, R., Klopper, W., 1994. Potential energy surface of the H_3^+ ground state in the neighborhood of the minimum with microhartree accuracy and vibrational frequencies derived from it. J. Chem. Phys. 101, 2231–2243. doi:10.1063/1.467663.

Rosenwaks, S., Steele, R.E., Broida, H.P., 1975. Chemiluminescence of ALO. J. Chem. Phys. 63, 1963–1965. doi:10.1063/1.431530.

Rothman, L.S. et al., 2010. HITEMP, the high-temperature molecular spectroscopic database. J. Quant. Spectrosc. Radiat. Transf. 111, 2139–2150. doi:10.1016/j.jqsrt.2010.05.001.

Saito, S., Kawaguchi, K., Hirota, E., 1985. The microwave spectrum of the H_2D^+ ion: The $2_{20} \leftarrow 2_{21}$ transition. J. Chem. Phys. 82, 45–47. doi:10.1063/1.448767.

Saksena, M.D., Deo, M.N., Sunanda, K., Behere, S.H., Londhe, C.T., 2008. Fourier transform spectral study of B $^2\Sigma^+$–X $^2\Sigma^+$ system of AlO. J. Mol. Spectrosc. 247, 47–56. doi:10.1016/j.jms.2007.10.002.

Saksena, M.D., Ghodgaonkar, G.S., Singh, M., 1989. The B $^2\Sigma^+$–X $^2\Sigma^+$ system of AlO. J. Phys. B-At. Mol. Opt. Phys. 22, 1993–1996. doi:10.1088/0953-4075/22/12/014.

Sarka, J., Das, D., Poirier, B., 2021. Calculation of rovibrational eigenstates of H_3^+ using ScalIT. AIP Adv. 11, 045033. doi:10.1063/5.0047823.

Sarka, J., Poirier, B., 2022. Assigning quantum labels and improving accuracy for the rovibrational eigenstates of H_3^+ calculated using ScalIT. Front. Phys. 10, 996001. doi:10.3389/fphy.2022.996001.

Sarvan, M., Perić, M., Zeković, L., Stojadinović, S., Belča, I., Petković, M., Kasalica, B., 2011. Identification of the C $^2\Pi$–X $^2\Sigma^+$ band system of AlO in the ultraviolet galvanoluminescence obtained during aluminum anodization. Spectroc. Acta Pt. A-Molec. Biomolec. Spectr. 81, 672–678. doi:10.1016/j.saa.2011.06.072.

Sato, N., Ito, H., Kuchitsu, K., 1995. Electronic transition moment of the AlO(B $^2\Sigma^+$–X $^2\Sigma^+$) emission. Analysis of the R dependence of the $Al^{2+}O^{2-}$ character in the X $^2\Sigma^+$ state. Chem. Phys. Lett. 240, 10–16. doi:10.1016/0009-2614(95)00495-P.

Saumon, D., Bergeron, P., Lunine, J.I., Hubbard, W.B., Burrows, A., 1994. Cool Zero-Metallicity Stellar Atmospheres. Astrophys. J. 424, 333. doi:10.1086/173892.

Sauval, A.J., Tatum, J.B., 1984. A set of partition functions and equilibrium constants for 300 diatomic molecules of astrophysical interest. Astrophys. J. Suppl. Ser. 56, 193–209. doi:10.1086/190980.

Schamps, J., 1973. The energy spectrum of aluminium monoxide. Chem. Phys. 2, 352–366. doi:10.1016/0301-0104(73)80038-2.

Schryber, J.H., Miller, S., Tennyson, J., 1995. Computed infra red absorption properties of hot water vapour. J. Quant. Spectrosc. Radiat. Transf. 53, 373–380.

Schwarz, H., Brogi, M., de Kok, R., Birkby, J., Snellen, I., 2015. Evidence against a strong thermal inversion in HD 209458b from high-dispersion spectroscopy. Astron. Astrophys. 576, A111. doi:10.1051/0004-6361/201425170.

Schwenke, D.W., 2001. Beyond the Potential Energy Surface: Ab initio Corrections to the Born-Oppenheimer Approximation for H_2O. J. Phys. Chem. A 105, 2352–2360. doi:10.1021/jp0032513.

Semenov, M., Tennyson, J., Yurchenko, S.N., 2022. ExoMol line lists – XLVI: Empirical rovibronic spectra of silicon mononitrate (SiN) covering 6 lowest electronic states and 4 isotopologues. Phys. Chem. Chem. Phys. 516, 1158–1169. doi:10.1093/mnras/stac2004.

Semenov, M., Yurchenko, S.N., Tennyson, J., 2017. Predicted Landé g-factors for open shell diatomic molecules. J. Mol. Spectrosc. 330, 57–62. doi:10.1016/j.jms.2016.11.004.

Seto, J., 2000. Direct Fitting of Analytic Potential Functions to Diatomic Molecule Spectroscopic Data. Master's thesis. Department of Chemistry, University of Waterloo. URL: http://hdl.handle.net/10012/1241. m. Sc. thesis.

Sharp, C.M., Burrows, A., 2007. Atomic and molecular opacities for brown dwarf and giant planet atmospheres. Astrophys. J. Suppl. Ser. 168, 140–166. doi:10.1086/508708.

Sheppard, K.B. et al., 2021. The Hubble PanCET Program: A Metal-rich Atmosphere for the Inflated Hot Jupiter HAT-P-41b. Astron. J. 161, 51. doi:10.3847/1538-3881/abc8f4.

Showman, A.P., Fortney, J.J., Lian, Y., Marley, M.S., Freedman, R.S., Knutson, H.A., Charbonneau, D., 2009. Atmospheric circulation of hot Jupiters: coupled radiative-dynamical general circulation model simulations of HD 189733b and HD 209458b. Astrophys. J. 699, 564–584. doi:10.1088/0004-637x/699/1/564.

Simeckova, M., Jacquemart, D., Rothman, L.S., Gamache, R.R., Goldman, A., 2006. Einstein A-coefficients and statistical weights for molecular absorption transitions in the HITRAN database. J. Quant. Spectrosc. Radiat. Transf. 98, 130–155. doi:10.1016/j.jqrst.2005.07.003.

Singh, A.P., Edwards, J.L., Ziurys, L.M., 2022. The Arizona Radio Observatory 1 mm Spectral Survey of the Hypergiant Star NML Cygni (215–285 GHz). Astron. J. 164, 230. doi:10.3847/1538-3881/ac8df0.

Singh, M., 1973. A new electronic transition F $^2\Sigma^+$–A $^2\Pi_i$ of AlO. J. Phys. B: At. Mol. Phys. 6, 521–526. doi:10.1088/0022-3700/6/3/020.

Singh, M., Narasimham, N.A., 1969. Isotope shift studies of the visible and ultra-violet bands of AlO. J. Phys. B-At. Mol. Opt. Phys. 2, 119–153–3. doi:10.1088/0022-3700/2/1/317.

Singh, M., Saksena, M.D., 1981. The ultraviolet-spectrum of ALO. Can. J. Phys. 59, 955–966. doi:10.1139/p81-125.

Singh, M., Saksena, M.D., 1982. A new electronic transition C $^2\Pi_r$–A $^2\Pi_i$, of AlO. Can. J. Phys. 60, 1730–1742. doi:10.1139/p82-233.

Singh, M., Saksena, M.D., 1983. C $^2\Pi_r$–X $^2\Sigma^+$ transition of AlO. Can. J. Phys. 61, 1347–1358. doi:10.1088/0953-4075/22/12/014.

Singh, M., Saksena, M.D., 1985. The D $^2\Sigma^+$–A $^2\Pi_i$ and C $^2\Pi_r$–A $^2\Pi_i$ transitions of AlO. Can. J. Phys. 63, 1162–1172. doi:10.1139/p85-190.

Singh, M., Zope, G.V., KrishnamachariI, S.L.N.G., 1985. The B $^2\Sigma^+$–X $^2\Sigma^+$ transition of AlO. J. Phys. B-At. Mol. Opt. Phys. 18, 1743–1745. doi:10.1088/0022-3700/18/9/009.

Snellen, I., 2014. High-dispersion spectroscopy of extrasolar planets: from CO in hot jupiters to O_2 in exo-earths. Phil. Trans. Royal Soc. London A 372, 20130075. doi:10.1098/rsta.2013.0075.

Sochi, T., Tennyson, J., 2010. A computed line list for the H_2D^+ molecular ion. Mon. Not. Roy. Astron. Soc. 405, 2345–2350.

Somogyi, W., Yurchenko, S.N., Yachmenev, A., 2021. Calculation of electric quadrupole linestrengths for diatomic molecules: Application to the h-2, co, hf, and o-2 molecules. J. Chem. Phys. 155. doi:10.1063/5.0063256.

Soo, M., Goroshin, S., Glumac, N., Kumashiro, K., Vickery, J., Frost, D.L., Bergthorson, J.M., 2017. Emission and laser absorption spectroscopy of flat flames in aluminum suspensions. Combustion and Flame 180, 230 – 238. doi:10.1016/j.combustflame.2017.03.006.

Spiegel, D.S., Silverio, K., Burrows, A., 2009. Can TiO explain thermal inversions in the upper atmospheres of irradiated giant planets? Astrophys. J. 699, 1487. doi:10.1088/0004-637X/699/2/1487.

Spinrad, H., Wing, R.F., 1969. Infrared spectra of stars. Ann. Rev. Astron. Astrophys 7, 249. doi:10.1146/annurev.aa.07.090169.001341.

Spinrad, H., Younkin, R.L., 1966. Infrared Bands of Vanadium Oxide in Three Mira Stars. Publ. Astron. Soc. Pac. 78, 65–67. doi:10.1086/128294.

Sriramachandran, P., Bagare, S.P., Rajamanickam, N., Balachandrakumar, K., 2008. Presence of LaO, ScO and VO Molecular Lines in Sunspot Umbral Spectra. Sol. Phys. 252, 267–281. doi:10.1007/s11207-008-9261-1.

Sriramachandran, P., Viswanathan, B., Shanmugavel, R., 2013. Occurrence of AlO Molecular Lines in Sunspot Umbral Spectra. Sol. Phys. 286, 315–326. doi:10.1007/s11207-013-0264-1.

Stallard, T. et al., 2008a. Complex structure within Saturn's infrared aurora. Nature 456, 214–217. doi:10.1038/nature07440.

Stallard, T., Miller, S., Melin, H., Lystrup, M., Cowley, S.W.H., Bunce, E.J., Achilleos, N., Dougherty, M., 2008b. Jovian-like aurorae on Saturn. Nature 453, 1083–1085. doi:10.1038/nature07077.

Stark, R., van der Tak, F.F.S., van Dishoeck, E.F., 1999. Detection of Interstellar H_2D^+ Emission. Astrophys. J. 521, L67–L70. doi:10.1086/312182.

Stone, N., 2005. Table of nuclear magnetic dipole and electric quadrupole moments. Atomic Data and Nuclear Data Tables 90, 75–176. doi:https://doi.org/10.1016/j.adt.2005.04.001.

Suenram, R.D., Fraser, G.T., Lovas, F.J., Gillies, C.W., 1991. Microwave-spectra and electric-dipole moments of X $^4\Sigma^-_{1/2}$ VO and NbO. J. Mol. Spectrosc. 148, 114–122. doi:10.1016/0022-2852(91)90040-H.

Sun, S., Zhou, M., Zhu, Z., 2023. Spectroscopic Parameters of 15 Low-Lying Doublet and Quartet Λ-Σ States as Well as 36 Ω States of VO. Russ. J. Phys. Chem. B 17, 268–282. doi:10.1134/S1990793123020161.

Šurkus, A.A., Rakauskas, R.J., Bolotin, A.B., 1984. The Generalized Potential-Energy Function for Diatomic-Molecules. Chem. Phys. Lett. 105, 291–294. doi:10.1016/0009-2614(84)85032-0.

Surmick, D.M., Dagel, D.J., Parigger, C.G., 2019. Spatial Molecular AlO Temperature Distributions in Laser-Induced Plasma. Atoms 7, 86. doi:10.3390/atoms7030086.

Surmick, D.M., Parigger, C.G., 2014. Aluminum Monoxide Emission Measurements in a Laser-Induced Plasma. Appl. Spectrosc. 68, 992–996. doi:10.1366/13-07379.

Syme, A.M., McKemmish, L.K., 2021. Full spectroscopic model and trihybrid experimental-perturbative-variational line list for CN. Mon. Not. Roy. Astron. Soc. 505, 4383–4395. doi:10.1093/mnras/stab1551.

Takigawa, A., Kamizuka, T., Tachibana, S., Yamamura, I., 2017. Dust formation and wind acceleration around the aluminum oxide–rich AGB star W Hydrae. Science Advances 3, eaao2149. doi:10.1126/sciadv.aao2149.

Tawde, N.R., Korwar, V.M., 1968. The problem of the uniqueness of the $r_e(r_{v'v''})$ function for the (a $^2\sigma$–x $^2\sigma$) system of alo. J. Phys. B: At. Mol. Phys. 1, 753–754. doi:10.1088/0022-3700/1/4/130.

Tawde, N.R., Tulasigeri, V.G., 1972. Franck-Condon factors and r centroids of the $^2\Sigma^+$–x $^2\Sigma^+$ band system of AlO using RKR potentials. J. Phys. B: At. Mol. Phys. 5, 1681–1687. doi:10.1088/0022-3700/5/9/011.

Tenenbaum, E.D., Ziurys, L.M., 2009. Millimeter detectionoOf AlO (X2Sigma+) in the oxygen-rich envelope Of VY Canis Majoris. Astrophys. J. 694, L59–L63. doi:10.1088/0004-637X/694/1/L59.

Tenenbaum, E.D., Ziurys, L.M., 2010. Exotic metal molecules in oxygen-rich envelopes: detection of AlOH ($X^1\Sigma^+$) in VY Canis Majoris. Astrophys. J. Lett. 712, L93. doi:10.1088/2041-8205/712/1/L93.

Tennyson, J., 2012. Accurate variational calculations for line lists to model the vibration rotation spectra of hot astrophysical atmospheres. WIREs Comput. Mol. Sci. 2, 698–715. doi:10.1002/wcms.94.

Tennyson, J. et al., 2009. IUPAC critical evaluation of the rotational-vibrational spectra of water vapor. Part I. Energy levels and transition wavenumbers for $H_2{}^{17}O$ and $H_2{}^{18}O$. J. Quant. Spectrosc. Radiat. Transf. 110, 573–596. doi:10.1016/j.jqsrt.2009.02.014.

Tennyson, J. et al., 2010. IUPAC critical evaluation of the rotational-vibrational spectra of water vapor. Part II. Energy levels and transition wavenumbers for $HD^{16}O$, $HD^{17}O$, and $HD^{18}O$. J. Quant. Spectrosc. Radiat. Transf. 111, 2160–2184. doi:10.1016/j.jqsrt.2010.06.012.

Tennyson, J., Furtenbacher, T., Yurchenko, S.N., Császár, A.G., 2024. Empirical rovibrational energy levels for nitrous oxide. J. Quant. Spectrosc. Radiat. Transf. 316, 108902. doi:10.1016/j.jqsrt.2024.108902.

Tennyson, J., Hill, C., Yurchenko, S.N., 2013. Data structures for ExoMol: Molecular line lists for exoplanet and other atmospheres, in: 6^{th} international conference on atomic and molecular data and their applications ICAMDATA-2012, AIP, New York. pp. 186–195. doi:10.1063/1.4815853.

Tennyson, J., Kostin, M.A., Barletta, P., Harris, G.J., Polyansky, O.L., Ramanlal, J., Zobov, N.F., 2004. DVR3D: a program suite for the calculation of rotation-vibration spectra of triatomic molecules. Comput. Phys. Commun. 163, 85–116. doi:10.1016/j.cpc.2003.10.003.

Tennyson, J., Lodi, L., McKemmish, L.K., Yurchenko, S.N., 2016a. The ab initio calculation of spectra of open shell diatomic molecules. J. Phys. B-At. Mol. Opt. Phys. 49, 102001. doi:10.1088/0953-4075/49/10/102001.

Tennyson, J., Pezzella, M., Zhang, J., Yurchenko, S.N., 2023. Data structures for photoadsorption within the ExoMol project. RAS Tech. Instr. 2, 231–237. doi:10.1093/rasti/rzad014.

Tennyson, J., Sutcliffe, B.T., 1984. On the rovibrational levels of the H_3^+ and H_2D^+ molecules. Mol. Phys. 51, 887–906. doi:10.1080/00268978400100591.

Tennyson, J., Sutcliffe, B.T., 1985. A calculation of the rovibrational spectra of the H_3^+, H_2D^+ and HD_2^+ molecules. Mol. Phys. 56, 1175–1183. doi:10.1080/00268978500102981.

Tennyson, J., Sutcliffe, B.T., 1986. The infrared spectra of H_3^+ and its isotopomers – a challenge to theory and experiment. J. Chem. Soc. 82, 1151–1162. doi:10.1039/F29868201151.

Tennyson, J., Yurchenko, S.N., 2012. ExoMol: molecular line lists for exoplanet and other atmospheres. Mon. Not. Roy. Astron. Soc. 425, 21–33. doi:10.1111/j.1365-2966.2012.21440.x.

Tennyson, J., Yurchenko, S.N., 2017. The ExoMol project: Software for computing molecular line lists. Int. J. Quantum Chem. 117, 92–103. doi:10.1002/qua.25190.

Tennyson, J., Yurchenko, S.N., 2018. The ExoMol atlas of molecular opacities. Atoms 6, 26. doi:10.3390/atoms6020026.

Tennyson, J., Yurchenko, S.N., 2019. The ExoMol project: an update, in: Salama, F., Linnartz, H. (Eds.), Laboratory Astrophysics: from Observations to Interpretation, pp. 287–296. doi:10.1017/S1743921319006343.

Tennyson, J. et al., 2016b. The ExoMol database: molecular line lists for exoplanet and other hot atmospheres. J. Mol. Spectrosc. 327, 73–94. doi:10.1016/j.jms.2016.05.002.

Tennyson, J. et al., 2020. The 2020 release of the ExoMol database: Molecular line lists for exoplanet and other hot atmospheres. J. Quant. Spectrosc. Radiat. Transf. 255, 107228. doi:10.1016/j.jqsrt.2020.107228.

Thomas, E.M., Melin, H., Stallard, T.S., Chowdhury, M.N., Wang, R., Knowles, K., Miller, S., 2023. Detection of the infrared aurora at Uranus with Keck-NIRSPEC. Nature Astron. doi:10.1038/s41550-023-02096-5.

Tinetti, G. et al., 2018. A chemical survey of exoplanets with ARIEL. Exp. Astron. 46, 135–209. doi:10.1007/s10686-018-9598-x.

Tinetti, G., Encrenaz, T., Coustenis, A., 2013. Spectroscopy of planetary atmospheres in our galaxy. Astron. Astrophys. Rev. 21, 1–65. doi:10.1007/s00159-013-0063-6.

Tinetti, G. et al., 2007. Water vapour in the atmosphere of a transiting extrasolar planet. Nature 448, 169–171. doi:10.1038/nature06002.

Tóbiás, R., Furtenbacher, T., Császár, A.G., 2017. Cycle bases to the rescue. J. Quant. Spectrosc. Radiat. Transf. 203, 557–564. doi:10.1016/j.jqsrt.2017.03.031.

Tobias, R. et al., 2020. Spectroscopic-network-assisted precision spectroscopy and its application to water. Nature Comms. 11, 1708. doi:10.1038/s41467-020-15430-6.

Tóbiás, R., Furtenbacher, T., Tennyson, J., Császár, A.G., 2019. Accurate empirical rovibrational energies and transitions of $H_2{}^{16}O$. Phys. Chem. Chem. Phys. 21, 3473–3495. doi:10.1039/c8cp05169k.

Torring, T., Herrmann, R., 1989. Fine and hyperfine structure in the X $^2\Sigma^+$-state of AlO. Mol. Phys. 68, 1379–1381. doi:10.1080/00268978900102981.

Towle, J.P., James, A.M., Bourne, O.L., Simard, B., Singh, M., Saksena, M.D., 1994. The C $^2\Pi$–X $^2\Sigma^+$ (0, 0) Band in AlO. J. Mol. Spectrosc. 167, 472–473. doi:10.1006/jmsp.1994.1252.

Trafton, L.M., Geballe, T.R., Miller, S., Tennyson, J., Ballester, G.E., 1993. Detection of H_3^+ from Uranus. Astrophys. J. 405, 761–766. doi:10.1086/172404.

Trafton, L.M., Miller, S., Geballe, T.R., Tennyson, J., Ballester, G.E., 1999. H_2 quadrupole and overtone H_3^+ emission from uranus: The Uranian thermosphere, ionosphere and aurora. Astrophys. J. 524, 1059–1083. doi:10.1086/307838.

Tsiaras, A. et al., 2018. A population study of gaseous exoplanets. Astron. J. 155, 156. doi:10.3847/1538-3881/aaaf75.

Tylenda, R., Crause, L.A., Gorny, S.K., Schmidt, M.R., 2005. V4332 Sagittarii revisited. Astron. Astrophys. 439, 651–661. doi:10.1051/0004-6361:20041581.

Tylenda, R., Kamiński, T., Schmidt, M., Kurtev, R., Tomov, T., 2011. High-resolution optical spectroscopy of V838 Monocerotis in 2009. Astron. Astrophys. 532, A138. doi:10.1051/0004-6361/201116858.

Tyte, D.C., 1964. Red (B $^2\Pi$–A $^2\Sigma$) Band System of Aluminium Monoxide. Nature 202, 383–384. doi:10.1038/202383a0.

Tyte, D.C., Hébert, G.R., 1964. The electronic transition moment of the A $^2\Sigma$–X $^2\Sigma$ system of AlO. Proc. Phys. Soc. 84, 830–832. doi:10.1088/0370-1328/84/5/122.

Uno, T., Kasaba, Y., Tao, C., Sakanoi, T., Kagitani, M., Fujisawa, S., Kita, H., Badman, S.V., 2014. Vertical emissivity profiles of Jupiter's northern H_3^+ and H_2 infrared auroras observed by Subaru/IRCS. J. Geophys. Res.-Space Phys. 119, 10,219–10,241. doi:10.1002/2014JA020454.

Uy, D., Gabrys, C.M., Jagod, M., Oka, T., 1994. Spectral lines and distribution of H_3^+ in high rotational levels. J. Chem. Phys. 100, 6267–6274. doi:10.1063/1.467089.

Uzunova, E.L., Mikosch, H., Nikolov, G.S., 2008. Electronic structure of oxide, peroxide, and superoxide clusters of the 3d elements: A comparative density functional study. J. Chem. Phys. 128, 094307. doi:10.1063/1.2831583.

Van Woerkom, T.A., Perram, G.P., Dolasinski, B.D., Berry, P.A., Phelps, C.D., 2018. Visible aluminum monoxide emission during long pulse mid-infrared ablation of aluminum in air. J. Opt. Soc. Am. B 35, B54–B61. doi:10.1364/JOSAB.35.000B54.

Varshalovich, D.A., Ivanchik, A.V., Babkovskaya, N.S., 2006. The $\lambda 0$ = 1.35 cm H_2O maser line: The hyperfine structure and profile asymmetry. Astron. Lett. 32, 29–38. doi:10.1134/S1063773706010051.

Vastel, C., Phillips, T.G., Yoshida, H., 2004. Detection of D_2H^+ in the Dense Interstellar Medium. Astrophys. J. 606, L127–L130. doi:10.1086/421265.

Velilla, L., Lepetit, B., Aguado, A., Beswick, J.A., Paniagua, M., 2008. The H_3^+ rovibrational spectrum revisited with a global electronic potential energy surface. J. Chem. Phys. 129, 084307. doi:10.1063/1.2973629.

Ventrudo, B.F., Cassidy, D.T., Guo, Z.Y., Joo, S., Lee, S.S., Oka, T., 1994. Near infrared $3\nu_2$ overtone band of H_3^+. J. Chem. Phys. 100, 6263–6266. doi:10.1063/1.467088.

Veseth, L., 1975. Fine-structure of $^4\Pi$ states in diatomic-molecules. Phys. Scr. 12, 125–128. doi:10.1088/0031-8949/12/3/004.

Virtanen, P. et al., 2020. SciPy 1.0: Fundamental Algorithms for Scientific Computing in Python. Nature Methods 17, 261–272. doi:10.1038/s41592-019-0686-2.

Viti, S., Jones, H.R.A., Richter, M.J., Barber, R.J., Tennyson, J., Lacy, J.H., 2008. A potential new method for temperature determination in low-mass stars. Mon. Not. Roy. Astron. Soc. 388, 1305–1313. doi:10.1111/j.1365-2966.2008.13489.x.

Viti, S., Tennyson, J., Polyansky, O.L., 1997. A spectroscopic linelist for hot water. Mon. Not. Roy. Astron. Soc. 287, 79–86.

Vogt, S.S. et al., 1994. HIRES: the high-resolution echelle spectrometer on the Keck 10-m Telescope, in: Crawford, D.L., Craine, E.R. (Eds.), Instrumentation in Astronomy VIII, International Society for Optics and Photonics. SPIE. pp. 362 – 375. doi:10.1117/12.176725.

Wakeford, H.R., Visscher, C., Lewis, N.K., Kataria, T., Marley, M.S., Fortney, J.J., Mandell, A.M., 2016. High-temperature condensate clouds in super-hot Jupiter atmospheres. Mon. Not. Roy. Astron. Soc. 464, 4247–4254. doi:10.1093/mnras/stw2639.

Wales, D.J., Doye, J.P.K., 1997. Global Optimization by Basin-Hopping and the Lowest Energy Structures of Lennard-Jones Clusters Containing up to 110 Atoms. J. Phys. Chem. A 101, 5111–5116. doi:10.1021/jp970984n.

Wales, D.J., Scheraga, H.A., 1999. Global Optimization of Clusters, Crystals, and Biomolecules. Science 285, 1368–1372. doi:10.1126/science.285.5432.1368.

Wallerstein, G., 1971. Spectroscopic Observations of VY Canis Majoris during 1969-1971. Astrophys. J. 169, 195. doi:10.1086/151131.

Walmsley, C.M., Flower, D.R., des Forets, G.P., 2004. Complete depletion in prestellar cores. Astron. Astrophys. 418, 1035–1043. doi:10.1051/0004-6361:20035718.

Warner, H.E., Conner, W.T., Petrmichl, R.H., Woods, R.C., 1984. Laboratory detection of the $1_{10} \leftarrow 1_{11}$ submillimeter wave transition of the H_2D^+ ion. J. Chem. Phys. 81, 2514–2514. doi:10.1063/1.447914.

Watson, J.K.G., 1984. Higher-order vibration-rotation energies of the X_3 molecule. J. Mol. Spectrosc. 103, 350–363. doi:10.1016/0022-2852(84)90062-6.

Watson, J.K.G., 1994. Erratum: Vibration-rotation calculations for using a Morse-based discrete variable representation. Can. J. Phys. 72, 702–713. doi:10.1139/p94-092.

Watson, J.K.G., Foster, S.C., McKellar, A.R.W., 1987. The infrared spectrum of the ν_2 fundamental band of the D_3^+ molecular ion. Can. J. Phys. 65, 38–46. doi:10.1139/p87-008.

Watson, J.K.G. et al., 1984. The infrared spectrum of the ν_2 fundamental band of the molecular ion. Can. J. Phys. 62, 1875–1885. doi:10.1139/p84-231.

Werner, H.J. et al., 2015. Molpro, version 2015.1, a package of ab initio programs. http://www.molpro.net.

Werner, H.J. et al., 2020. The molpro quantum chemistry package. The Journal of Chemical Physics 152, 144107. doi:10.1063/5.0005081.

Western, C.M., 2017. PGOPHER: A program for simulating rotational, vibrational and electronic spectra . J. Quant. Spectrosc. Radiat. Transf. 186, 221–242. doi:10.1016/j.jqsrt.2016.04.010.

Whiting, E.E., Schadee, A., Tatum, J.B., Hougen, J.T., Nicholls, R.W., 1980. Recommended conventions for defining transition moments and intensity factors in diatomic molecular spectra. J. Mol. Spectrosc. 80, 249 – 256. URL: http://www.sciencedirect.com/science/article/pii/002228528090137X, doi:http://dx.doi.org/10.1016/0022-2852(80)90137-X.

Windsor, C.G., Astbury, J.O., Davidson, J.J., McFadzean, C.J., Morgan, J.G., Wilson, C.L., Humphry-Baker, S.A., 2021. Tungsten boride shields in a spherical tokamak fusion power plant. Nuclear Fusion 61, 086018. doi:10.1088/1741-4326/ac09ce.

Wing, R.F., Lockwood, G.W., 1973. The period and spectral range of IK Tauri. Astrophys. J. 184, 873. doi:10.1086/152376.

Wing, R.F., Spinrad, H., Kuhi, L.V., 1967. Infrared Stars. Astrophys. J. 147, 117. doi:10.1086/148985.

Wu, K.Y., Lien, Y.H., Liao, C.C., Lin, Y.R., Shy, J.T., 2013. Measurement of the ν_2 fundamental band of H_3^+. Phys. Rev. A 88, 032507. doi:10.1103/PhysRevA.88.032507.

Xu, E., Tennyson, J., 2023. Empirical rovibrational energy levels for carbonyl sulphide. Mol. Phys., e2279694. doi:10.1080/00268976.2023.2279694.

Xu, L., Gabrys, C., Oka, T., 1990. Observation of the $2\nu_2$(l=2) $\leftarrow$ 0 overtone band of H_3^+. J. Chem. Phys. 93, 6210–6215. doi:10.1063/1.458990.

Xu, L.W., Rosslein, M., Gabrys, C.M., Oka, T., 1992. Observation of infrared forbidden transitions of H_3^+. J. Mol. Spectrosc. 153, 726–737. doi:10.1016/0022-2852(92)90507-K.

Yamada, C., Cohen, E.A., Fujitake, M., Hirota, E., 1990. The microwave-spectrum of the AlO radical. J. Chem. Phys. 92, 2146–2149. doi:10.1063/1.458005.

Yang, H., Cao, J., Su, Z., Rui, J., Zhao, B., Pan, J.W., 2022. Creation of an ultracold gas of triatomic molecules from an atom–diatomic molecule mixture. Science 378, 1009–1013. doi:10.1126/science.ade6307.

Yonezu, T., Matsushima, F., Moriwaki, Y., Takagi, K., Amano, T., 2009. THz spectroscopy of H_2D^+. J. Mol. Spectrosc. 256, 238–241. doi:10.1016/j.jms.2009.04.006.

Yoshimine, M., McLean, A.D., Liu, B., 1973. Band strengths for electric dipole transitions from *ab initio* computation: LiO ($X\ ^2\Pi$–$X\ ^2\Pi$), ($A\ ^2\Sigma^+$–$A\ ^2\Sigma^+$), ($X\ ^2\Pi$–$A\ ^2\Sigma^+$); AlO ($X\ ^2\Sigma^+$–$X\ ^2\Sigma^+$), ($A\ ^2\Pi$–$A\ ^2\Pi$), ($X\ ^2\Sigma^+$–$A\ ^2\Pi$), ($B\ ^2\Sigma^+$–$B\ ^2\Sigma^+$), ($X\ ^2\Sigma^+$–$B\ ^2\Sigma^+$). J. Chem. Phys. 58, 4412–4429. doi:10.1063/1.1679002.

Yu., S., Pearson, J.C., Amano, T., Matsushima, F., 2017. THz spectroscopy of D_2H^+. J. Mol. Spectrosc. 331, 6–8. doi:10.1016/j.jms.2016.10.012.

Yurchenko, S.N., Al-Refaie, A.F., Tennyson, J., 2018. ExoCross: a general program for generating spectra from molecular line lists. Astron. Astrophys. 614, A131. doi:10.1051/0004-6361/201732531.

Yurchenko, S.N., Blissett, A., Asari, U., Vasilios, M., Hill, C., Tennyson, J., 2016a. ExoMol Molecular linelists – XIII. The spectrum of CaO. Mon. Not. Roy. Astron. Soc. 456, 4524–4532. doi:10.1093/mnras/stv2858.

Yurchenko, S.N., Brady, R.P., Tennyson, J., Smirnov, A.N., Vasilyev, O.A., Solomonik, V.G., 2024a. ExoMol line lists – LIII. Empirical Rovibronic spectra Yttrium Oxide (YO). Mon. Not. Roy. Astron. Soc. 527, 4899–4912. doi:10.1093/mnras/stad3225.

Yurchenko, S.N., Lodi, L., Tennyson, J., Stolyarov, A.V., 2016b. Duo: A general program for calculating spectra of diatomic molecules. Comput. Phys. Commun. 202, 262 – 275. doi:10.1016/j.cpc.2015.12.021.

Yurchenko, S.N., Nogué, E., Azzam, A.A.A., Tennyson, J., 2023. ExoMol line lists – IL. Rovibronic spectrum of aluminium monochloride (AlCl). Mon. Not. Roy. Astron. Soc. 520, 5183–5191. doi:10.1093/mnras/stac3757.

Yurchenko, S.N., Owens, A., Kefala, K., Tennyson, J., 2024b. ExoMol line lists – LVII. High accuracy ro-vibrational line list for methane (CH_4). Mon. Not. Roy. Astron. Soc. 528, 3719–3729. doi:10.1093/mnras/stae148.

Yurchenko, S.N., Szabo, I., Pyatenko, E., Tennyson, J., 2018a. ExoMol Molecular line lists XXXI: The spectrum of C_2. Mon. Not. Roy. Astron. Soc. 480, 3397–3411. doi:10.1093/mnras/sty2050.

Yurchenko, S.N., Szajna, W., Hakalla, R., Semenov, M., Sokolov, A., Tennyson, J., Pavlenko, Y., Schmidt, M.R., 2024c. ExoMol line lists – LIV. Empirical line lists for AlH and AlD and Emission spectroscopy of AlD in $A\ ^1\Pi$ ($v = 0, 1, 2$). Mon. Not. Roy. Astron. Soc. 527, 9736–9756. doi:10.1093/mnras/stad3802.

Yurchenko, S.N., Tennyson, J., Bailey, J., Hollis, M.D.J., Tinetti, G., 2014. Spectrum of hot methane in astronomical objects using a comprehensive computed line list. Proc. Nat. Acad. Sci. 111, 9379–9383. doi:10.1073/pnas.1324219111.

Yurchenko, S.N. et al., 2022. ExoMol line lists – XLIV. IR and UV line list for silicon monoxide ($^{28}Si^{16}O$). Mon. Not. Roy. Astron. Soc. 510, 903–919. doi:10.1093/mnras/stab3267.

Yurchenko, S.N., Thiel, W., Jensen, P., 2007. Theoretical ROVibrational Energies (TROVE): A robust numerical approach to the calculation of rovibrational energies for polyatomic molecules. J. Mol. Spectrosc. 245, 126–140. doi:10.1016/j.jms.2007.07.009.

Yurchenko, S.N., Williams, H., Leyland, P.C., Lodi, L., Tennyson, J., 2018b. ExoMol line lists XXVIII: The rovibronic spectrum of AlH. Mon. Not. Roy. Astron. Soc. 479, 1401–1411. doi:10.1093/mnras/sty1524.

Zare, R.N., 1988. Angular Momentum: Understanding Spatial Aspects in Chemistry and Physics. Wiley.